

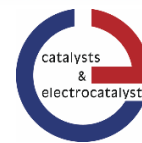
Advanced Characterization of Fe-N-C Catalysts using Nuclear Resonance Techniques



TECHNISCHE
UNIVERSITÄT
DARMSTADT



Graduate School of
**Energy Science
and Engineering**



Vom Fachbereich Material- und Geowissenschaften
der Technischen Universität Darmstadt

Zur Erlangung des akademischen Grades
Doktor-Ingenieur (Dr.-Ing.)
genehmigte Dissertation von

M.Sc. Stephan Wagner aus Florstadt

Erstgutachter: Prof. Dr. Ulrike I. Kramm
Zweitgutachter: Prof. Dr. Volker Schünemann

Darmstadt 2022



Title: Advanced Characterization of Fe-N-C Catalysts using Nuclear Resonance Techniques

Tag der Einreichung: 04.11.2021

Tag der mündlichen Prüfung: 14.01.2022

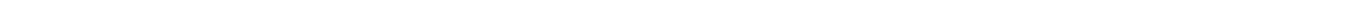
M.Sc. Stephan Wagner

Title: Advanced Characterization of Fe-N-C Catalysts using Nuclear Resonance Techniques
Darmstadt, Technische Universität Darmstadt

Jahr der Dissertationsveröffentlichung auf TUprints: 2022

Veröffentlicht unter CC BY-SA 4.0 International

<https://creativecommons.org/licenses/>



„Denken wir nur, wie bei der unvergleichlich bequemen und biegsamen Verteilung, welche die elektrische Energie gestattet, sich das Aussehen unserer Industrieorte ändern wird! Kein Rauch, kein Russ, kein Dampfkessel, keine Dampfmaschine, ja kein Feuer mehr, denn Feuer wird man nur noch für die wenigen Prozesse brauchen, die man auf elektrischem Wege nicht bewältigen kann, und deren werden täglich weniger werden.“

“Let us just think how the incomparably comfortable and flexible distribution which electrical energy permits will change the appearance of our industrial locations! No smoke, no soot, no steam boiler, no steam engine, yes no more fire, because fire will only be needed for the few processes that cannot be dealt with electrically, and they will be less every day.”

- Prof. Dr. Ostwald (1894)



Thesis Statement

I hereby formally declare that the presented dissertation is based on my original research and the result of my own independent work. I certify that this dissertation contains no material which has been accepted for the award of any other degree in my name, at any university or other tertiary institution and, to the best of my knowledge and belief, contains no material previously published or written by another person, except where references have been made in the text. In the submitted thesis the written copies and the electronic version are identical in content.

Florstadt, 04.11.2021

Stephan Wagner

Abstract

Catalyst systems for fuel cell applications are an important and auspicious aspect to turn the fossil fuel-based economy into a sustainable one based on regenerative energy stocks like solar, wind and water power. To efficiently regulate the demand and consumption of energy from such sources, a suitable storage medium is crucial. One such medium is hydrogen, which serves as a means for easy transportation, storage, direct energy conversion, or as a feedstock for additional chemical processes. The high costs of precious metals like platinum, which is most commonly used as catalysts in fuel cells, is one reason for the high acquisition costs of such systems and one reason that hydrogen has been largely neglected as a medium for commercial applications so far. New synthesis and fabrication approaches have reduced the overall use of platinum group metals (PGMs) as catalysts but such systems remain expensive in comparison to fossil fuels.

For the use in fuel cells, a nature-inspired catalyst system based on iron, nitrogen and carbon, the so called Fe-N-Cs, can be a cheaper alternative to precious group metal (PGM) catalysts for the oxygen reduction reaction (ORR). They have the advantage of high abundance of the three required elements and the fact that the preparation based on various and cheap precursors. To replace PGM catalysts by Fe-N-Cs, performance and lifetime need to reach specific target values. Therefore, knowledge about the structure and reaction mechanism are crucial to fully comprehend their degradation and durability behavior in order to replace platinum-based catalysts in fuel cell applications.

In this work, Fe-N-C-catalysts are examined using a custom-made, operando fuel cell assembly that is installed at a synchrotron beamline to characterize the catalyst's active site under operation conditions by nuclear forward scattering (NFS). NFS has the advantage of much faster measurement time in comparison to Mössbauer spectroscopy, while the spectra are much more difficult to analyze. In addition, Mössbauer spectroscopy (MS), nuclear inelastic scattering (NIS) and rotating disc electrode (RDE) of as prepared and deactivated catalysts, fuel cell measurements and post mortem analyses were performed and assessed as suitable techniques to conspicuous the active site. These techniques were accomplished in cooperation by electron paramagnetic resonance (EPR), as well as density functional theory (DFT) calculations for the interpretation of NIS.

Table of Content

1.....Scope of this Work.....	1
2.....Introduction	2
3.....Theoretical Background.....	9
3.1. Fe-N-C Catalyst Systems.....	9
3.2. Oxygen Reduction Mechanism.....	12
3.3. Electrochemistry.....	15
3.3.1. Rotating Disc Electrode (RDE).....	15
3.3.2. Fuel Cells.....	18
<i>Fuel Cell Performance</i>	21
<i>Impact of Operation Condition</i>	25
3.4. Nuclear Resonant Techniques	25
3.4.1. Mössbauer Spectroscopy.....	25
<i>Room-Temperature ⁵⁷Fe Transmission Mössbauer Spectroscopy (RT-MS)</i>	27
<i>Physical Concepts of the Mössbauer Effect:</i>	28
<i>Hyperfine Interaction</i>	32
<i>Spin Hamiltonian</i>	38
<i>Superparamagnetic Relaxation in Magnetic Nanoparticles</i>	39
<i>Low-Temperature ⁵⁷Fe Transmission Mössbauer Spectroscopy (LT-MS)</i>	40
3.4.2. Synchrotron.....	41
3.4.3. Nuclear Inelastic Scattering (NIS).....	41
3.4.4. Nuclear Forward Scattering (NFS).....	44
3.4.5. Synchrotron based ⁵⁷ Fe-Mössbauer Spectroscopy (SMS).....	46
3.5. Electron Paramagnetic Resonance (EPR)	47
4.....Experiments.....	48
4.1. Elucidating the Structural Composition of Fe-N-C Catalysts.....	48
4.2. Deactivation Experiments of the Active Site	52
4.3. Post Mortem MEA Characterization	55
4.4. Operando Fuel Cell Setup for Synchrotron-based Nuclear Resonant Techniques	57
5.....Results and Discussion.....	67
5.1. Elucidating the Structural Composition of Fe-N-C Catalysts	67
5.2. Deactivation Experiments of the Catalyst	77
5.3. Post Mortem MEA Characterization	91
5.4. Operando Fuel Cell Setup for Synchrotron based Nuclear Resonant Techniques	104
6.....Summary and Outlook.....	117
7.....Bibliography	i
8.....Appendix	xvi

1.....Conferences / Meetings	a
2.....List of Puplications.....	c

Table of Figures

- Figure 1: Overview of energy carrier of the net power generation in Germany 2018 (left). The values are given in TWh⁶. Prognosticated power mix of Germany in 2050 in GW⁷ (right).2
- Figure 2: Breakdown of the 2016 projected fuel cell stack cost at 1,000, 100,000, and 500,000 systems per year²⁴. Further information is given in the text.6
- Figure 3: Possible scheme of a Fe-N-C system. An iron atom (dark red) is four-fold coordinated by nitrogen (blue) embedded in a graphitic matrix (grey). The dangling bonds are saturated by oxygen (red) or hydrogen (white). The structure of the catalytic Fe-N-C site is still under investigation. Therefore, a five-, or six-fold coordinated iron atom as active site is still discussed in literature (see text).10
- Figure 4: Scheme for ORR. The index notation of the rate constant (k) is given as follow: (1) four-electron direct reduction to water (or OH⁻), (2) two-electron reduction to H₂O₂ (or H₂O₂⁻); (-2) oxidation of H₂O₂ (or H₂O₂⁻) to O₂; (3) electrochemical reduction of H₂O₂ to water (or OH⁻); (4) catalytic decomposition of H₂O₂ (or H₂O₂⁻) yielding reducible product (O₂); (5) desorption of adsorbed H₂O₂ (or H₂O₂⁻); (6) adsorption of H₂O₂ (or H₂O₂⁻). Indices b, *, and a, designate the bulk, vicinity of the disc electrode, and adsorbed species, respectively¹²⁰.12
- Figure 5: One plausible mechanism for ORR reaction catalyzed by a fivefold coordinated Fe porphyrin. For X = imidazole or a similar nitrogenous heterocycle. The catalysis probably proceeds, as it does in hemoproteins, such as peroxidase, catalase, and cytochromes P450, possibly with a minor contribution from side reaction H⁺ → H₂O₂. For simple Fe porphyrins lacking the suitable distal and proximal environments (X = H₂O or a residue of the graphite surface), the ferric-hydroperoxo intermediate decomposes via reactions H⁺ → H₂O₂ and by release of ·OH. At sufficiently reducing potentials it probably undergoes reduction to the ferrous-hydroperoxo intermediate, which is more susceptible to O-O bond heterolysis than the ferric analog¹²⁶.14
- Figure 6: Schematic scheme of the RDE setup in a three-electrode-configuration for current carrying electrodes (left). The setup contains the reference electrode (RE) which is connected by a high-ohmic resistance with the setup to avoid a current load. The potential difference between the RE, and the potential between the rotating working electrode (WE), where the catalyst is placed and the counter electrode (CE) give access to the overpotential of the WE. Here, V stands for a voltmeter, I for an ammeter, R for resistor and U for voltage. A closed view of the radial flow field under rotation to minimize the concentration gradient on the WE is given (right).16
- Figure 7: Current density overvoltage curve with the superposition of charge passage and absorption. This leads to the formation of an adsorption and desorption limit flow. The curve is separated in three regions: The kinetic region, where kinetic controlled process characterizes the system, a mixed region where transport and kinetic mechanism overlap and the diffusion-controlled region, here the species transport limits the reaction.16
- Figure 8: Profile of a fuel cell site cut. Hydrogen (red) is injected on the anodic side and streams through the gas flow channels, which are separated by the bridges of the bipolar plate (black), (left). By diffusing through the GDL the anodic catalyst accelerates the hydrogen oxidation reaction. The generated electrons have to pass the electric circuit (generation of electricity) in order to get to the cathodic side. The hydrogen ions (light red) diffuse through the MEA and recombine with oxygen (light blue) and electrons on the cathodic side catalyst. The formation and transport of water molecules (dark red, blue) goes along the flow field of the cathodic side (right).19
- Figure 9: Fuel cell performance. The impact of different types of losses is depicted as described in the text. This figure was taken from¹⁴⁷.23
-

- Figure 10: Scheme of Mössbauer setup (left). The vibrator moves the radioactive source with a constant velocity and controlled by the velocity feedback and driver. The source emits the radiation which excited the sample nucleus. The decay of the excited state emits a γ -quant which will be collected by the proportional counter. The single and multi-channel analyzer will process the data, whereas the master oscillator is used for adjustment. Signal processing (right): The source will be moved with constant acceleration. Each decay can be connected with a defined velocity by the channel analyzer. The total number of pulses will show twice the spectrum for positive and negative velocity, respectively. Folding and transforming the spectrum to absorption or transmission per percent follows in the common Mössbauer spectrum. Adopted from V. Schünemann lecture "Grundlagen der Mößbauerspektroskopie" ¹⁶⁶.27
- Figure 11: Three separated energy sections of the γ -emission and absorption lines caused by recoil of resting free nuclei. Resonant absorption is not possible, since there is no overlap between the emission and absorption line. (Picture traced in from ¹⁵¹). Only if the emitted γ -quant has an energy $E_0 + ER$ and $E_0 \lesssim \Gamma$ the emission and absorption lines overlap and resonance fluorescence can occur.....29
- Figure 12: The ⁵⁷Co decay scheme is shown (left)^{175, 176}. The detailed description of the mechanism is given in the text. Transition scheme of the source with the emission and absorption of the γ -quant by the sample nuclei (right)¹⁷⁷.32
- Figure 13: Energy scheme of the electric monopole interaction between the nucleus and the electron density which results in a shift of the nuclear state visible as isomer shift in the Mössbauer spectrum. As the source is not ideal, a shift of δE_g and δE_e in the energy level is already obtained (left). Resulting Mössbauer spectrum of the monopole interaction which results in a singlet. The resulting isomer shift represents the different chemical environment of source and absorber (right).34
- Figure 14: Energy scheme of the quadrupole splitting. A nuclear state with $I = 12$ and an EFG = 0 shows no quadrupole interaction. Therefore, the ground state of ⁵⁷Fe is not affected (left). For the first excited nuclear state $I > 32$ the splitting in two nuclear sublevels is observed as an EFG $\neq 0$ caused an eigenvalue $V_{zz} > 0$. Resulting Mössbauer spectrum of the quadrupole interaction which results in a doublet. The resulting isomer shift represents the different chemical environment of source and absorber, whereas the splitting gives the energy difference of both states (right).36
- Figure 15: Energy scheme of the magnetic dipole splitting (left). Simulated six-line pattern with the intensity ratio 3:2:1:1:2:3 (right). The energy shift is caused by the electric monopole interaction, whereas the value $3\Delta EM, g + \Delta EM, e$ gives access to the internal magnetic field and therefore information about the electronic configuration.38
- Figure 16: Schematic Illustration of the NIS experiment. In the storage ring, the electrons are accelerated. By distraction of the electrons by the undulators the synchrotron light is emitted and hits the carbon based high-heat monochromator. The included high-resolution monochromator, based on a silicon single crystal, cuts the full width at half maximum to less than 1 meV. The synchrotron pulse hits the sample and excites the nuclear states. The resulting inelastic spectra is recorded by an avalanche photodiode detector (APD). During the pulses the APD is switched off, in order to gate out elastically scattered 14.4 keV photons, so that only delayed fluorescence photons corresponding to nuclear absorption are detected, Figure taken from ²⁰¹.43
- Figure 17: Scheme of a NFS experiment. In the storage ring, the electrons are accelerated. By distraction of the electrons by the undulators the synchrotron light is emitted and hits the carbon based high-heat monochromator. The included high-resolution monochromator, based on a silicon single crystal, cuts the full width at full maximum to less than 1 meV. The synchrotron pulse hits the sample and excites the nuclear states. The resulting quantum beats are detected by an

(avalanche photodiode detector (APD). Only the desired forward scattering is detected, as the APD is switched off during the synchrotron light pulses ²⁰¹	44
Figure 18: Position of measuring spots located on the MEA and investigated by SMS (top). The series of cooper sample holders shows the cut MEA pieces in line (bottom). Each holder was stacked over one another and fixed by screws. The so realized stack was mounted in the cryostat.	57
Figure 19: The operando fuel cell stack is shown. Top view on the flow field with the blue selling (left). The red cables are part of the cell heating system which is implemented in the cell. Both flow-fields with the prepared MEA before closing the cell (middle). The drill holes on the site are needed for the temperature sensor to adjust the cell temperature. The closed cell with the blue selling can be seen (right). The incoming synchrotron beam will be shot through the cell in the faced view.	59
Figure 20: Operando fuel cell setup. For reason of simplicity the wiring is not shown. A fully explanation of the setup is discussed in the text.	61
Figure 21: Top view of the standard flow field from Scribner Associates as it is used in our laboratory (left) and the operando fuel cell flow field (right).	63
Figure 22: Pt-Pt reference measurement on the standard fuel cell test station in our laboratory (left). Operando fuel cell test with Pt-Pt reference (right). Experimental conditions for both setups: H ₂ -O ₂ , cathode loading 3.2 – 3.5 mgPt cm ⁻² , N212 membrane, 1 bar gauge back pressure, 0.2 L min ⁻¹ oxidant and fuel flow, cell temperature 80 °C, 100% relative humidity, whereas for the operando cell, the temperature of the pipes where set to 75 °C to avoid condensation inside the cell.	63
Figure 23: Photograph of the complete operando fuel cell setup as tested in the lab and used at the synchrotron. Further information on the component and functions are given in the text.	64
Figure 24: Operando fuel cell mounted at P01 beamline. The flexible pipes allow for adjusting the cell's position for the experiments.	65
Figure 25: Electrochemical performance of HT600Cl at 1500 rpm in 0.1 M H ₂ SO ₄ (left) . Related RT-Mössbauer spectrum fitted only with FeN ₄ containing sites (right). No inorganic iron species are indicated ⁵¹	68
Figure 26: STEM images of the investigated catalyst, including a count line profile. No iron related clusters are observed ⁵¹	69
Figure 27: X-band EPR spectra of the catalyst and carbon-supported porphyrin (FeTMPPCl/CB) that was used as a precursor and reference ⁵¹	69
Figure 28: pDOS vibration data of the reference Fe-porphyrin sample (left) and FePc as measured during the beam time (right).	71
Figure 29: NIS spectrum of the investigated catalyst (left) and the resulting pDOS vibration data (right) ⁵¹	72
Figure 30: Mössbauer spectra obtained at 77 K, B = 0 T (left), 4.2 K with B = 0.1 T (middle) and 4.2 K with B = 5 T (right). The Mössbauer parameters are listed in Table 8 ⁵¹	73
Figure 31: Calculated iron pDOS spectra with specific vibration modes as addressed in the text. (left) Model A (fir green, top left): Fit of the iron pDOS based on the simulated spectra of iron oxide clusters, low spin oxy-heme type site with trimethylamine and O ₂ as axial ligands (green), iron phthalocyanine-type coordination embedded in carbon (mid spin) (blue) and high spin ferric FeN ₄ -sites (FeTMPPCl) with chlorine as axial ligand (dark red). (right) For model B (orange): The simulated spectra of iron oxide clusters, low spin oxy-heme type site with trimethylamine and O ₂ as axial ligands (green) and iron phthalocyanine-type coordination embedded in carbon (mid spin) (blue) were included similar to model A. Further a ferric FeN ₄ -site with pyridine as axial ligand was added (red). The atom color code is given as follow: grey: carbon, white: hydrogen, blue: nitrogen, green: iron, cyan: chlorine, red: oxygen.	77

Figure 32: RDE curves of the three different pure and poisoned catalysts recorded at 1500 rpm, 10 mV s ⁻¹ , in 0.1 M H ₂ SO ₄ . The category plots of kinetic current densities at 0.75 V for the pristine (dark color filled) and deactivated catalysts (light color filled). Due to the deactivation a reduction of current density is seen ⁵²	78
Figure 33: Models for the deactivation of FeN ₄ sites by anion binding: The anion interacts with the active site, while the ORR is still possible (X= O ₂). (left) The active site is completely deactivated if a five-fold active site is assumed. (right).....	79
Figure 34: Mössbauer spectrum of pristine (left) and deactivated HT800Cl catalyst with the new doublet species (right) ⁵²	79
Figure 35: Mössbauer spectrum of pristine (left) and deactivated HT800Cl Mössbauer spectrum with the new doublet species (right) ⁵²	80
Figure 36: Difference spectra of normalized absorption of the initial and poisoned catalyst is given. For the sulfur free catalysts, a reduced area is seen, whereas for the sulfur containing catalyst the area increases ⁵²	83
Figure 37: Free running isomer shift and quadrupole splitting are plotted against each other, with the corresponding errors. Introducing SO ₃ ²⁻ ions result in higher isomer shifts and quadrupole splitting values. This is true for both, HT600HCl and HT800HCl catalysts, whereas HT800HCl+S shows a converse dependency.	84
Figure 38: Possible axial binding of sulfite species to FeN ₄ -sites by assuming a six-fold coordinated iron site where the SO ₃ ²⁻ ion can attach.....	85
Figure 39: The pDOS data of the deactivated and pristine catalyst HT600HCl.	86
Figure 40: Change in NFS spectra by introducing the anion to the catalyst system. The pristine and deactivated catalyst HT600HCl is seen.	89
Figure 41: LT-Mössbauer spectra of the pristine and deactivated catalyst HT600HCl at 77 K with no applied external magnetic field. (left) The same catalysts measured at 4.2 K with a magnetic field of 5 T. The fitted deactivated species is given in cyan. (right)	90
Figure 42: RT-Mössbauer spectra of the investigated catalyst powder with three organic iron sites. (left) LT-SMS spectrum of the prepared MEA at position C at 4 K. Beside the three doublet sites three inorganic sextet species appear. (right)	92
Figure 43: LT-SMS spectra obtained at 4 K of the fresh prepared MEA at three different positions. The insert gives schematically the flow field with the investigated positions. (left) Magnetic field dependent LT-SMS spectra at position C. (right)	94
Figure 44: LT-SMS spectra obtained at 4 K of the low temperature treated MEA at four different positions. The insert gives schematically the flow field with the investigated positions. (left) Magnetic field dependent LT-SMS spectra at position C. (right)	95
Figure 45: (left) LT-SMS spectra obtained at 4 K of the HT-PEM MEA at four different positions. The insert gives schematically the flow field with the investigated positions. (bottom) the resulting loss of absorption for each position. (right) Magnetic field dependent SMS LT-Mössbauer spectra at position C.....	97
Figure 46: Direct comparison of the different MEAs measured with LT-SMS. Untreated MEA at 0 T (black), MEA with applied magnetic field of 5 T (grey). MEA after fuel cell test at low operation temperature (orange) and with applied magnetic field (dark yellow). MEA treated at high operation temperature during fuel cell operation without magnetic field (purple), whereas the field depend Mössbauer spectrum is given (rose).....	98
Figure 47: Temperature depend SMS measurements of the sample for four different temperatures are shown.	99
Figure 48: Temperature dependence of isomer shift δ_{iso} from the found doublet species (left, top), whereas the temperature dependence of the quadrupole splitting is depicted ΔEQ . (right, top) .	101

Figure 49: Temperature dependency of the relative species area. The value of the relative species area is given on the vertical-axis in percent.....	102
Figure 50: Temperature dependency calculated with ΘM values and related errors as published by Sougrati et al. ¹⁶⁵	103
Figure 51: RT Mössbauer spectra of the porphyrin (FeTMPPCl/CB) based reference system (left), the freshly sprayed GDL with FeTMPPCl/CB (middle), and Mössbauer spectrum after the fuel cell operation in the standard fuel cell test station $t = 2 \text{ h } 20 \text{ min}$ (right), are given.....	104
Figure 52: Standard fuel cell measurement of the porphyrin-model system as obtained in the SCRIBNER Associates Inc. setup (left). Operando fuel cell measurement recorded during the beamtime (right). Experimental conditions for the standard setup: H_2/O_2 , cathode loading $3.2 - 3.5 \text{ mg cm}^{-2}$, N212 membrane, 1 bar gauge back pressure, 0.2 L min^{-1} oxidant and fuel flow, cell temperature $80 \text{ }^\circ\text{C}$, 100% relative humidity, whereas for the operando cell, the temperature of the pipes where set to $75 \text{ }^\circ\text{C}$ to avoid condensation inside the cell. All other conditions were kept the same.....	106
Figure 53: NFS spectra of the porphyrin-based model catalyst powder, GDL and after the fuel cell test (top), and recorded under operation conditions in the operando fuel cell setup at the P01 beamline at DESY (bottom). Given intensity values reflect logarithmic plots of normalized data.	107
Figure 54: Averaged potential and current density that were applied during the recording of the NFS spectra. Under H_2/N_2 (left) and H_2/O_2 conditions (right).	108
Figure 55: RT Mössbauer spectra of the investigated Fe-N-C catalyst at different stages of MEA preparation and after operation. Mössbauer spectrum of the fresh prepared catalyst powder (left, top), sprayed GDL without considering the sextet species (right top), hot pressed MEA (left bottom) and MEA after the fuel cell operation in the standard fuel cell test station are given (right, bottom).....	110
Figure 56: Pt-Fe-N-C catalyst reference measurement in the standard fuel cell setup (left). Operando fuel cell measurement with Pt-catalyst on the anode, MEA measured during the beamtime (right). Experimental conditions for the standard setup: H_2/O_2 , cathode loading $3.2 - 3.5 \text{ mgPt cm}^{-2}$, N212 membrane, 1 bar gauge back pressure, 0.2 L min^{-1} oxidant and fuel flow, cell temperature $80 \text{ }^\circ\text{C}$, 100% relative humidity, whereas for the operando cell, the temperature of the pipes where set to $75 \text{ }^\circ\text{C}$ to avoid condensation inside the cell.	112
Figure 57: NFS spectra at three different states in the operando fuel cell. (dark green) Reduced catalyst state under nitrogen (cathode) and hydrogen (anode) at 0.6 V . (blue). The catalyst during oxygen reduction reaction with oxygen at the cathode and hydrogen on the anode, measured at a potential of 0.6 V . (light green) Same condition as for the dark green spectrum but after the degradation test and the measurement of a second polarization curve.....	113
Figure 58: Averaged potential and current density that were applied during the recording of the Fe-N-C NFS spectra. Under H_2/N_2 (left) and H_2/O_2 (right) conditions.	115

List of Tables

Table 1: Most common fuels and chemical storage systems. Data taken from Karl-Friedrich Ziegahn ¹⁴ .	4
Table 2: Overview of the PEMFC system. Data are taken from ^{143, 144}	19
Table 3: 3d orbital population of iron in the most common spin and oxidation states. Table is inherited from DeBrunner ¹⁷⁹	35
Table 4: Overview of the most common isomer shift ranges appearing in Fe-N-C catalysts and molecular FeN ₄ centers. The data is obtained as a combination of Ref ¹⁵¹ , Ref ¹⁰⁷ and Ref ¹⁸⁰ and given for room temperature.....	36
Table 5: Comparison between a 3 rd generation undulator source and a commercially available 57Co source with 370 MBq activity (values taken from Sturhahn et al. ¹⁹³ and ¹⁵²).....	41
Table 6: Comparison between NFS and conventional Mössbauer spectroscopy. Table taken from Paulsen et al. ²⁰⁹	45
Table 7: RT-Mössbauer parameters of HT600Cl ⁵¹	68
Table 8: Mössbauer parameters as obtained from the analysis of the LT-Mössbauer spectroscopy displayed in Figure 30. The absorption areas are given for the spectrum obtained at 4.2 K, 0.1 T. All simulations shown in Figure 30 have been analyzed with one consistent data set, except some different values in linewidths G, line ratio I1: I2: I3, area, and hyperfine field <i>Bhf</i> are given in the corresponding footnotes ⁵¹	74
Table 9: Mössbauer parameters of the three investigated pristine and deactivated catalyst ⁵²	81
Table 10: Related Mössbauer parameters of deactivated species ⁵²	82
Table 11: Comparison of Mössbauer parameters observed for different axial ligands to ferrous FeN ₄ -sites. Data indicated with * were taken from Taube ²⁵⁴ and Kramm ²⁴⁵	83
Table 12: Lamb-Mössbauer factors <i>fLM</i> as obtained from the normalized, inelastic area of the investigated poisoned and initial catalysts.	88
Table 13: Mössbauer parameters of the deactivated species as found by LT-MS.	90
Table 14: Electrochemical characteristics as obtained from the RDE measurements.	91
Table 15: Mössbauer parameters of the investigated catalyst at RT.	93
Table 16: RT Mössbauer parameters of the porphyrin (FeTMPPCl/CB) based reference system and at different preparation steps.....	105
Table 17: Mössbauer parameters of the catalyst investigated in the operando fuel cell at the different preparation steps.....	111

Table of Supporting Figures and Tables

S 1: Calculated Lamb-Mössbauer factor based on equation (29) for ^{57}Fe . Different values for θM (from $\theta M = 60 \text{ K}$ to $\theta M = 360 \text{ K}$) are given ²⁷⁵	xvi
S 2: Circuit diagram of the electronic load to measure and manipulate the potential and current of the fuel cell during operation. The IRFS7430TRL7PP is the electric consumer made of a MOSFET. .	xvii
S 3: Experimental X-band EPR spectra of the catalyst powder (a) and the precursor (b) ($\nu_{\text{mw}} = 9.39 \text{ GHz}$ and EPR spectral simulations for (c) the catalyst powder (Simulation parameters: $g_{\text{eff}} = [5.983 \ 5.983 \ 1.985]$ and Lorentzian line broadening of $10.6 - 10.9 \text{ mT}$) and (d) the precursor (Simulation parameters: $g_{\text{eff}} = [5.982 \ 5.983 \ 1.9956]$ and Lorentzian line broadening of $7 - 7.7 \text{ mT}$ for the precursor.). See also SI of Wagner et al. ⁵¹	xviii
S 4: NIS spectrum of HT600HCl in the pristine and deactivated state.	xix
S 5: DFT calculations of four possible ways of sulfite ion attachment on FeN4-site, a) Trimethylamin + SO_3^{2-} over O, b) $\text{O}_2 + \text{SO}_3^{2-}$ over O, c) $\text{O}_2 + \text{SO}_3^{2-}$ over S and d) Trimethylamin + SO_3^{2-} over S.....	xx
S 6: Low temperature ($80 \text{ }^\circ\text{C}$) fuel cell polarization curves of the Fe-N-C catalyst used for the post mortem Mössbauer study (5.3) at beginning of test, after 12h and 24 h. MEA 6 PEMFC was used for in total 24 hours.	xxi
S 7: High temperature ($165 \text{ }^\circ\text{C}$) fuel cell polarization curves of the Fe-N-C catalyst used for the post mortem Mössbauer study (5.3) at beginning of test and after 12h	xxi
S 8: Fitting approach of the resulting operando NFS data of the model catalyst under different operation conditions.....	xxii
S 9: Simulated Mössbauer spectra considering the iron species that were used for the fit of the NFS data. Data are provided in Table S 3.....	xxiii
S 10: Mössbauer fitting with the Sext4 species.....	xxiv
S 11: fuel cell polarization curve measured at the synchrotron after 1 h of operation with the operando FC setup. The test was performed for the Fe-N-C catalyst, catalyst loading and further conditions can be found in chapter 5.4.	xxv
S 12: (left) The sealing like it was used for the operando cell. The custom-made silicon sealing (blue) fix the membrane (orange) and tied the cell. (right) An advanced sealing design is shown. Here, two O-rings are used to close the cell. The lower O-ring (dark blue) is placed in a hollow, whereas the upper O-ring is fixed on a stamp. By bringing both flow fielder (black) together the membrane is fixed in between the O-rings and the cell is closed tightly without cutting through the membrane.	xxv
Table S 1: Spectral areas and spin counts determined from X-band EPR ($\nu_{\text{mw}} = 9.39 \text{ GHz}$) on two precursor samples (FeTMPPCl/CB) with known Fe(III) content ⁵¹	xviii
Table S 2: Spectral areas, spin count and Fe(III) content determined from X-band EPR measurements on three samples of the catalyst by comparison with the precursor sample. Spin quantitation was performed based on a simulation of the high-spin Fe(III) EPR signal (values in parentheses are determined from the experimental data directly) ⁵¹	xix
Table S 3: Calculated Mössbauer parameters based on the model approach of S 9 and S 10.	xxiii
Table S 4: Mössbauer parameters for the fitting approach including the sextet species.	xxiv

Index of Abbreviations and Symbols

AFC	Alkaline Anion Exchange Membrane Fuel Cell
APS	Advanced Photon Source
BEV	Battery Electric Vehicle
CE	Counter Electrode
CV	Cyclic Voltammetry
DEMS	Differential Electrochemical Mass Spectrometry
DESY	Deutsches Elektronen-Synchrotron
DFT	Density Functional Theory
DOE	Department of Energy
EC	Electron Capture
EFG	Electric Field Gradient
EPR	Electron Paramagnetic Resonance
ESRF	European Synchrotron Radiation Facility
ESRR-EBS	European Synchrotron Radiation Facility-Extremely Brilliant Source
EXAFS	Extended X-Ray Absorption Spectroscopy
FC	Fuel Cell
FCEV	Fuel Cell Electric Vehicle
FeAc	Iron Acetate
FEL	Free Electron Laser
Fe-N-C	Class of Iron Containing Catalyst System with a Four Fould Coordination by Nitrogen and Possible Ligands
FePc	Iron Phthalocyanine
Fe-phen	Iron 1,10 Dicyandiamide, -Phenanthroline Chloride
FeTMPPCL	Iron Porphyrin
GC	Glassy Carbon
HAADF	High-Angle Annular Dark-Field
HER	Hydrogen Evolution Reaction
HOR	Hydrogen Oxidation Reaction
IBAME	International Board on the Application of the Mössbauer Effect
LHV	Lower Heating Value
LT-MS	Low Temperature Mössbauer Spectroscopy
MCFC	Molten Carbonate Fuel Cells
Me-N-C	Class of Metal Containing Catalyst System with a Four Fould Coordination by Nitrogen
MOF	Metallic Organic Framework
MOSFET	Metal-Oxide-Semiconductor Field-Effect Transistor
MS	Mössbauer Spectroscopy
NAA	Neutron Activation Analysis
NFS	Nuclear Forward Scattering
NIS	Nuclear Inelastic Scattering
NPMC	Non-Precious Metal Catalyst
NRXS	Nuclear Resonance Vibrational Inelastic X-Ray Scattering
NRVS	Nuclear Resonance Vibration Spectroscopy
OCP	Open Circuit Potential
OER	Oxygen Evolution Reaction
ORR	Oxygen Reduction Reaction
PAFC	Phosphoric Acid Fuel Cell
pDOS	Partial Iron Density of Phonon States

PEEK	Polyetheretherketone
PEM	Proton Exchange Membrane
PEMFC	Proton Exchange Membrane Fuel Cell
PETRA III	Positron-Electron Tandem Ring Accelerator III
PETRA IV	Positron-Electron Tandem Ring Accelerator IV
PGM	Platinum Group Metals
ph	Photon
pH	Logarithmic and Inversely Indicator the Concentration of Hydrogen Ions in Solution
POM	Polyoxymethylene
PPI	Polypropylene Polybenzyl Isocyanate
PTFE	Polytetrafluoroethylene
RDE	Rotating Disc Electrode
RE	Reference Electrode
RHE	Reverse Hydrogen Electrode
rpm	Rounds Per Minute
RT-MS	Room Temperature Mössbauer Spectroscopy
SHE	Standard Hydrogen Electrode
SMS	Synchrotron based Mössbauer Spectroscopy
SOFC	Solid Oxide Fuel Cell
Spring-8	Super Photon Ring – 8 GeV
Spring-8-II	Super Photon Ring – 8 GeV II
STEM	Scanning Transmission Microscopy
TEM	Transmission Electron Microscopy
THF	Tetrahydrofuran
ToF-SIMS	Turn of Flight Second Ion Mass Spectroscopy
TPD	Temperature Programmed Desorption
WE	Working Electrode
XANES	X-Ray Absorption Near-Edge Structure Spectroscopy
XAS	X-ray Absorption Spectroscopy

1. Scope of this Work

The present thesis describes the planning, construction, and successful implementation of an operando fuel cell setup for synchrotron-based nuclear resonance experiments that allows the structural examination of iron-nitrogen-carbon (Fe-N-C) catalysts. The experiments, intended to uncover the processes at the active site, are based on Mössbauer spectroscopy (MS), synchrotron based Mössbauer spectroscopy (SMS) nuclear inelastic scattering (NIS) and nuclear forward scattering (NFS). Further deactivation experiments of the catalyst are introduced as well as post mortem analyses of membrane electrode assemblies (MEAs) to shed light on the reaction mechanism and degradation.

The thesis first discusses the urgency of a global energy transition from fossil fuel-based to renewable energies and the associated problems of energy storage, before describing the role that a hydrogen economy may play in reconciling climate change and the industrial and social challenges that come with such an energy transformation (Chapter 2).

Chapter 3 introduces the chosen catalyst system (Fe-N-C), the oxygen reduction reaction (ORR), electrochemical setups as well as electron- and nuclear resonant techniques used in the experiments. Moreover, this chapter explains the importance of the physical background and acknowledges the limitations of the research design.

Chapter 4 describes the experiments performed for different synchrotron beamtimes and the associated laboratory work, as well as additional deactivation experiments that were analyzed with nuclear resonance techniques and electrochemically with rotating disc electrode (RDE) measurements. Furthermore, a combination of different nuclear resonance techniques was combined to better understand Fe-N-C catalysts. The benefits of operando fuel cell experiments (under reaction conditions) at the synchrotron are discussed and the usefulness of post mortem analysis of differently treated membrane electrode assemblies (MEAs) is demonstrated.

The last chapter summarizes the implemented experiments and their results and offers some promising avenues of future experiments, which have been thought through but lay beyond the scope of this thesis.

2. Introduction

The twenty-first century marks a turning point in the history of humankind. Never before was the impact that people have on our planet so obvious. Owing to the work of an international network of scientists and novel possibilities to generate and analyze large amounts of data, the dramatic dimensions of anthropogenic climate change and the concomitant destruction of our environment have become accessible and tangible¹⁻³. In 2015, the Paris Agreement of the United Nations Framework Convention on Climate Change set the goal to reduce global CO₂-emissions until 2100 and to limit the increase of the average global temperature to at most 2 °C above the pre-industrial level⁴. For Germany, this implies a reduction of CO₂-emissions from 977 million tons in the base year 1990 to at most 195 million tons and in best case 48.9 million tons until 2050, which equals a reduction of 80% and 95%, respectively⁵. Another key challenge is the ambitious target to back out of coal, natural gas, and nuclear power as energy sources until 2050. As Figure 1 shows, a variety of different energy sources were used in 2018. More than 40% of the produced energy came from renewable sources like biomass, photovoltaic, water and wind. In 2050, approximately 46% of the energy production is expected to be supplied by photovoltaic only. Together with off- and on-shore wind turbines, 87% of the total energy production will be based on solar and wind power. However, the mismatch between the available energy from renewable sources and energy consumption levels already results in considerable fluctuations in price and overloading power grids. Therefore, an effective and flexible storage medium is needed for the excess energy which provides sufficient energy for consumption during dark doldrums, thus stabilizing the power grids. Chemical storage media like hydrogen are the only feasible option to provide an energy storage system for postindustrial society based on renewable energy sources and opens the way for commercial use of electrolyzers and fuel cells.

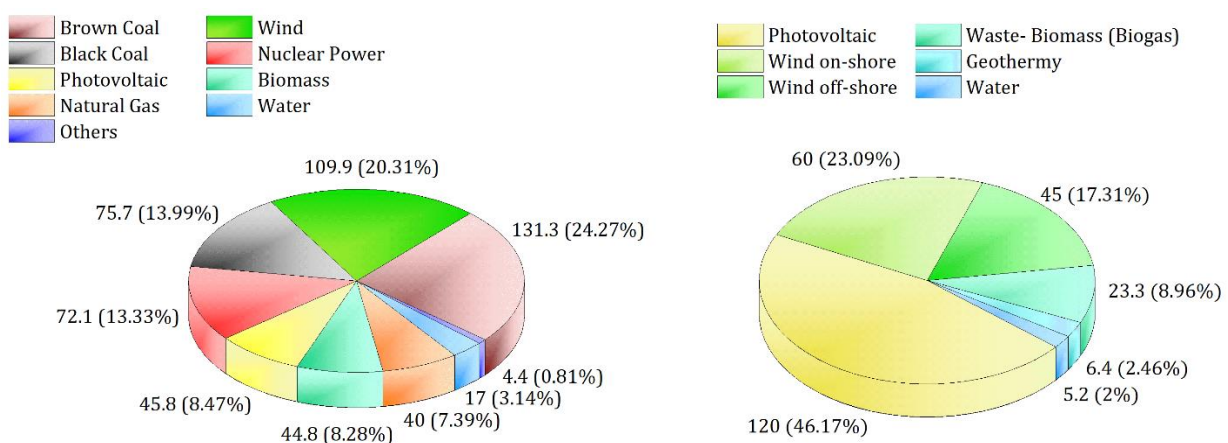


Figure 1: Overview of energy carrier of the net power generation in Germany 2018 (left). The values are given in TWh⁶. Prognosticated power mix of Germany in 2050 in GW⁷ (right).

The present work gives insights to the complex nature of Fe-N-C catalysts, which are used for fuel cell applications and can play an important role for a hydrogen-based economy. So far, precious metal catalysts are used to accelerate the ORR in fuel cell systems but have the general drawback of high costs. To reduce the costs of fuel cell systems, cheaper catalysts or a dramatic reduction of the catalyst load need to be realized. Here, Fe-N-C catalysts are found as cheaper and non-toxic alternative^{8, 9}. Nevertheless, the lack of understanding the reaction mechanism and degradation processes are the most challenging tasks to replace precious metal catalysts by Fe-N-C systems for fuel cell applications.

The hydrofication of the transport sector may be considered as first step towards a hydrofication of energy production as a whole and could make the energy transition possible if it spreads to the heating-, industry- and mobility sectors. Shane et al. have paved the way using solar-powered technologies for the electrochemical production of hydrogen through water electrolysis. The authors investigated, i) the environmental aspects of the production processes, ii) the generation of hydrogen close to the point of utilization, and iii) the purity of the produced hydrogen. They also suggested plausible early-stage applications in seven distinct areas: (i) grid-level energy storage, (ii) local or isolated permanent energy systems, (iii) transportation, (iv) precursors for the production of high-margin products, (v) the military industry, (vi) the space industry, and (vii) the agricultural sector¹⁰.

Energy consumption, most notably energy used for transportation and mobility, has a large impact on global CO₂-emissions, which are caused mainly by the burning of fossil fuels, and has more than doubled since 1970¹¹. The transport sector has also been criticized for releasing noxious gases and fine dust⁶. Therefore, alternative propulsion systems with low or no emissions, which are based on renewable energies, are needed¹². However, to achieve the goals of the Paris agreement, not only the transport sector needs to find alternatives; the human carbon footprint needs to be reduced across the board. It is thus necessary to enhance the acceptance of new technologies and to invalidate political and societal concerns to encourage the use of renewable energies and storage systems.

As seen in Table 1 hydrogen shows higher energy densities per kilogram than fossil fuels or battery systems. Further, the volumetric energy density is higher than that for common Lithium-Ion batteries. But the high storage pressures and the need of very pure gas, make advanced, oil free compressors and pressure systems necessary, whereas the electrochemical reaction inside the fuel cell are mainly accelerated by the use of expensive and rare precious metals like platinum (Pt). Table 1 illustrates the advantages of liquid fuels, caused by the high energy density, low specific weight and the relatively easy handling, which are a few reasons for their wide spread use. Nevertheless, the emission of CO₂, fine dust and noxious gases, as well as the finite resources of fossil energy carriers are the main drawback of these resources. A lot of research is done in the field of power-to-X (X: gas, synthetic fuels, etc.), especially in the reduction of CO₂ to hydrocarbons for synthetic fuels¹³. This approach can reduce the consumption of fossil fuels by creating carbon neutral process loops. For automotive propulsion, fuel cell applications

are promising if so-called green hydrogen is used, i.e., using renewable energy sources like solar, wind and water power. It utilizes the energy stored in the chemical bond of the H₂ and O₂ molecules to overcome the emission of CO₂, fine dust and noxious gas.

Table 1: Most common fuels and chemical storage systems. Data taken from Karl-Friedrich Ziegahn ¹⁴.

	Volumetric Energy Density		Specific Weight	Mass-related Energy Density	
	kWh l ⁻¹	MJ l ⁻¹	kg l ⁻¹	kWh kg ⁻¹	MJ kg ⁻¹
Benzine	8.6	31.0	0.7	12.2	44.0
Super	8.4	30.3	0.7	12.0	43.2
Bioethanol	5.9	21.2	0.8	7.4	26.6
Diesel	9.6	35.0	0.8	11.8	42.7
Plant Oil	9.2	33.1	0.9	10.2	36.8
Biodiesel	8.9	32.0	0.8	10.3	37.0
Synthetic Fuel	8.0 – 10.0	30.0 – 35.0	0.8 – 0.9	10.0 – 12.0	38.0 – 44.0
Liquefied Petroleum Gas	6.4	23.0	0.5	12.8	46.1
Compressed Natural Gas (CNG)	11.5	41.4	0.7	8.6	8.6
Hydrogen (liquid, –253 °C)	2.3	8.3	0.07	33.3	119.9
Hydrogen 200 bar	0.5	1.8	0.02	33.3	119.9
Hydrogen 690 bar	1.3	4.5	0.04	33.3	119.9
Battery (Lead)	0.05	0.2	1.1	0.06	0.22
Battery (Li-Ion)	0.5	1.8	0.4	0.2	0.72
Black Coal	8.8	31.7	1.1	8.1	29.3
Wood Pellets	3.1	11.2	0.7	4.8	17.3

To produce 1 kg of H₂ (dry) 9.7 kWh of heat and 2.8 kWh of power are necessary ¹⁵. The resulting hydrogen will be stored in pressure tanks or fed directly into an existing gas grid as a combustion additive, similar to the early day used city gas ¹⁴. The subsequent combustion in thermal power stations or gas turbine power plants is one option to use the stored energy, which is useful as long as pure hydrogen cannot be used in fuel cell systems on a larger scale. The latter would be an elegant way to transform excess electric power produced by the high fluctuation inherent renewable energy systems and to store it for short- or long-term needs. To avoid CO₂ emissions the direct use of hydrogen is intended to replace natural gas and use hydrogen as fuel for commercial applications and industrial processes.

The transformation of electric energy in electrical-, chemical- or mechanical storage systems comes with energy dissipation. Conversion losses occur, for instance, due to (dis-)charging of batteries or the

splitting of water to hydrogen and oxygen. Here, efficient conversion systems need to be realized to minimize such losses and make the storage of energy more effective.

As the values given in Table 1 are not very feasible, an overview contrasting diesel, fuel cell and battery storage systems for automotive vehicles is provided here.

Imagine a car using a combustion engine with an average range of 600 km. This car is filled with 33 kg of diesel (400 kWh to reach the average range) and uses a gasoline tank of 43 kg. The tank needs a volume of 46 l, 37 l thereof for the fuel. A fuel cell electric vehicle (FCEV) with a range of 600 km needs a pressure tank of 700 bar instead of a gasoline tank. The tank weighs 150 kg in total and stores 6 kg of hydrogen (200 kWh). Here, the tank has a volume of 250 l and stores 150 l of hydrogen (equal to 6 kg). A battery electric vehicle (BEV) with the same range needs an energy of 120 kWh, but 840 kg and 432 kg for the system and battery, respectively. Moreover, the battery system needs a total volume of 650 l, 350 l thereof for the battery itself¹⁶. It is immediately obvious that the high weight of the BEV is a crucial issue, raising the question whether a vehicle of more than 2.5 tons is really necessary to transport a person of 100 kg. An additional drawback of BEVs are the high costs for resources like lithium, aluminum and cobalt, the geopolitical dependence on a few countries of origin, the problematic mining conditions and the associated environmental destruction, the charging time of the battery, and the enormous challenge for the power grid^{6, 17-21}.

The transition to a hydrogen-driven society can only be successful if the lifetime, performance and reliability of fuel cell electric vehicles (FCEV) are in the same range as other commercially available transportation systems with combustion engines. This includes service intervals, the maximum range, refueling time, costs, etc. In short, despite all political and societal incentives, the technology needs to fulfill the same and even higher standards as existing solutions to be widely adopted.

Especially for heavy-duty and midsize commercial vehicles, fuel cell systems are superior to battery systems¹⁶. Unfortunately, FCEV are still more expensive as combustion engines and the hydrogen station network across Germany and Europe is still in its infancy^{22, 23}.

In 2016, the U. S. Department of Energy (DOE) calculated the cost allocation of a 80 kW_{net} automotive polymer electrolyte membrane fuel cell system (PEMFC) based on next-generation laboratory technologies assuming three different annual productions of 1,000, 100,000 and 500,000 fuel cell systems respectively (Figure 2). These systems are developed to operate with hydrogen at a projected cost of \$ 53 kW_{net}⁻¹ when manufactured at a volume of 500,000 units/year and \$ 59 kW_{net}⁻¹ at a volume of 100,000 units/year. For their analysis the DOE further assumed i) a significant reduction in Pt loading on the electrodes, ii) higher bipolar plate forming and welding costs, and iii) modified gas diffusion layers²⁴. For small series, a relatively homogenous cost distribution over all components are observed. With increasing unit numbers, the main costs shift to the bipolar plates and the catalyst itself. Whereas the increase in costs for the bipolar plates is related to the commodity materials and processing costs,

the catalyst costs arise mainly from the reliance on platinum group metals (PGM) and platinum alloys PtNi/C or PtCoMn. Even using small PGM loadings for both the anodic and cathodic sides (in total $0.134 \text{ mg}_{\text{PGM}} \text{ cm}^{-1}$), the fuel cell stack would constitute 52% of the total system costs ²⁴.

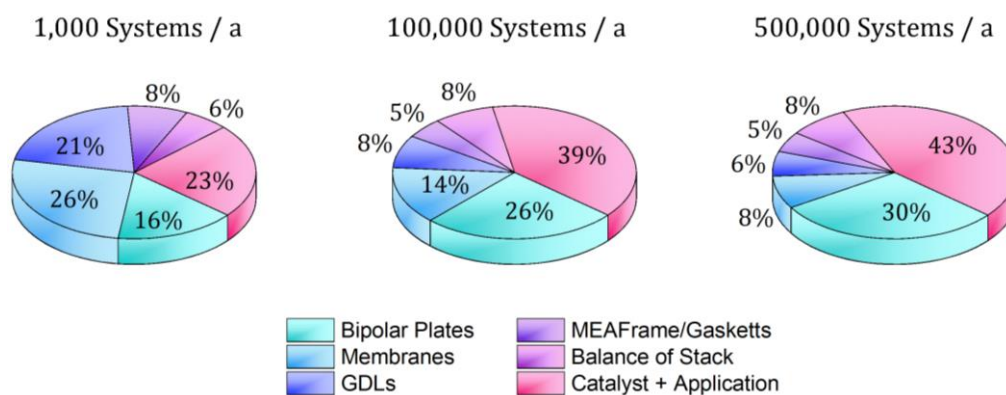


Figure 2: Breakdown of the 2016 projected fuel cell stack cost at 1,000, 100,000, and 500,000 systems per year ²⁴. Further information is given in the text.

In the same year, the DOE released the EERE Program Record from the Office of Energy Efficiency and Renewable Energy (EERE) which is a blueprint for launching the nation’s leadership in the global clean energy economy. The EERE Program Record assesses the use of PGM in combustion engines and FCEV ²⁵. It is figured out that the overall use of PGM is expected to increase, which will likely have a negative impact on the market trend. The annually published PGM Market Report draws a similar conclusion. Although the automotive platinum consumption reached a five-year low in 2018, mainly due to the diesel emission scandal, a stabilization or even a rise in demand is expected for the coming years. The report also assesses the growth in fuel cell platinum in the previous year, which was driven primarily by the automotive market but is expected to be driven largely by stationary power generation in the following years ²⁶. It is clear that the demand for PGM and its alloys represents a serious limitation for the broad-range adoption of hydrogen technologies, as it is one of the most critical and expensive compounds ²⁷.

The costs could be greatly reduced if the overall amount of PGM needed could be decreased from $30 \text{ g}_{\text{PGM}}$ per stack to the sustainable target of 5 g_{PGM} per stack. In a recent publication, Ott et al. have presented a solution to reduce the platinum content by 50% or more compared to state of the art PEMFC systems ²⁸. More details on this, are found in literature ²⁹⁻³².

Another approach to reduce the catalyst costs inside the fuel cell is the development of cheaper, non-PGM based catalyst systems like the described Fe-N-C, in which the industry has already signaled interest ³³ and which are the main focus of the research group affiliated with this thesis.

In PEMFCs, PGM-based catalysts accelerate the hydrogen oxidation reaction (HOR) and oxygen reduction reaction (ORR). The amount of platinum needed on the anodic side is very low and thus not

critical, initiating an easy and fast reaction with a very low overpotential. On the cathodic side, however, a much higher amount of platinum is needed to improve the reactivity during the ORR due to its indolence. As discussed above, it would be economically desirable to replace the PGM-based catalyst on the cathode. Here, Fe-N-C catalysts are the most promising substitute, as different groups have identified the nature-inspired molecular FeN_4 center as an ORR active site³⁴⁻³⁸. Fe-N-C catalysts will be introduced in more detail in the following section. Suffice it to say that these catalysts are synthesized in an oven process, in which iron, nitrogen and carbon precursor construct an iron-site that – to the current consensus of researchers – seems fourfold coordinated by nitrogen atoms and embedded in a (graphitic-like) carbon matrix. This structure is well known from the oxygen carrier hemoglobin in mammals' blood, which transports oxygen through the body.

Due to the preparation process Fe-N-C catalysts are generally very heterogeneous in their composition, a variety of iron- nitrogen- and oxygen species can appear, which make it hard to identify the active site and the mechanisms underlying the catalytic reactions. Resonance techniques like ^{57}Fe Mössbauer spectroscopy (MS) have proven as useful tools to access the iron states of the pure catalyst powders^{35, 39, 40} but their application is challenging under operation conditions^{41, 42}. In situ Mössbauer spectroscopy coupled with electrochemical measurements have only been performed on a limited number of samples with similar coordination environments⁴²⁻⁴⁸. So far, it was not possible to investigate the catalyst behavior with Mössbauer spectroscopy under real fuel cell operation conditions, as the radioactive Mössbauer sources are unsuitable for such measurements and due to the low iron content and the heterogeneous character of the catalyst itself. However, in situ and operando fuel cell tests for Pt-based catalyst have been performed using other techniques⁴⁹.

In the joint project NUKFER (05 K16 RD1) financed by the “Bundesministerium für Bildung und Forschung (BMBF)” the project partners planned to install a new nuclear resonant measuring unit for synchrotron-based Mössbauer spectroscopy (SMS) and further nuclear resonant experiments at the PETRA III synchrotron. Beside the possibility for SMS, experiments were suggested for the investigation of iron containing biological samples and catalytic samples as well as in the field of nanotechnology. This work addresses the catalysis subproject: An operando fuel cell setup for nuclear resonant techniques (mainly for SMS). It was planned to finish the new measuring unit within three years and directly conduct the related experiments. Unfortunately, the subproject related to SMS implementation was delayed, so that instead of SMS experiments, nuclear forward scattering (NFS) at PETRA III was performed. Therefore, some pre-experiments were done on the ESRF at Grenoble, where a nuclear resonant unit for SMS already exists. Due to the limiting opportunities for beamtime at ESRF and the following maintenance from 2019, onwards, only very simple pretests were possible. Further pretests at the P01 beamline at PETRA III were rejected. Not due to the scientific interested of the topic but due to the overbooking of beamtime at the facility. These problems lead to the decision to revise the investigated

fuel cell setup for SMS and use nuclear inelastic scattering (NIS) for the powder characterization and nuclear forward scattering (NFS) for the operando fuel cell characterization, instead. As Kneebone et al.⁵⁰ demonstrated, nuclear inelastic scattering (NIS) is a useful method to identify the active site structure in Fe-N-C catalysts. For powder samples, NIS helps to identify the composition of the catalyst, as shown in our recent publication⁵¹. In contrast, NFS shows the same requirements on the setup as SMS, even though the data interpretation is much more challenging and was so far only realized for simple systems (i.e., one or two iron signatures but not multicomponent systems). Hence, an operando fuel cell setup was developed to investigate the catalyst system in working conditions over a 24 h measurement time slot at the P01 beamline. Severe changes in catalyst behavior could be observed across the individual preparation steps, from the pure powder to the used membrane electrode assembly (MEA), as well as in the transition to the catalyst under operating conditions for the first time. These results show the considerable advantage of synchrotron based nuclear resonant techniques for understanding and characterizing the structure, composition and intimates of Fe-N-C catalyst systems, even in operation conditions. The combination of fuel cell tests with nuclear inelastic and nuclear forward scattering are a completely new approaches to examine the nature of Fe-N-C catalysts' activity. Another promising option to uncover the structural behavior of the active site is its deactivation by a suitable inhibitor and identify the electronic changes of the active iron site by Mössbauer spectroscopy. We have demonstrated the possibility to deactivate the catalyst's active site using sulfite ions and underline the power of Mössbauer spectroscopy to investigate Fe-N-C in the deactivated state⁵². The structure of Fe-N-C catalysts was investigated for three differently prepared Fe-N-C catalysts and characterized by electrochemical measurements and Mössbauer spectroscopy. As Mössbauer spectroscopy is significantly more sensitive to identify the iron states than other spectroscopic techniques^{34, 36, 37, 53}, the induced axial ligand changes and orbital occupations in FeN₄-sites affects the Mössbauer parameters, namely quadrupole splitting and isomer shift. This offers important information about the coordination environment of the changing iron site(s) that might be relevant for catalysis. The presented work aims to contribute the basic understanding of the active site structure by using nuclear resonance techniques on as prepared or deactivated catalysts. Beside room temperature Mössbauer spectroscopy (RT-MS), low temperature Mössbauer spectroscopy (LT-MS) was applied. A special emphasis is given to synchrotron-based resonance techniques like NFS, NIS and SMS and the design of an operando fuel cell setup.

3. Theoretical Background

3.1. Fe-N-C Catalyst Systems

The use of transition metal containing N_4 -macrocycle (chelates) as catalysts dates back to the work of C. Paquot who documented the catalytic activity of iron-, nickel- and cobalt-phthalocyanines for the oxidation of pinene in 1939⁵⁴. R. Jasinski investigated cobalt-, nickel- and platinum-containing phthalocyanines and was the first person who considered these chelates as catalyst materials for fuel cells in 1964⁵⁵. The ability to chemisorb oxygen without degradation made cobalt-phthalocyanine with a carbon support an interesting option for alkaline fuel cells⁵⁶. Due to reasons of activity and stability, this focus has since switched to iron-containing chelates. Metal complexes of N_4 -macrocycles, such as porphyrins and phthalocyanines, are widely studied due to their numerous physico-chemical properties and their various applications across different fields⁵⁷.

In addition to biological applications, transition metal-porphyrins and -phthalocyanines possess a versatile and reversible redox chemistry, which is what makes them suitable mediators in multi-electron transfer reactions. In both, porphyrin- and phthalocyanine-like complexes, the iron coordination sphere is square planar and the iron is coordinated to four nitrogen atoms situated in pyrrolic rings. In porphyrins, these rings are connected with bridging carbon atoms, whereas in phthalocyanines, nitrogen atoms serve as bridges⁵⁶. The interacting variety of porphyrins is caused by the open d -shell which allows distinct electronic configurations and can support different spin-multiplets (low spin, intermediate, and high spin states and give rise to spin-crossover appearance⁵⁸. In 1976, Jahnke et al. showed that the central atom has a strong impact on the catalytic activity, whereas a variation of the organic skeleton shows only a marginal effect⁵⁹. Even more important, a thermal treatment of the chelates at around 700 – 1000 °C resulted in a considerably increased resistance against acidic electrolytes, whereas higher temperatures decreased both the chemical resistance and the activity^{59, 60}. Further, Jahnke et al. found that the electrocatalytic properties of chelates are determined more by the electron-donor action of the metal-containing center than by the conductivity, because the delocalization of π -electrons of the polymeric compound is disturbed by the central metal atom. The ORR activity of chelates increases in the order of $Cu < Co < Fe$ as the center atom, as the respective metals can accommodate different changes in valency⁵⁹. Several years later, S. Gupta and coworkers first synthesized chelates by mixing a transition metal with a nitrogen-containing polymer, either before or after the heat treatment with a carbon support, to receive catalytic active sites for the ORR⁶¹. Their results showed that a precursor mixture of any iron, nitrogen and carbon support can result in the construction of iron-containing active sites, which after a heat treatment exhibit similar activity and stability as expensive and complex macrocycles. Various synthesis routes and preparation methods have been explored to develop new, highly active and more stable transition-metal-based Me-N-C catalysts since then^{9, 39, 54, 56, 62-87}.

To understand the origin of the active site three different models were assumed in the beginning. The Van Veen Model postulates that the heat treatment (500 – 600 °C) will induce a ligand modification rather than a complete destruction of the macrocycles⁸⁸⁻⁹⁰. The Yeager Model assumes that the active species is formed during contact with the electrolyte, as the pyrolysis temperature destroys the macrocycles and forms oxidic species which dissolve in the electrolyte. The free metal-ions can reconnect to the carbon surface with nitrogen. That means the resulting active site might look similar to van Veen's, a metal-N_x-C structure^{43, 61, 91}. In contrast, in the Wiesner Model, it is supposed that during the pyrolysis the metal helps to keep nitrogen functionalities in the carbon, thus the metal supports the growing of presumed active N_x-C species but does not play a role in the ORR.⁹²⁻⁹⁴ J.-P. Dodelet summarizes the genesis of and the controversial discussion about the role of the metal center in ORR catalysts^{57, 95}. Those models were continuously refined and still a very important field of Fe-N-C development^{82, 96, 97}. Today, it is widely accepted that the most active site of the catalyst system is a metal center (Fe or another transition metal) by nitrogen atoms bound to the carbon matrix^{34, 37, 98-101}. It became clear that there is a direct correlation between the number of Fe-N-C sites and the catalyst performance and that those sites are produced during pyrolysis from different precursors^{39, 102, 103}.

Figure 3 displays the possible coordination structure of an Fe-N-C catalyst, a four-fold coordinated iron site embedded in an amorphous carbon matrix. Fe-N-C catalysts generally contain between 80 and 90 wt% of carbon, less than 5 wt% of iron, and between 3 – 10 wt% of nitrogen. As an oven process is commonly performed during catalyst preparation, the catalyst material ends with an heterogeneous contribution of active sites and inorganic species. This makes the identification and nature of the origin of the ORR activity complicated.

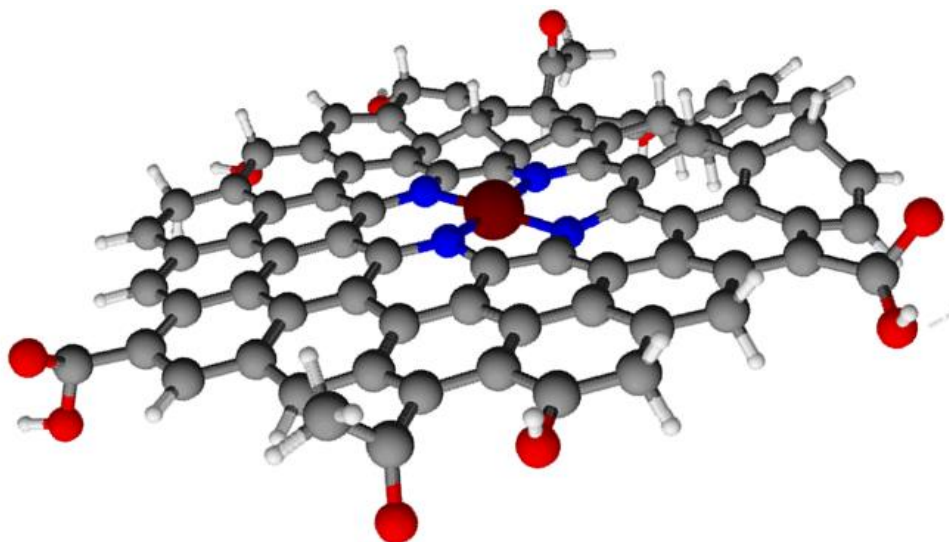


Figure 3: Possible scheme of a Fe-N-C system. An iron atom (dark red) is four-fold coordinated by nitrogen (blue) embedded in a graphitic matrix (grey). The dangling bonds are saturated by oxygen (red) or hydrogen (white). The structure of the catalytic Fe-N-C site is still under investigation. Therefore, a five-, or six-fold coordinated iron atom as active site is still discussed in literature (see text).

In the group of J.-P. Dodelet, ToF-SIMS (turn of flight second ion mass spectroscopy) was used, among other techniques, to investigate Fe-N-C catalysts. The ejection of several FeN_xC_y^+ ions from the top molecular surface layer of the probed catalyst indicated a strong correlation between the relative intensity of the FeN_2C_4^+ type ions detected by ToF-SIMS and the ORR catalytic activity in Fe-N-C catalysts treated with various temperatures. The group concluded that the FeN_2 catalytic site is the most active site in Fe-N-C catalysts while acknowledging that the proposed moiety was only part of the complete molecular site^{104, 105}. Lefèvre et al. proposed an additional active site, and confirmed the two possible active sites in Fe-N-C catalyst systems with Mössbauer spectroscopy data^{106,100}. For this purpose, an iron-acetate-based catalyst was prepared on a nonporous carbon black and heat-treated in NH_3 at 950 °C. Several Fe-containing species were detected in the Mössbauer spectra, namely three broader doublets (D1, D2, and D3) and two narrow doublets (D4 and D5) as given by Kramm et al.¹⁰⁰. Based on the Mössbauer parameters, the species D1 ($\delta_{\text{iso}} = 0.35 - 0.38 \text{ mm s}^{-1}$, $\Delta E_{\text{Q}} = 0.9 - 1.5 \text{ mm s}^{-1}$), D2 ($\delta_{\text{iso}} = 0.36 - 0.40 \text{ mm s}^{-1}$, $\Delta E_{\text{Q}} = 2.40 - 2.65 \text{ mm s}^{-1}$), and D3 ($\delta_{\text{iso}} = 0.35 - 0.38 \text{ mm s}^{-1}$, $\Delta E_{\text{Q}} = 1.2 - 1.5 \text{ mm s}^{-1}$) were assigned to three different FeN_4 -like sites^{100, 107}. For the D4 ($\delta_{\text{iso}} = 0.43 \text{ mm s}^{-1}$, $\Delta E_{\text{Q}} = 0.30 \text{ mm s}^{-1}$) and D5 ($\delta_{\text{iso}} = 0.29 \text{ mm s}^{-1}$, $\Delta E_{\text{Q}} = 0.31 \text{ mm s}^{-1}$) doublets relaxed iron nitride nanoparticles were assumed, which are instable during the following acid leaching and therefore inaccessible for the ORR. The remaining species D1, D2, and D3 were identified as iron (II) sites in the low, intermediate, and high spin state, respectively. As discussed in chapter 3.4.1, the spin states are a crucial part of the electronic structure which determines the oxidation state and ground state energy of a molecule. A detailed study of the oxidation and spin states and the related *d*-orbital configurations of iron porphyrins is presented, for example, by Walker et al.¹⁰⁸. As only the $3d_{z^2}$ orbital can interact with O_2 ¹⁰⁹, the D2 species, which have a filled $3d_{z^2}$ orbital, cannot contribute to the ORR. Only the D1 and D3 sites are able to interact with O_2 , as they exhibit an empty and half-filled $3d_{z^2}$ orbital, respectively. This implies that only a four-fold or five-fold coordinated iron site can interact with oxygen, resulting in a five- or six-fold coordination symmetry and contributing to ORR as described in the following chapter.

Although it is widely accepted that the metal- N_4 site is responsible for the catalytic performance of Fe-N-C catalysts^{34, 100, 105, 106, 110-112}, but the mechanism behind the coordination environment of the Fe(II), the spin, and the oxidation state are still under debate^{51, 113}.

Nevertheless, significant activity improvements have started to make Fe-N-C catalysts industrially more relevant, while still the stability needs to be improved¹¹⁴⁻¹¹⁶. Banham et al.¹⁰³ named three main hypotheses for the degradation: i) the dissolution/leaching of the active metal site, ii) an oxidative attack by H_2O_2 (or the resulting free radicals), and iii) protonation of the active site or protonation of a N-species next to the active site followed by anion adsorption. They do not mention carbon oxidation of the structure-building matrix, which could be a fourth point of degradation^{117, 118}. Given the variety of

synthetic approaches and designs, it is not realistic to identify one exclusive and exhaustive degradation mechanism for all Fe-N-C-based catalyst systems¹⁰³. Most likely, several degradation mechanisms are involved, which strongly depend on structure, composition and operation conditions. Further, the influence of ligands, porosity and amorphousness result in a different emphasis of the observed degradation mechanisms and directly impacts the catalytic performance and cannot be neglected but are hard to be investigate.

3.2. Oxygen Reduction Mechanism

Understanding the oxygen reduction reaction (ORR), not only for Fe-N-C catalysts, is essential for fuel cell applications as well as various other fields such as material dissolution, energy conversion or biological metabolism. Yet, even for metallic surfaces, several parts of the mechanism remain unknown: The stages of the proton-coupled electron transfer on the surface, which preset the reaction path, as well as the nature of formed intermediates remain unclear. In consequence, the breaking of the O-O bond is not fully understood. For Pt(111), Nørskov et al. demonstrated that the overpotential of the ORR results from the tendency of the electrode-adsorbed oxygen to become too stable at high potentials, rendering the proton and electron transfers impossible. By lowering the potential, the stability of the oxygen will be decreased and the reaction can proceed¹¹⁹. Wroblowa et al. represented the ORR in the following scheme¹²⁰:

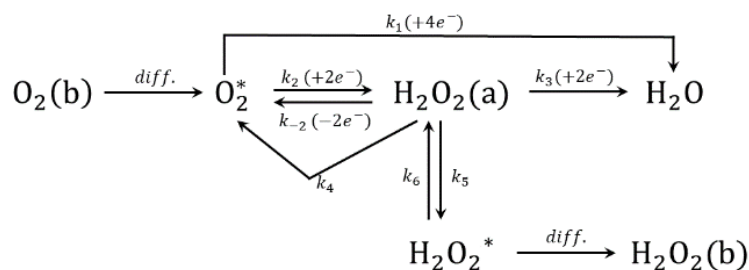


Figure 4: Scheme for ORR. The index notation of the rate constant (k) is given as follow: (1) four-electron direct reduction to water (or OH^-), (2) two-electron reduction to H_2O_2 (or HO_2^-); (-2) oxidation of H_2O_2 (or HO_2^-) to O_2 ; (3) electrochemical reduction of H_2O_2 to water (or OH^-); (4) catalytic decomposition of H_2O_2 (or HO_2^-) yielding reducible product (O_2); (5) desorption of adsorbed H_2O_2 (or HO_2^-); (6) adsorption of H_2O_2 (or HO_2^-). Indices b, *, and a, designate the bulk, vicinity of the disc electrode, and adsorbed species, respectively¹²⁰.

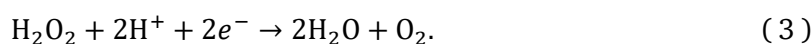
As the ORR is a four-electron transfer reaction, the overall reaction is represented by the following equation, which is known as the direct four-electron pathway:



Besides the direct pathway, a 2 + 2 pathway is possible. Here, oxygen reacts with hydrogen and forms a peroxide intermediate, in a first step:



In a second reaction step, the peroxide reacts further to form water:



The steps of the 2 + 2 pathway have potentials of 0.67 V and 1.77 V, respectively, in acidic solution under standard conditions⁹¹. If fully converted, the reactions given in equations (2) and (3) will result in the same amount of H₂O as the direct pathway, but the latter is preferred for applications due to a higher current per used oxygen molecule and the fact that peroxide, formed in equation (2) is able to degrade the membrane and the catalyst⁵⁷. In addition, a Fenton-like reaction can disrupt the desired reaction in Fe-N-C catalysts, when an Fe(II) is oxidized by peroxide, forming a hydroxyl radical and a hydroxide ion. Choi et al. discovered that Fe-N-C catalysts exposed to H₂O₂ leave iron-based catalytic sites untouched, but decrease their turnover frequency (TOF) via oxidation of the carbon surface, and weaken O₂-binding on iron-based sites¹²¹. Rotating ring disc electrode (RRDE) measurements are used to determine the ratio of both pathways. A more detailed discussion of the ORR mechanism is found in Robson et al.¹²², who showed that the direct 4 electron transfer pathway is superior due to the low peroxide yield, but the preferred pathway is via the peroxide intermediate.

The high potentials which are necessary to run the direct and indirect 2 + 2 pathways represent the low electrochemical reaction kinetics and underlines the need of a suitable oxygen reduction catalyst to accelerate the ORR. In case of a metal-containing catalyst, oxygen binding involves the *d*-orbitals of the metal. It has been inferred that the ORR occurs by way of a hydroxyl intermediate¹²³.

Observing individual steps of the ORR mechanism in Fe-N-C catalyst system is difficult, due to the low amount of catalytic active iron and nitrogen, as well as the high amount of carbon. To overcome this issue, theoretical models are used as done by several authors^{42, 124, 125}. Nevertheless, the electrochemical reduction of O₂ was systematically investigated for iron porphyrins, as it is important for biological metabolism. Boulatov¹²⁶ describes a plausible mechanism, which is illustrated in Figure 5.

The catalytic active site is presented as a five-fold coordinated Fe(II) porphyrin with the possible ligands X = imidazole, H₂O, or a similar nitrogenous heterocycle. The mechanism starts with the attachment of an oxygen molecule and the formation of an iron-superoxo structure that reacts to a ferric-hydroperoxo if a hydrogen ion and an electron are available, or release a hydroperoxyl radical if only a hydrogen ion is available. Merely the reaction path over an oxoferryl cation radical, either by a ferrous-hydroperoxo

the catalyst in the presence of ionomer. They concluded that a high surface concentration of hydrogenated nitrogen at the surface of an iron-nicarbazin derived Fe-N-C catalyst causes inefficient ionomer morphology, whereas an abundance of surface oxides promotes both an efficient distribution of active sites and an optimal ionomer-catalyst interface. They further suggest that the protonation of nitrogen within the catalytic layers plays a critical role in inhibiting proton transport during fuel cell operation¹³¹. In a recent publication of our group, the impact of ionic liquid modification was examined and a significant performance enhancement through ionic liquid modified catalysts was observed¹³². The named publications underscore the reciprocal action between the catalytic active site, the combination of binding sites, and the surface interactions between the catalyst, ionomer and carbon support to boost the ORR and minimize side reaction.

3.3. Electrochemistry

The oxygen reduction reaction (ORR) is one of the most important reactions in life processes and for energy converting systems like fuel cells¹³³. To enhance the reaction, a catalyst is introduced, which influences the kinetics, but cannot change the thermodynamics. Electrochemical experiments give an insight into the reaction kinetics and performance of the catalyst and are therefore the most important tool to understand catalytic systems and the electrochemical behavior^{98, 101, 132, 134}. In combination with spectroscopic techniques, electrochemical experiments enable to analyze the charge carrier transport and the formation of intermediates.

3.3.1. Rotating Disc Electrode (RDE)

The rotating disc electrode (RDE) is used to characterize the capacitive and diffusive behavior of a catalyst^{57, 89, 110, 135, 136}, relying on a three-electrode setup (Figure 6). The electrode rotates with a defined velocity, avoiding the influence of a stationary concentration distribution at the electrode surface. In consequence, the diffusion overpotential towards the transfer overpotential (η_D) is negligible as long as the system does not operate too close to the current limitation region¹³⁷. The difference in potential between the working electrode (WE) prepared with the catalyst ink and the counter electrode (CE) made from a glassy carbon (GC) root is measured by the current-less connected reference electrode (RE).

A standard hydrogen electrode or an electrode of the second kind is used as reference electrode (RE). A standard-hydrogen electrode (SHE) refers to a Pt-mesh saturated with hydrogen under standard conditions. Per definition, the potential for the SHE is 0.0 V in the electrochemical series. As this electrode needs to be connected via a salting bridge, it is difficult to use it directly in a setup. Another commonly used Pt-hydrogen electrode is the reverse hydrogen electrode (RHE), which is directly placed in the measuring electrolyte. The advantage of the SHE and RHE are the fast and reproducible adjustment of

the equilibrium potential, but a contamination of the electrolyte results in a deactivation of the used Pt-mesh and an unspecified potential change. To avoid this, an electrode of the second kind, e.g., an Ag / AgCl electrode, is used. In Figure 7 the related current density overvoltage curve from a cyclic voltammetry (CV) measurement is given. In the beginning of operation, the kinetic-controlled region defines the electrochemical behavior of the electrode, followed by a mixed region where transport and kinetic mechanism overlap and the diffusion-controlled region, where the species transport limits the reaction.

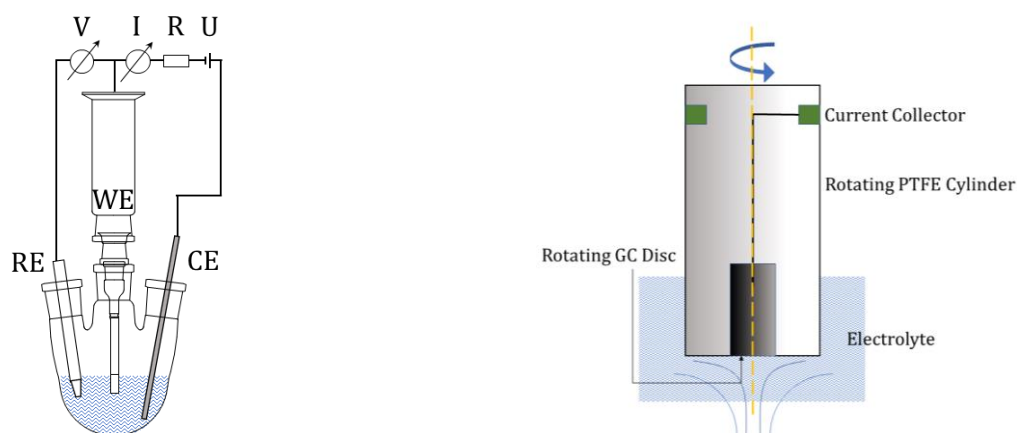


Figure 6: Schematic scheme of the RDE setup in a three-electrode-configuration for current carrying electrodes (left). The setup contains the reference electrode (RE) which is connected by a high-ohmic resistance with the setup to avoid a current load. The potential difference between the RE, and the potential between the rotating working electrode (WE), where the catalyst is placed and the counter electrode (CE) give access to the overpotential of the WE. Here, V stands for a voltmeter, I for an ammeter, R for resistor and U for voltage. A closed view of the radial flow field under rotation to minimize the concentration gradient on the WE is given (right).

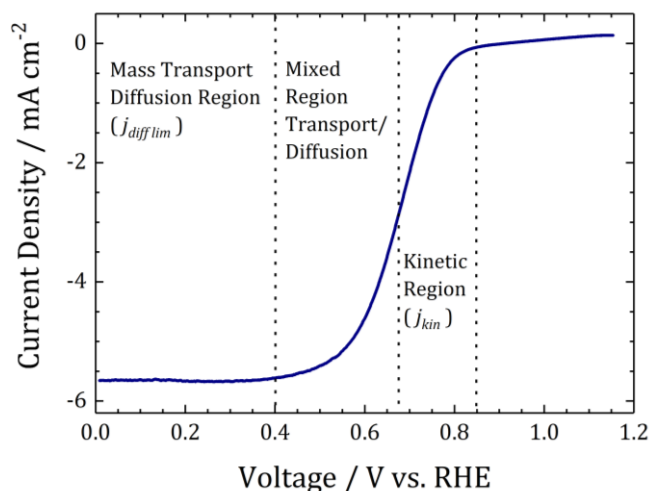


Figure 7: Current density overvoltage curve with the superposition of charge passage and adsorption. This leads to the formation of an adsorption and desorption limit flow. The curve is separated in three regions: The kinetic region, where kinetic controlled process characterizes the system, a mixed region where transport and kinetic mechanism overlap and the diffusion-controlled region, here the species transport limits the reaction.

As the measured electric current at an electrode from an electrochemical reaction is a function of the kinetic activity and the mass transport of reactants, the kinetic current density j_{kin} is determined from the capacity-corrected CV in O₂ saturated electrolyte by using the Koutecký–Levich equation

$$\frac{1}{i} = \frac{1}{i_{kin}} + \frac{1}{i_{diff}}. \quad (4)$$

Here, i is the measured current, i_{kin} the kinetic current and i_{diff} the mass transport current. From this, the kinetic current density is given as:

$$j_{kin} = -\frac{(j_{diff} \cdot j(u))}{(j_{diff} - j(u))}. \quad (5)$$

To describe the concentration dependence of the electrode potential, the Nernst-equation

$$\varphi_0 = \varphi_{00} + \frac{R \cdot T}{n \cdot F} \ln \left(\frac{a_{ox}}{a_{red}} \right), \quad (6)$$

which gives the equilibrium-Galvani potential φ_0 (ideal electrode potential) of the working electrode, is used. Here, φ_{00} is the standard Galvani potential of the half-cell reaction, R is the molar gas constant, T is the temperature, n is the molar number of contributing electrons, F is the Faraday constant, and a_{ox} and a_{red} are the activities of the species in the oxidized and reduced state, respectively. The Nernst potential can thus determine the Gibbs free energy ΔG of the electrochemical reactions.

Due to a finite reaction rate at the electrodes a deviation from the open circuit potential occurs, the so called overpotential. Using the Butler-Volmer equation, the charge transfer current density j_D (dt. Durchtrittsströmdichte) is calculated as a function of the overpotential η_D

$$j_D = j_0 \cdot \left\{ \exp \left[\frac{\alpha \cdot n \cdot F}{R \cdot T} \cdot \eta_D \right] - \exp \left[-\frac{(1 - \alpha) \cdot n \cdot F}{R \cdot T} \cdot \eta_D \right] \right\}, \quad (7)$$

which describes the electrochemical reaction kinetics for the anodic (left part) and cathodic half-cell reactions (right part). Here, j_D is defined as the current density, j_0 gives the exchange current density, η_D the passage overpotential with $\eta_D = E - E_{eq}$ and α describes the charge transfer coefficient. Two limiting cases of the Butler-Volmer equation are determined. In the low overpotential region, the Butler-Volmer equation is simplified to a linearized version

$$j_D = j_0 \cdot \frac{n \cdot F}{R \cdot T} \cdot \eta_D. \quad (8)$$

Whereas in the high overpotential region it follows

$$j_D = j_0 \cdot \left\{ \exp \left[\frac{\alpha \cdot n \cdot F}{R \cdot T} \cdot \eta_D \right] \right\}, (\eta_D > 0) \quad (9)$$

and

$$j_D = j_0 \cdot \left\{ \exp \left[\frac{(1 - \alpha) \cdot n \cdot F}{R \cdot T} \cdot \eta_D \right] \right\}, (\eta_D < 0). \quad (10)$$

The equation (9) and (10) are the theoretical justification of the Tafel-equation for the anodic and cathodic half-cell reaction, respectively (for $|\eta_D| > 0.1$ V). Thus, in this regime the kinetic current density j_{kin} is therefore described by the simplified Butler-Volmer equation. The logarithmic plot of j_{kin} over η_D gives the Tafel diagram and enables the determination of the charge transfer coefficient α from the linear region and the exchange current density from the intercept at $\eta_D = 0$.

3.3.2. Fuel Cells

The first fuel cells were developed by C. F. Schönbein and W. R. Grove in the late 1830s. In 1839, Grove designed a gas-voltaic cell made of platinum electrodes fixed in glass tubes that were alternately filled with hydrogen and oxygen¹³⁸. These assemblies were immersed in acid diluted with water and connected in series¹³⁹, constituting the first known working fuel cell, despite similar experiments Schönbein conducted in 1838¹⁴⁰. From this time on fuel cell system reached a growing interest for different applications^{141, 142} and became one of the most intensively recognized technical application for a fossil energy carrier free economy^{12, 31, 32}.

Fuel cells work with a continuous supply of mostly gaseous reactants which flow over electrodes covered with a catalytic layer, initiating a redox reaction and producing electricity and marks another advantage fuel cells offer over battery systems. As a product, water (PEMFC) or a mixture of water and carbon dioxide are formed (e. g., DMFC). Moreover, the fuel is continuously fed by a reservoir and, hence, the operation time is only limited by refueling the reservoir and the provision of reactants, but not by the storage capacity of the electrochemical device, as in case of batteries. The properties and general information of a PEMFC is summarized in Table 2. Because of the low operation temperature (~ 80 °C)

and the more convenient handling, PEMFCs are further an interesting candidate to fuel light-duty transportation applications¹⁴³. Beside the PEMFC and DMFC a variety of different fuel cell concepts exist, working with a range of different fuels, electrode materials, catalysts, and operation temperatures.^{143,144} Ideally, a fuel cell operates with carbon free fuels and combustion products, adding the absolute advantage of an energy system free of CO₂-emissions.

Table 2: Overview of the PEMFC system. Data are taken from^{143, 144}

Electrolyte	Primary Application	Electrodes	Catalyst	Interconnect	Operation Temperature	Charge Carrier	Power Density / kW m ⁻³
Hydrated Polymeric Ion Exchange Membrane	Automotive & Stationary	Carbon	Platinum	Carbon or Metal	40 – 80 °C	H ⁺	3.8 – 6.5

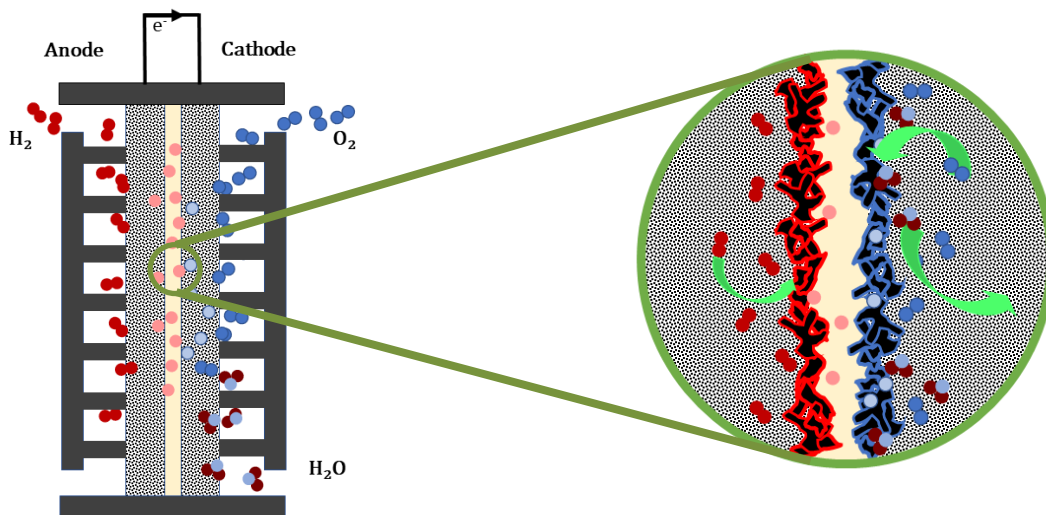


Figure 8: Profile of a fuel cell site cut. Hydrogen (red) is injected on the anodic side and streams through the gas flow channels, which are separated by the bridges of the bipolar plate (black), (left). By diffusing through the GDL the anodic catalyst accelerates the hydrogen oxidation reaction. The generated electrons have to pass the electric circuit (generation of electricity) in order to get to the cathodic side. The hydrogen ions (light red) diffuse through the MEA and recombine with oxygen (light blue) and electrons on the cathodic side catalyst. The formation and transport of water molecules (dark red, blue) goes along the flow field of the cathodic side (right).

In Figure 8 a profile of a PEMFC is given. The left panel of Figure 8 shows a PEMFC scheme, whereas on the right a close up of the MEA is depicted. A fuel cell is separated in an anodic and cathodic side, where the electron and gas transport are realized through bipolar plates and the engraved flow field. The hydrogen (red dots) streams from the anodic side through the flow field, whereas the oxygen (blue dots)

streams over the cathodic side. In a commercial fuel cell systems the flow fields for both sides can show different designs to full fill operation concepts and increase performance ¹⁴⁵.

The centerpiece of a modern PEMFC is the membrane electrode assembly (MEA) (Figure 8, right), where the hydrogen oxidation reaction (HOR) on the anode and the oxygen reduction reaction (ORR) on the cathode takes place. The MEA can be separated into three areas: the anodic side, the membrane, and the cathodic side. At the anodic side, a PGM catalyst interconnects with carbon (black shapes with red borders) is sprayed on a gas diffusion layer (GDL) given in gray. To increase the electronic conductivity and minimize pore filling of the wetted and porous GDL by condensed water during operation, the GDL is made of an electricity-conductive and hydrophobic carbon fiber mesh. An ion-exchange-membrane (yellow), normally made of a perfluoro sulfonic acid tetrafluoroethylene copolymer membrane (e.g., Nafion™), transports the protons from the anodic to the cathodic side, whereas the electrons are separated and used for the power supply. The protons produced on the anode are transported through the membrane in a hydrated cloud (light red), and reach the cathode. On the cathode the recombination of hydrogen, electrons and oxygen takes place on the catalyst layer (black shapes with blue borders), known as oxygen reduction reaction (ORR).

For laboratories, the bipolar plates are made out of carbon, whereas coated drawing sheets with embossed flow fields for electron conductivity and gas transport are often used on an industrial scale. Together, the MEA and the bipolar plates constitute the unit cell. A so-called stack with a desired output capacity is built by electrically connecting several unit cells.

Like the anodic side, the catalyst at the cathodic side, where the sluggish oxygen reduction reaction (ORR) takes place, is sprayed on a GDL. To run the fuel cell reaction the catalyst's active sites must i) be exposed to the reactant, ii) stay in electrical contact with the electrode, and iii) be in ionic contact with the electrolyte ¹⁴³. In addition, the transport of reactants to the catalyst and of water or any other reaction product from the catalyst through the GDL pores must be ensured and applies for both the anodic and cathodic side. Hence, even a highly reactive catalyst will perform badly if the three-phase interface of the GDL, the catalyst layer, and the membrane is not optimized. The importance of adjusting a perfect interplay between the catalyst and a layer design strategy is a specified research field and described amount others by Banham et al. ¹⁴⁶. In a recent publication, we examined the activity and stability of Fe-N-C catalysts in acidic media and found that decreases in catalytic performance are associated with the demetallation of FeN₄-sites and the subsequent formation of iron or iron-oxide clusters, but not with the deactivation of the active site ¹¹⁴.

As described before, fuel cells offer i) direct energy conversion, ii) no moving parts in the energy converter, iii) low noise levels, iv) modular installations to match performance tuning and increase the reliability, and v) rapid refilling capability ¹⁴³. Another important advantage of fuel cells over other power technologies is that small and large fuel cell plants have similar operation efficiencies in terms of

cost dependencies. Conversely, the lacking infrastructure and the high market entry costs are one of the main drawbacks, impeding widespread commercial use.

Fuel Cell Performance

To optimize the performance of fuel cells, it is important to understand the influence of operation conditions such as the gas pressure, temperature and reaction kinetics. The Gibbs free energy ΔG determines the maximum electrical work W_{el} produced by a fuel cell at the constant temperature T and pressure:

$$W_{el} = -nFE = \Delta G = \Delta H - T\Delta S. \quad (11)$$

Here, W_{el} consist of the number of electrons n participating in the reaction, the Faraday constant F , and the ideal potential of the cell E . ΔG is a product of the enthalpy change ΔH , minus the quantity of the unavailable energy resulting from the entropy change ΔS and the system temperature T . Mathematics reveal that the Gibbs free energy can also be expressed as:

$$\Delta G = \Delta G^0 + R \cdot T \cdot \ln \frac{a_C^\gamma \cdot a_D^\delta}{a_A^\alpha \cdot a_B^\beta}, \quad (12)$$

where ΔG^0 is the Gibbs free energy of the reaction at the standard pressure of 1 atm and standard temperature of 298.2 K. The logarithmic term contains the activity a of product (A and B) and reagent (C and D), the Greek letters represent stoichiometric factors. The fugacity (f) of a real gas can be approximated by the partial pressure if the operation pressure is low enough. Substituting equation (11) in equation (12) once again returns the Nernst equation:

$$E = E^0 + \frac{R \cdot T}{n \cdot F} \ln \frac{f_C^\gamma \cdot f_D^\delta}{f_A^\alpha \cdot f_B^\beta}. \quad (13)$$

From the connection between the standard potential (E^0) of the cell reaction and the ideal equilibrium potential (E), it is clear that the cell voltage is a result of the total species amount. Increasing the partial pressure of reactants and decreasing the partial pressure of products both increase the cell voltage. At the same time, the Nernst equation represents the upper limit of the performance, as it calculates the ideal open circuit potential.

To understand the standard potential E^0 of a fuel cell in which hydrogen and oxygen react, the half-cell reactions need to be considered. At the anode, one hydrogen molecule is split into two hydrogen ions (protons) and two electrons:



At the cathode, on the other hand, an oxygen is reduced to a water molecule:



The overall cell reaction is written as:



Implying the following corresponding Nernst equation:

$$E = E^0 + \frac{R \cdot T}{2 \cdot F} \ln \frac{p_{\text{H}_2}}{p_{\text{H}_2\text{O}}} + \frac{R \cdot T}{2 \cdot F} \ln p_{\text{O}_2}^{\frac{1}{2}}, \quad (17)$$

which gives the potential E . Given standard conditions in which H_2 and O_2 reacts, the standard potential E^0 of a fuel cell is 1.229 V assuming that liquid water is produced or 1.18 V if gaseous water is produced. The difference in Gibbs free energy results exclusively from the energy change associated with the vaporization of water. As PEMFCs are more commonly operated at 80 °C than in standard conditions, the resulting open circuit potential decreases to 1.17 V.

Similar to the open circuit potential, the cell efficiency is limited by the Gibbs free energy. The usable electric energy produced in an electrochemical converter is calculated using the change in Gibbs free energy ΔG of the reaction and the thermal energy ΔH . Therefore, the thermal efficiency η is the product of ΔG (usable energy) and the thermal energy:

$$\eta = \frac{\Delta G}{\Delta H} \quad (18)$$

For the thermal efficiency η in standard conditions $\Delta H^0 = 285.8$ kJ (hydrogen- and oxygen reaction) and $\Delta G^0 = 237.1$ kJ (available work), it follows that:

$$\eta_{\text{ideal}} = \frac{\Delta G^{\circ}}{\Delta H^{\circ}} = \frac{237.1 \text{ kJ}}{285.8 \text{ kJ}} = 0.83. \quad (19)$$

Thus, an ideal fuel cell operating reversible on pure hydrogen and oxygen in standard conditions has a maximum efficiency of 83%.

ΔG is calculated by multiplying the actual voltage under operation (V_{actual}) with the resulting current I ; therefore, the ideal potential E_{ideal} is described as the ideal voltage (V_{ideal}) multiplied with the product of the current I and divided by the electric efficiency η_{ideal} . This yields the thermal efficiency of a reversible operating cell on pure H_2 and O_2 in standard conditions:

$$\eta = \frac{\Delta G}{\Delta H} = \frac{V_{\text{actual}} \cdot I}{V_{\text{ideal}} \cdot \frac{I}{\eta_{\text{ideal}}}} = \frac{0.83 \cdot V_{\text{actual}}}{E_{\text{ideal}}} = \frac{0.83 \cdot V_{\text{cell}}}{1.229 \text{ V}}. \quad (20)$$

These ideal conditions cannot be implemented in real operating setups, as cell operating effects reduce the efficiency and, in addition, the fuel is not completely converted in a fuel cell. Hence, fuel utilization is an important further requisite for efficient operation. Especially in gas-fueled cells, the reactant activity drops as the utilization rises, limiting the efficiency. These potential drops are known as mixed potential loss, in which parasitic reaction loss dominates. In a real fuel cell, several types of irreversible losses have to be considered, for example, activation losses, mass-transport-related or ohmic losses, which impact the cell voltage under operation conditions. Figure 9 illustrates the ideal and real behavior of a fuel cell under operation condition, including the main losses detailed below.

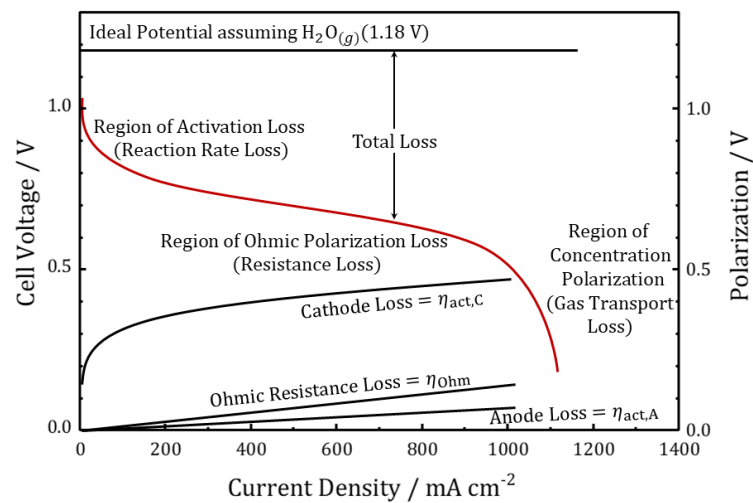


Figure 9: Fuel cell performance. The impact of different types of losses is depicted as described in the text. This figure was taken from ¹⁴⁷.

Ohmic resistance losses have a linear impact across the current density, which are determined with the ohmic law due to the cell geometry and the used materials. As the temperature influences the specific electric resistance of a material, the operation temperature affects ohmic resistance losses. Hence, the ohmic polarization of the fuel cell includes electronic, ionic and contact resistance, as well as solid electrolyte resistance. It is obvious that ohmic losses, which are a direct function of current and voltage changes, dominate during operation.

In contrast, the reaction kinetics losses on the anodic side range from 10 to 50 mV vs. RHE and are thus negligible¹⁴⁸. However, activation related losses on the cathodic side strongly influence the fuel cell performance, as the three-phase interface and the inert electrode kinetics of the oxygen reduction reaction result in an activation polarization, which limits the fuel cell performance. The magnitude of the activation losses depends on the current density and ranges between 500 and 800 mV vs. RHE¹⁴⁸. The electrode design and the catalyst properties are important to improve the fuel cell performance and decrease electrode losses, partly because the resulting voltage drop must be overcome by the reacting species. If the voltage decreases around ~ 100 mV due to activation polarization, the semi-empirical Tafel equation is used to illustrate the activation polarization η_{act} :

$$\eta_{\text{act}} = \frac{R \cdot T}{\alpha \cdot n \cdot F} \ln \frac{i}{i_0}. \quad (21)$$

Catalyst systems with lower Tafel slope behavior are preferred, as increases in current density are followed by a lower activation polarization in this case. Increasing the current, follows with a higher production of products, which is significantly affected by the mass transport limitations of educts and products. These limitations are mitigated through smart electrode structure and surface designs and adjusted operation conditions, which eliminate mass transport as an issue of operation.

As the performance of fuel cells strongly depends on the cell design and the used materials, activation and concentration polarization data necessarily reflect the experimental conditions and are therefore hard to compare across different conditions. Moreover, the losses depicted in Figure 9 are expressed as polarizations, suggesting that the polarization results in a voltage shift of the electrodes. The thermodynamics force the cell to reach the equilibrium; therefore, the net current increases the anode potential and decreases the cathode potential, reducing the cell voltage.

The consideration of losses occurring during operation and the operation conditions affecting the performance results in a valid operation window, where the fuel cell efficiency increases. This is the reason for the targeted efficiency given by the DOE, as discussed above¹⁴⁹. As a consequence, the fuel cell might exhibit a higher total efficiency, although parts of the system work at lower component efficiency.

The balance of the fuel cell system is the most important part apart from the inner of the stack, as it comprises all necessary parameters such as the feed stream conditioning, the thermal management of the cell, the temperature of the pipes, and the gas and water regulation. It further controls the electric power conditions, regulating voltage and current peaks during the start-stop cycles to avoid cell damage. PEMFC applications imply several technical challenges, including water management inside the unit cell to avoid draining or flooding, the thermal management of large stationary stacks with high electronic loads, the reflected heat for cogeneration and in bottoming cycles¹⁴³, and the deactivation possibility of PMCs, at trace levels of CO, sulfur species or ammonia. Solutions to avoid severe potential drops and improve the lifetime and performance include i) shifting the operation window to lower operating current densities, ii) increasing the PMC loading, or iii) exchanging the PGM catalyst with a PGM-free catalyst system unaffected by the known deactivations. Whereas the first two options considerably increase the operation costs of the stack, the third option may even decrease the costs, underscoring the benefits of Fe-N-C catalysts. Still, PEMFCs have the advantage of generating very high current densities of up to 4 A cm^{-2} ¹⁴³, which in combination with the low operation temperature makes them not only attractive for automotive applications. The low operation temperature enables a rapid start-up and the high current density minimizes the total stack volume and reduces the overall cost. The DOE has set the technical targets for automotive applications ($80 \text{ kW}_{\text{e}(\text{net})}$) integrated transportation fuel cell power systems which operate on direct hydrogen to 2 W kg^{-1} , corresponding to 65% stack efficiency at 25% of rated power for 2015. Hence, the requested stack efficiency at rated power is given with 55%¹⁴⁹. These benchmarks have to be achieved to compete with combustion engines.

3.4. Nuclear Resonant Techniques

This chapter briefly describes the physical background of the Mössbauer effect, which is known as the recoil-free resonant emission or absorption of γ -radiation. Further, it introduces the used nuclear resonant techniques, including room temperature ^{57}Fe transmission Mössbauer spectroscopy (RT-MS), low temperature ^{57}Fe transmission Mössbauer spectroscopy (LT-MS), synchrotron based Mössbauer spectroscopy (SMS), nuclear inelastic scattering (NIS), and nuclear forward scattering (NFS). For a more thorough discussion, the following literature is recommended¹⁵⁰⁻¹⁵⁶.

3.4.1. Mössbauer Spectroscopy

The history of nuclear resonance absorption spectroscopy goes back to the work of Kuhn¹⁵⁷, who first suggested the possibility to observe γ -radiation absorption by nuclear resonance. In 1957,

Rudolf L. Mößbauer investigated the recoilless nuclear resonance absorption of γ -rays for his doctoral thesis^{158, 159}. He was able “to attack the problem of recoil-energy loss at its root in a manner which, in general, ensures the complete elimination of this energy loss”¹⁶⁰. His experiment was carried out using a ^{191}Ir radioactive source, which emits a 129 keV γ -quanta leading to the ground state of ^{191}Ir . In contrast to the suggestion by his supervisor (Heinz Maier-Leibnitz), Mößbauer believed that lower temperatures would more easily enable a resonant absorption, enabling the detection of measurable changes in the nuclear absorption. Because the shape and energy of the emission and absorption lines were treated not as free particles but in crystalline form, Mößbauer was able to explain the “anomalous resonance absorption” by showing that the recoil momentum was not transferred to a single nucleus, but to an assembly of nuclei or atoms, which include the nearest or next-nearest neighbors surrounding the excited nucleus¹⁶⁰.

The recoil-free nuclear resonance fluorescence, now known as Mössbauer effect was awarded with the Noble Prize in physics in 1961 and resulted in a new measurement technique, the Mössbauer spectroscopy (the different spelling of Mößbauer (person) and Mössbauer (effect, technique) results from the recommendation of the international board on the application of the Mössbauer effect (IBAME)). Advantages of Mössbauer spectroscopy are the high sensitivity to energy changes in the order of 10^{-8} eV, and the accuracy to the 10^{-13} th decimal place. This makes it a unique technique for investigating Mössbauer active isotopes like ^{57}Fe , as it facilitates the modification of hyperfine interactions of the nucleus and the electron shell and, hence, the observation of electric monopole interactions (δ_{ISO}), electric quadrupole interactions (ΔE_{Q}), and magnetic dipole interactions (ΔE_{M}), which offer information about oxidation states, spin states, magnetic interactions, bonds character, electronegativity of ligands, and molecular symmetry^{151, 161, 162}. Compare to X-ray absorption spectroscopy (XAS), near-edge X-ray absorption fine structure (XANES) or extended X-ray absorption fine structure (EXAFS), Mössbauer spectroscopy has several advantages in the characterization of Fe-N-C catalysts. It is practically not limited on the sample thickness and shows only for strong absorbing samples double resonance effects the information about the investigated isotope comes directly from the nucleus and is not a product of shell electron excitation nor relaxation processes and no complex data analysis has to be deployed. Today, the Mössbauer Effect has been described for 44 elements, 81 nuclides, with 102 Mössbauer transitions and Mössbauer spectroscopy is a very common technique in the fields of solid state research, physics, chemistry, geo- and material science as well as biology and archeology¹⁵¹.

^{57}Fe transmission Mössbauer spectroscopy (RT-MS) is most commonly used to investigate Fe-bearing compounds¹⁶³. However, in the field of Fe-N-C catalyst a steadily growing number of groups use the technique^{86, 110, 164, 165}.

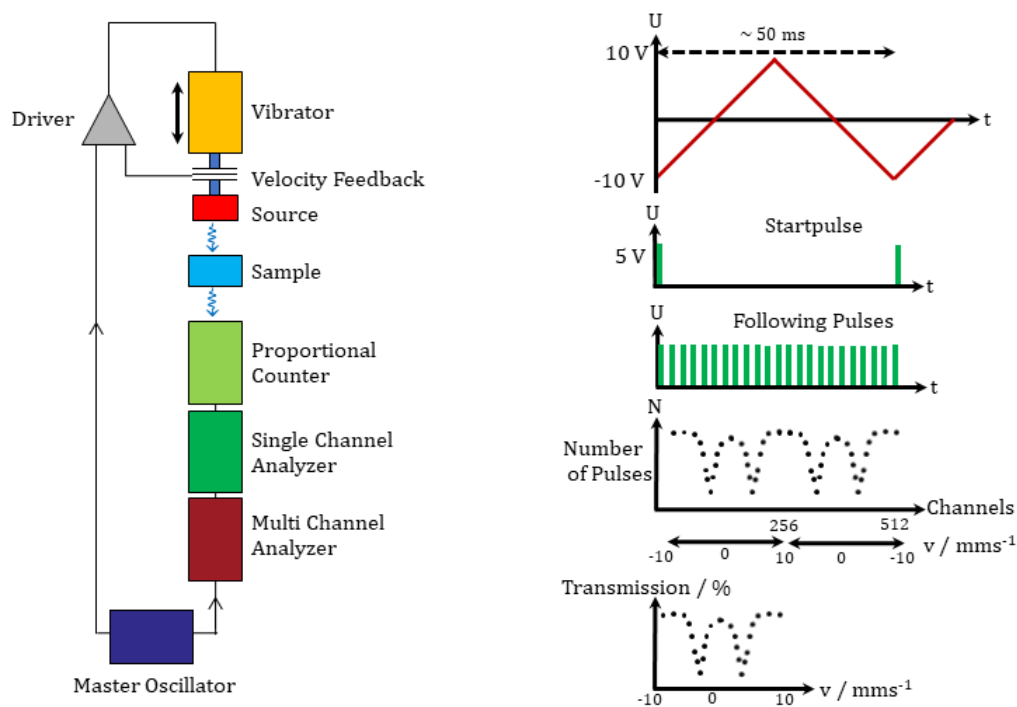


Figure 10: Scheme of Mössbauer setup (left). The vibrator moves the radioactive source with a constant velocity and controlled by the velocity feedback and driver. The source emits the radiation which excited the sample nucleus. The decay of the excited state emits a γ -quantum which will be collected by the proportional counter. The single and multi-channel analyzer will process the data, whereas the master oscillator is used for adjustment. Signal processing (right): The source will be moved with constant acceleration. Each decay can be connected with a defined velocity by the channel analyzer. The total number of pulses will show twice the spectrum for positive and negative velocity, respectively. Folding and transforming the spectrum to absorption or transmission per percent follows in the common Mössbauer spectrum. Adopted from V. Schünemann lecture “Grundlagen der Mößbauerspektroskopie”¹⁶⁶.

In Figure 10 the generalized setup of a room temperature Mössbauer spectrometer is shown. In a standard RT-MS setup, the radioactive source is mounted on an electro-mechanical velocity transducer (vibrator) to provide the constant energy modulation of the emitted γ -quanta by the Doppler-effect. Between source and vibrator, the velocity feedback and driver tune the constant acceleration mode and control the transduced, triangular function. The emitted radiation is partly absorbed, re-emitted by the fixed sample, and then hits the detector. Here, a proportional counter filled with an argon, krypton or xenon gas mixture is used with a quench gas like methane. Using a proportional counter as detector has the advantage of high-count rates and high resolution but the disadvantage of low efficiency. In comparison, a scintillation detector like NaI or Si(Li) has a high efficiency but a lower resolution and interacts with Compton scattering, resulting in a broad non-resonant background. The pulses of resonant

energy are distinguished by the single channel analyzer and conducted to the multi-channel analyzer for data collection. The master oscillator functions as an interface between the electronic components. The resulting spectrum is an unfolded (forward and backward velocity), point (number of points depends on the number of single channels) transmission spectrum. Due to the missing correlation between the single channels and the velocity, a calibration is needed for each velocity. Usually, this is done by measuring a pure α -iron foil and calibrating the velocity axis by the six-line positions of the iron spectrum for which the energetic positions are well known.

Physical Concepts of the Mössbauer Effect:

Mössbauer spectroscopy uses the nucleus of a Mössbauer active isotope to determine the electronic character of the isotope, offering information about the structural and electronic properties of the Mössbauer nuclei¹⁶⁷. To understand the results of Mössbauer spectra, it is thus important to understand nuclear and electronic processes and its interactions.

The emission of a γ -quant with the energy E_0 , realized by the radioactive nucleus, entails a recoil impulse p_N with the energy:

$$E_R = \frac{p_N^2}{2M} = \frac{E_0^2}{2Mc^2}, \quad (22)$$

where M is the mass of the emitted nucleus and c the speed of light. This nonrelativistic approximation is used because of the large nuclear mass and the low recoil velocity. The transition energy E_γ of the γ -quant is given as,

$$E_\gamma = E_0 - E_R, \quad (23)$$

where E_R is the recoil energy absorbed by the nuclei due to momentum conservation. The energy of the emitted γ -quant is the difference between the excited state E_e and the ground state E_g of the nucleus,

$$E_e - E_g = E_0. \quad (24)$$

Each nuclear level has a unique energy, spin parity, decay constant λ (decay probability per unit time), and mean lifetime τ_N of the excited nuclear state. The mean lifetime is defined by the re-emission of a γ -quant from the excited state back to the ground state and must be in the range of $10^{-6} \geq \tau_N \geq 10^{-11}$ s, as a lifetime longer than 10^{-6} s will result in an insufficient overlap of the emission and absorption lines,

whereas a lifetime shorter than 10^{-11} s will induce too broad resonance overlap, resulting in a smeared and thus indistinguishable spectrum. For ^{57}Fe , the mean lifetime of the excited nuclear state is $\tau_N = 1.43 \cdot 10^{-7}$ s, which fits well for observing the recoil-free resonance. For an excited nuclear state, which is determined by the width of the resonance lines, it follows that the mean-life time τ_N is defined as the average time the excited state exist before decay and is a product of λ and the half-life time $t_{1/2}$:

$$\tau_N = \frac{1}{\lambda} = t_{1/2} \cdot \ln 2 = 1.44 \cdot t_{1/2}. \quad (25)$$

Multiplying life-time and width, one finds that:

$$\tau \cdot \Gamma = \hbar, \quad (26)$$

where Γ is the natural line width. This equation can be interpreted in terms of Heisenberg's uncertainty relation $\Delta t \cdot \Delta E \geq \hbar$. To measure the energy of the state within an uncertainty $\Delta E = \Gamma$, a time $\Delta t = \tau$ is needed. For ^{57}Fe , the lifetime of the first excited state is 141 ns and the width of this state is given by $\Gamma = \hbar \cdot \tau^{-1} = 4.67 \cdot 10^{-9}$ eV. The ratio of decay energy is 14.41 keV of the first excited state and the width is given by $E \cdot \Gamma^{-1} = 3.1 \cdot 10^{12}$. Figure 11 depicts the different energy sections, which illustrate the recoil-free resonant emission.

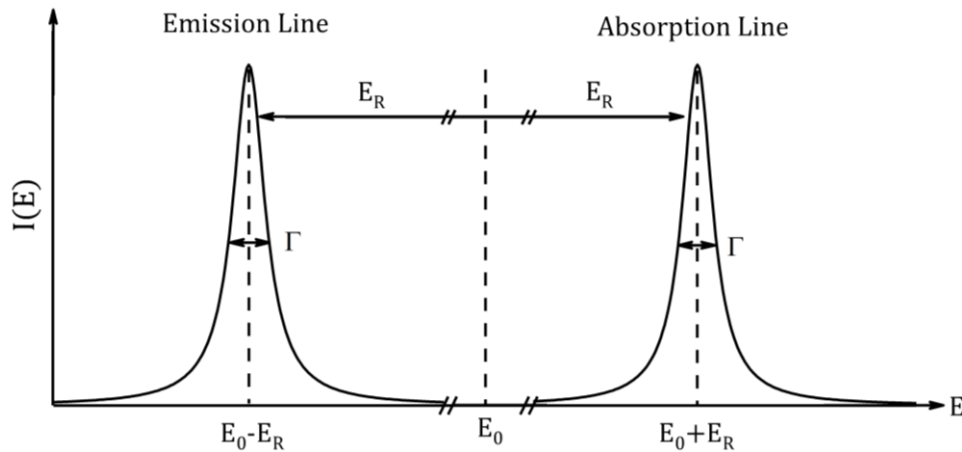


Figure 11: Three separated energy sections of the γ -emission and absorption lines caused by recoil of resting free nuclei. Resonant absorption is not possible, since there is no overlap between the emission and absorption line. (Picture traced in from ¹⁵¹). Only if the emitted γ -quant has an energy $E_0 + E_R$ and $E_0 \lesssim \Gamma$ the emission and absorption lines overlap and resonance fluorescence can occur.

To estimate the natural line width Γ and the energy related intensity $I(E)$ of decay events, a Lorentzian-like distribution is needed, which is given by the Breit-Wigner formula:

$$I(E) = \frac{\left(\frac{\Gamma}{2}\right)^2}{(E - E_0)^2 + \left(\frac{\Gamma}{2}\right)^2}. \quad (27)$$

For the transition of ^{57}Fe , $E_0 = 14.41 \text{ keV}$ and $E_R = 1.96 \cdot 10^{-3} \text{ eV}$ and is thus 10^6 times larger than the natural line width of the excited state. The most important conclusion drawn from this equation is that the decay energy is not constant and distributed across a region whose width is determined by the decay constant. If a γ -quant is emitted by a free atom, a linear recoil momentum with the recoil energy E_R is transmitted to the nucleus. As seen in equation (23), the recoil effect reduces the energy of the γ -quant and increases the transition energy by the same amount. This conservation law also holds for the absorption process. The resonance between the absorber and the source of the free nucleus cannot be assumed; only if the atom is fixed in a molecular lattice and the emitted γ -quant has an energy $E_0 + E_R$ and $E_0 \lesssim \Gamma$, the emission and absorption lines overlap and resonance fluorescence occurs.

In a solid or crystalline system, the recoil-free emission is inhibited by excitation or annihilation of phonons. This process also results in a vibrational energy with magnitudes higher than the natural line width Γ . In the quantum mechanical description of the solid, a finite probability f is declared, which describes the zero-phonon process in the static phonon system, that is without any phonon excitation. This factor f is known as the Debye-Waller-Factor and is described in the Debye model, which estimates the phonon distribution in a solid. Instead of the Einstein model, where the decrease of specific heat is explained qualitatively, the Debye model uses the T^3 dependence and thus improves the fit between theory and experiment for low temperatures. In addition, it introduces a continuum of oscillator frequencies, ranging from zero to a maximum frequency ω_Θ , the so called Debye frequency ¹⁶¹. In nuclear resonance absorption this factor is described as Lamb-Mössbauer-Factor f_{LM} and calculated as the recoil-free fraction of γ -quanta, which are emitted and absorbed without recoil over a time average. The Lamb-Mössbauer-Factor f_{LM} describes the vibration properties of the solid and is calculated by using the mean square displacement $\langle x^2 \rangle$ of the nucleus from equilibrium position and the transition energy of the γ -quant (E_γ):

$$f_{LM}(T) = \exp \left[\frac{-\langle x^2 \rangle E_\gamma^2}{(\hbar c)^2} \right] \quad (28)$$

As the recoil-free fraction depends on the temperature and is further affected by the lattice properties, several assertions about f_{LM} are possible: i) a weakly bound Mössbauer active nucleus in the crystal exhibits a larger mean-square displacement than a strongly bound nucleus, resulting in a smaller f_{LM} value and a smaller resonance effect; ii) as the transition energy E_γ increases, the resonance effect decreases, limiting the number of Mössbauer nuclei with excited energies beyond 0.2 MeV¹⁵¹; and, iii) increases in the Debye temperature θ_D lead to increases in f_{LM} . As the elastic properties of the lattice limit the Debye temperature to $\hbar\omega_\theta$, the recoil-free fraction f_{LM} is expressed in terms of the corresponding Debye temperature θ_D . The Debye temperature should be replaced by the Mössbauer temperature θ_M , which is specific to the local environment of the Mössbauer nuclei, as θ_D is based on the assumption of a continuous distribution of phonon frequencies and determined from specific heat. It should be noted that the quantity θ_M is derived from Mössbauer data and therefore has little physical meaning, as it is not directly related to a structural characteristic¹⁶⁸. For the Lamb-Mössbauer factor, it follows that:

$$f_{LM}(T) = \exp \left[-\frac{3E_R}{2k_B\theta_M} \left\{ 1 + 4 \cdot \left(\frac{T}{\theta_M} \right)^2 \int_0^{\theta_M/T} \frac{x}{e^{-x} - 1} dx \right\} \right], \quad (29)$$

where E_R is the free nucleus recoil energy given in equation (22), k_B is the Boltzmann's constant, and T is the given sample temperature. The resulting temperature dependent f_{LM} is given in the supporting Figure S 1. In the low-temperature region, where $T \ll \theta_M$, the following approximation is used:

$$f_{LM}(T) = \exp \left[-\frac{E_R}{k_B\theta_M} \left(\frac{3}{2} + \frac{\pi^2 T^2}{\theta_M^2} \right) \right], \quad (30)$$

where the integral yields a T^2 dependence. However, in the higher temperature region, where $T \geq \frac{1}{2}\theta_M$, a linear regime approach is more suitable:

$$f_{LM}(T) = \exp \left[-\frac{6E_R T}{k_B\theta_D^2} \right]. \quad (31)$$

As already mentioned above, f_{LM} relies on the bound character of the Mössbauer nuclei. In fact, it is very common to assume an equal f_{LM} for all species that appear in a measured sample. Nevertheless, several authors argue that the impact of f_{LM} is not negligible^{165, 168-170}. Still, as our current estimates show, for the relation between FeN₄ centers and inorganic impurity species typically found in Fe-N-C, f_{LM} can be

neglected for comparison of absorption areas, specifically, as the exact values for the different FeN₄ sites in most Fe-N-C catalysts are unknown¹⁰⁷.

In addition to the described possibility to calculate the Lamb-Mössbauer factor, Frauenfeld has proposed an alternative measure using the temperature dependency of the spectral area change in Mössbauer spectra under different temperatures¹⁶¹. This method is suitable if the overall species amount does not change and there is no superparamagnetic relaxation of iron-containing nanoparticles, which split into sub spectra during the temperature change. As Sturhahn et al.¹⁷¹ demonstrate, determining the area density is the most common source of systematic errors. The unknown behavior of the sample geometry, isotopic abundance, or mass density of the sample, as well as the unknown f_{LM} of the source, are the main reasons for flawed calculations. An ideal Mössbauer source, found for instance at the ESRF, eliminates some of these problems and offers the possibility to estimate the f_{LM} directly using NIS or SMS data¹⁷¹⁻¹⁷³.

Hyperfine Interaction

In the previous paragraphs, some general aspects of nuclear resonance and recoil-free interaction were described. The following section focuses on the most important Mössbauer nucleus, iron. Over 90% of all Mössbauer-related publications reference to ⁵⁷Fe-Mössbauer spectroscopy¹⁷⁴.

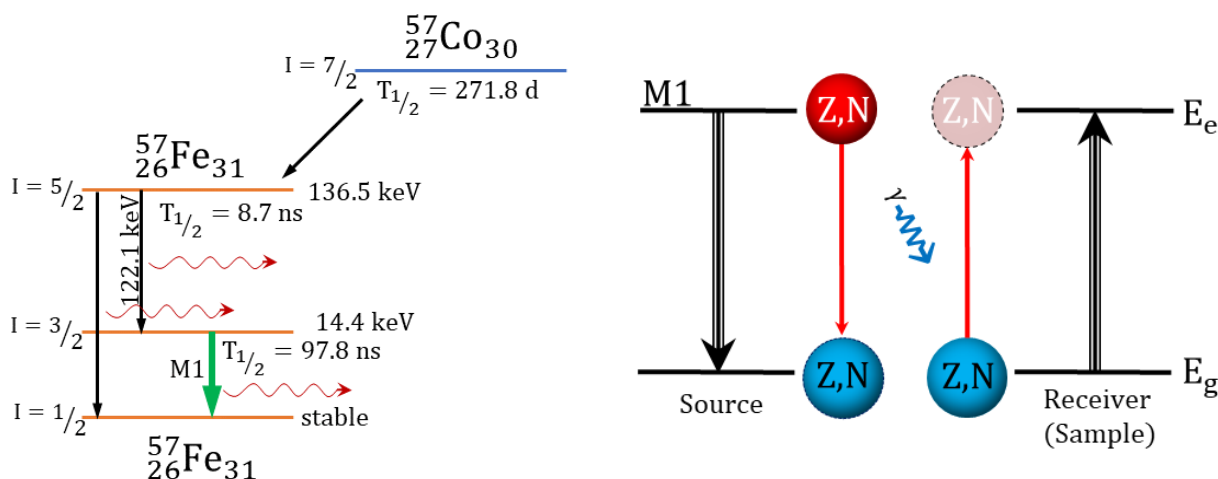


Figure 12: The ⁵⁷Co decay scheme is shown (left)^{175, 176}. The detailed description of the mechanism is given in the text. Transition scheme of the source with the emission and absorption of the γ -quant by the sample nuclei (right)¹⁷⁷.

Figure 12 depicts the γ -decay scheme of ⁵⁷Co to ⁵⁷Fe. The radioactive ⁵⁷Co, with a half-life time of 271.8 days decays by an electron capture (EC) from the K-shell with an efficiency of 99.84% to ⁵⁷Fe and initially occupies the 136.5 keV nuclear level with the nuclear spin quantum number $I = 5/2$. After 8.7 ns, the excited state decays to the nuclear level $I = 3/2$ by emitting a γ -quant with 122.1 keV with a

probability of 85% or directly to the ground state with a probability of 15%. The half-life of the $I = 3/2$ nuclear state is 97.8 ns and decays with the M1 transition by emitting a γ -quant of 14.4 keV to the stable nuclear state of ^{57}Fe .

Only 11 % of M1 transitions result in the emission, whereas 89% are lost due to internal conversion processes, caused mainly by the energy transfer to a K-shell electron, and will be ejected as so-called conversion electrons. The internal conversion coefficient $\alpha_T = 8.17$ for ^{57}Fe is rather high compared to other isotopes and defines the ratio between conversion electrons and γ -photons. Indeed, the natural abundance of ^{57}Fe is rather low (2.19% of the overall iron amount), but the high cross-section of $\sigma = 2.57 \cdot 10^{-18} \text{ cm}^2$, which results in a high interaction probability of the γ -quant with the nucleus, makes iron particularly interesting for Mössbauer spectroscopy. Therefore, an additional enrichment with ^{57}Fe ^{150, 151} is only necessary for a small sample amount or to achieve short measurement times and to increase the signal to noise ratio.

The nature and strength of the hyperfine interactions are reflected in the spectrum by the position, shape and number of transition lines. Three possible types of interactions are distinguished: i) the isomer shift δ_{ISO} , which identifies the position of the resonance lines and results from Coulomb interaction; ii) the quadrupole splitting (ΔE_Q), which causes twofold degeneration of nuclear states, and iii) the magnetic dipole interaction with magnetic dipole splitting (ΔE_M). Figure 13 illustrates the impact of the hyperfine interaction resulting in the isomer shift, the energy scheme, and the effect on the Mössbauer spectrum. As source and absorber exhibit different chemical environments, the nuclear charge distribution ZeR^2 and the electronic charge density $e|\psi(0)|^2$ of both the ground and the excited state differ ($ZeR_g^2 \neq ZeR_e^2$), result in a shift of the nuclear states. The unequal mean square radius of the ground (g) and excited state (e), $R_g^2 \neq R_e^2$ induces a change in nuclear volume and different $(\delta E)_g$ and $(\delta E)_e$ compared to the bare nucleus. The isomer shift is written as:

$$\delta_{\text{iso}} = E_A - E_S = \frac{2 \cdot \pi}{5} Z \cdot e^2 \cdot \{|\psi(0)|_A^2 - |\psi(0)|_S^2\} \cdot (R_e^2 - R_g^2), \quad (32)$$

where the atomic number Z and E_A are given as:

$$E_A = E_0 \cdot \frac{2 \cdot \pi}{5} Z \cdot e^2 \cdot |\psi(0)|_A^2 \cdot (R_e^2 - R_g^2). \quad (33)$$

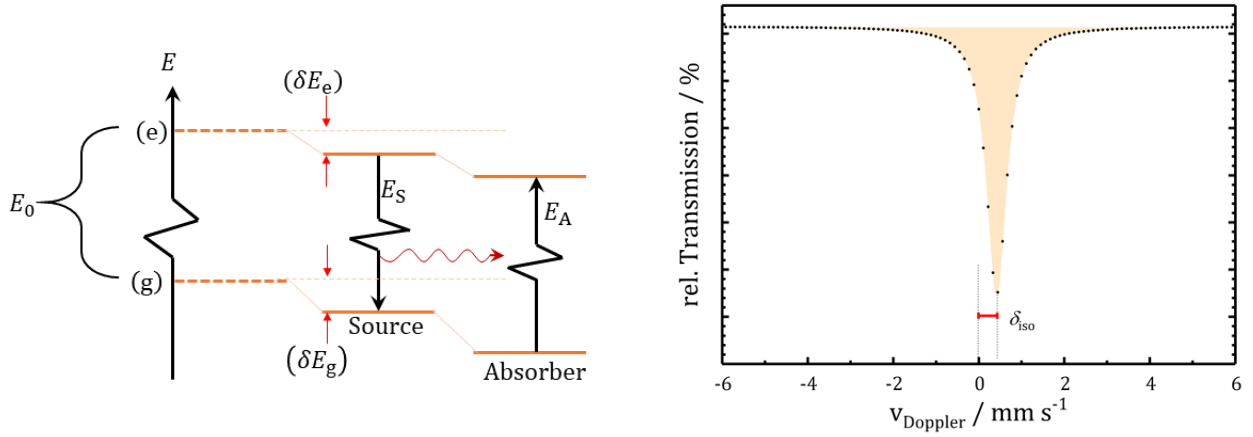


Figure 13: Energy scheme of the electric monopole interaction between the nucleus and the electron density which results in a shift of the nuclear state visible as isomer shift in the Mössbauer spectrum. As the source is not ideal, a shift of δE_g and δE_e in the energy level is already obtained (left). Resulting Mössbauer spectrum of the monopole interaction which results in a singlet. The resulting isomer shift represents the different chemical environment of source and absorber (right).

As the electron densities of the emitted and the absorbed nuclei are different, the transition energies of the source E_S and the absorber E_A shift the transmission line. The shift of the different nuclear levels offers information about the oxidation state, the electronic spin state, the electronegativity, and the character of bonds and ligands¹⁷⁷. As the 4s-electrons have a finite probability of presence inside the nucleus and, therefore, show the highest impact on the isomer shift. Shielding effects from the p -, d - or f -electron orbitals can reduce the 4s-electron density and increase the value of the isomer shift. Nevertheless, the shielding effects are less important for the variation of the isomer shift, whereas the variation of the 4s population has an equal or stronger impact. To explain the contribution of 4s-electrons to the charge density at the nucleus, molecular orbital calculations (MO) are required¹⁵¹. Hence, the most important information δ_{iso} offers is the valence state of the atom.

In addition, the isomer shift δ_{iso} includes a temperature dependent, relativistic contribution term as described by de Grave et al.^{168, 170}:

$$\delta(T) = \delta_1 + \delta_{\text{SOD}}(T) \quad (34)$$

where δ_1 is the temperature-independent genuine isomer shift and δ_{SOD} the so-called second-order Doppler shift, which results from the temperature difference between source and sample and the resulting thermal motion variety.

As δ_{SOD} arises from the non-zero average of the quadratic velocity of the absorbing nuclei,

$$\delta_{\text{SOD}} = -E_\gamma \frac{\langle v^2 \rangle}{2c^2} \quad (35)$$

the Debye model is drawn on for determination^{170, 178}:

$$\delta_{\text{SOD}} = -\frac{9k_B E_V}{16M_{\text{eff}}c^2} \left(\theta_M + 8T \left(\frac{T}{\theta_M} \right)^3 \int_0^{\frac{\theta_M}{T}} \frac{x^3}{e^x - 1} dx \right), \quad (36)$$

where M_{eff} is the effective vibrating mass. As the vibrating mass and δ_{SOD} are influenced by the binding of the resonant nucleus in the lattice and the variation of material composition, the lattice structure and environmental conditions¹⁷¹, this parameter offers a better understanding of the dynamic properties of the solid. The influence of δ_{SOD} decreases with the sample temperature and can generally be neglected for liquid helium temperature¹⁵¹. Under standard condition the δ_{SOD} has not to be considered.

The isomer shift itself is not sufficient to gain information about electron occupation and spin states. Here, the investigation of the 3d-electrons is necessary. Table 3 gives the 3d-electron levels for an octahedral aligned rhombic field in axial direction and helps to clarify the electron position and spin states in iron compound systems, using the crystal-field approximation.

Table 3: 3d orbital population of iron in the most common spin and oxidation states. Table is inherited from DeBrunner¹⁷⁹

3d Single Electron Levels in Octahedral + Axial + Rhombic Field	Fe(I) $3d^7$		Fe(II) (ferrous) $3d^6$			Fe(III) (ferric) $3d^5$			Fe(IV) $3d^4$
	Spin	$1/2$	2	1	0	$5/2$	$3/2$	$1/2$	1
	$d_{x^2-y^2}$		↑			↑			
	$d_{3z^2-r^2}$	↑	↑	↑		↑	↑		
	d_{yz}	↑↓	↑	↑	↑↓	↑	↑	↑	↑
	d_{xz}	↑↓	↑	↑↓	↑↓	↑	↑	↑↓	↑
	d_{xy}	↑↓	↑↓	↑↓	↑↓	↑	↑↓	↑↓	↑↓

In Table 4 the common isomer shift values of FeN_4 -sites found in Fe-N-C catalysts are listed. The isomer shift for the different compounds shows a strong overlap between the Fe(II) low-, and intermediate spin, and the Fe(III) low-, intermediate-, and high spin. It is thus necessary to combine the isomer shift with further parameters, for instance quadrupole splitting and additional techniques like low temperature Mössbauer spectroscopy or EPR, to distinguish and quantify the different iron compounds.

While the isomer shift only affects the position of the transition line, the quadrupole interaction deals with the rotational confirmations that a non-spherical nucleus can take in the in-homogeneous electric

field generated by a noncubic charge distribution¹⁵¹. Hence, the quadrupole splitting reflects the population of the iron 3d-orbitals, as well as the ligand charges surrounding the iron¹⁶⁷. This behavior is described by a non-symmetric electric field gradient (EFG). The quadrupole splitting can only appear for $I > 1/2$ with an EFG $\neq 0$ and, therefore, the ground state of ^{57}Fe is not affected. For the first excited nuclear state $I > 3/2$, the splitting appears in two nuclear sublevels (Figure 14).

Table 4: Overview of the most common isomer shift ranges appearing in Fe-N-C catalysts and molecular FeN₄ centers. The data is obtained as a combination of Ref¹⁵¹, Ref¹⁰⁷ and Ref¹⁸⁰ and given for room temperature.

Component	Spin	$\delta_{\text{iso}} / \text{mm s}^{-1}$	Coordinated	Electron config.
Fe(II)	0	-0.25 – 0.5		$3d^6$
FePorph(X) ₂ , X = py, NH ₃	0	0.35 – 0.38	Sixfold	$3d^6$
Fe(II)	1	0.25 – 0.5		$3d^6$
α -Fe Phtalocyanin	1	0.36 – 0.4	Fourfold	$3d^6$
Fe(II)	2	0.6 – 1.4		$3d^6$
Cytochrome c Heme	2	0.9 – 0.95	Fivefold	$3d^6$
Fe(III)	$1/2$	-0.2 – 0.4		$3d^5$
FePorph axial ligands like CN ⁻ , OH ⁻ , N ₃ ⁻	$1/2$	0.15 – 0.25	Sixfold	$3d^5$
Fe(III)	$3/2$	0.2 – 0.4		$3d^5$
(Very) weak axial ligands	$3/2$	0.3	Sixfold	$3d^5$
Fe(III)	$5/2$	0.25 – 0.6		$3d^5$
Halogen ions	$5/2$	0.3 – 0.45	Fivefold	$3d^5$

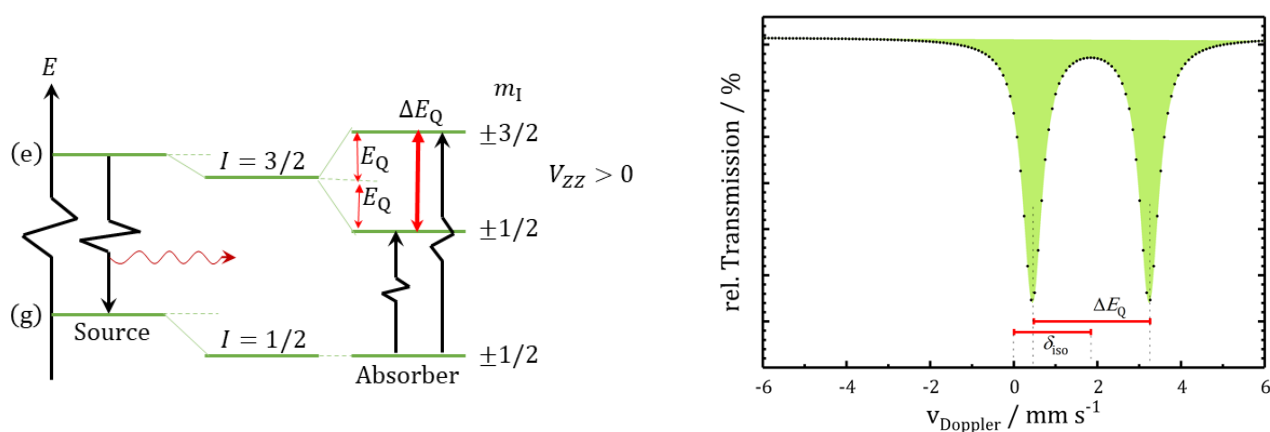


Figure 14: Energy scheme of the quadrupole splitting. A nuclear state with $I = 1/2$ and an EFG = 0 shows no quadrupole interaction. Therefore, the ground state of ^{57}Fe is not affected (left). For the first excited nuclear state $I > 3/2$ the splitting in two nuclear sublevels is observed as an EFG $\neq 0$ caused an eigenvalue $V_{zz} > 0$. Resulting Mössbauer spectrum of the quadrupole interaction which results in a doublet. The resulting isomer shift represents the different chemical environment of source and absorber, whereas the splitting gives the energy difference of both states (right).

The electric field gradient (EFG) is generated by the impact of ligands on the electron density surrounding the ^{57}Fe nucleus. Conventionally, the resulting eigenvalues $|V_{xx}|, |V_{yy}|, |V_{zz}|$ are chosen such that $|V_{xx}| \leq |V_{yy}| \leq |V_{zz}|$. This gives the asymmetry parameter η :

$$\eta = \frac{V_{xx} - V_{yy}}{V_{zz}}, \quad (37)$$

and is used to evaluate the quadrupole splitting (ΔE_Q):

$$\Delta E_Q = \frac{1}{2} eQV_{zz} \sqrt{1 + \frac{\eta^2}{3}}. \quad (38)$$

To compute the quadrupole interaction; the spin-Hamiltonian needs to be considered:

$$\hat{H}_Q(E2) = \frac{eQV_{zz}}{4(2I - 1)} \left[3\hat{I}_z^2 - I(I + 1) + \frac{\eta}{2} (\hat{I}_x^2 + \hat{I}_y^2) \right]. \quad (39)$$

Here, Q describes the nuclear quadrupole momentum, I the nuclear spin state, and $\hat{I}_x^2, \hat{I}_y^2, \hat{I}_z^2$ the corresponding spin operators. To understand the magnetic dipole interaction, the quantum mechanical formalism of Hamiltonian needs to be introduced, which is also important for low-temperature ^{57}Fe transmission Mössbauer spectroscopy (LT-MS) with an external applied magnetic field. In this case, the Hamiltonian formalism is needed to interpret the resulting spectra. The hyperfine interactions are written as a Hamiltonian of the nucleus \hat{H}_N :

$$\hat{H}_N = \hat{H}_N^0 + \hat{H}^{\text{hf}} = \hat{H}_N^0 + \hat{H}_1(E0) + \hat{H}_M(M1) + \hat{H}_Q(E2) + \dots, \quad (40)$$

which is the sum of \hat{H}_N^0 , the unperturbed nuclear Hamiltonian and the perturbation Hamiltonian \hat{H}^{hf} . \hat{H}^{hf} summarizes $\hat{H}_1(E0)$, the electrical monopole interactions (Figure 13), $\hat{H}_M(M1)$ the magnetic dipole interaction results in the magnetic splitting in the six-line pattern (Figure 15), and the quadrupole splitting $\hat{H}_Q(E2)$ (Figure 14).

The magnetic Hamiltonian $\hat{H}_M(M1)$ includes the Zeeman term, which describes the coupling of the external applied magnetic field \vec{B}_0 and the magnetic moment of the nucleus with the internal magnetic hyperfine field $\vec{B}_{\text{hf}} = -\langle \vec{S} \rangle \cdot \vec{A} / g_N \mu_N$. Further, the nuclear Zeeman effect causes the split into $2I + 1$ (in total six) equally spaced nondegenerate sub-states, resulting in equidistant transition signals with the

intensity ratio 3:2:1:1:2:3, which are known from homogeneously distributed internal hyperfine fields and the velocity calibration measurement of α -iron (Figure 15). It follows that:

$$\hat{H}_M(M1) = \langle \vec{S} \rangle \cdot \vec{A} - g_N \mu_N \vec{B}_0 \cdot \vec{I} = -g_N \mu_N (\vec{B}_{\text{hf}} + \vec{B}_0) \cdot \vec{I}, \quad (41)$$

with the nuclear g -factor $^{181} g_N$, the nuclear magneton μ_N , and \vec{A} as the tensor coupling the spin-expectation value $\langle \vec{S} \rangle$ to the nuclear spin I . The related Zeeman energies (magnetic dipole splitting) for the ground $\Delta E_{M,g}$ and excited $\Delta E_{M,e}$ states are given as:

$$\Delta E_{M,g} = g_g \mu_N \vec{B}_0 \quad \text{and} \quad \Delta E_{M,e} = g_e \mu_N \vec{B}_0, \quad (42)$$

with the g -factor for the ground g_g and excited g_e states, respectively. Combining equations (39), (40), and (41) results in the nuclear Hamiltonian:

$$\hat{H}_N = \frac{eQV_{zz}}{4(2I-1)} [3\hat{I}_z^2 - I(I+1) + \eta(\hat{I}_x^2 + \hat{I}_y^2)] - g_N \mu_N \vec{B} \cdot \vec{I} + \langle \vec{S} \rangle \cdot \vec{A} \cdot \vec{I}. \quad (43)$$

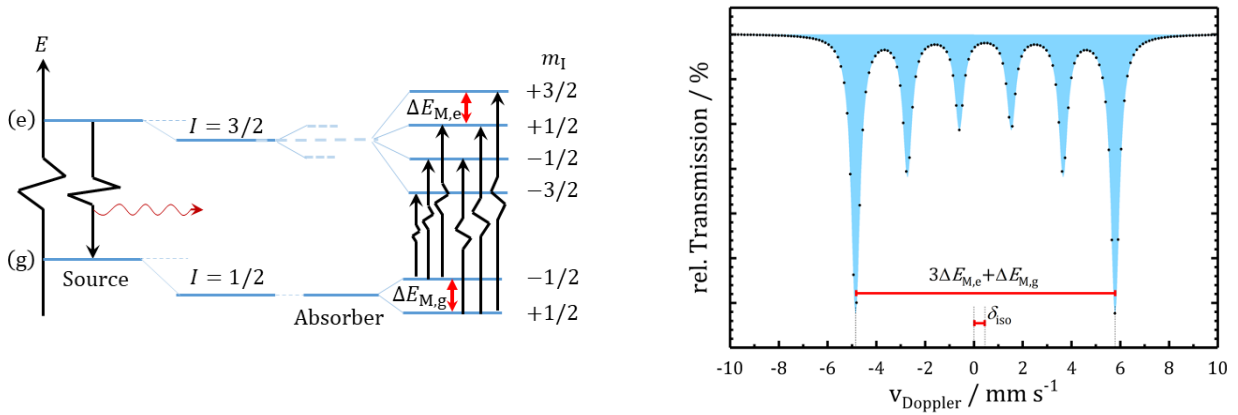


Figure 15: Energy scheme of the magnetic dipole splitting (left). Simulated six-line pattern with the intensity ratio 3:2:1:1:2:3 (right). The energy shift is caused by the electric monopole interaction, whereas the value $3\Delta E_{M,g} + \Delta E_{M,e}$ gives access to the internal magnetic field and therefore information about the electronic configuration.

Spin Hamiltonian

To calculate a paramagnetic iron with spin S , the nuclear spin Hamiltonian \hat{H}_N (equation (43)) and the electronic spin Hamiltonian \hat{H}_S need to be considered, because of the influence of ligand field. The calculates are represented as:

$$\hat{H}_S = D \left[\hat{S}_z^2 - \frac{S(S+1)}{3} + \frac{E}{D} (\hat{S}_x^2 - \hat{S}_y^2) \right] + \mu_B \cdot \vec{S} \cdot \vec{g} \cdot \vec{B}, \quad (44)$$

and used to determine the spin expectation values $\langle \vec{S} \rangle$ ^{179, 182, 183}. Here, D is the zero-field splitting (dependence on the strength of ligand field splitting between the orbital states and thus on the chemical bonds), $\frac{E}{D}$ is the rhombicity parameter, and μ_B is the Bohr magneton describing the influence of the crystal field. Equations (43) and (44) enable the simulation of low temperature Mössbauer spectra with an external applied field.

Superparamagnetic Relaxation in Magnetic Nanoparticles

The magnetic characteristics of small nanoparticles or atomic clusters often differs from those known from a bulk material due to a nonstable magnetization direction of the domains at finite temperatures^{174, 184, 185}. In general, an uniaxial magnetic anisotropy of the nanoparticle is assumed, given the magnetic anisotropic energy as

$$E_a(\theta) = KV \sin^2 \theta, \quad (45)$$

where both, the magnetic anisotropy constant K and the particle volume V , given the energy barrier for a permanent oriented magnetic moment, whereas θ is defined as the angle between the magnetization direction and the easiest direction of magnetization. It is shown mathematically that two minima at $\theta = 0^\circ$ and $\theta = 180^\circ$ are found, respectively. If the resulting energy barrier is smaller than the thermal excitation energy, a spontaneous fluctuation of the magnetization direction between the two minima may appear, the so-called superparamagnetic relaxation. Under the assumption of noninteracting nanoparticles in a zero applied magnetic field, the average time between two magnetization inversions is given by the Néel-Brown expression

$$\tau = \tau_0 \exp\left(\frac{KV}{k_B T}\right), \quad (46)$$

which is valid under the approximation of $KV \cdot (k_B T)^{-1} \gtrsim 1$. The value of $KV \cdot (k_B T)^{-1}$ is normally in the range between 2 – 9, whereas for τ_0 typical values around $10^{-13} - 10^{-9}$ s are found. As the time resolution of Mössbauer spectroscopy overlaps with the relaxation time, the expected sextet line shape of a magnetic nanoparticle collapses to a singlet or doublet if the relaxation time is smaller than the time

resolution. Normally, a huge particle size distribution is found in a sample, which results in a broad relaxation time distribution and overlapping line shapes in the resulting Mössbauer spectrum. Whereas, if the relaxation time of the nanoparticles is in the order of the time resolution, the contribution to the Mössbauer spectrum is barely visible and the relative surface area would be misleading. Hence, the time window for measurement needs to be smaller than the relaxation ^{34, 43, 51, 64, 86}.

Low-Temperature ⁵⁷Fe Transmission Mössbauer Spectroscopy (LT-MS)

In order to quantify a species nature, it is necessary to overcome small f_{LM} -values and to limit the effects of relaxation times of small domain structures on the spectrum. Field-dependent Mössbauer spectroscopy at low temperatures is used to slow the relaxation time and, in combination with an external applied field, depress fast relaxation processes. The fast domain switching, caused by the domain size or spin-spin-coupling processes, are slowed through a change in the population of ionic energy levels ¹⁸⁶. The setup is slightly different from a conventional RT-Mössbauer spectrometer, as the sample is installed inside a closed-cycle cryostat equipped with a superconducting magnet, as described, for example, by Janoschka et al. ¹⁸⁷. The radioactive source and the detector are normally not implemented into the cryostat, so δ_{SOD} needs to be considered. For the data analysis the spin and the nuclear Hamiltonian have to be consulted, as described before. Trautwein et al. ¹⁸⁸ contend that the full power of Mössbauer spectroscopy can only be obtained if the performed measurements are field- and temperature-dependent. Note that, under these circumstances, only indirect information about the electron configuration are obtained, as the nuclear environment is determined by the Mössbauer nucleus through an interchange of the hyperfine coupling. As described above, the magnetic hyperfine field is the product of the magnetic hyperfine tensor and the spin expectation values of the electrons and results in the magnetic splitting. To access relevant chemical information like zero-field splitting, electron spin coupling, and spin fluctuations, the magnetic hyperfine tensor must be known. Complementary and independent data like electron paramagnetic resonance (EPR), neutron activation analysis (NAA), or other spectroscopy techniques are thus crucial to complete the picture.

Room-temperature ⁵⁷Fe Mössbauer spectroscopy is used by different groups to investigate the oxidation states and chemical environment of Fe-N-C catalysts ^{39, 50, 52, 64, 189}. To gain additional insight into the iron sites and their hyperfine interactions, LT-Mössbauer spectroscopy causes magnetic splitting due to the reduced spin relaxation. The resulting spectral shape is given by the ground-state spin multiplets and, therefore, needs to be determined by the Spin Hamiltonian ¹⁹⁰. LT-Mössbauer spectroscopy is widely used for iron-containing biomolecules, heme proteins and corresponding model complexes ¹⁹¹ but rather innovative in the investigation of Fe-N-C catalysts ^{51, 165}.

3.4.2. Synchrotron

The advantage of applying nuclear resonant techniques at synchrotrons is that the right resonant energy of each Mössbauer isotope can be adjusted by the X-ray beam, as no radioactive source is needed. Especially for ^{57}Fe Mössbauer, the extremely high energy resolution with a width of $\Gamma_f = 7.07 \cdot 10^6 \text{ s}^{-1}$ in the frequency scale, $\Gamma_e = 4.65 \cdot 10^{-9} \text{ eV}$ in the energy scale, and $\Gamma_v = 0.097 \text{ mm s}^{-1}$ in the velocity range, are only accessible with synchrotron radiation and permit the division of atomic motion into high and slow atomic velocities ¹⁹².

Table 5: Comparison between a 3rd generation undulator source and a commercially available ^{57}Co source with 370 MBq activity (values taken from Sturhahn et al. ¹⁹³ and ¹⁵²).

Property	Synchrotron Radiation	Radioactive Source
Spectral Flux / $\text{ph s}^{-1} \text{ eV}$	$2.5 \cdot 10^{12}$	$2.5 \cdot 10^9$
Brightness / $\text{ph s}^{-1} \text{ eV sr}$	$2.8 \cdot 10^{22}$	$2.5 \cdot 10^{12}$
Brilliance / $\text{ph s}^{-1} \text{ eV sr mm}^2$	$2.8 \cdot 10^{22}$	$2.5 \cdot 10^{10}$
Typical Beam Size / mm^2	1×1	10×10
Focused Beam Size / μm^2	6×6	-
Energy Resolution / neV	variable	4.7
Time Resolution / ns	0.7	-
Polarization	linear or circular	unpolarized

The effect of the two is very different, fast spatially, unlimited atomic motion destroys coherent resonant scattering completely, whereas fast motion limited in space, only changes the intensity. However, low velocities enable the probing of diffusive atomic motion ¹⁹², rendering new characterization techniques examining the energy domain (e. g., synchrotron based Mössbauer spectroscopy and nuclear inelastic scattering) or the time domain (nuclear forward scattering) of excited nuclear states. Furthermore, the outstanding brilliance, transverse coherence, and polarization of the synchrotron beam enables unique studies in the field of material science ¹⁵², geology ¹⁶³, and biology ¹⁹⁴. Especially for fast reactions (as in situ or operando techniques), small sample volumes (e.g., nanostructure, ultrathin films, or clusters), high pressure experiments, or measurements with a narrow space resolution, synchrotrons are indispensable.

3.4.3. Nuclear Inelastic Scattering (NIS)

The possibility to use the nucleus recoil to determine the frequency distribution by crystal lattice vibrations was introduced by Visscher in 1979 ¹⁹⁵. The phonon energy spectrum was first observed with

synchrotron radiation by Seto et al. in 1995¹⁹⁶. In Mössbauer spectroscopy, the recoil-free fraction (f_{LM}) of the emitted sample radiation describes the probability to observe iron related resonance. Some resonant absorption events proceed to transfer recoil energy to the solid and are observed as nuclear inelastic scattering (NIS)¹⁵². To determine the probability of events with recoil, the difference of the recoilless fraction $1 - f_{LM}$ is used. This difference provides information about the dynamics of the studied system such as phase transitions and vibrational anisotropy^{197, 198}. As relevant nuclear transitions appear in the low-energy range of 6–30 keV in Mössbauer spectroscopy, the energy of incident X-rays coincides precisely with the energy of the nuclear transition and a peak in elastic nuclear absorption occurs. The power of NIS is given by the Mössbauer isotope selective observation of vibrational sidebands in the lattice vibration with creation ($E > 0$) or annihilation ($E < 0$) of lattice vibrations, the so-called phonons¹⁹⁹. Instead of prompting the ground state to the excited state without a change in the vibrational state, as it is the case in Mössbauer spectroscopy, NIS accesses the vibrational energy caused by discrete changes in normal mode frequencies. Therefore, the absorption spectrum includes peaks relayed from the recoilless Mössbauer resonance by energies equal to the vibrational quanta¹⁹⁴. As described by Ruffer and Chumakov²⁰⁰, temperature influences the energy spectra of inelastic absorption. Decreases in temperature eliminates the phonon-annihilation parts of the spectra. Phonon creation, on the other hand, can even occur at temperatures below 24 K.

To investigate samples with NIS, a 3rd generation synchrotron needs to be combined with a high-heat load monochromator and a high-resolution monochromator to cut the full width at half maximum of the incoming X-ray pulse to less than 1 meV (Figure 16). Unlike other methods, NIS provides the ultimate limit in selectivity, because only the vibrational dynamics of the probe nucleus contribute to the observed signal and, thus, NIS is not limited by optical selection rules like Raman or infrared spectroscopy²⁰¹. In consequence, it provides important additional information about the molecular dynamics¹⁹⁴. By plotting the resulting energy spectrum over the density of phonon states (pDOS), the vibration modes derived directly^{199, 201}. However, NIS is not easily to implement, as only synchrotrons with tunable ultra-high-resolution monochromators which provide an extremely narrow X-ray beam and an energy resolution in the order of 1 meV (7-8 cm⁻¹), namely APS, PETRA III, Spring 8, and ESRF, enable such experiments. The associated beamlines are further equipped with optimized timing electronics to discern the prompt elastic scattering signal, which is ~ 107 times larger than the observed inelastic scattering. Therefore, the detector should be as close as possible to the sample, without being irradiated with the main beam. In case of ⁵⁷Fe, the desired nuclear resonance signals appear with a delay of 141 ns and are given during the lifetime of the nuclear excited state. The sample standards are equally high, as the sample should be pure in terms of molecular populations, to match the quantitative extraction of atomic displacements. Otherwise, a complex spectrum will appear and makes rendering data interpretation rather difficult. Further, it is useful to enrich the sample with ⁵⁷Fe, as the resulting NIS signal is proportional to the

number of resonant nuclei in the effective sample volume and to the excitation probability²⁰². Crystalline (oriented), powder or liquid samples are possible two investigate if operation temperatures below 50 K are chosen¹⁹⁴.

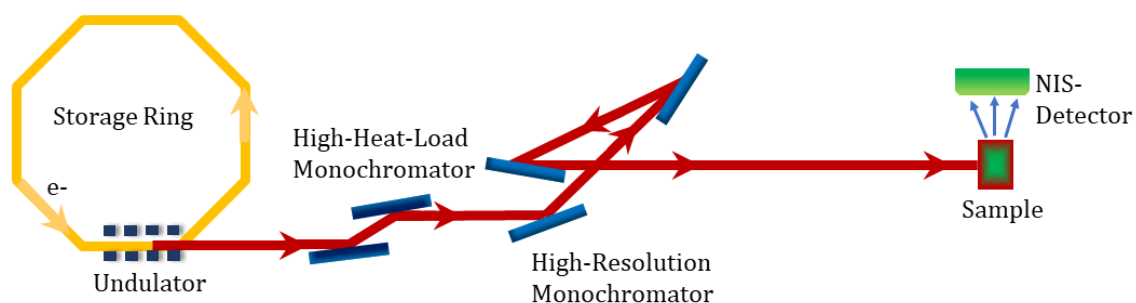


Figure 16: Schematic Illustration of the NIS experiment. In the storage ring, the electrons are accelerated. By distraction of the electrons by the undulators the synchrotron light is emitted and hits the carbon based high-heat monochromator. The included high-resolution monochromator, based on a silicon single crystal, cuts the full width at half maximum to less than 1 meV. The synchrotron pulse hits the sample and excites the nuclear states. The resulting inelastic spectra is recorded by an avalanche photodiode detector (APD). During the pulses the APD is switched off, in order to gate out elastically scattered 14.4 keV photons, so that only delayed fluorescence photons corresponding to nuclear absorption are detected, Figure taken from²⁰¹.

Every excited vibration mode of the Mössbauer active nuclei results in a lattice vibration, whereas all other modes are silent. Thus, NIS offers more details about the ligand vibration modes than IR or resonant Raman spectroscopy. One drawback of nuclear inelastic vibration scattering is the challenge to make detailed vibrational assignments, which are impaired by significant mode mixing¹⁹⁴. According to Lipkin, the resulting dataset has to be normalized using a harmonic approximation²⁰³, which describes molecular vibrations in terms of independent oscillations. A detailed description of data processing to calculate the phonon density of states (pDOS) is given by Zeng et al.²⁰² and Sage et al.²⁰⁴.

As the Fe-N-C catalyst system is related to a heme-like structure, similar frequencies for vibration modes are assumed. Scheidt et al.¹⁹⁴ give an overview of related frequencies. Phonon modes resulting from heme translation in the solid are typically seen below 50 cm^{-1} in broad and low frequency modes. In the range below 200 cm^{-1} , primarily plane midrange modes are found, whereas the highest frequency modes are found between $400 - 600\text{ cm}^{-1}$. These frequencies involve iron and the vibration modes of axial ligands.

Related Mössbauer data is helpful to construct a meaningful model of the investigated system to quantify the obtained pDOS. Density functional theory (DFT) calculations support this model and allows the simulation of a pDOS spectrum and the comparison with pDOS data obtained from the origin NIS. Nevertheless, DFT calculations are a challenging and complex science interconnect with integrating chemistry and solid-state physics. In addition to the computational quantum mechanical modeling of

electronic and nuclear structures in many body systems, countless different electronic structure methods should be used.

3.4.4. Nuclear Forward Scattering (NFS)

The nuclear resonant techniques described before examine certain physical parameters and related chemical properties as using energy, whereas nuclear forward scattering (NFS) is a time-based technique. Importantly, the transformation of time is not as straightforward as the transformation between spatial coordinates and the momentum space, which is a linear superposition of constituent components. The operation on the time scale is restricted by causality, with periodic oscillations known as quantum beats caused by the frequencies of different resonance lines¹⁵². Therefore, a Fourier transformation of the frequency-dependent amplitude transmission spectrum is needed¹⁵⁶.

Figure 17 shows a setup scheme of the NFS method. The main difference in setup compared to NIS is the position of the detector and the time resolution of the measurement.

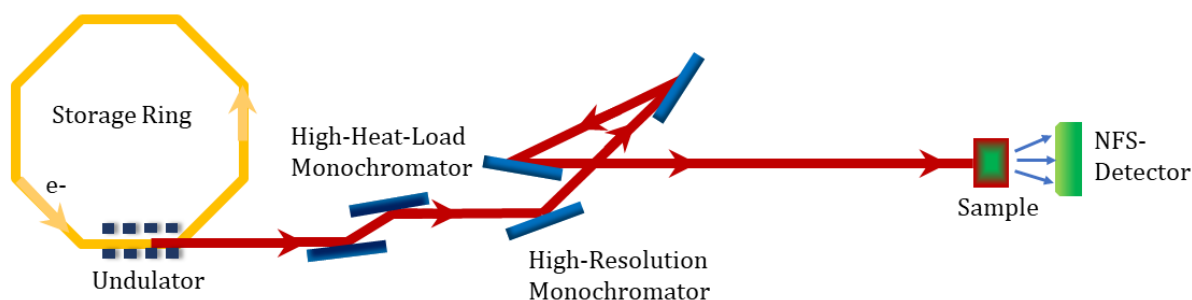


Figure 17: Scheme of a NFS experiment. In the storage ring, the electrons are accelerated. By distraction of the electrons by the undulators the synchrotron light is emitted and hits the carbon based high-heat monochromator. The included high-resolution monochromator, based on a silicon single crystal, cuts the full width at full maximum to less than 1 meV. The synchrotron pulse hits the sample and excites the nuclear states. The resulting quantum beats are detected by an (avalanche photodiode detector (APD)). Only the desired forward scattering is detected, as the APD is switched off during the synchrotron light pulses²⁰¹.

Synchrotrons of the 3rd and soon the 4th generation enable coherent scattering in the forward direction. The operation in the bunching mode, where electron bundles are accelerated in the synchrotron resulting in a pulsed synchrotron light flash, prompts several coherent nuclear sublevel states of the Mössbauer isotope. These states will oscillate at their various natural frequencies and observed in the quantum beat pattern²⁰⁵. As the oscillators in the sample are coupled through the radiation field, the simultaneous excitation of these oscillators results in quantum beats and acceleration phenomena¹⁵². The beat frequency from the coherent inelastic scattering reveals the relative isomer shift between two different chemically bonded Mössbauer active nuclei, but not their absolute value, as known from conventional Mössbauer experiments. However, direct determination of the hyperfine splitting is possible²⁰⁵. Indeed,

only a shift between the levels of Mössbauer nuclei located in different chemical sites or the hyperfine splitting of the nuclear levels results in a periodic constructive / destructive interference between waves of different frequency. The latter results in the striking “quantum beat” modulation of the spatially coherent decay rate and is the reason why only the slope obtained by NFS changes for singlet species²⁰⁶. Therefore, the delay between two adjacent electron bunches from the synchrotron must be longer than the mean lifetime of the excited nuclear state, which is between ns and μ s, depending on the probed Mössbauer nucleus¹⁵². Winkler et al.²⁰⁷ offer several reasons why NFS provides new insights about the investigated sample. Measurements in the time domain i) show an improved signal-to-noise ratio, ii) are insensitive to mechanical vibrations, iii) have a precise and stable time scale, and iv) additional external parameters like polarization and the time structure of the probing radiation are introduced²⁰⁸. Furthermore, the reduction of measurement time due to the extremely intense beam is attractive, especially for small samples. The coherent beam enables diffraction and interferometry experiments that combine information about internal fields with the spatial arrangement of sample atoms¹⁵². Based on Paulsen et al.²⁰⁹, Table 6 compares a conventional Mössbauer source and the synchrotron based nuclear forward method.

Table 6: Comparison between NFS and conventional Mössbauer spectroscopy. Table taken from Paulsen et al.²⁰⁹

	Resonant Forward Scattering	Conventional Resonant Absorption
Sample Cross Section	0.1 – 1.0 mm ²	10 – 100 mm ²
Amount of ⁵⁷ Fe	≈ 3 μ g	≈ 30 μ g
Data Acquisition Time	Minutes to Hours	Days to Weeks
Background	≤ 1%	≥ 90%
Data Analysis	Complex, Visually Controlled Simulations	Simple, Fits with Lorentzian

Haas et al.²¹⁰ illustrate the experimental limits of NFS by investigating a 1:1 superposition of two quadrupole splittings. Whereas the position is easily determined in a conventional (energy domain) Mössbauer experiment, a numerical analysis is necessary in the time domain. Therefore, NFS is not well suited to study highly complex phases containing iron in different spin states, valence states, and chemical environments, as only relative isomer shifts are identified and species with a relatively similar quadrupole splitting can overlap and are thus not distinguishable²¹⁰. Moreover, the position of magnetic moments, potentially determined by the domain structure or the preferred orientation, causes a significant difference between conventional MS and NFS. In the forward scattering pattern, the coherent excitation of a multitude of nuclear resonance beatings depends strongly on their respective magnetic

quantum numbers, resulting in a different beating pattern²⁰⁸. Even though the data acquisition time and data analysis are outstanding, the accessibility of synchrotrons operating in the multi-bunch mode remain challenging. The multi-bunch operation is necessary to observe the periodic oscillations in the time differential mode, as it can reduce the possibilities to perform other experiments at the synchrotron facility¹⁵².

3.4.5. Synchrotron based ⁵⁷Fe-Mössbauer Spectroscopy (SMS)

Using synchrotron radiation as an ultimate Mössbauer source combines the outstanding properties of a synchrotron, as described in the previous chapters and summarized in Table 5 and Table 6, with the advantages of Mössbauer spectroscopy to access the chemical environments, as well as the oxidation and spin states of Mössbauer active nuclei. Besides the RT-measurements, low temperature measurements in combination with a magnetic field are possible. However, only two facilities in the world (ESRF and Spring 8) provide this technique to their users.

Synchrotron-based Mössbauer spectroscopy is optimized for highest intensity and best energy resolution, with a bandwidth of 15 neV and tunable in energy over a range of about $\pm 0.6 \mu\text{eV}$. In addition, the source is nearly fully resonant, fully polarized and features a high brilliance and a focus spot size of $10 \mu\text{m} \times 5 \mu\text{m}$ ²¹⁰. To achieve these outstanding parameters, the synchrotron radiation passes a high-resolution monochromator and illuminates a highly orientated, fully enriched iron borate ($^{57}\text{FeBO}_3$) crystal. The iron borate crystal is heated close to its Néel temperature of 348.35 K, where the antiferromagnetic behavior of the crystal switches to paramagnetic. This is followed by a collapse of the multiline spectrum to a single line around the Néel temperature caused by the particular interaction where magnetic dipole and electric quadrupole hyperfine interactions are strongly mixed²¹⁰. In consequence, a pseudo-single-line resonance Mössbauer source is produced and tuned over a defined Mössbauer velocity by a sinusoidal movement of the crystal.

SMS has several advantages: i) the analytical strategy is straightforward, as it is identical to conventional Mössbauer spectroscopy, ii) a narrow spot size in combination with the outstanding intensity overcomes absorption problems of in situ and operando cells such as fuel cells or electrochemical cells, as the cells design are optimized for best performance and the restrictions of radiation transmission through the cell are not as limiting as for conventional Mössbauer sources, iii) the measurement time is in the range of minutes (using highly enriched samples), access slow catalytic processes through experiments using fixed potentials to stabilize quasi-stable states, iv) even complex systems like Fe-N-C catalysts with a mixture of different species that show similar Mössbauer parameters are qualitatively and quantitatively analyzed, and v) electrochemical experiments in which the cell is directly frozen during the electrochemical treatment by simultaneous measurement of the SMS care possible. This is helpful to

investigate the catalyst's nature under working conditions or under fixed potentials, as well as in using low temperatures with or without a magnetic field for a full investigation of catalyst species.

3.5. Electron Paramagnetic Resonance (EPR)

In Electron paramagnetic resonance spectroscopy (EPR), transitions between magnetic dipole-moment eigenstates of a paramagnetic ion induced by microwave radiation are observed. The microwave region between 1 and 300 GHz is a good compromise between optimum sensitivity, sample size, homogeneity, strength of the required field and component cost¹⁸⁸. To observe an EPR signal, unpaired electrons must be present. The strength of the applied magnetic field modifies the energy separation between the involved states. For X-band EPR, a field of about 0.35 T is needed to obtain resonance absorption at 10 GHz. In the resulting spectrum the position of the resonance is related to the sample orientation and given by the so called g -value, which reflects the splitting of a magnetic sublevel pair under the influence of an external magnetic field:

$$g = \frac{h \cdot \nu}{\mu_B \cdot B_r} \quad (47)$$

Here, ν is the spectrometer frequency, h is the Planck constant, μ_B is the Bohr magneton expressing the magnetic moment of an electron caused either by its orbital or spin angular momentum, and B_r is the resonance field. In general, EPR spectroscopy offers direct accessible information only for single crystalline samples. If a polycrystalline or powder sample is examined, a line shape analysis is needed to quantify the spin behavior. The so-called lock-in technique is used to record the spectrum. For this purpose, the static magnetic field is modulated and the EPR-signal is detected with a narrowband band-pass filter to increase the signal to noise ratio. This explains why the measuring points are plotted over the first derivative of the absorption signal²¹¹ and additional simulations are required.

4. Experiments

4.1. Elucidating the Structural Composition of Fe-N-C Catalysts

As described in 3.1, the structure and nature of active sites in Fe-N-C catalysts remain unclear, as the high temperature oven process is not suitable to build a defined and ordered matrix to host catalytic active sites. Moreover, a variety of organic sites, like different FeN₄-sites, or inorganic sites, such as carbides or oxides, are formed during or after the pyrolysis and thus need to be removed by an additional acid leaching. Van Veen^{43, 61, 91} assumed that, at low temperature treatments, the macrocycles will not be completely destructed but result in a ligand modification, whereas Yeager⁸⁸⁻⁹⁰ postulated that the active species are formed during the contact with the electrolyte and not during pyrolysis. Especially above 800 °C, the macrocycles are destroyed and form oxidic species, which dissolve in the electrolyte. Nevertheless, the use of independent Fe and N precursors for synthesis necessitates a temperature above 600 °C. Although the synthesis routes show a wide variety, Mössbauer investigations found catalyst compounds assigned to FeN₄ environments^{36, 37}. Koslowski et al.³⁴ found a direct correlation between the iron content related to the so-called D1-site ($\sim \delta_{\text{iso}} = 0.3 \text{ mm s}^{-1}$, $\sim \Delta E_{\text{Q}} = 0.9 \text{ mm s}^{-1}$) and ORR activity in terms of kinetic current density, which they attributed to a ferrous low-spin iron in a N₄ coordinated site^{34, 39}. In short, the optimum synthesis temperature during pyrolysis strongly depends on the selected precursors. It was further shown by Kramm et al.²¹² and Bouwkamp-Wijnoltz et al.⁴⁵ that pyrolyzed carbon-supported iron porphyrins and phthalocyanines are suitable model systems due to the initial presence of FeN₄ coordination and resulting formation of ORR-active materials even at low pyrolysis temperatures.

The first temperature-dependent Mössbauer study of Fe-N-C catalysts was performed by Sougrati et al. to determine Lamb-Mössbauer factors of different iron components in the catalyst¹⁶⁵. Measurements at 5 K showed an overlay of FeN₄ sites with iron oxide nanoparticles, which was not unexpected, as the catalyst was prepared from ZIF-8, iron acetate, and phenanthroline during high-temperature pyrolysis (> 900 °C) without an additional acid leaching. Even at low iron loadings, the N₄-environment is likely to be disturbed when oxidic species are formed upon air contact. Kneebone et al.⁵⁰ investigated a PANI-based Fe-N-C catalyst with LT-Mössbauer spectroscopy at 80 K and NIS, suggesting that edge-hosted sites of FeN₄-type or Fe₂N₅-type are responsible for O₂ and NO attachments. However, the authors were unable to clarify the nature of the catalyst, as the Fe-N-C system showed seven different iron-containing species.

To eliminate possible inorganic sites, acid leaching is generally performed for all catalysts prepared in our group. Possible remaining iron-oxide species were excluded so far, since they are not stable under acidic conditions and should be completely resolved during the acid leaching. Recently, our group demonstrated that inorganic iron species such as elemental iron, iron oxide or iron carbide are

neglectable for low pyrolysis temperatures¹⁰⁷. Nevertheless, the active species, oxidation states, and intermediates under reaction conditions remain unclear. Understanding active site formation during or after the baking process using a combination of different nuclear- and electron-resonance techniques promises important insights into the structural composition of Fe-N-C catalysts. Therefore, a catalyst was prepared following the model of van Veen and examined with different nuclear- and electron resonant, as well as electrochemical techniques, complemented by DFT calculations and TEM.

To prepare the catalyst, highly enriched (95% ⁵⁷Fe) iron porphyrin (FeTMPPCl) from TriPorTech was mixed with Ketjen Black 600 as carbon support. For a sufficient mixing of the precursor, FeTMPPCl was dissolved in THF and the carbon support was added to the solution. The solution was treated in an ultrasonic bath for one hour, and afterwards evaporated with a rotary evaporator. The absolute iron content in the precursor was calculated to 2.1 wt%. The precursor was subsequently heat-treated in an inert gas atmosphere, using a heating ramp of 300 °C h⁻¹ to 600 °C, and holed for 30 min. The final temperature was set to 600 °C, as previous results have indicated that FeN₄-sites remain intact around 600 °C²¹². In addition, an acid leaching was performed by transferring the sample into 1 M HCl. The resulting suspension was placed in an ultrasonic bath for one hour and remained in the acid overnight. Afterwards, the solvent / catalyst mixture was filtrated and dried to receive the black catalyst powder. The so-obtained sample is labeled as HT600HCl.

To investigate the electrochemical performance of the catalyst, RDE experiments were performed with a three-electrode setup as described in 3.3.1. To this end, an ECI-200 potentiostat from Nordic Electrochemistry was combined with a rotating disc electrode setup from Radiometer (EDI101). As reference electrode an Ag / AgCl / 3 M KCl from C3 Prozess- und Analysetechnik GmbH was used. Here, a liquid phase of metal ions (Ag⁺) stays in equilibrium with a solid phase (AgCl). Ag / AgCl electrodes are much less affected by contamination and can therefore be used for deactivation experiments of the catalyst active sites. The potential of an electrode of the second kind depends on the used electrolyte. To make the resulting measurements comparable, the resulting potentials are given versus RHE. Measurements in 0.1 M H₂SO₄ revealed the potential shift of the proton concentration to be ~270 mV in comparison to RHE. As counter electrode a glassy carbon (GC) rod was used. The reference electrode was measured against an RHE, Hydroflex® from Gaskatel GmbH for all described electrochemical experiments in this work. The GC working electrode with an area of 0.1963 cm² was prepared with the catalyst ink. For this section, the catalyst ink was primed using 5 mg catalyst powder, mixed with 223 µl of a 5 wt% Nafion™ solution with a Nafion™ to carbon ratio of N/C = 0.48. To homogenize the suspension, the ink was placed in an ultrasonic bath for 15 minutes and dispersed with an ultrasonic finger. Afterwards, the ink was placed on a Vortexer for 5 minutes. From the thus prepared solution, 5 µl were dropped on the GC disk and left to dry. The resulting catalyst loading on the electrode was calculated to 0.57 mg cm⁻². For the cyclic voltammetry (CV), a protocol similar to the one presented by

Herranz et al.¹³⁴ was used. First, the 0.1 M H₂SO₄ electrolyte was saturated with O₂ and two CV scans between 1.15 V and 0.0 V (vs. RHE), with an infeed of 10 mV s⁻¹ and 1500 rpm were recorded. Afterwards, the electrolyte was saturated with nitrogen and 20 cycles with a sweep rate of 300 mV s⁻¹ followed by two scans with 100 mV s⁻¹ and 10 mV s⁻¹ infeed, respectively, were measured. The last recorded scan is needed to correct the capacity contribution which participates the oxygen-saturated electrolyte scan.

As RDE experiments uncover the electrochemical performance, Mössbauer spectroscopy identifies all iron-containing species sites in the catalyst system. Therefore, room temperature ⁵⁷Fe transmission Mössbauer spectroscopy was performed using a CMCA-550 from WissEl in combination with a constant electronic drive system, a triangular reference wave form manufactured by Halder Electronics and equipped with a RITVERC 3.7 GBq, ⁵⁷Co / Rh source. A proportional counter was used as detector. The Mössbauer sample was prepared by filling ~ 90 mg catalyst powder in a one-side-closed sample holder made of POM. After compressing the powder, the open side was closed with a TESA strip. The Mössbauer spectra were primed and measured under standard conditions. Afterwards, the isomer shifts were determined relative to an α -Fe foil spectrum recorded at 298 K.

The spectrum resolution is given by the number of channels in the channel analyzer (1024 channels), the used detector, the adjusted velocity of (± 6 mm s⁻¹) and the subsequent folding of the spectrum. The resulting Mössbauer spectrum was analyzed using the program MossWin 4.0i²¹³. It should be noted that, due to the half-life time of 271.8 days for the radioactive ⁵⁷Co, the activity of the source decreases over time. This not only increases the measuring time, but also changes the chemical environment of the source. As described in 3.4, the source environment has a significant impact on the measured isomer shift of the sample. Therefore, it is necessary to measure the α -Fe foil in regular intervals to minimize this effect.

To realize the full potential of Mössbauer spectroscopy, low temperature and magnetic field measurements were performed. For this purpose, LT-Mössbauer spectroscopy measurements were prepared in cooperation with H. Auerbach at the Technical University Kaiserslautern in the group of Prof. V. Schünemann, within the NUKFER project. Therefore, a WissEl LT-transmission Mössbauer spectrometer was used with a horizontal geometry and constant acceleration, operating in conjunction with a 512-channel analyzer in time-scale mode. The detector consists of a proportional counter filled with an argon-krypton-xenon mixture. Here, a 1.6 GBq, ⁵⁷Co / Rh source was used. Similar to the Mössbauer measurements described before, the spectra were calibrated against α -Fe at room temperature (RT). To measure at 77 K, the samples were mounted in an Optistat DN, continuous flow cryostat from Oxford Instruments. To measure field-dependent Mössbauer spectra at low temperatures, a closed-cycle cryostat from CRYO Industries of America, Inc. equipped with a superconducting magnet,

as described earlier¹⁸⁷, was used. Spectral data were analyzed with the public domain program Vinda, running on an Excel 2003® platform²¹⁴. The spectra fitting was done by least-squares fits using Lorentzian line shapes and, in case of magnetically split spectra, by the spin Hamiltonian approximation as described by Trautwein et al¹⁸⁸. In case of the LT-Mössbauer spectra, the experimental errors of the given isomer shifts δ_{iso} , quadrupole splittings ΔE_Q , and line widths Γ are in the order of $\pm 0.02 \text{ mm s}^{-1}$. For magnetic hyperfine fields, B_{hf} , errors of $\pm 1 \text{ T}$, and for the asymmetry parameters η of ± 0.2 , are found.

In addition to Mössbauer measurements, the catalyst was successfully measured during the synchrotron beamtime I-20160285, to investigate the sample at the dynamic beamline P01 at PETRA III (DESY), by nuclear forward and nuclear inelastic scattering. The synchrotron worked in the 40 bunches filling mode with a photon energy of 14.4 keV in combination with a high-resolution monochromator for ⁵⁷Fe. For the analysis of powder samples, a catalyst powder package with the highly enriched ⁵⁷Fe (95%) catalyst was prepared using Kapton foil and mounted with a cooper sample holder in the closed cycle cryostat (6 – 800 K). The sample was cooled down to $40 - 46 \pm 4 \text{ K}$ and the NFS spectra were recorded in forward direction, whereas the NIS spectra were recorded perpendicular through the beam. To analyze the related iron pDOS, optimized structure models with different axial ligands, oxidation and spin-states of the investigated iron containing Fe-N-C catalyst by DFT calculations, were performed with GAUSSIAN 09²¹⁵ and the functional B3LYP, with the basis set CEP-31G for density function theory implemented by H. Auerbach.

In Chapter 3.5, the advantages of EPR spectroscopy in characterizing transitions between magnetic dipole moment eigenstates of paramagnetic ions were described. In cooperation with the Freie Universität Berlin, measurements and simulations were thankfully prepared by C. Thait in the group of Prof. J. Behrends, where the catalyst was examined by X-band EPR. For EPR sample preparation, 2.4 mg of the catalyst powder was filled in OD quartz tubes (3.9 mm diameter). After multiple cycles of pumping and purging with helium, the tubes were flame-sealed. X-band continuous wave EPR measurements were performed with a Bruker ER 041 MR microwave bridge combined with an ER 048 R microwave controller. An AEG electromagnet with a Bruker BH15 was used as Hall effect field controller. For field modulation and lock-in detection, a Stanford Research SR810 lock-in amplifier with a Wangine WPA-120 amplifier was used. The sample was placed inside an ER 4122 SHQE resonator and cooled to 5 K using an Oxford ESR910 helium flow cryostat with an ITC temperature controller. The spectra were recorded at a microwave frequency of 9.39 GHz and a microwave power of 62 μW with a 100 kHz modulation frequency and 0.5 mT modulation amplitude. To increase the signal-to-noise ratio, the background of an empty EPR tube inside the resonator cavity was measured and subtracted from the original data. For each measurement, the Q-value of the resonator was determined from the mode picture for quantitative analysis and comparison of the relative intensities. Spin (S) quantitation for high spin Fe(III) ($S = 5/2$)

was performed by comparing a reference sample of FeTMPPCl/CB (Fe(III)-Tetrakis(4-methoxyphenyl)-porphine chloride on carbon black) with a determined Fe(III) content of 1.62 wt% (obtained by NAA). The resulting spectra were quantified by EPR spectral simulations, performed with the EasySpin toolbox²¹⁶ for an effective $S' = 1/2$ spin system in Matlab.

Moreover, transmission electron microscopy (TEM) and scanning transmission microscopy (STEM) were used to characterize the structural composition of the investigated catalyst. Thanks to our cooperation partner Prof. Dr. C. Kübel and S. C. N. Kumar for acquiring STEM and TEM images using an aberration (image)-corrected Titan 80 – 300 from FEI Company operating at 300 kV and equipped with an US1000 low-scan CCD camera powered by Gatan Inc. for TEM imaging and high-angle annular dark-field (HAADF) for recording STEM images. The used camera length for STEM imaging was 195 mm with a nominal spot size of 0.27 nm. The sample preparation for TEM imaging was performed by directly spreading the catalyst powder on holey carbon coated copper grids coated with an additional 3 nm carbon layer prepared by Quantifoil.

4.2. Deactivation Experiments of the Active Site

In order to assess the structure of the active sites in Fe-N-C catalysts, deactivation experiments are particularly useful, as a strong ligand attached to the active site suppresses the ORR activity and changes the nuclear resonant behavior. The attachment of the ligand further changes the electronic characteristics of the iron and thus results in different Mössbauer parameters, which are accessible for NFS, NIS and Mössbauer spectroscopy. Some parts of this work were already published by Wagner et al.⁵².

Carbon monoxide (CO) is assumed to be a good deactivation candidate since it is well known to poison hemoglobin in neutral pH. However, Birry et al.²¹⁷ have shown that Fe-N-C systems are unaffected by introducing CO in RDE experiments. Sahraie et al.⁴⁰ discovered a way to deactivate the active site with CO, describing the use of low-temperature CO pulse chemisorption and temperature programmed desorption (TPD) as chemical interrogation tools offering quantitative insights into the density of active adsorption sites of the catalyst. Gewirth and collaborators performed electrochemical analysis in a pH 6 phosphate buffer solution containing sodium fluoride (NaF), potassium thiocyanate (KSCN), or ethane thiol (C_2H_5SH) to deactivate the active site of a carbon-supported FePc or pyrolyzed FePc at 800 °C. They found that only KCN is able to strongly decrease the oxygen reduction activity²¹⁸, as KCN builds very strong complexes with iron²¹⁹⁻²²¹. Malko et al.²²² have shown that nitric oxide (NO) disables Fe-N-C catalysts at RT conditions. Although the activity of the investigated catalyst strongly decreases, our recent Mössbauer analysis of the deactivated NO catalyst detects only a narrow changes in Mössbauer spectra. This raises the question if the poison attaches through the iron-site or successfully blocks the periphery of the catalyst and prevents the mass transfer during reaction²²³.

Markus Knauer²²⁴ described the poisoning effect for (Co,Fe)-N-C with several possible salts like ammonium thiocyanate (NH₄SCN), sodium sulfide (Na₂S), and sodium sulfite (Na₂SO₃) in RDE experiments and found a negative impact when these salts were dissolved in the electrolyte on the catalyst performance¹. This means, the deactivation species was present in the electrolyte during the electrochemical measurement, whereas in the here described work the catalyst powder was deactivated followed by a removal of access salt and then characterized prior to the electrochemical measured of the ORR activity of the poisoned sample. Nonetheless, his work was taken as a starting point and adopted for our own Fe-N-C catalyst systems.

Three different Fe-N-C catalysts were prepared for the deactivation experiments: one catalyst with a high temperature treatment (at 800 °C, HT800HCl), a second catalyst with a low temperature treatment (600 °C, HT600HCl), both following the procedure described in 4.1 except for the final temperature, and a third catalyst (800 °C), for which sulfur was added to the synthesis route. A detailed description of the preparations for the different catalyst types are found in Kramm et al.²¹² and Janßen et al.²²⁵. Here, only the third catalyst is shortly described, which was prepared by slightly modifying the procedure presented by Janßen et al.²²⁵. The precursor mixture is based on dicyandiamide, 1,10-phenanthroline, iron acetate (FeAc), and sulfur with an S/Fe = 2.45 ratio. A heat ramp of 300 °C h⁻¹ was chosen, with a first holding point at 300 °C for 30 minutes and a second at 500 °C for 30 minutes. The final temperature of 800 °C was held for 60 minutes. A subsequent acid leaching was performed in 2 M HCl to dissolve acidic- soluble impurities. After filtration and drying of the catalyst, a second heat treatment was realized for 30 minutes at 800 °C using a heating ramp of 600 °C h⁻¹ to increase the catalytic activity and repair defects caused by the acid leaching. All heat treatment processes were realized in an inert gas atmosphere of pure nitrogen to avoid catalyst burning. The resulting catalyst is labeled HT800HCl+S. To deactivate the catalyst powders, 50 mg of the pure catalysts were mixed with 100 ml, 0.1 M H₂SO₄, and 5 mM Na₂SO₃ dissolved in the mixture. In order to enhance the interaction, each sample was placed in an ultrasonic bath for 1 hour. Afterwards, the catalysts were filtered, washed with distilled water, and dried overnight at 80 °C in an oven. The electrolyte was chosen based on its deactivation stability.

In this study, all electrochemical experiments of the catalysts were made using the rotating disc electrode (RDE) measurements. The inks were prepared by filling 5 mg catalyst powder into an Eppendorf tube and adding 223 µl of a 1.1 wt% NafionTM solution (N/C = 0.48). Afterwards, the suspensions were placed in an ultrasonic bath for 15 minutes, followed by dispersion with an ultrasonic finger and 5 minutes on a Vortex to homogenize the inks composition. 5 µl of each ink was dropped on the working electrode and left to dry. The resulting catalyst loading was calculated to 0.57 mg cm⁻². To avoid detachment of the attached anion by the activation of the catalyst, the electrochemical measurements were started

¹ Note: in the Knauer work the catalyst is assigned as Co-N-C; however, as the preparation also involved iron oxalate and the Mössbauer signature is similar to iron-only Fe-N-C catalysts, it is likely that at least part of the active sites constitutes of FeN₄.

directly in O₂ saturated electrolyte with two CV scans between 1.15 V and 0.0 V (vs. RHE) with a forward speed of 10 mV s⁻¹ and 1500 rpm instead of the activation cycling in nitrogen as usual. Afterwards, the electrolyte was saturated with nitrogen and the prepared electrode was cycled 20 times, with a sweep rate of 300 mV s⁻¹ followed by a scan with 100 mV s⁻¹ and a scan rate of 10 mV s⁻¹. Whereas the last-named scan is required for capacity correction, which are contributing during the scans in oxygen-saturated electrolyte. The used protocol was similar to the one described by Herranz et al.¹³⁴. The ink recipe and the electrode loading was the same for the deactivated catalysts, but the suspension was only shaken manually to avoid the detachment of the anion from the catalyst⁵⁰ due to the energy entry of the ultrasound bath.

To investigate the kinetic behavior of the deactivated system, the kinetic current density j_{kin} from the capacity-corrected CV curve in O₂-saturated electrolyte at 1500 rpm was used and calculated with the Koutecký–Levich equation (4). For determining averages and errors, two scans of each measurement and two measurements per sample were made. The effect of the attached anion was evaluated by comparing the kinetic current densities j_{kin} at 0.75 V vs. RHE, whereas the diffusion limited current density j_{diff} was read from the diffusion plateau of the capacity corrected RDE curve. Further investigations by NIS (and NFS), during the beamtime I-20160285 at the P01 beamline was used to analyze the impact to the nuclear resonance behavior and the change in vibration modes, respectively. For Mössbauer measurements, a “MS96” from RCPTM, equipped with a RITVERC 3.7 GBq, ⁵⁷Co / Rh radioactive source, in combination with a built-in scintillation detector, was used. The collimators before and after the sample holder were set to 4 and 5, respectively. The natural abundance of the Mössbauer relevant isotope ⁵⁷Fe is 2.2%. Thus, a ~ 100 mg of catalyst powder sample for Mössbauer measurement is required. In case of enriched samples, containing up to 100% ⁵⁷Fe, even a few milligrams of catalyst powder are sufficient to result a meaningful spectrum. Nevertheless, ~ 90 mg of the pristine catalyst powder and ~ 30 mg of the deactivated catalyst powder was used to obtain a meaningful spectrum in a reasonable time. The high amount of ⁵⁷Fe results in an overall measurement time of less than 24 hours, even for low powder loadings. The measurements were performed in a velocity range of ± 6 mm s⁻¹. Besides the RT-MS measurements, LT-MS was performed for selected samples under the same conditions as described in the previous section.

To investigate the samples at the dynamic beamline P01, nuclear forward and nuclear inelastic scattering were used. The synchrotron worked in the 40 bunches filling mode with a photon energy of 14.4 keV, in combination with a high-resolution monochromator for ⁵⁷Fe. For the analysis of powder samples, catalyst powder packages with highly enriched ⁵⁷Fe (95%) catalyst powders (HT600HCl, HT800HCl and their poisoned variants) were prepared and mounted with a cooper sample holder in a closed cycle cryostat (6 – 800 K). The samples were cooled to 40 – 46 ± 4 K and the NFS spectra were recorded in forward direction by an APD detector. The resulting NIS data from the poisoned and initial catalysts

were compared to DFT calculations using the software package G16 A.03 + nisspec B3LYP / CEP-31g. These calculations have been performed by Hendrik Auerbach, a doctoral researcher in the research group of V. Schünemann at the TU Kaiserslautern.

4.3. Post Mortem MEA Characterization

Membrane electrode assemblies (MEAs) that were degraded during fuel cell operation were already successfully characterized post mortem using Mössbauer spectroscopy²²⁶. The authors have shown that the presence of NafionTM and water inside the MEA strongly affects the probability that the iron nuclei absorb γ -rays and result in significantly longer measurement time. They highlighted that the observed activity decay is mainly due to carbon oxidation, which causes a leaching of active iron sites in the graphitic matrix. In short, strong oxidizing conditions result in an activity loss which correlates with a leaching of the ORR active FeN₄ centers, in parallel with a burn-off of carbon. While this study offers important insights about the overall degradation mechanism, the mechanism related to the deactivation of Fe-N-C catalysts can be more closely illuminated using local studies, in which local changes are compared to local profiles. Schröder et al.²²⁷ used neutron radiography to investigate the current distribution of direct methanol cathodic flow fields and found a dependency of temperature, current, and water distribution by through plane neutron radiography. In case of Fe-N-C catalyst systems, it was not possible to identify the origin of deactivation, nor to ascertain if a uniform degradation through the MEA exists^{71, 226, 228}. In this work, local resolved post mortem measurements with synchrotron-based Mössbauer spectroscopy (SMS) are used to scrutinize the degradation process, as the narrow spot size and the high intensity enable local profiling. The question how degradation processes are influenced by temperature, current, or reactant gradients is a big issue for fuel cell performance and catalyst lifetime, and thus of great interest for fuel cell development. Against this background, an experiment was planned to explore local degradation phenomena for Fe-N-C catalysts and a post mortem SMS analysis of three different treated MEAs was successfully performed.

The preparation of the catalyst was adapted from previous publications of the group. The preparation and fuel cell testings were thankfully performed by Markus Kübler. For the preparation, 200 mg of a fully enriched ⁵⁷Fe porphyrin (FeTMPPCl) were dissolved in 50 ml THF and sonicated for two minutes under N₂ saturation to avoid possible peroxide formation of THF. Afterwards, 800 mg of PXC (carbon support) were added and sonicated for one hour under N₂ saturation. The THF was evaporated under reduced pressure, first for two hours at 30 °C and then overnight at 100°C. The resulting powder was milled and placed in the oven. A heating ramp of 300 °C h⁻¹, with the final temperature of 700 °C was adopted and held for 45 minutes, followed by an acid leaching in 2 M HCl, for one hour in an ultrasonic bath under N₂ saturation. The obtained catalyst was filtered, washed with two liters of water, and placed in the drying oven overnight at 80 °C. The resulting catalyst was characterized by RDE. To this

end, 5 mg of the catalyst powder was mixed with 250 μl , 25 μl NafionTM solution, 142 μl water and 83.3 μl isopropanol, subsequently sonicated for two hours in an ice bath and homogenized with the Vortex for 30 seconds. 8 μl of the resulting ink was dropped on the glassy carbon disc, joining a droplet of 5 μl water to reduce the surface tension and receive a flat catalyst layer after drying. The so-prepared electrode was left to dry for 60 minutes and additionally placed one minute in the oven at 80 °C to completely dry the electrode surface. A catalyst loading on the working electrode of 0.8 mg/cm² was determined.

Rotating disc electrode measurements were performed in N₂-saturated 0.1 M H₂SO₄ electrolyte, beginning with 20 cycles in the potential region from 0 – 1.2 V vs. RHE with a sweep rate of 100 mV s⁻¹ for cleaning and activating the catalyst surface. After cycling, two scans with a sweep rate of 20 mV s⁻¹ were taken to clarify the surface stability, whereas the last two scans with a forward speed of 10 mV s⁻¹ were recorded for capacity correction of the following oxygen scan. Afterwards, the electrolyte was saturated with O₂ and one scan was recorded with a sweep rate of 10 mV s⁻¹, at 0 rpm, 200 rpm, 400 rpm, 900 rpm and 1500 rpm, respectively. To investigate the degradation behavior of the catalyst under fuel cell operation conditions, MEAs and fuel cell tests needed to be prepared. Hence, MEAs were tested under two different temperature conditions at the Fraunhofer ICT. For now, the catalyst's loading is given. For low-temperature-treated MEA (LT-MEA), high-temperature-treated MEA (HT-MEA), and untreated MEA, catalyst loadings of $\sim 3.7 \text{ mg}_{\text{Kat}} \text{ cm}^{-2}$ on the cathode and $\sim 0.6 \text{ mg}_{\text{Pt/C}} \text{ cm}^{-2}$ of Pt/C catalyst (Pt/C, 46.6% Tanaka) on the anode were realized. In case of the HT-MEA, a PTFE-containing ink was sprayed directly on the PPI membrane, whereas for the LT-MEA and untreated MEA, inks based on NafionTM were prepared and sprayed directly on a NafionTM membrane. No gas diffusion layers were used for any of the MEAs. As the PPI membrane was saturated with phosphoric acid, the evaporation of ink during spraying resulted in a weight reduction of the membrane. Therefore, it was not possible to calculate the exact loading, but it is assumed to be very similar to the LT-MEA and the untreated MEA, due to the same way of preparation and used weight of components.

For high temperature degradation treatment, the fuel cell stack was heated up to 165 °C and ran for 12 hours at a constant potential of 0.6 V. The LT-MEA was running for 24 hours at 0.6 V with an operation temperature of 80 °C. After the fuel cell tests, both LT-MEA and HT-MEA were demounted and brought together with the untreated MEA to the dynamic beamline ID18 to quantify i) the degradation of Fe-N-C sites, ii) the demetallation of FeN₄ sites, resulting in a removal of iron from the MEA, or morphing into iron oxide / hydroxide during operation and iii) the difference in contribution of the catalyst changes at the membrane.

To illuminate the degradation, the MEAs were cut into six, several millimeter pieces at defined positions (Figure 18) and glued on top of copper sample holders using Kapton. As the flat samples show a dramatic increase of cross-section, the absorption effect is maximized and the measurement time decreased, whereas the localized position becomes less precise. Each holder was stacked on top of each other using

additional spacers between the copper holders to avoid the compression of the sample pieces. The stack with 20 sample pieces in total was mounted on the cryostat holder and cooled down, enabling a fast and continuous measurement of all samples. The positions A, B, C, and F were chosen for SMS measurements, as it is assumed that the largest changes are observed at the gas inlet (Pos A) and gas outlet (Pos F). Positions E and D were discarded. For magnetic field-dependent measurements from 0 T – 5 T, Pos C was chosen, as it allows to compare all investigated MEAs. The magnetic field was applied perpendicular to the incoming beam. Furthermore, during the heating up of the cryostat temperature-dependence of the Mössbauer parameters were investigated.

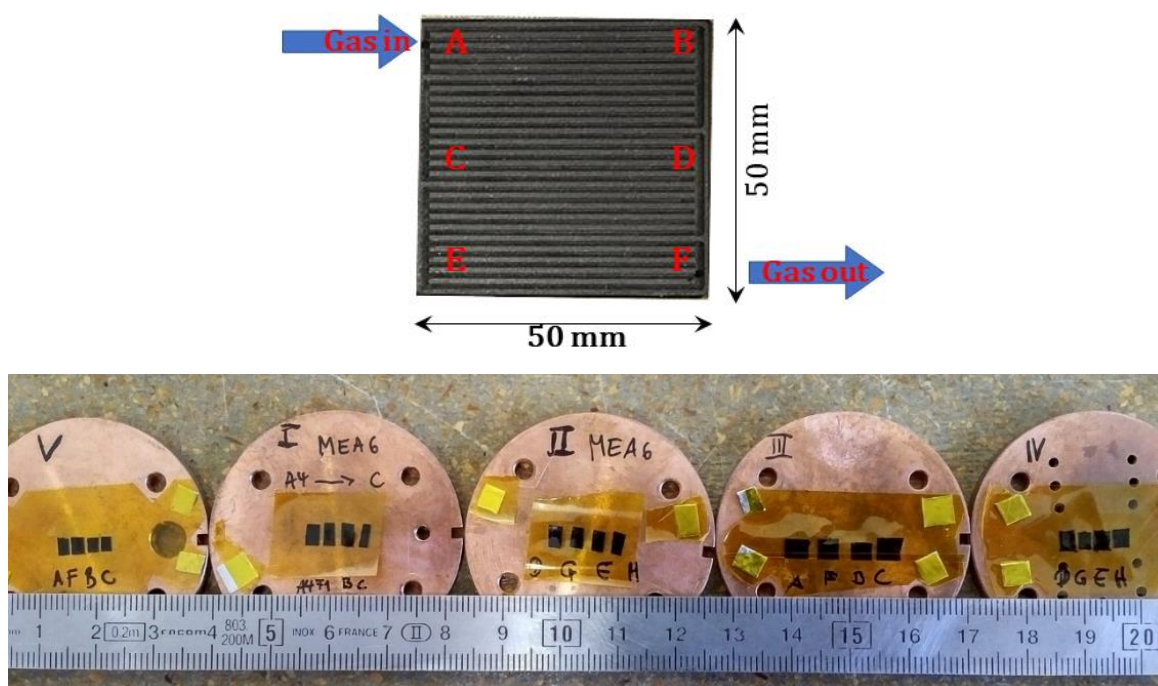


Figure 18: Position of measuring spots located on the MEA and investigated by SMS (top). The series of cooper sample holders shows the cut MEA pieces in line (bottom). Each holder was stacked over one another and fixed by screws. The so realized stack was mounted in the cryostat.

4.4. Operando Fuel Cell Setup for Synchrotron-based Nuclear Resonant Techniques

The main topic of this work is the design, construction, and use of a self-made operando fuel cell setup for synchrotron-based Mössbauer spectroscopy (SMS) or related synchrotron-based nuclear resonant techniques. Only operando observations can clearly identify the emergence of intermediate species under operation, which are not accessible by post mortem analysis and only possible with thermodynamic-based theoretical calculations. In addition to the fuel cell, the periphery was set together by the author. The available commercial standard fuel cell setups 840e from Scribner Associates Inc. could not be used due to the required settings during the operando measurements at the beamtime. The post mortem SMS

measurements of MEAs showed that it is necessary to measure in parallel to the flow field to enlarge the absorption area (compare Figure 17). The synchrotron beam needs to impinge upon the fuel cell parallel to the flow field and the detector hence needs to be placed in line with the beam. Further limitations of the standard setup that needed to be overcome with the operando design were the weight and size of the setup as well as the minimum input pressure of 3 bar.

The flow field design was developed and produced in cooperation with the “Kompetenzzentrum Brennstoffzelle” by V. Loose in the group of Prof. G. Hoogers at the Hochschule Trier, Umwelt-Campus Birkenfeld. The interchange of aims, needs, material properties, and construction limitations, resulted in the design shown in Figure 19. The flow-field was designed to provide, on the one hand, the functionality of a fuel cell and, on the other hand, to enable operando measurements with the synchrotron beam. To this end, a cell design with broad channels and short horizontal channel lines was chosen. Nevertheless, broad channel lines and the short horizontal ways have an additional impact on the fuel cell performance under operation. The design is discussed in detail later in this section.

The left panel of Figure 19 shows one flow field site. The black, H-shape piece is the bipolar plate with a CNC-milled flow field. Four drilling holes and the blue silicon sealings are needed to close the cell gas tide (electric isolation made by Kapton not shown). The sintered, silver metal piece is the conductive back contact and is necessary for collecting the resulting cell current and has the additional purpose to provide a constant and uniform temperature and pressure distribution over the cell. The red cables are part of the cell heating system, which is implemented at the back contact of the cell (black rectangle on the back of each site). The center panel displays the anodic and cathodic flow-fields with a prepared MEA. To prepare the MEA, a special punching tool was designed and built, enabling the reproducible manufacturing of both, cathodes and anodes. The drilling holes, which seen on the site of the cell, are needed for the sensor which adjusts and controls the cell temperature. The right panel shows the closed cell. The blue sealing in the middle closes both half-cells and the yellow Kapton foil in between prevents electric short-circuits. Olive type tube fittings are used to connect the gas in- and outlet pipes.



Figure 19: The operando fuel cell stack is shown. Top view on the flow field with the blue selling (left). The red cables are part of the cell heating system which is implemented in the cell. Both flow-fields with the prepared MEA before closing the cell (middle). The drill holes on the site are needed for the temperature sensor to adjust the cell temperature. The closed cell with the blue selling can be seen (right). The incoming synchrotron beam will be shot through the cell in the faced view.

The electronic load was developed and built, in cooperation with M. Weber from the construction office of the Material Science Department. The circuit diagram in the appendix (S 2) shows the electronic load used to measure and manipulate the current of the fuel cell during operation. In the circuit diagram, IRFS7430TRL7PP represents the electric consumer made of a MOSFET (metal-oxide-semiconductor field-effect transistor). The electronic load is constructed for a maximum current of 50 A and a maximum potential of 5 V, with a maximum cell voltage of 2 V. The data processing and communication with the computer was realized using a National Instrument interface. For data collection, plotting and to change the parameters, a small LabView program was set up, allowing the export of the data files with given parameters and values. The program was not able to control or change the temperature of the heated parts, as no interface for the different heaters was integrated. Besides the program and the electronic load, the temperature regulation of the fuel cell stack, the pipes, and gas humidifiers are important. To avoid water condensation, blocking of the gas channels, or filling of pores, a homogeneous temperature distribution needs to be guaranteed. The used gases need to be humidified to prevent the membrane from desiccating. Hence, heat-resistant humidifiers from BriskHeat Corporation were used. Since the humidifiers were taken from an older fuel cell setup, all installed olive type tube fittings needed to be exchanged due to partially damaged threads or synthetic connections. The humidifiers were further extended with dielectric bolting's to electrically separate the fuel cell from the rest of the setup. This is a safety precaution, designed to minimize the probability of electric shocks and to avoid leakage currents from current-carrying components.

A very susceptible part during operation are the flexible heating pipes as temperature fluctuations in the pipes will result in water condensation. Here, a heating wire from Hillesheim was wrapped around a

flexible, gas-impermeable pipe. To increase the thermal conductivity and to homogenize the heating behavior across the whole tube, a thick, multi-flex copper cable was included. This construction is flexible, but not suitable without fixation of the parts. Thus, a shrinking pipe was used to fix the heating and copper wires. A homogeneous temperature distribution is necessary for a well-performing cell, whereas good thermal isolation of the pipes is important to avoid burning and to facilitate manual handling. Therefore, the wrapped pipes were covered with multi-layered aluminum tape for thermal isolation. In addition, the thermally isolated pipes were covered with two additional shrinking pipes to ensure electric isolation. The multi-layer, flexible heating pipes were connected to the dielectric bolting's of the humidifiers and the fuel cell stack itself. All described components for the operando fuel cell setup are depicted in Figure 20. The discussion about the fuel cell performance (3.3.2) already mentioned that, following from the Nernst equation, a higher pressure of the reactance offers a better performance during operation. To increase the pressure in the system, a back-pressure unit was built and connected to the fuel cell. The back-pressure units contain needle valves and manometers for both the anodic and cathodic side. It is important to place the back-pressure units below the gas outlets of the cell to avoid a filling of the cell by condensate. The back pressure was adjusted to 1 bar during operando fuel cell testing.

To regulate and manipulate the gas flow, two Legacy mass flow controllers from MKS, plus a mass flow unit were used. The mass flow unit has the advantage that the K-values for the gases are already programmed into the mass flow unit directly. The gas flow was adjusted manually. The last component was the gas supply. Here, nitrogen, oxygen, and hydrogen from AirLiquide with the purity of 99.999%, 99.998% and 99.999%, respectively, were used. Before and after operation, the overall system was flushed with nitrogen to remove the remaining hydrogen and oxygen from the system. To this end, the hydrogen and oxygen pathways were connected and separated by needle valves as shown in Figure 20.

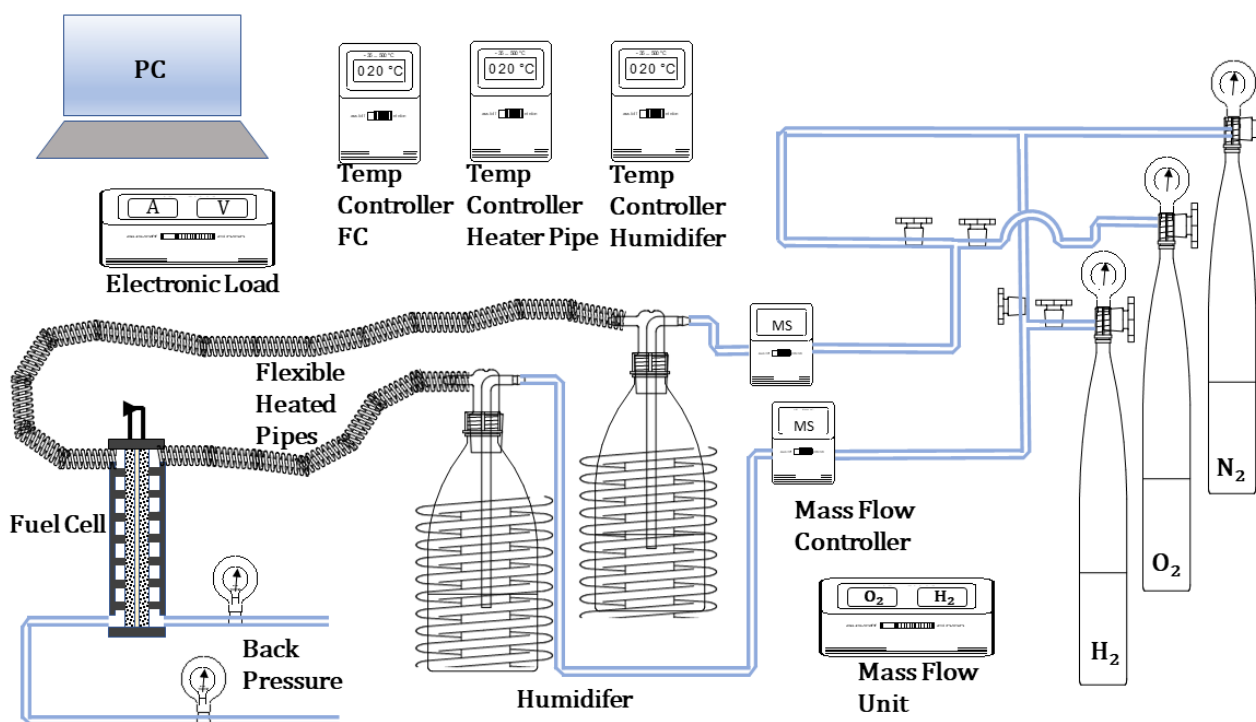


Figure 20: Operando fuel cell setup. For reason of simplicity the wiring is not shown. A fully explanation of the setup is discussed in the text.

To qualify the performance of the operando fuel cell setup, a direct comparison with the standard fuel cell setup from Scribner Associates Inc. is demonstrated. Therefore, a Pt-Pt reference MEA was prepared for the standard and the operando setup. For both MEAs a catalyst loading of $0.54 \text{ mg}_{\text{Pt}} \text{ cm}^{-2}$ on the cathode and $0.16 \text{ mg}_{\text{Pt}} \text{ cm}^{-2}$ on the anode was calculated. As Pt-catalyst an Umicore Pt20-380 for the anode, whereas for the cathode a Pt50-0550 was sprayed on a coated H23C9 GDL from Freudenberg, fixed on a heating plate and heated up to $90 \text{ }^\circ\text{C}$ for faster drying. The ink recipe for the anode is given as follow. 80 mg of the catalyst Pt20-380 was mixed with $800 \text{ } \mu\text{l}$ H_2O by adding $1600 \text{ } \mu\text{l}$ isopropanol and $800 \text{ } \mu\text{l}$ of 5 wt% Nafion™ solution. The mixture was placed for 60 minutes in an ultra-sonic bath and cooled with ice and the resulting ink was afterwards sprayed as described. For the cathodic ink, 120 mg Pt50-0550 where mixed with $1200 \text{ } \mu\text{l}$ H_2O adding $2400 \text{ } \mu\text{l}$ isopropanol and $1200 \text{ } \mu\text{l}$, 5 wt% Nafion™ solution. The cathode ink was placed for 60 minutes in an ultra-sonic bath and cooled with ice and afterwards sprayed as described. As Nafion™ membrane a N115 was used with a thickness of $127 \text{ } \mu\text{m}$. The relative thick membrane was necessary as the mechanical tension in the mounted operando single cell was too high and the edges of the flow fields too sharp, so the membrane showed hairline cracks along the connected area of both flow fields. To avoid a damage of the membrane and a short circuit of the cell, the edges were polished and the thicker membrane was chosen. This means a higher resistance

of the membrane and a reduced performance but a fully functional cell. To use the Nafion™ membrane as a proton conductive separator, an activation of the membrane is necessary. This was done by heating the membrane in 3% H₂O₂ for one hour at 90 °C. In addition, the membrane was washed with milli pure water and heated in 0.05 M H₂SO₄ for three hours at 90 °C. Afterwards, the membrane was washed in milli pure water again and in the last step heated for three hours in milli pure water at 90 °C. Before bringing the membrane and GDL's together, both prepared GDL's were sprayed with pure Nafion™ solution and arranged on the pressing plate with the wet, activated Nafion™ membrane in between. The assembled disposal was placed in the hot press and pressed at 125 °C with a contact pressure of 17 kN for two minutes. Afterwards, the cooling was switched on and the MEA was cooled down to less than 40 °C under 5 kN contact pressure. The as-prepared MEA was removed from the hot press and build in the fuel cell.

Beside the area of the operando and standard cell, the flow field design, thickness of the channels and crosspieces are different compared to a standard test cell and need to be discussed (Figure 21). The standard flow field has a surface area of 4.85 cm², whereas the operando fuel cell has a surface area of 4.5 cm². For the standard cell 14 horizontal channels with a length of 2.25 cm and a channel thickness of 0.5 mm are connected with vertical channels of 1.5 mm length. The aspect ratio is 0.066̄. The operando cell comes up with 20 horizontal channels, a channel thickness of 1.5 mm and a channel length of 0.8 cm. The vertical channels have a length of 4 mm with a resulting aspect ratio of 0.5. Not only the stack geometry is different, subtly different measurement protocols have to be used. All measurements done with the operando fuel cell setup were prepared at a cell temperature of 80 °C, identical to the standard setup. The humidifier and the pipe system were set to 75 °C each, to avoid condensation inside the pipes and the floating of channels, whereas for the standard setup 80 °C was set as it was found, that the connections between the cell and the pipe system get easily affected by water condensation. Here, the reduction of temperature in the pipe system, slightly reduces the total humidification of gas inside the fuel cell and helps to avoid the formation of water droplets in the channels but results in an increase of the ohmic resistance¹⁴⁷. In the standard setup the gas flow was set to 0.200 ml min⁻¹ for each gas. The temperature was fixed to 80 °C for the humidifiers, pipes and cell, respectively. A back pressure of 1 bar was adjusted. In case of the operando setup the gas flow was set to 0.400 ml min⁻¹ (H₂) at the anode and 0.200 ml min⁻¹ (O₂) at the cathode. The higher hydrogen flow was necessary, as the right calibration of the hydrogen mass flow controller was not possible and the amount of hydrogen would be otherwise too low to avoid a potential drop during operation. In general, the anodic reaction is not limiting due to fast kinetics and low overpotential. Therefore, increasing the hydrogen flow will not influence the overall reaction as the oxygen reduction reaction is the limiting reaction. The back pressure was adjusted to 1.1 bar for the anodic and cathodic site, respectively.

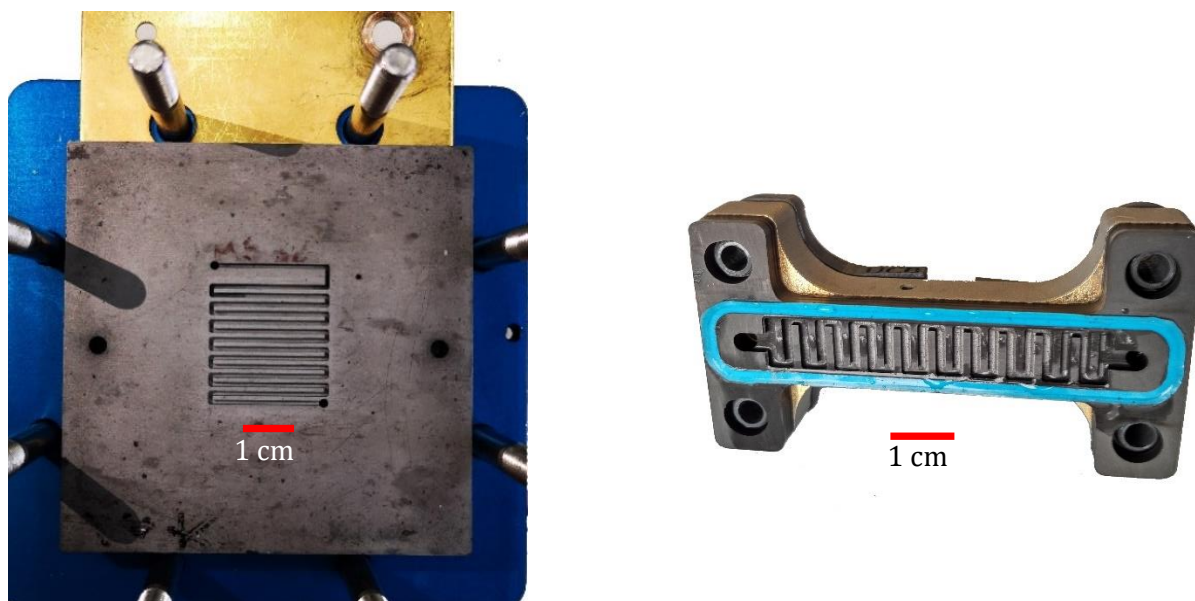


Figure 21: Top view of the standard flow field from Scribner Associates as it is used in our laboratory (left) and the operando fuel cell flow field (right).

As discussed in 3.3.2 the fuel cell performance depends not only on the catalyst but also on other parameters. To qualify the performance of the operando fuel cell setup a direct comparison with the standard fuel cell setup from Scribner Associate Inc. is necessary to characterize the performance difference of both setups (Figure 22).

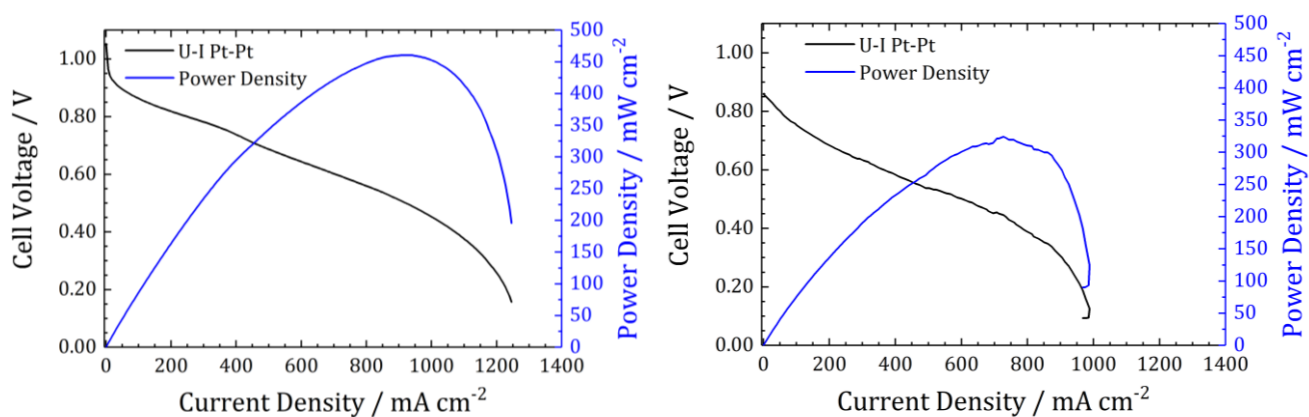


Figure 22: Pt-Pt reference measurement on the standard fuel cell test station in our laboratory (left). Operando fuel cell test with Pt-Pt reference (right). Experimental conditions for both setups: H₂-O₂, cathode loading 3.2 – 3.5 mg_{Pt} cm⁻², N212 membrane, 1 bar gauge back pressure, 0.2 L min⁻¹ oxidant and fuel flow, cell temperature 80 °C, 100% relative humidity, whereas for the operando cell, the temperature of the pipes were set to 75 °C to avoid condensation inside the cell.

Both cell voltage curves are not IR-corrected. For the standard setup (left) an OCP of 1.05 V and a maximum current density of 1.25 A cm⁻² with a power density of 424.6 mW cm⁻² at 0.6 V is measured. In the operando fuel cell setup (right) the electrochemical response looks similar. The shape of the curves

is almost identical, whereas the values; OCP, maximum current density and power density differ. For the operando fuel cell the resulting OCP is found at 0.86 V which means a drop of 18.5%. A power density of 220.7 mW cm^{-2} at 0.6 V (– 52%) was found. The unsteady curve behavior is a result of water condensation in the flow field which results in a potential drop during operation. Based on the different geometry and material components, the total ohmic resistance is higher for the operando cell, which is reflected in the reduced power density, cell voltage and maximum current density. This explains at least to some extent the lower values, but has no impact onto the reaction mechanism inside the cell. The operando setup is therefore proved to be suitable for operando fuel cell tests, investigated by synchrotron resonant techniques, even so the optimum values of a standard cell are not reached.

The preparation of the catalyst layers based on porphyrin or Fe-N-C, investigated with the operando fuel cell setup at the synchrotron follows the same preparation procedure as described for the Pt-Pt MEA. Only the hot pressing is different. Yin et al.²²⁹ showed that the preparation of MEA's using Fe-N-C as cathodic catalyst have to be pressed with lower contact pressure as otherwise the porous structure collapses and the mass transport resistance will increase. Even though, the model catalyst based on porphyrin and carbon support is not treated at high temperature oven process to produce a Fe-N-C catalyst, the contact pressure was reduced to 5 kN from the beginning to realize comparable conditions. Whereas, all other preparation steps are as described as for the Pt-Pt MEA.

Figure 23 displays the overall setup, with the components as described with respect to Figure 19. This setup was tested in the lab, dismantled, and rebuilt on the synchrotron hutch at the P01.

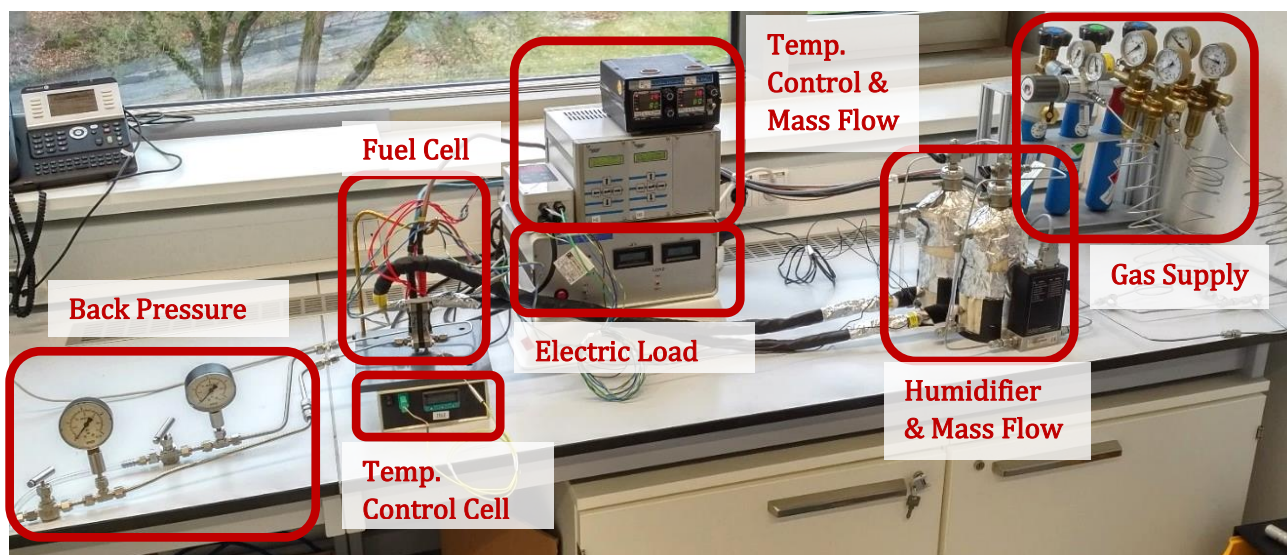


Figure 23: Photograph of the complete operando fuel cell setup as tested in the lab and used at the synchrotron. Further information on the component and functions are given in the text.

For the operando measurements at the synchrotron, as seen in Figure 24, the cell is mounted on top of a dielectric plate to fix the position of the cell, ensure electric isolation, and enable a mounting on the x-

y-z table at the synchrotron. Therefore, the drilling holes correspond to the mounting panel at the beamline. Further, the cable routing is fixed on the dielectric plate to avoid those cables to cover the beam. The radiation pulses originate from the tube in front of the image and penetrate the fuel cell. The APD detector is placed at the end of the hutch and is not visible in this picture. Using the variable table, it is possible to move the cell towards different positions.

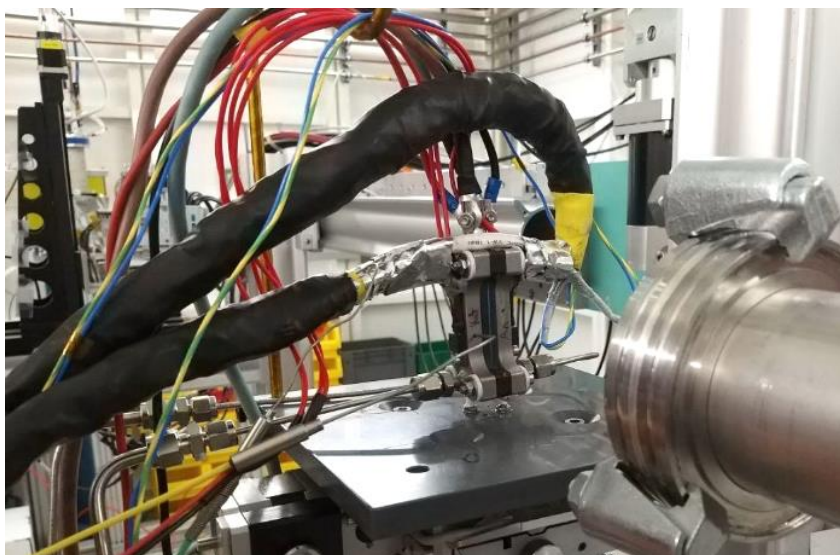


Figure 24: Operando fuel cell mounted at P01 beamline. The flexible pipes allow for adjusting the cell's position for the experiments.

Due to the completely new experimental setup in combination with NFS, a detailed pre-characterization of the investigated catalyst is necessary to make the interpretation of the obtained data possible. Therefore, a model catalyst was prepared based on iron porphyrin mixed with carbon black (FeTMPPCl/CB). Here, no heat treatment was applied. To get a first impression of the porphyrin-based reference system, Mössbauer spectroscopy was performed from the origin catalyst powder, the sprayed GDL and after the fuel cell test in the standard fuel cell setup. Before the model catalyst was measured with NFS in the operando fuel cell, the different membrane preparation steps were characterized by NFS to identify the impact to the catalyst state. Therefore, the pristine powder (powder), the sprayed electrode (GDL), the pressed MEA (Dry MEA) and the MEA after the fuel cell test (After FC) measured before in the standard setup were characterized with NFS and Mössbauer spectroscopy, respectively. Due to the fully enrichment with ^{57}Fe of the porphyrin and the catalyst, each NFS spectra were recorded for 3 minutes. Afterwards, the operando setup was put into operation by heating up first the cell and the pipe system and subsequently the humidifiers to avoid an oversaturation and condensation of water inside the pipes or the cell. The temperature, gas flow and back pressure was adjusted and the cell was purged with nitrogen during the heating. After all system parameters were stable the first NFS measurement was prepared with the wetted MEA under nitrogen flow of the anode and cathode

(Wet,N₂,N₂). In the next step the nitrogen on the anode was replaced by hydrogen and a further NFS spectrum without applying any potential was recorded (Wet,N₂,H₂). So, a fixed potential of ~0.6 V was adjusted and after the system reached equilibrium conditions a second NFS spectrum was recorded to obtain the fully reduced catalyst site (Wet,N₂,H₂_0.6 V). The nitrogen on the cathodic site was afterwards replaced by oxygen and again a potential of ~0.6 V was applied, to investigate the catalyst under working conditions (Wet,O₂,H₂_0.6 V). By removing the potential, the OCP of the fuel cell was measured after the equilibrium condition of the electrodes was adjusted (Wet,O₂,H₂_OCP).

The investigation of the Fe-N-C catalyst in the operando cell during the beamtime followed the described steps. The catalyst powder (Powder) was first measured by NFS. The GDL sample with the sprayed catalyst (GDL) and the MEA measured after the fuel cell test (MEA_af_FC) were cut and directly mounted on the optical path of the beam and measured with NFS. Whereas the fresh prepared MEA was measured inside the operando cell before the setup was switched on. In the next step the gas supply was opened and the system was heated up to operation temperature as described before. After the system remained stable the first NFS measurement under nitrogen gas and wet conditions (N₂,N₂) was recorded. To reduce the cathodic side catalyst and remove the oxygen out of the system, a potential of ~0.6 V was applied followed by the traced NFS spectrum (N₂,H₂_0.6 V). In addition, the nitrogen on the cathodic side was replaced by oxygen and on the anodic side by hydrogen. A stable OCP was found at 995 ± 2 mV and the NFS spectrum (O₂,H₂) was recorded. By applying a potential of ~0.6 V, the oxygen reduction reaction is observed and the catalyst was investigated by NFS under real fuel cell conditions (O₂,H₂_0.6 V). To obtain possible changes in performance, a second polarization curve was recorded and is given in the appendix (Figure S 11). The used experimental protocol enables the investigation of catalytic states which will appear during fuel cell operation. Similar to the model catalyst, the Fe-N-C catalyst was prepared with fully enriched ⁵⁷Fe. Therefore, it was possible that each operation step was measured with NFS for only three minutes.

5. Results and Discussion

In this chapter, first the application of Mössbauer spectroscopy (RT and LT) in combination with nuclear inelastic scattering and electron paramagnetic resonance spectroscopy is described to get insights on the structural composition of Fe-N-C catalysts. Here, most of the results are already presented in Wagner et al.⁵¹. Afterwards (chapter 5.2) the extent of sulfite as a deactivator induces structural changes in the related iron signatures will be discussed. In chapter 5.3 the first set of post mortem SMS experiments are illuminated. These experiments were particularly helpful for the design of the flow field geometry of the operando cell and to estimate possible measurement times of the operando spectra. Finally, in chapter 5.4 the results of the operando fuel cell beamtime are summarized.

5.1. Elucidating the Structural Composition of Fe–N–C Catalysts

Main parts from the here discussed results were already published in Wagner et al.⁵¹. In a previous work it was concluded that for porphyrin based catalysts prepared at low pyrolysis temperature (≤ 600 °C) only a reconstruction of the existing FeN₄ environments occurred, while no side phases were found on the basis of RT Mössbauer spectroscopy²¹². Based on this, a similarly prepared catalyst was selected for this study, to enable a focus on FeN₄ environments, but to use LT Mössbauer spectroscopy e.g., to clarify whether the previously as ORR active assigned D1 doublet ($\delta_{\text{iso}} \approx 0.30$ mm s⁻¹ and $\Delta E_Q \approx 0.88$ mm s⁻¹) is of ferric high-spin or ferrous low spin nature.

The combination of electrochemical experiments with nuclear and electron resonant techniques enables a detail structural investigation of the Fe-N-C composition. In Figure 25 (left) rotating disc electrode (RDE) measurement of HT600HCl is shown. An onset potential of $U_{\text{onset}} = 0.790$ V, a half-wave potential of $U_{\text{hw}} = 0.668$ V vs. RHE, and a diffusion-limiting current density of $I_{\text{diff lim}} = -5.7$ mA cm⁻² are measured. The kinetic current density (j_{kin}) at 0.75 V of 0.6 mA cm⁻² was calculated using the Tafel-plot equation.

The electrochemical performance which is described by the voltage versus current density plot shows a well-known characteristic which is typical for porphyrin-based catalyst systems⁶⁹. Also, the obtained Mössbauer spectrum (Figure 25, right) is in good agreement with previous observations. Three different FeN₄ containing iron species are identified in the Mössbauer spectrum, very similar to other porphyrin-based catalysts prepared at low pyrolysis temperature^{36, 45, 230}. Taking the related Mössbauer parameters into account, the species are assigned as Fe(II)-site in the low spin state (D1), FePc-like site (D2) and a heme-like site (D3). This result is in accordance to other Mössbauer spectra which were reported for similar porphyrin-based catalyst^{34, 37, 231}. Due to the performed acid leaching and the low synthesis temperature, no inorganic species were found. The resulting Mössbauer parameters as well as the relative absorption areas are summarized in the Table 7.

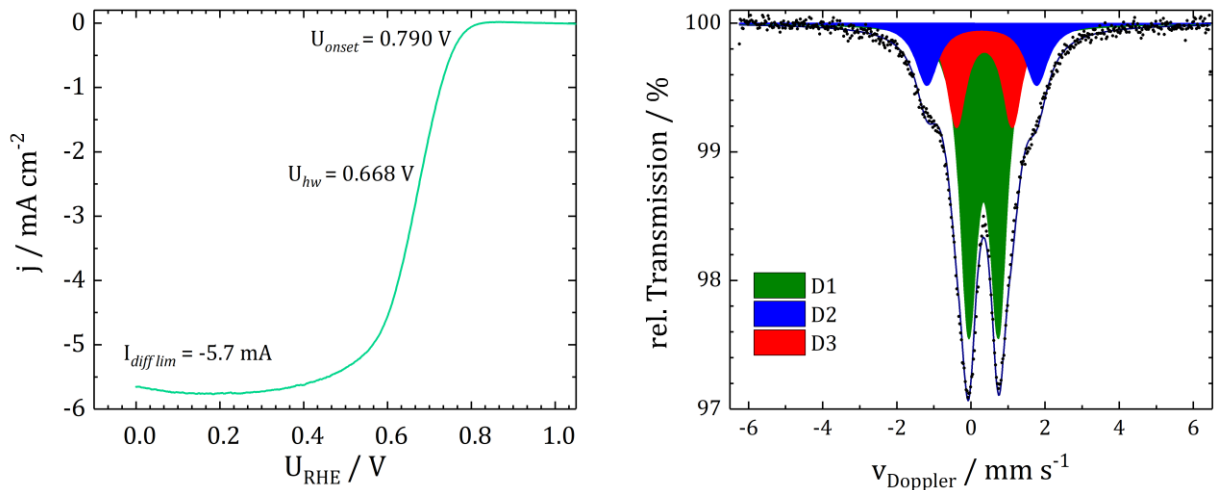


Figure 25: Electrochemical performance of HT600Cl at 1500 rpm in 0.1 M H_2SO_4 (left) . Related RT-Mössbauer spectrum fitted only with FeN_4 containing sites (right). No inorganic iron species are indicated ⁵¹.

Table 7: RT-Mössbauer parameters of HT600Cl ⁵¹.

Component	D1	D2	D3
Assignment	Fe(II) low spin	FePc-like	heme-like
$\delta_{\text{iso}} / \text{mm s}^{-1}$	0.34	0.29	0.36
$\Delta E_Q / \text{mm s}^{-1}$	0.81	2.96	1.50
$\Gamma / \text{mm s}^{-1}$	0.54	0.72	0.62
Area / %	59.4	16.9	23.7

TEM and STEM as used imaging techniques confirm the missing of iron oxide- or iron-clusters after the catalyst preparation. Figure 26 shows two STEM images of HT600HCl. Beside the granular morphology of the carbon particles, no iron, iron oxide nanoparticles or clusters are observable. Solely, an atomic dispersed Fe-rich shell, formed by the melting and carbonization of iron porphyrin, is found. The line profile over the carbon areas of lower and higher density (see inset in Figure 26, left) confirms the absence of iron and iron oxide nanoparticles.

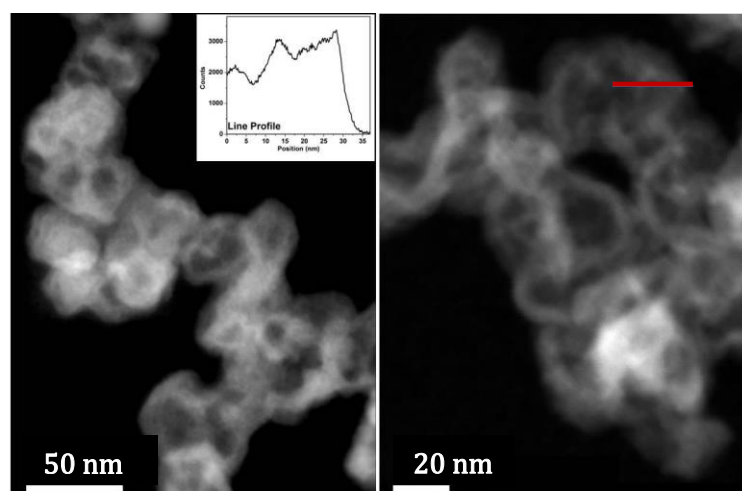


Figure 26: STEM images of the investigated catalyst, including a count line profile. No iron related clusters are observed ⁵¹.

X-band EPR measurements were performed (Figure 27), to quantify the amount of ferric spin states within the catalyst. Whereas, the large zero-field splitting of ferrous FeN_4 -sites prevent the detection under the given experimental conditions. The X-band EPR spectrum of the catalyst and the carbon-supported porphyrin ($\text{FeTMPPCl}/\text{CB}$), which was used as precursor, are shown. Both, the catalyst and the precursor were prepared and measured several times as the heterogeneous character of the catalyst result in a high relative error. Even though, the catalyst weight and volume are similar. The detail values and further related spectra are given in the Appendix (S 3, Table S 1 and Table S 2).

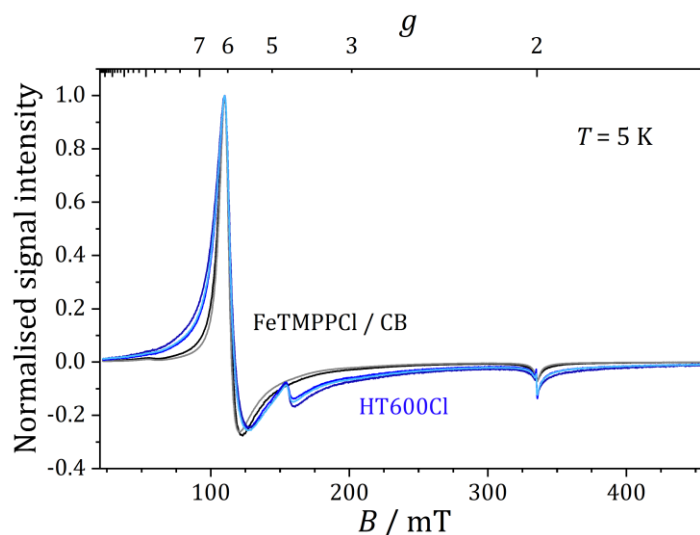


Figure 27: X-band EPR spectra of the catalyst and carbon-supported porphyrin ($\text{FeTMPPCl}/\text{CB}$) that was used as a precursor and reference ⁵¹.

For the precursor an axial EPR signal, as expected for a square pyramidal ferric high-spin FeN₄-site with chlorine as axial ligand, is observed. The effective g -values around 6.0 and 2.0 are related to a fivefold-coordinated ferric high spin porphyrins and originate from the $|5/2; \pm 1/2\rangle$ ground state Kramers doublet of an $S = 5/2$ spin system in an axial ligand field with positive D and a rhombicity parameter $E/D \approx 0$ ²³²⁻²³⁴. In the EPR spectrum of the catalyst the same high spin Fe(III) signal, as for the precursor is observed and results from similar immediate environments. Due to the presence of a heterogeneous distribution of iron in the sample a broadened signal, compared to the precursor signal, is seen. Heteroatom doping, distortion of the graphene layers and slight deformation of the FeN₄-sites are possible reasons for this observation. Beside the pronounced features a minor contribution at $g_{eff} = 4.3$ is found and originates from the middle Kramers doublet of an $S = 5/2$ spin system in a rhombic ligand field ($E/D \approx 0.33$), caused by a minor amount of impurity species^{235, 236}. To determine the ferric iron content in the catalyst, the precursor FeTMPPCl/CB with known Fe(III) content was used as reference. The spin concentration was determined from the double integral of the simulated catalyst spectrum (S 3). For an accurate determination of high spin Fe(III) and exclusion of errors, the presence of additional impurity signals and background contributions, have to be considered. From this data a total amount of 20–40% of the overall iron content is assigned as Fe(III) high spin. This is only slightly larger than those estimated from RT-MS, but as discussed below, in good agreement with the LT-Mössbauer data.

To observe the vibration mode behavior of the catalyst system and study the substituted ligands, nuclear inelastic scattering was chosen in combination with DFT calculations. As described by Scheidt et al.¹⁹⁴, vibration spectroscopy methods are very common to investigate heme proteins and metalloporphyrin's. Therefore, chloro-iron-tetrakis-methoxyphenylporphyrin (FeTMPPCl) and iron-phthalocyanine (FePc) were measured by NIS (Figure 28) as reference systems to build up a model for the subsequent DFT calculations of the catalyst system.

The defined vibration modes of the centered iron atom are visible. In case of the low-lying spin state of Fe-porphyrin, Kozłowski et al.²³⁷ described the resulting mode by density functional methods and identified the ground state as $^3A_{2g}$ state. The D_{4h} symmetry of the porphyrin result in Fe motion contributing only to a view possible modes which have either E_u or A_{2u} symmetry¹⁹⁴ and are IR-active but forbidden for Raman transitions due to the molecule symmetry of the iron center. The dominant mode is identified as ν_{53} in plane stretching of the Fe-N_{pyrrole} bonds. Indeed, the ν_{53} mode of the FeTMPPCl shows a higher wavenumber compare to other Fe-porphyrins^{194, 237, 238} but can be explained by slightly different chemical environments. The assignment of vibration modes follows existing NIS and pDOS data on porphyrins and related systems given in literature. As described by Zeng et al.²³⁹ the vibration modes between 120 cm⁻¹ to 230 cm⁻¹ are related to Fe-N_{His} vibration, whereas the found modes between 250 cm⁻¹ to 380 cm⁻¹ are related to Fe-N_{pyr}. The vibration modes seen at 430 cm⁻¹ and

660 cm^{-1} are assigned to the heme center interaction with diatomic axial ligands and a result of the interaction with O_2 . Sutherlin et al.²⁴⁰ give further vibrations for the Fe-OO interaction. The vibration modes between 300 cm^{-1} and 340 cm^{-1} are addressed to in plane iron motions that are either parallel or perpendicular to the projection of the Fe- O_2 plane²⁴¹.

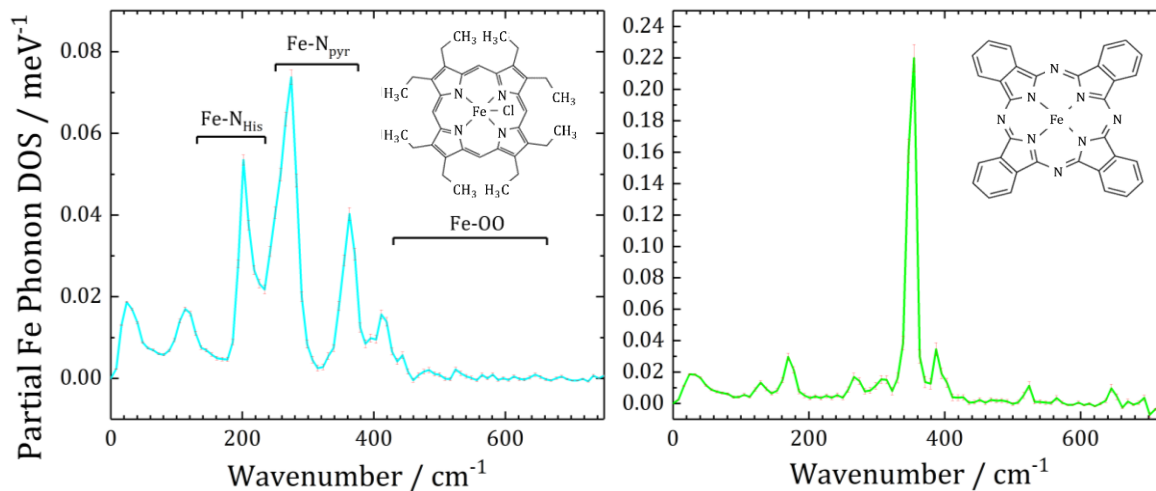


Figure 28: pDOS vibration data of the reference Fe-porphyrin sample (left) and FePc as measured during the beam time (right).

In Figure 29 (left) the obtained NIS spectrum of the catalyst at ~ 40 K is given. Only lattice vibrations with phonons creation ($E > 0$) are visible at this temperature. The resulting partial iron density of phonon states (pDOS) as derived from the NIS measurements is shown on the right site of Figure 29. Comparing the pDOS given in Figure 28 with the one measured for the catalyst, several findings are made. For the precursor, defined vibration modes are seen and dedicated to in-plane, out-of-plane, stretching, in-plane rocking, ring symmetrized deformation or torsions modes²³⁷. In case of the catalyst only areas of modes are assigned. The typical wavenumber range for Fe-N_{pyrrole}, Fe-N_{His}, and vibrations related to oxygen coordination on FeN₄-sites are indicated, respectively. Scheidt et al. classified three main vibrational mode categories for heme-like samples. The vibrational modes involving iron and the axial ligand are found in the range of 400 cm^{-1} to 600 cm^{-1} , the mid-range modes mainly assigned as in-plane modes from 200 cm^{-1} to 400 cm^{-1} and modes below about 200 cm^{-1} mainly containing out-of-plane modes¹⁹⁴. This is in good agreement with the findings from Zeng et al. who differentiate the related vibrational modes between 120 cm^{-1} and 230 cm^{-1} to Fe-N_{His} and modes between 250 cm^{-1} and 380 cm^{-1} to Fe-N_{pyrrole} modes, respectively²³⁹. For the investigated catalyst, a very dominant feature between 381 cm^{-1} and 395 cm^{-1} is observed, which was not found for the Fe-N-C catalyst investigated by Kneebone et al.⁵⁰. Indeed, Kneebone et al. did not see any vibration mode in this energy window for their PANI-based catalyst in any of the probed states, reduced nor NO-treated.

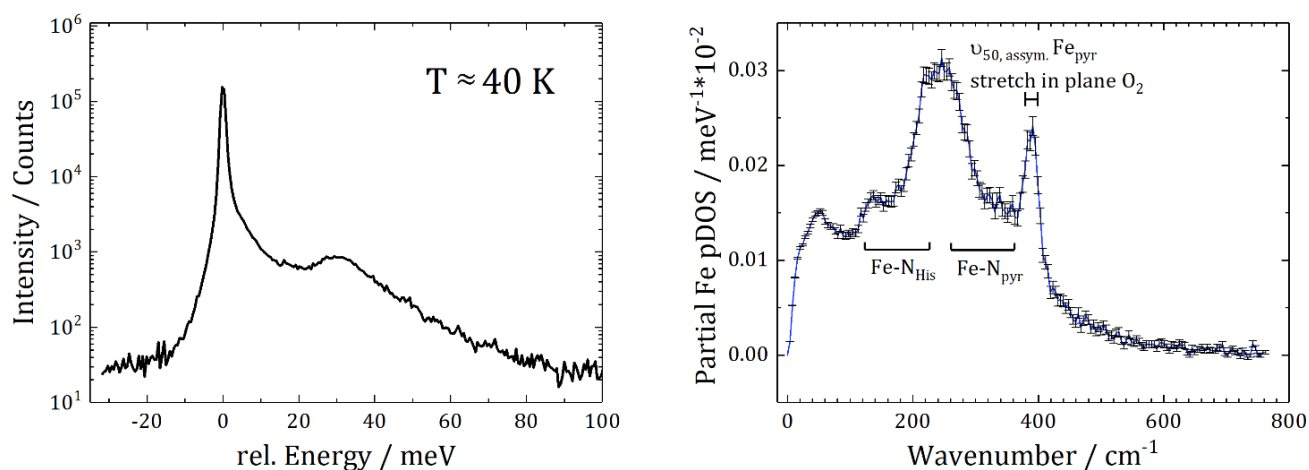


Figure 29: NIS spectrum of the investigated catalyst (left) and the resulting pDOS vibration data (right) ⁵¹.

The position of the most intensive peak at 400 cm^{-1} seems to be in line with the vibration of a heme-type FeN_4 center interacting with an end-on bonded oxygen molecule and result in a six-fold coordination of the catalytic active iron-site ²⁴¹. Consistently to Rai et al. ²⁴² the vibration mode is assigned as an in-plane asymmetric stretching mode. Indeed, it is assumed that this vibration shows the attachment of molecular oxygen to the catalytic active FeN_4 -site. The active sites should already be oxygenated, as the powder was stored in air. The surprisingly large background of the spectrum is untypical for FeN_4 -type iron environments (compare Figure 28) but shows a reasonably good agreement with iron oxide clusters and possibly iron clusters as described in literature ^{243, 244}.

This is rather unexpected as no consideration of iron oxide clusters or iron clusters agglomerates were indicated neither by RT-Mössbauer spectroscopy nor STEM. Therefore, the iron clusters in both iron sites must be very small as a collapse of Mössbauer sites appear at relaxation times below the half-life time of the excited state ^{34, 43, 64, 86}. Those findings might explain why similarly prepared catalysts show no ordered phase in X-ray diffraction as the particles size is too small for observing a diffraction pattern ²⁴⁵. Here, the advantage of synchrotron-based methods is proven and underlines the use of diffraction techniques only for particles above 3 nm ²⁴⁶. To identify the additional iron sites, undetectable for RT-MS and STEM, low temperature Mössbauer spectroscopy (LT-MS) was used in combination with an applied magnetic field, given in Figure 30 to verify the NIS results.

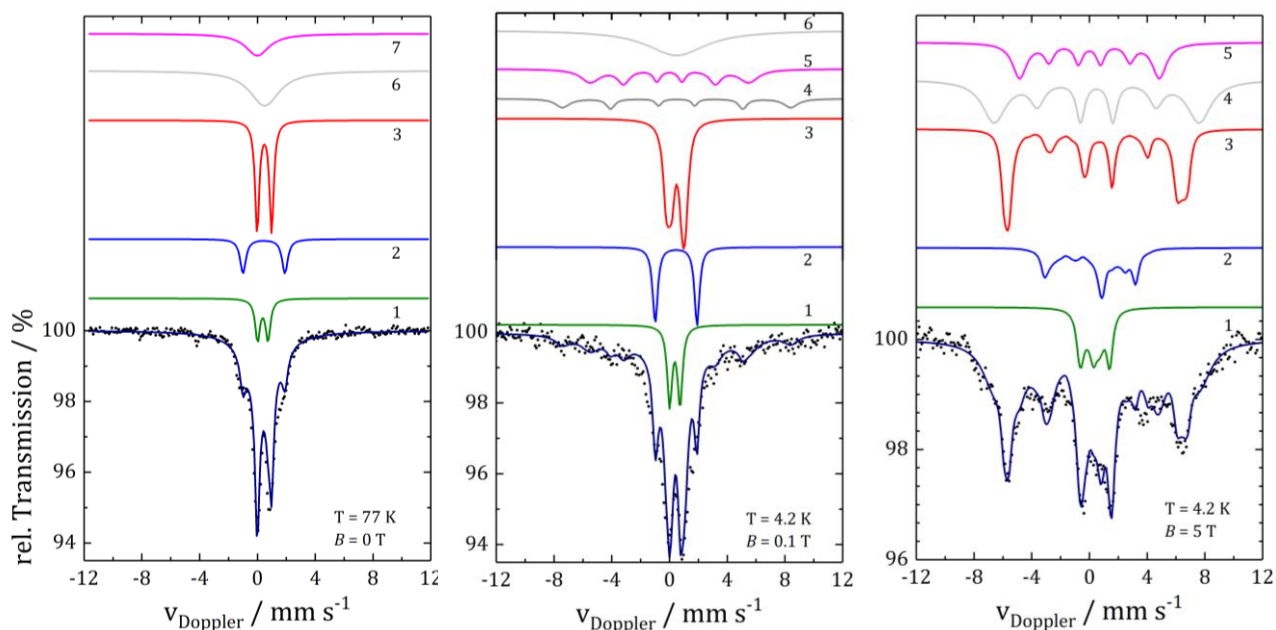


Figure 30: Mössbauer spectra obtained at 77 K, $B = 0$ T (left), 4.2 K with $B = 0.1$ T (middle) and 4.2 K with $B = 5$ T (right). The Mössbauer parameters are listed in Table 8 ⁵¹.

The picture of iron sites in the catalyst changes by applying LT-MS as a result of this, two new iron sites appear by cooling down the sample to 77 K (Figure 30, left). The new sites indeed attributed to α -iron and iron oxide which confirm the NIS measurement and underlines a missing magnetic order of these sites at room temperature. It is very likely, that small iron clusters of only a distinct number of atoms contributed to the found iron-sites. Therefore, only LT-MS is able to increase the lifetime of excited states and helps to enable magnetic ordering by stabilizing the Larmor precession of the magnetic moment about the external magnetic field and make those sites detectable. A temperature of 4.2 K with 0.1 T is required to stabilize the magnetic order of α -iron clusters. Nevertheless, even at this condition, a partial fraction of iron oxide clusters remain in the relaxed state and full magnetic ordering only appears at an external magnetic field of 5 T (Figure 30, right). Sougrati et al. ¹⁶⁵ observed for their probed $\text{Fe}_{0.5d}$ catalyst, larger sized iron oxide phases. As the temperature was 5 K and full magnetic ordering without an external magnetic field, appeared.

In Table 2 the related LT-Mössbauer parameters are given, as resulted from the catalyst displayed in Figure 30. The absorption areas are given for the spectrum obtained at 4.2 K and 0.1 T with a fitting model based on one consistent data set, except some different values in linewidths Γ , line ratio $I_1:I_2:I_3$, area and hyperfine field B_{hf} as given in the corresponding footnotes. The fitted absorption areas of the FePc and heme-like site are in good agreement with the corresponding RT-Mössbauer spectrum, whereas the area related to Fe(II) low spin-site decreases in evidence. Only 12% of the overall iron of D1 found by RT-MS is attributed to a ferrous low-spin site, whereas the other half has to be assigned to α -iron and

iron oxide, respectively. Thus, based on the performed LT-Mössbauer and NIS spectra, clear evidence is given that even under these mild preparation conditions, for the given iron content in the catalyst almost half of the contributed iron sites in the catalyst has to be assigned to inorganic iron species. This is a rather unexpected finding as the subsequent acid leaching should especially remove small inorganic agglomerates but seems not sufficient to remove encapsulated clusters.

Table 8: Mössbauer parameters as obtained from the analysis of the LT-Mössbauer spectroscopy displayed in Figure 30. The absorption areas are given for the spectrum obtained at 4.2 K, 0.1 T. All simulations shown in Figure 30 have been analyzed with one consistent data set, except some different values in linewidths G , line ratio $I_1:I_2:I_3$, area, and hyperfine field B_{hf} are given in the corresponding footnotes ⁵¹.

Component	1 (D1)	2 (D2)	3 (D3)	4(Sext2)	5	6 (Sext1)	7
	Fe(II)	FePc	Heme	Part. Fe-O relax	Part. α -Fe	Part. α -Fe relax	Part. Fe-O
S	0	1	5/2 ^s	—	—	—	—
$\delta_{iso} / \text{mm s}^{-1}$	0.37	0.46	0.48	0.50	0.00	0.50	0.00
$\Delta E_Q / \text{mm s}^{-1}$	0.72	2.90	1.00	—	—	0.00	0.00
η	0.5	1.0	0.0	—	—	—	—
B_{hf} / T^+	—	—	—	49.0	34.0	—	—
$\Gamma / \text{mm s}^{-1}\S$	0.40	0.42	0.50	0.50; 0.70; 1.20	0.60; 1.00; 1.60	0.50	—
$I_1:I_2:I_3^\#$	—	—	—	3.0: 2.0: 1.0	3.0: 2.0: 1.0	—	—
D / cm^{-1}	—	8 ± 1	5 ± 1	—	—	—	—
E/D	—	0.33	0.005	—	—	—	—
$\beta / ^\circ$	—	43	32	—	—	—	—
$A_{xx,yy,zz} / \mu_N g_N / \text{T}$	—	22.0 ± 1 ; 22.0 ± 1 ; 22.0 ± 1 ;	20.0 ± 0.5 ; 18.0 ± 0.5 ; 20.0 ± 0.5 ;	—	—	—	—
$Area / \%^\dagger$	12.0 ± 2	12.0 ± 2	28.0 ± 1	8.0 ± 1	16.0 ± 1	24.0 ± 2	0.0

^S The spin-Hamilton simulations of comp. 3 at $T = 77 \text{ K}$ in Figure 30(a) were performed with an external field of $B = 44 \mu\text{T}$ orthogonal to the γ -ray, which corresponds to the strongest part of the earth's magnetic field in Kaiserslautern, Germany.

⁺ B_{hf} at 4.2 K and 5 T for comp. 4: 44.0 T and for comp. 5: 30.0 T.

^S Γ at 77 K in Figure 30(b) for comp. 2: 0.48 mm s^{-1} ; comp. 3: 0.35 mm s^{-1} ; comp. 6: 2.50 mm s^{-1} ; comp. 7: 2.00 mm s^{-1} . Γ at 4.2 K and 5 T in Figure 30(c) for comp. 1: 0.50 mm s^{-1} ; comp. 2: 0.45 mm s^{-1} ; comp. 3: 0.50 mm s^{-1} ;

comp. 4: $\Gamma_{1,2,3} = (0.70 \text{ mm s}^{-1}, 1.20 \text{ mm s}^{-1}, 2.00 \text{ mm s}^{-1})$; comp. 5: $\Gamma_{1,2,3} = (0.70 \text{ mm s}^{-1}, 0.80 \text{ mm s}^{-1}, 1.20 \text{ mm s}^{-1})$.

[#] $I_1:I_2:I_3$ for comp. 4 and comp. 5 at 4.2 K and 5 T: (3.0: 1.0: 1.0).

[†] Area at 77 K in Figure 30(a) for comp. 4: 0%; for comp. 5: 0%; comp. 6: $32.0 \pm 1 \%$; comp. 7: $16.0 \pm 1 \%$. Area at 4.2 K and 5 T in Figure 30(c) for comp. 4: $32.0 \pm 1 \%$; comp. 5: $16.0 \pm 1 \%$; comp. 6: 0%.

Two possible ways of α -iron and iron oxide cluster formation seem realistic. The precursor consists of carbon black and FeTMPPCl, with an assumed low oxygen content in the precursor. Therefore, oxide cluster formation must have taken place after the pyrolysis either during the acid leaching or later. It can further be proven that no oxidative dissolution is visible in nitrogen saturated cyclic voltammetry measurements, which means that these clusters are not accessible to the electrolyte ²⁴⁷. Consulting the

Pourbaix diagram for iron, a leaching under acidic conditions would be very likely. The same is true for the α -iron clusters which have to be embedded in carbon, as otherwise oxidation of the particles would take place. The second possible way is related to the oven process. Carbon black has a high surface area. It is well known from XPS that carbon easily adsorbs aromatics and other carbon and oxygen containing species. During the oven process at low temperatures these components possibly interact with the iron containing precursor and form iron oxide cluster which become encapsulated by carbon during the ongoing oven process or reduce already existing iron oxide clusters to α -iron and encapsulate these cluster in a carbon shell. This would prevent these clusters from dissolving during the acid leaching. Only an assembly of a few atoms can be encapsulated in a carbon shell as bigger particles would result in a disturbed shell structure and dissolved during the leaching process or CV measurements. The two possible explanations cannot be clarified without further experiments, e. g., a complete oxygen free synthesis route with an additional Mössbauer characterization. The presence of such clusters explains the observed improvement in composition and activity as found by Kramm et al.²³¹ for a purification treatment in forming gas. Such clusters possibly react with the forming gas and afterwards being removed from the catalyst by the subsequent second acid leaching.

With LT-MS a method exists which is able to identify and assign all existing iron species in the catalyst system. Beside the organic iron sites, which were seen in RT-MS, iron oxide and α -iron clusters are part of the iron containing species inside the catalyst system. Based on available data in recent publications, such species^{50,113} – even though not assigned by the authors of the related publication – seem also to be present in Fe-N-C catalyst prepared by different approaches. Thus, their presence seems to be a general problem for Fe-N-C catalysts.

It is clear that iron oxide has no contribution to the ORR but can disturb and reduce the electronic conductivity in the prepared catalyst layer and limit the reaction, whereas a leaching out of iron sites can contaminate the membrane. Here, Fe^{3+} causes the formation of pinholes in the membrane as described by Li et al.²⁴⁸. The existence of even small amounts of metallic cations like Al, Fe, Cr and Ni in the membrane were investigated by Sulek et al.²⁴⁹ and the highest reduction of performance was found for $\text{Al}^{3+} \gg \text{Fe}^{3+}$. Already 5 ppm of Fe^{3+} are sufficient to reduce the performance during fuel cell operation by 44%. It is therefore crucial to avoid the leaching of iron ions during fuel cell operation, which can be implemented by a proper cleaning step or by direct prevention of cluster formation during the syntheses. Nevertheless, the content of ferric FeN_4 -sites is in better agreement with the EPR data compared to the RT-MS data. Approximately 30% is assigned to the ferric state and shows up with the largest contribution among of FeN_4 -type sites for mild preparation parameters. Fitting the LT-MS spectra by introducing two new species helps to find a sufficient model for modelling the pDOS data obtained from NIS. Indeed, iron oxide clusters similar as found by Marx et al.²⁴⁴ and small iron nanoparticles and layers^{243,250} have to be considered as well. So, a more qualitative analysis of the pDOS by comparison

of literature data^{194, 204, 242, 243, 250, 251} and adapting DFT calculations, is possible. Based on the given data, two DFT based models A and B were calculated and are given in Figure 31. Both models take two FeN₄-sites as basis structure, aFePc like (blue), an oxy-heme type (green) and the found iron oxide clusters given by Marx et al.²⁴⁴. For model A (fir green) a Fe³⁺heme-site with nitrogen as axial ligand (red) is additional added, whereas a Fe-porphyrin with chlorine as axial ligand (dark red) is used for model B (orange). The related weighting factor of components was chosen as found by LT-MS. The ferrous low spin FeN₄-site (D1) is typically six-fold coordinated¹⁰⁷ and in relation to Zitolo et al. and Li et al.^{37, 38} the presence of an oxygen molecule as one axial ligand seems likely. Therefore, the related ferrous low spin site was modulated with oxygen as one axial ligand and over the nitrogen of a trimethylamine connected as possible sixth ligand (green). This oxy-heme-type site can participate the ORR as oxygen is already present. The ferrous FePc-like site (D2) is most likely fourfold coordinated, but might interact in axial direction with graphene planes located above and below, thus being not accessible for the ORR²⁵². The idea of using two different porphyrin-type structures, with chlorine as axial ligand (dark red) and pyridine as axial ligand (red) are caused by thermogravimetry coupled mass spectrometry, as it indicates that at 600 °C, still 30–50% of the chlorine ligands remains²⁴⁵. It would be possible that to some extent, this porphyrin-type coordination still remains intact and contribute to the pDOS data. Even with consulting LT-MS it is not possible to entirely fit the obtained pDOS data. But some important characteristic features are projected by those DFT calculations. The heterogeneous character of Fe-N-C systems make it difficult to gain more details about single iron components, as small variation in the carbon coordination result in a slightly different vibration mode obtained by NIS and confirms the EPR results, where the heteroatom doping, distortion of the graphene layers, and slight deformation of the FeN₄-sites are possible results in a signal broadening. Further iron clusters will contribute to the pDOS, but were not considered due to the different size effects of nano particles²⁴³ in the DFT calculations. All this results in a broadening and blurred pDOS spectra as it is further observed by Kneebone et al.⁵⁰. It is shown that nuclear inelastic scattering in combination with LT-MS and DFT calculations is very useful to analyze the structural behavior of Fe-N-C systems even so, particle size effects will limit the modelling of components. In fact, very mild preparation conditions and a subsequent acid leaching of Fe-N-C catalyst are not sufficient to prevent and remove considerable fractions of inorganic clusters (iron and iron oxides). Except of these inorganic species, very strong evidence for an oxy-heme-type site that most probably is the origin of the ORR activity was found by NIS and the related DFT calculations. The presence of an oxygenated FeN₄-site makes its involvement in ORR catalysis very likely. Additionally, the limits of RT-MS underline the importance of LT-MS measurements or more advanced characterization methods like synchrotron-based resonance techniques. These findings are of great importance for the further improvement of Fe-N-C preparation strategies and for a fundamental

understanding of the reaction mechanism related to the oxygen reduction in either fuel cells or metal-air batteries.

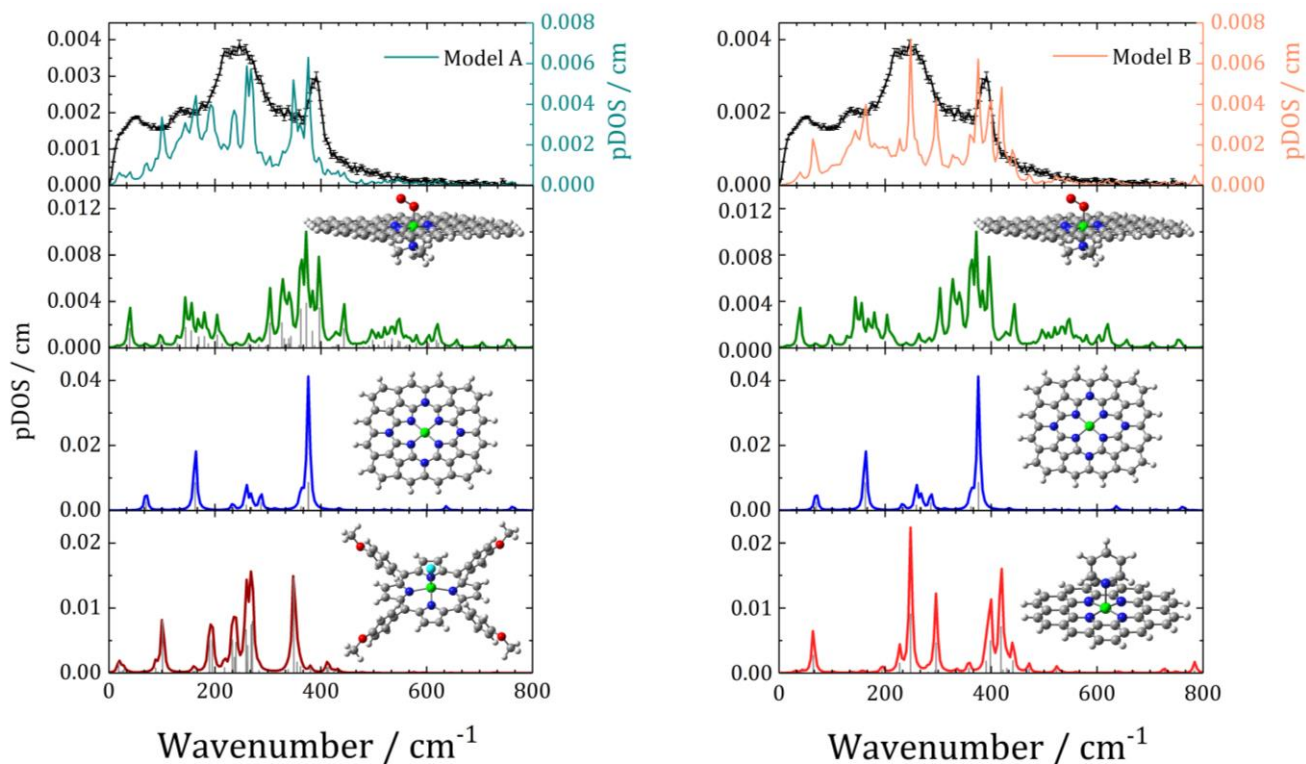


Figure 31: Calculated iron pDOS spectra with specific vibration modes as addressed in the text. (left) Model A (fir green, top left): Fit of the iron pDOS based on the simulated spectra of iron oxide clusters, low spin oxy-heme type site with trimethylamine and O_2 as axial ligands (green), iron phthalocyanine-type coordination embedded in carbon (mid spin) (blue) and high spin ferric FeN_4 -sites (FeTMPPCl) with chlorine as axial ligand (dark red). (right) For model B (orange): The simulated spectra of iron oxide clusters, low spin oxy-heme type site with trimethylamine and O_2 as axial ligands (green) and iron phthalocyanine-type coordination embedded in carbon (mid spin) (blue) were included similar to model A. Further a ferric FeN_4 -site with pyridine as axial ligand was added (red). The atom color code is given as follow: grey: carbon, white: hydrogen, blue: nitrogen, green: iron, cyan: chlorine, red: oxygen.

5.2. Deactivation Experiments of the Catalyst

As mentioned in chapter 3.1 deactivation species are helpful to elucidate the structural environment of active sites. Inspired by a previous work, a sulfide species was used as deactivator and probe molecule for the Fe-N-C catalysts. The results were published in Wagner et al.⁵² In chapter 4.2 the preparation of the catalyst is given in detail. Electrochemical tests of the deactivated and pristine catalyst powder were performed by RDE experiments as described in the experimental part 4.2, in order to identify the activity changes induced by sulfite-treatment. The use of Na_2SO_3 as deactivator for the catalyst powder results in a significant reduction of performance during RDE experiments for the three investigated catalysts as seen in Figure 32, where the forward and backward scans of the RDE measurements are given.

Two effects are addressed by the treatment with sodium sulfite. On one side the diffusion limiting plateau is lowered, whereas on the other side the onset potential for ORR is shifted to lower potentials. To compare the effect of the introduced anion on the catalyst, the kinetic current densities j_{kin} at 0.75 V vs. (RHE) of the initial and deactivated catalyst is determined (Figure 32). For the given setting, the diffusion limiting current density depends mainly on the number of transferred electrons n_e . The oxygen reduction reaction is converted by the direct reduction to water with $n_e = 4$ or an indirect reduction, with hydrogen peroxide as intermediate species given by two $n_e = 2$ transfers (compare equation (1) – (3)). As the diffusion limiting current density is lowered, the selectivity for the undesired hydrogen peroxide formation is preferred for the deactivated site. By taken the category plot of the kinetic current densities into account, the shift in onset potential, which causes a lowering of the ORR activity for the three catalyst becomes apparent. The loss of activity is most pronounced for HT600HCl followed by HT800HCl and lowest for HT800HCl+S.

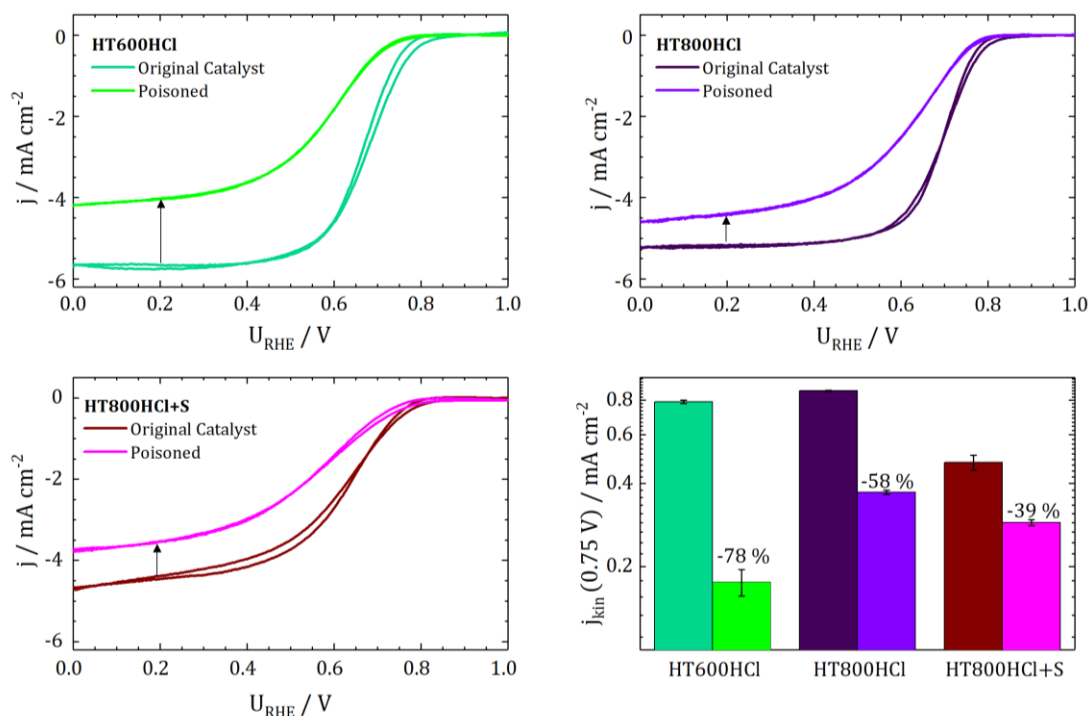


Figure 32: RDE curves of the three different pure and poisoned catalysts recorded at 1500 rpm, 10 mV s⁻¹, in 0.1 M H₂SO₄. The category plots of kinetic current densities at 0.75 V for the pristine (dark color filled) and deactivated catalysts (light color filled). Due to the deactivation a reduction of current density is seen ⁵².

Herranz et al. proposed anion binding as a main degradation mechanism for their Fe-N-C catalyst ¹³⁴ It was shown that 80% of the activity, attributed to the recovered state were lost by anion binding. Additionally, it was assumed that an anion binding took place on protonated nitrogen species in the vicinity of active sites. It should be figured out, that here the final step of preparation was an acid-leaching for the probed catalyst HT600HCl and HT800HCl. Therefore, an additional loss of activity can

only be induced by sulfite ions as all protonated sites should be already blocked by anions. Indeed, the extend of deactivation is similar to Herranz et al.¹³⁴ for HT600HCl, whereas for both catalysts prepared at 800 °C a lower impact is observed.

Beside the possible deactivation mechanism according to Herranz et al.¹³⁴, two further mechanisms might appear. In Figure 33 (left) the anion binds as axial ligand to the active site, but an interaction with oxygen is still possible if a six-fold active site is assumed. This would not result in a complete deactivation but, due to electronic changes could reduce the turn-over frequency. Whereas, Figure 33 (right) depicts a five-fold active site where the anion blocks the interaction, so no reaction with oxygen would be possible anymore. In this case, the active site would be completely deactivated by the introduced anion.

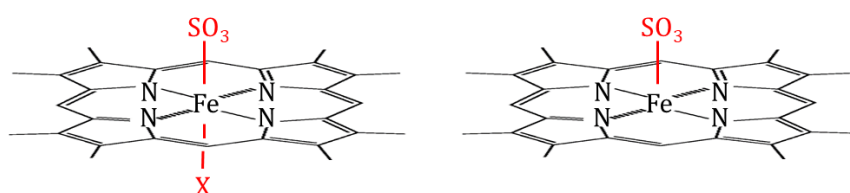


Figure 33: Models for the deactivation of FeN₄ sites by anion binding: The anion interacts with the active site, while the ORR is still possible (X= O₂). (left) The active site is completely deactivated if a five-fold active site is assumed. (right)

A change in Mössbauer parameters is expected for both deactivation scenarios. Therefore, Mössbauer spectroscopy was performed to investigate the impact of sulfite anions on the iron signature of HT800HCl (Figure 34) and HT600HCl (Figure 35).

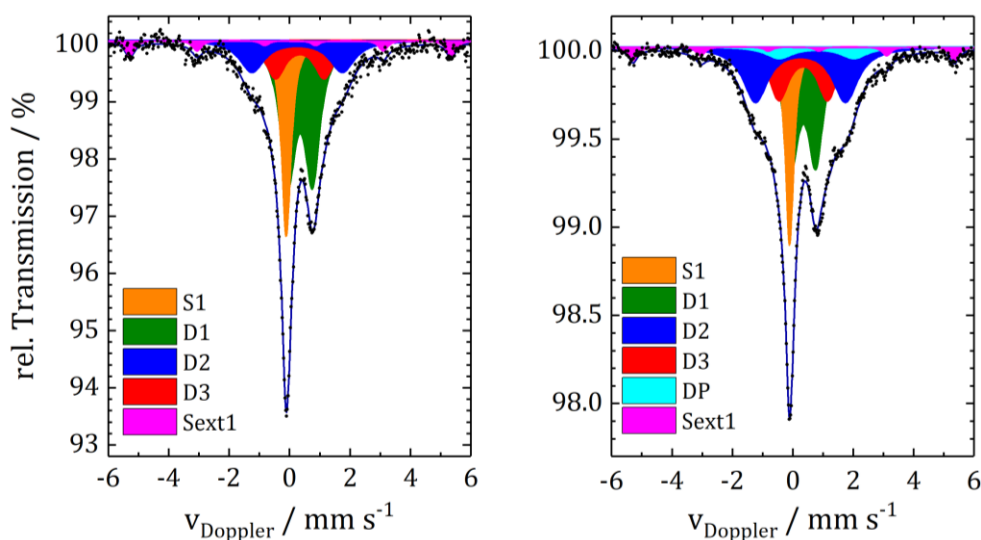


Figure 34: Mössbauer spectrum of pristine (left) and deactivated HT800Cl catalyst with the new doublet species (right)⁵².

Both pristine catalyst powders were fitted assuming the presence of three different FeN₄-sites as previously identified for Fe-N-C catalysts^{34, 36, 212} and already discussed in the previous chapter. For the

sulfur containing catalyst HT800HCl+S, in addition a fourth species was found (D4) assigned as ferrous iron sulfide site. This catalyst will be discussed elsewhere. In addition, inorganic iron species are present in the catalysts prepared at 800 °C, caused by the high preparation temperature and the destruction of FeN₄-sites. The Mössbauer parameters are summarized in Table 9. The fitting of the deactivated catalyst powders were realized by using the same iron species as found for the pristine catalyst by allowing only absorption areas to change (Table 9). Whereas, the Mössbauer parameters of the deactivated species are given in addition, were set free. It is assumed that the ligand field strength changes for the Fe-site due to the attachment of the anion and will result a new species. Indeed, this behavior is observed in the raw spectrum data. Therefore, a fourth symmetric doublet (DP) was added with open parameters for all adjustable specific values.

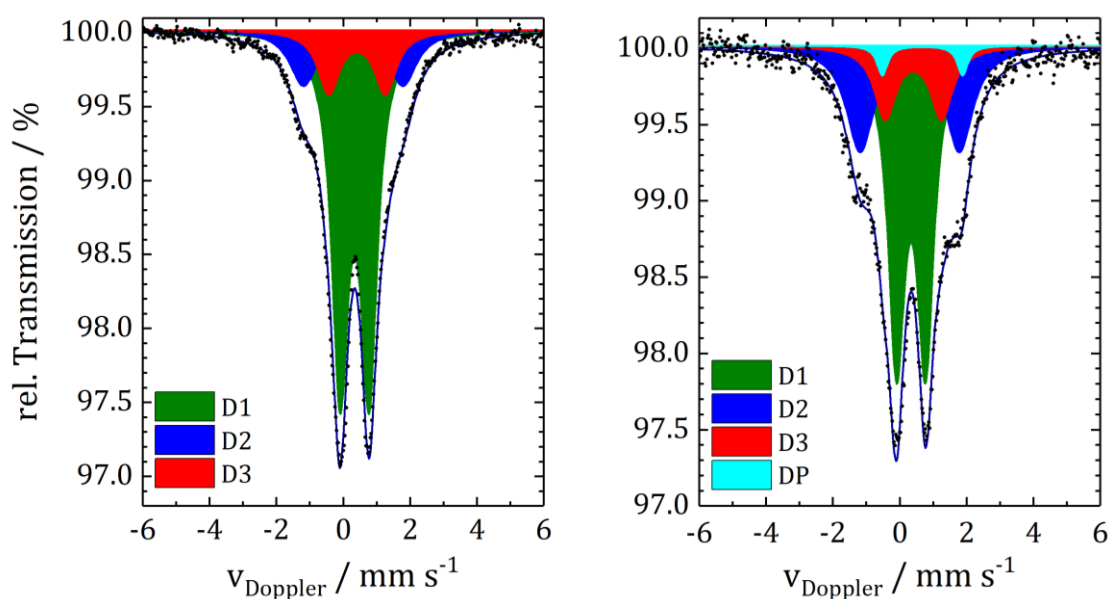


Figure 35: Mössbauer spectrum of pristine (left) and deactivated HT800Cl Mössbauer spectrum with the new doublet species (right) ⁵².

The investigated pristine catalyst powders are fitted with up to five different iron containing sites. The found singlet species S1 and sextet species Sext1 are assigned to superparamagnetic iron and alpha-iron, respectively ^{64, 150, 212}. D1 is related to ferrous FeN₄ moieties in the low-spin state as identified by several authors as ORR active site ^{34, 36} and as found in this work, as most likely six-fold oxy-heme type-site ²⁴⁷. A ferrous iron structure similar to FePc in the mid-spin state was assigned for the second doublet (D2) ¹¹⁰. Whereas, for the third doublet D3 a heme-like site, CFeN₂ or a charged FeN₄-like site ^{253, 254} is suggested. The sulfur containing sample (HT800HCl+S) shows two additional iron sites (D4 and Sext2) which both are assigned to iron sulfide (Fe₃S₄) nanoparticles with a different size distribution as discussed in Janßen et al. ²²⁵. Caused by the sodium sulfite treatment a deactivation doublet appears in the

deactivated catalyst spectra denoted as DP. The related Mössbauer parameters are compared for the three catalysts in Table 10.

Table 9: Mössbauer parameters of the three investigated pristine and deactivated catalyst ⁵².

	$\delta_{\text{iso}} /$ mm s^{-1}	$\Delta E_{\text{Q}} /$ mm s^{-1}	$\Gamma /$ mm s^{-1}	B_{hf} $/ \text{T}$	HT600HCl		HT800HCl		HT800HCl+S	
					Area / %		Area / %		Area / %	
					OC	P	OC	P	OC	P
S1	-0.11 (0.01)	-	0.38 (0.02)	-	-	-	19.2 (0.8)	15.0 (0.2)	-	-
D1	0.36 (0.02)	0.89 (0.07)	0.6 ^{*1}	-	66.6 (0.7)	51.6 (0.7)	42.2 (3.0)	30.5 (0.6)	35.4 (1.1)	42.5 (0.4)
D2	0.31 (0.07)	2.69 (0.34)	1.0 [*]	-	17.6 (0.6)	29.2 (1.0)	16.7 (1.5)	25.1 (1.2)	35.4 (1.3)	31.8 (0.7)
D3	0.38 (0.03)	1.66 (0.23)	0.8 [*]	-	15.9 (0.6)	3.2 (1.1)	15.6 (2.9)	19.0 (0.8)	-	-
D4	0.98 (0.02)	2.58 (0.04)	0.7 [*]	-	-	-	-	-	16.9 (1.0)	12.2 (0.8)
DP	As reported in Table 10									
Sext1	0.40 (0.37)	-	0.38 (0.04)	31.9 (1.1)	-	-	6.4 (1.7)	4.5 (0.5)	6.0 (1.2)	3.2 (0.6)
Sext2	1.06 (0.01)	-	0.28 (0.04)	9.8 (0.09)	-	-	-	-	6.4 (1.3)	7.5 (0.8)

¹Parameters with * were set constant.

The D1-site is assumed to be the active site in Fe-N-C systems. Here the SO_3^{2-} ion can attach and decrease or block the ORR activity and change the Mössbauer parameters of the related iron site. As seen from the area changes, it is concluded that the relative loss of the absorption area accounts to 30% and 27% for HT600HCl and HT800HCl, respectively. Indeed, it would be unlikely if all ORR active sites are blocked due to the accessibility of sites and steric hinderance, which is in agreement with a partial loss of ORR activity and the fact that the utilization factor of ORR active sites is often $\ll 100\%$ ²⁵⁵. Further, as seen in the previous section, the D1-site can overlay with iron containing clusters which lowers the total amount of active sites. Comparing the area changes after deactivating the catalyst, with the values obtained from LT-MS measurements of the previous chapter, a good agreement is observed. However,

in case of HT800HCl+S an increase of D1 by 20% is recognized. In Figure 36 the difference spectra of normalized absorption of the pristine and deactivated catalyst are given. For the sulfur free catalysts, a reduced area is seen, whereas for the sulfur containing catalyst the area increases. The formation of the new doublet DP is visible in terms of negative contribution in the difference spectra, whereas, the lowering of the D1 species is indicated by the positive contribution. The data were used to identify the Mössbauer parameters of DP, as given in Table 10.

Table 10: Related Mössbauer parameters of deactivated species ⁵².

DP	$\delta_{\text{iso}} /$ mm s^{-1}	$\Delta E_{\text{Q}} /$ mm s^{-1}	$\Gamma /$ mm s^{-1}	Area / %
HT600HCl	0.68 (0.03)	2.40 (0.05)	0.38 (0.1)	3.2 (1.1)
HT800HCl	0.79 (0.01)	2.48 (0.12)	1.10 (0.26)	5.9 (2.2)
HT800HCl+S	1.2 (0.03)	1.94 (0.06)	0.34 (0.14)	2.2 (0.8)

It is not clear, why the sulfur containing catalyst behaves nearly opposite compared to the other two catalysts. But different preparation conditions like, i) the alternative Fe-N-precursor in comparison to the porphyrin, ii) a heat-treatment as final preparation step of this catalyst and iii) the presence of sulfur in the precursor mixture are possible reasons. Indeed, an effect of the Fe-N-precursor should be excluded as the active site seems to be too similar as found in alternatively prepared catalysts ^{35, 255, 256} but the periphery of the active site can be different and not detectable by Mössbauer spectroscopy. The heat treatment step at the end of the catalyst preparation, possibly result in a recoverable activity decay and a deactivation by sulfite ions. That is why an impact based on the heat treatment as final preparation step on the different behavior cannot be excluded. It would be possible that HT800HCl+S is not as sensitive to a deactivation treatment with sulfite ions due to the already existence of sulfur species in the catalysts. Therefore, a possible interpretation is given by the presence of sulfur containing species, as HT800HCl+S is already in a deactivated state. Nevertheless, the right assignment of the DP doublet cannot be defined without further investigations.

R. Taube successfully probed the effect of anion binding to molecular FePc moieties and figured out that new doublets were formed by anion binding in axial direction. This results in an increased quadrupole splitting by a decreased ligand field strength of the anion ²⁵⁴. The change of Mössbauer parameters caused by the anion binding is given in Table 11 and compared to the observed values obtained for the sulfite species. The Mössbauer parameters given in Taube's work are reported vs. $\text{Na}_2[\text{Fe}(\text{CN})_5\text{NO}] \cdot 2\text{H}_2\text{O}$ and therefore transferred to an α -iron reference ²⁵⁴. Additionally, parameters found in the PhD work by Kramm, caused by the interaction of FeN_4 -sites with HSO_4 in porphyrin-based Fe-N-C catalysts

were added ²⁴⁵. A good agreement by comparing the different anions investigated by Taube and Kramm with found parameters for the deactivated site is not observed as all of them are weak ligands. Indeed, the spectrochemical series of ligand field strength for anions increases in the order $I < \text{HSO}_4 < \text{Br} < \text{S}_2 < \text{Cl} \ll \text{SO}_3^{2-}$. The impact of sulfite ions should further influence the Mössbauer parameters of all FeN_4 -sites, as Taube showed the effect of anion binding for FePc whereas, in this work it is assumed that the sulfite anion should bound on an oxy-heme site. Therefore, an overlay of effects influencing the Mössbauer spectra cannot be excluded.

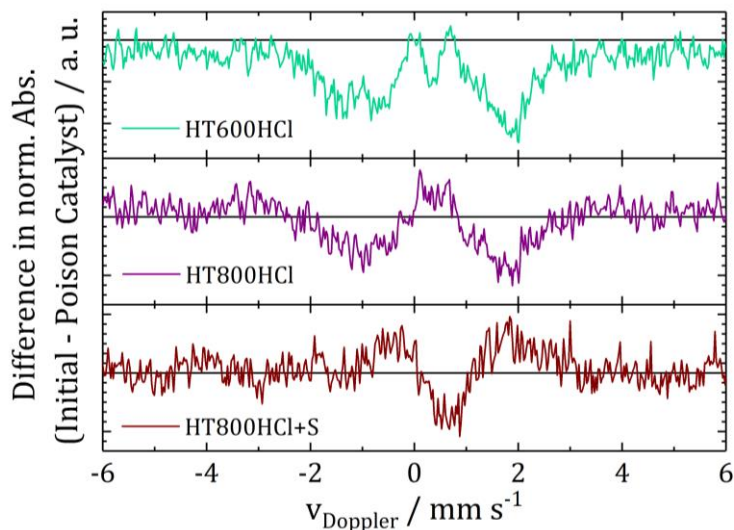


Figure 36: Difference spectra of normalized absorption of the initial and poisoned catalyst is given. For the sulfur free catalysts, a reduced area is seen, whereas for the sulfur containing catalyst the area increases ⁵².

Table 11: Comparison of Mössbauer parameters observed for different axial ligands to ferrous FeN_4 -sites. Data indicated with * were taken from Taube ²⁵⁴ and Kramm ²⁴⁵.

	I_2^*	HSO_4^*	Br^*	Cl^*	HT600HCl	HT800HCl	HT800HCl+S
$\delta_{\text{iso}} / \text{mm s}^{-1}$	0.18	0.08	0.11	0.20	0.68	0.79	1.18
$\Delta E_{\text{Q}} / \text{mm s}^{-1}$	3.3	3.28	3.16	2.75	2.40	2.48	1.94

Due to the interaction of FeN_4 -sites with SO_3^{2-} anions, ferric high-spin complexes are formed. On the contrary, the ligand field strength of sulfite is significantly more pronounced so that a low-spin state can be expected. By deactivating the FeN_4 -sites, the resulting deactivated state remains ferrous as the pristine ORR active iron sites, but a change of spin state, from low- to high-spin is observed. It is assumed that the parameters of the doublet assigned to the deactivation treatment are similar for HT600HCl and HT800HCl, whereas significant different values are found for HT800HCl+S. As some Mössbauer parameters were fixed during the first fitting procedure, a second fit model was applied where all

Mössbauer parameters known from Table 9 were set free to investigate the influence of the attached SO_3^{2-} anion on all FeN_4 -sites of the catalyst (Figure 37).

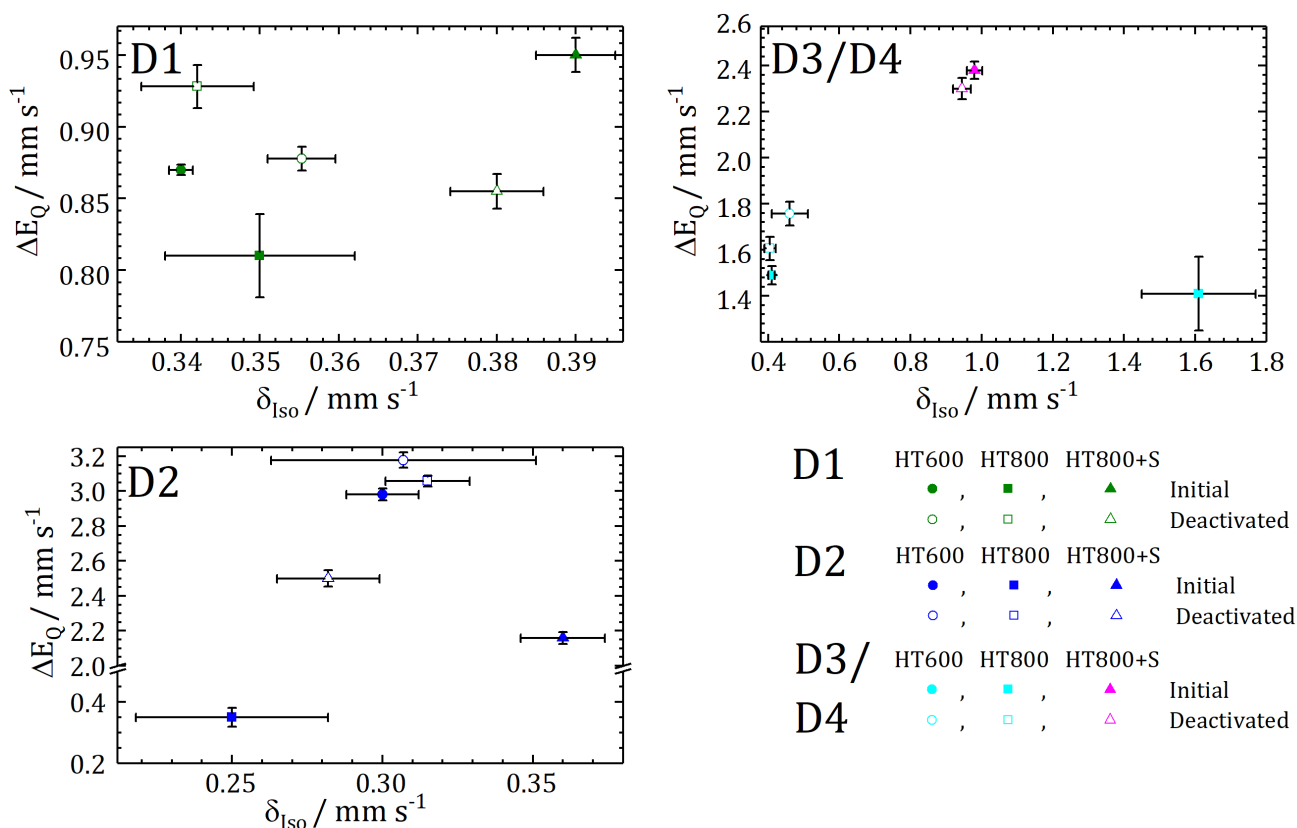


Figure 37: Free running isomer shift and quadrupole splitting are plotted against each other, with the corresponding errors. Introducing SO_3^{2-} ions result in higher isomer shifts and quadrupole splitting values. This is true for both, HT600HCl and HT800HCl catalysts, whereas HT800HCl+S shows a converse dependency.

After fitting the spectra with the free running parameters, HT600HCl and HT800HCl show an increase in both, isomer shift and quadrupole splitting, whereas HT800HCl+S shows a converse dependency. In case of a six-fold coordinated Fe(II) compound, the increase of isomer shift corresponds to a decrease of π -electron distribution by the antibonding orbitals of the ligand, whereas an increase of σ -bonding to hybrid d^2sp^3 orbitals will result in a decrease of the isomer shift. For the change of quadrupole splitting more positive values will appear if the π back-bonding is increased, whereas increasing the σ -bonding results in a more negative value¹⁷⁵. From this, the question of the different behavior of Mössbauer parameters arises. A possible explanation might be the assumption that the way of anion attachment changes. In Figure 38, four possible coordination's of sulfite anion to the FeN_4 center are given. Based on the characteristics for oxygen and sulfur ligands it is assumed that the ligand field strength increases from left to right and top to bottom. In addition, the electric quadrupole interaction is assumed to be smaller for the symmetrically attached options, given in b) and d) in comparison to asymmetric attachment as seen in a) and c).

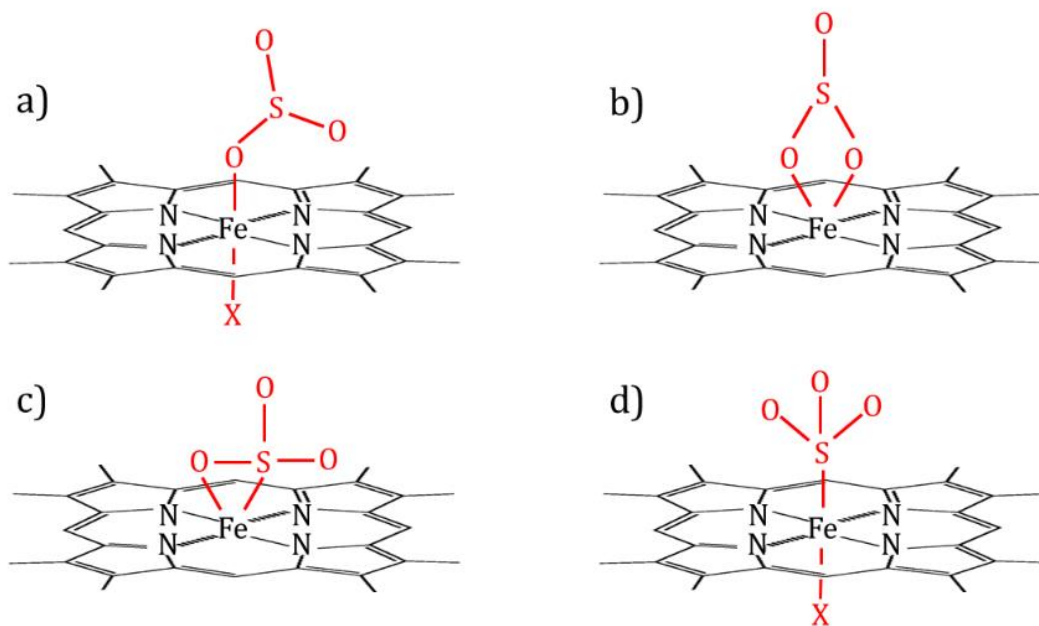


Figure 38: Possible axial binding of sulfite species to FeN_4 -sites by assuming a six-fold coordinated iron site where the SO_3^{2-} ion can attach.

Here, the limitation of Mössbauer spectroscopy becomes obvious. Due to the free run of parameter the degree of freedom increases. It is hard to distinguish between the change of areas, the shift of parameters and the contribution of the changes influenced by the single components and by the introduced anion. Especially, if the components are similar to each other as in the given case, the change in areas can be misleading. Even if the way of fitting results in some errors, it is clear that the impact of the anion influences the electron density and disturb the isotropy at the metal center, causing variations of the Mössbauer parameters of the corresponding iron sites. But the nature of anion attachment cannot be satisfied discussed by the given experiments.

Based on the findings it is most likely that the anion binds directly to the active sites. However, it is not possible to distinguish between the two options of a lowered turn-over frequency as found by RDE (Figure 32) or a complete deactivation of FeN_4 -sites that adsorb sulfite (Figure 38). Further, electronic changes that might affect the ORR activity are caused by the integration of sulfite groups in the carbon matrix. So, the pristine and deactivated catalysts of the sulfur free synthesis route (HT600HCl) was investigated by nuclear inelastic scattering (spectra given in the Appendix S 4) to obtain the pDOS (Figure 39) and nuclear forward scattering (Figure 40) of the catalyst systems to receive information of the time domain. A detail discussion of the pDOS spectrum of HT600HCl was already given in the previous chapter.

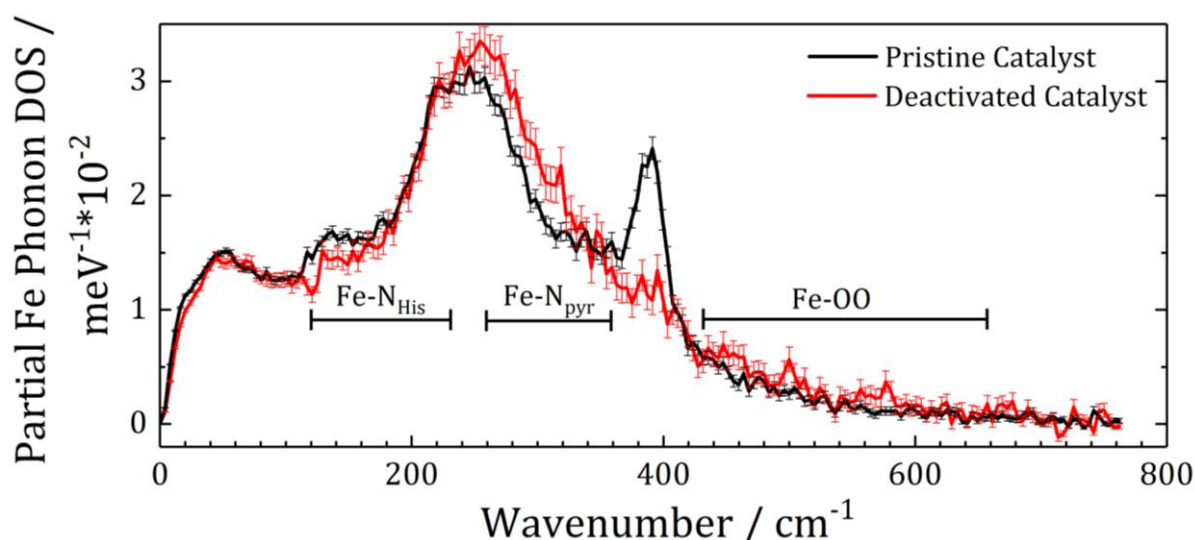


Figure 39: The pDOS data of the deactivated and pristine catalyst HT600HCl.

Comparing the pDOS characteristics of the pristine and deactivated catalysts (Figure 39) some general similarities and differences are pointed out. Starting from the lowest modes, between 0 cm^{-1} to 200 cm^{-1} , the pristine catalyst shows two broad frequency modes with the maxima around 49 cm^{-1} and 137 cm^{-1} , respectively. In this frequency range mainly out-of-plane modes, overlapping with doming modes in which the iron atom moves out of the porphyrin plane while the periphery of this ring moves in the opposite direction^{194, 257}, appear. The detail understanding of the doming mode characteristics can be used to determine the reactivity of oxygen with the heme proteins²⁵⁷ but is not further examined. As discussed in the work of Marx et al.²⁴⁴ iron oxide nanoparticles show shoulders in the same vibration range which were already considered in the previous discussion.

Scheidt et al.¹⁹⁴ assigned the modes below 50 cm^{-1} as phonon modes resulting from heme translation in the solid. Which are typically found for systems with diatomic ligands. Indeed, those divisions are hard to distinguish as spectral-frequencies overlap and must be resolved in order to provide detailed assignments. Interestingly, the observed low frequency modes are less pronounced in the work of Kneebone et al., whereas between 50 cm^{-1} to 200 cm^{-1} two dominant modes are seen.⁵⁰ This could be caused by the higher number of inorganic species, especially oxide nanoparticles as described by Marx et al.²⁴⁴ compare to the investigated catalyst of this work. Here, one maximum of vibration modes is found around 240 cm^{-1} where Kneebone and co-worker observed only a small mode. In this area the porphyrin and phthalocyanine modes are found. As already discussed, the small coordination variation of iron sites, result in a slightly shift of frequencies and lead to the observed pDOS behavior. By comparing the pDOS regime for both catalysts it is obvious that NIS is very suitable for the investigation of catalyst systems which are pure in case of iron sites whereas a higher number of different species result in a smearing of modes. The second dominant feature around 381 cm^{-1} and 395 cm^{-1} was

previously addressed as asymmetric ν_{50} in-plane stretching mode of Fe_{pyr} with oxygen binding. At higher wavenumbers no further modes are seen for the pristine catalyst. Introducing of the anion (red curve) shows below about 50 cm^{-1} no significant impact. For the deactivated catalyst a suppression of the mode at 137 cm^{-1} is observed, whereas, starting from 210 cm^{-1} up to 360 cm^{-1} modes shifted by about 30 cm^{-1} and the nearly full suppression of the dominant mode around 381 cm^{-1} is seen. New modes appear in the range between 420 cm^{-1} to 600 cm^{-1} . In this range mostly peroxy- and oxy intermediates interacting with organic iron sites^{239, 240, 258} are reported. In our cases, it is assumed that they might be caused by the impact of sulfite ion binding through the active site. This gives the first hint to a more concrete nature of interaction between the sulfite ion and the iron center. DFT calculations were conducted by H. Auerbach (AG V. Schünemann) for four different variation possibilities. In the supporting figure S 5a), a six-fold iron site is bound on the bottom with a trimethylamin and deactivated by SO_3^{2-} over an O bond of the sulphite ion. For the possibility b) an O_2 molecule is bonded on the bottom of the iron site and deactivated by SO_3^{2-} over an O bond. Whereas for c) and d) $\text{O}_2 + \text{SO}_3^{2-}$ over the S and trimethylamin + SO_3^{2-} over S are bonded to the iron site, respectively.

Comparing the different models with the real pDOS data obtained from the NIS measurement, it seems most likely that the interaction of the anion with the catalyst active site takes place through the oxygen site of the sulfite ion. The simulations done for an attachment of anion through the iron site over the sulfur atom did not result in a similar mode characteristic as found by NIS measurements. Comparing the DFT calculation of a) and b) in the supplemented figure S 5a vibration mode at a wavenumber of 384 cm^{-1} is seen. This is a very interesting finding as it was figured out before, that at 381 cm^{-1} , the interaction of the active site with oxygen was assumed. After deactivating the catalyst powder, this mode completely vanishes but cannot be confirmed by the resulting DFT calculations. based on this finding it is questionable if the investigated sixth ligand seems realistic.

Indeed, a possible interaction of a six-fold iron site with an oxygen molecule and peroxy- or oxy-molecule seems not unlikely as already mentioned by Hoon et al.⁹⁸, where DFT calculation were applied on an OH ligand attached through a bulk-hosted FeN_4 -site. They figured out that O_2 does not exothermically bind on the iron site if OH already bond as ligand and suggested that an OH-modified site may not act as a single reaction site on an associative ORR pathway. Nevertheless, the assumed zigzag edge-hosted FeN_4 with OH ligand is able to bind O_2 and participate to the ORR activity. The prepared DFT calculations were done for a five-fold iron site, whereas in our case a six-fold site is discussed. Further, the limitations of those DFT calculations are given by the adjusted boundary conditions. It is well known that the interaction of the active site and intermediates with the environment e.g., NafionTM, water molecules, etc. cannot be neglected but rarely considered in the calculation due to the complexity and limited computational power. The same applies for the DFT calculations given here. But, as only the pure powders were investigated, interactions are not as dynamic as under operation conditions with an

applied and adjustable potential. Considering this, the results of this work are more reliable. Beside the use of nuclear inelastic scattering to analyze vibration modes and ligand sites, further, NIS was used to provide information of the atomic lattice rigidity by the supplemental factor known as Lamb-Mössbauer factor f_{LM} . As described by Chumakov et al.^{199, 203} the nuclear recoil in a lattice is equal to the recoil energy $E_R = 1.956$ meV of a free nucleus for the first momentum of the energy spectrum, which follows Lipkin's sum rule. Therefore, it is possible to calculate the recoil fraction of nuclear absorption from the area of the normalized, inelastic NIS part of the spectrum. This approach was applied for both, pristine and deactivated catalysts according to the corresponding temperature. The resulting average f_{LM} are given in Table 12.

Table 12: Lamb-Mössbauer factors f_{LM} as obtained from the normalized, inelastic area of the investigated poisoned and initial catalysts.

	HT600HCl	HT600HCl+ SO ₃ ²⁻	HT800HCl	HT800HCl+ SO ₃ ²⁻
Temperature / K	50	40	48	48
f_{LM}	0.73	0.80	0.81	0.76

Introducing the anion through the catalyst results in a reduced Lamb-Mössbauer factor for HT800HCl. This is explained by the high mass absorption coefficient of sulfur for the 14.4 keV Mössbauer radiation of $\mu_e = 17.0$ cm²g⁻¹¹⁵¹. As shown by different authors^{165, 168, 171}, the temperature dependency of f_{LM} is not linear at the given range and cannot be easily extrapolated but is a possible explanation for the increase of f_{LM} found for the deactivated HT600HCl system. A significant drawback of using NIS to estimate f_{LM} is the fact that only a summed value of all iron sites is obtained, which is not very suited for a multi component system. Therefore, the evaluation of the Lamb-Mössbauer factor for the single sites like shown by Sougrati et al.¹⁶⁵ will be discussed in the following chapter. Beside the NIS and resulting pDOS data, the pristine and deactivated were investigated by NFS (Figure 40).

The anion changes the quantum beat behavior and therefore the valance state of the iron in the catalyst, but as described in 3.4.4 a full analysis is rather complicated due to the speed up characteristics of quantum beats and the possible overlay of components. Even under the assumption that the impact of the anion is identical for both pristine catalysts a straight forward interpretation as known for Mössbauer spectroscopy is not possible. Nevertheless, the anion impact entails an even more pronounced change as seen in the Mössbauer spectrum. The here present results are the first NFS investigation of Fe-N-C catalyst and show the promising capabilities of this technique.

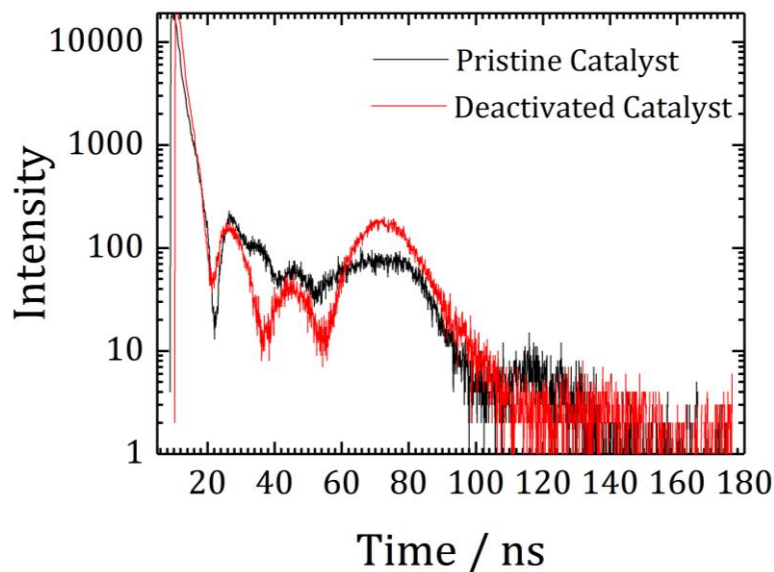


Figure 40: Change in NFS spectra by introducing the anion to the catalyst system. The pristine and deactivated catalyst HT600HCl is seen.

Beside the synchrotron-based analysis, LT-MS was performed for characterizing the impact of sulfite ions. In Figure 30 the LT-Mössbauer spectra of the pristine catalysts HT600HCl at 77 K with no applied magnetic field and at 4.5 K with applied external magnetic field of 5 T were already discussed. By introducing the anion, an additional sextet species appears (Figure 41). It was not possible to fit the spectra with an adequate model as the area of iron components cannot be satisfied assigned. The Mössbauer parameters (Table 13) of the new site make the assumption of a diamagnetic species likely. But the interactions of the introduced anion with other iron sites need to be further investigated as it is possible that the sulfite ion interacts with other iron sites. Therefore, additional experiments are necessary to elucidate the deactivation behavior.

In this chapter the effect of sulfite ions on the ORR activity and structural constitution of Fe-N-C catalysts were investigated for three differently prepared Fe-N-C catalysts. By using RDE measurements it was possible to show that those anions are able to deactivate the active iron site and result in a decreased electrochemical activity and the appearance of a new Mössbauer species⁵². Interestingly, other investigated salts showed only a neglectable impact to the Mössbauer parameters. Even though, the performance under RDE conditions decrease, the question of deactivation mechanism immediately arises for these salts. It is rather unlikely that a ligand can directly attach to the iron site and change the electronic structure in a way, that under RDE conditions, a decreased performance is observed, but the Mössbauer parameters left unchanged. It is known that the ligand field and the coordination chemistry can cause such a behavior, but so far, cannot be confirmed based on the given experiments. Similar to

our recent publication ²²³ it is possible that these salts do not interact directly with the iron site but change the chemical and kinetic boundary conditions of the FeN₄-site.

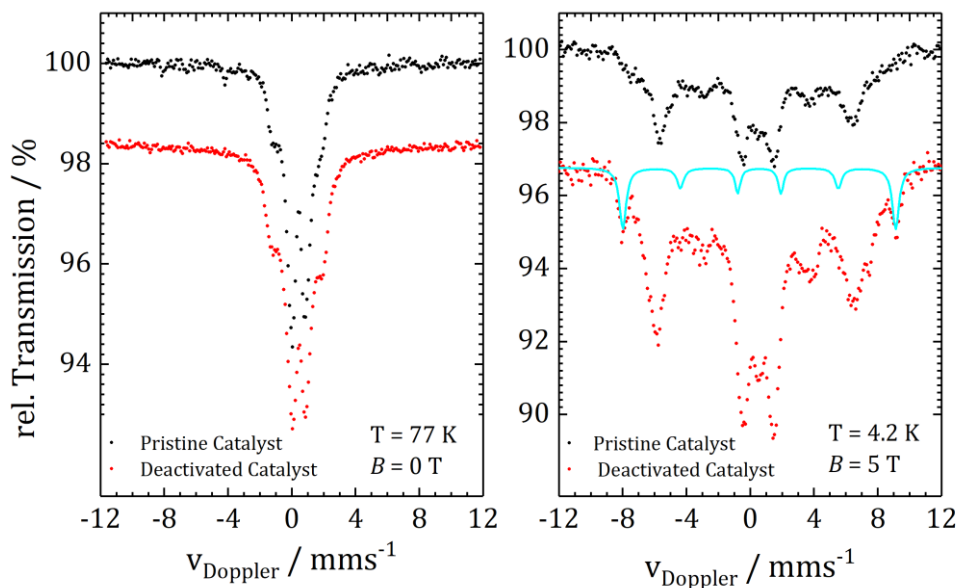


Figure 41: LT-Mössbauer spectra of the pristine and deactivated catalyst HT600HCl at 77 K with no applied external magnetic field. (left) The same catalysts measured at 4.2 K with a magnetic field of 5 T. The fitted deactivated species is given in cyan. (right)

Table 13: Mössbauer parameters of the deactivated species as found by LT-MS.

	HT600HCl+ SO ₃ ²⁻	HT800HCl+ SO ₃ ²⁻
$\delta_{\text{iso}} / \text{mm s}^{-1}$	0.56	0.47
$\Delta E_{\text{Q}} / \text{mm s}^{-1}$	0	0
B_{hf} / T	53	54

Room temperature Mössbauer measurements reveal an almost homogeneous composition with mainly FeN₄ sites for HT600HCl and HT800HCl catalysts and a small contribution of inorganic sites, were found by LT-MS. For HT800HCl inorganic iron species are more pronounced, whereas the addition of sulphur (HT800HCl+S) shows FeN₄ species and iron sulphide sites which eventually affects the interaction of this catalyst with the anion. To elucidate the overall effect of sulfide and sulfite species during catalyst preparation and/or electrochemistry on the performance of the catalyst, additional preparation routes and experiments are required and currently conducted in a master thesis project (S. Schmid 2021 Master thesis ESE). Further, the degree of deactivation induced by anion binding is different for porphyrin-based catalysts compared to the alternatively prepared, sulphur-added catalyst as observed by the changes in RT-Mössbauer spectra. The new doublet is assigned as an axial ligation of sulfite bonded over

oxygen to the centered iron and was determined by NIS and the related DFT calculations. Using LT-MS the new deactivated species is suggested as diamagnetic component but withdraw a full characterization. For all investigated catalysts the ORR active FeN₄-site is assigned to D1, and displays some catalytic activity even after introducing the anion. It is therefore difficult to say whether those anion-blocked sites are completely deactivated or significantly lowered in their turn-over frequency.

5.3. Post Mortem MEA Characterization

As pre-experiment for identifying the best conditions and expectations for the operando fuel cell testing a beamtime at ESRF was performed to measure SMS of a pristine MEA and two MEAs after performance in low temperature (80 °C) and high temperature (160 °C) operating fuel cell tests. The catalyst preparation and fuel cell tests were done by Markus Kübler as described in 4.3. In Table 14 the initial performance data in RDE of the used catalyst are summarized.

Table 14: Electrochemical characteristics as obtained from the RDE measurements.

U_{onset} / V	U_{hw} / V	$j(0.75) / \text{mA cm}^{-2}$	$j_{diff} / \text{mA cm}^{-2}$	$j_{kin} / \text{mA cm}^{-2}$	Information
0.8	0.65	-0.51	-5.41	-0.57	No 2 nd HT

The electrochemical performance of the catalyst is in good agreement with values reported in literature⁶⁹. Compared to the values indicated in Figure 25. The catalyst shows a less dominant D1-site in the Mössbauer spectrum, whereas the D2 and D3 sites are more pronounced (Figure 42 left).

A second heat treatment is usually applied after an acid leaching step to purify the catalyst, reduce inorganic iron sites and heal out defects. So, the relative number of active sites increase, even so the total number of iron sites decrease. As described in the previous chapter, small inorganic clusters can contribute to the doublet sites, not resolvable as independent species due to the fast relaxation of domains and similar Mössbauer parameters, in RT-MS. Indeed, the LT-Mössbauer spectra measured at 4 K of the prepared MEA (Figure 42 right) identifies three sextet sites that are assigned to inorganic iron species. They are addressed to α -iron (Sext1, pink), iron-oxide particles, showing a broad size and coordination distribution as visible from the large line width (Sext2, grey) and a third sextet, which fits best to iron-nitride species (Sext3, yellow) as described by Borsa et al.²⁵⁹ and Kurian et al.²⁶⁰. Due to the extremely broad line width and the resulting error, it cannot be clearly distinguished between an iron oxide or an iron hydroxide site. Indeed, a hydroxide site would be likely after the fuel cell treatment as the MEAs were under operation, whereas an oxidic species would be more likely for the untreated MEA and for the pure catalyst powder. Iron nitride in the form of a sextet was first reported in a Fe-N-C catalyst by Ferrandon et al.⁸⁶, whereas as doublet species was reported by Kramm et al.^{35, 39, 100, 110, 231}.

The origin in the different observations might be the different preparation approaches in the cited publications. A doublet might indicate a higher N/Fe ratio in the nitride ²⁶¹ or smaller particle size ²⁶². It is very likely that similar prepared catalysts show a similar distribution and number of different iron sites. The Mössbauer parameters of both, RT-MS and LT-SMS are given in Table 15.

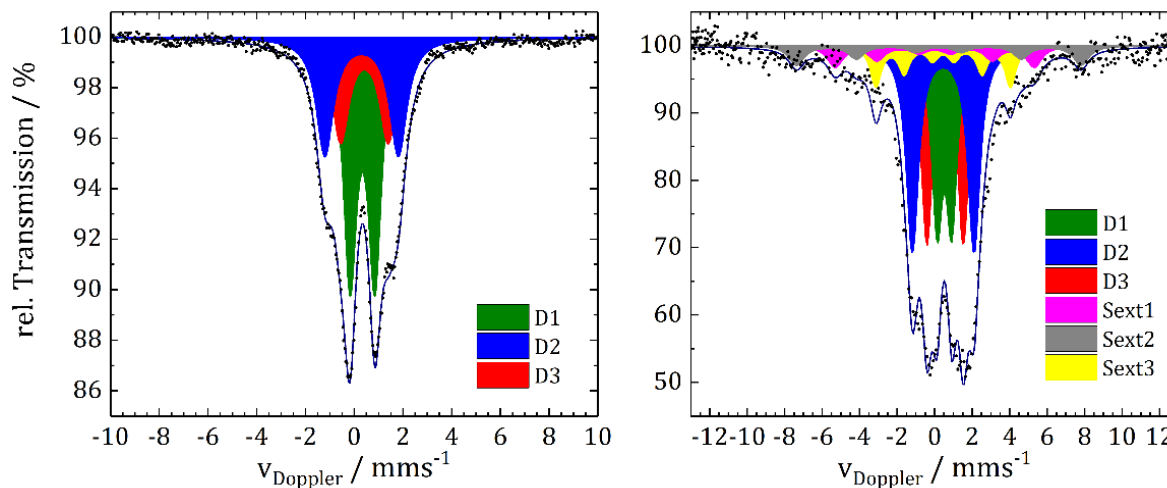


Figure 42: RT-Mössbauer spectra of the investigated catalyst powder with three organic iron sites. (left) LT-SMS spectrum of the prepared MEA at position C at 4 K. Beside the three doublet sites three inorganic sextet species appear. (right)

The fixation of Γ is often necessary to find a suitable fit model for the investigated catalyst. The broad half widths for e. g., the sextet species are the result of an undefined particle sizes distribution of the inorganic sites and normally avoided through a second or third heat treatment and an additional leaching step for purification. As described in chapter 4.1, LT-Mössbauer measurements with and without an external magnetic field, are able to slow down the particle relaxation time and enable their identification. However, a fixation of the line width is problematic for the fitting models for both RT-MS and LT-MS, as Debrunner ¹⁷⁹ figured out that especially for oxy-derivative ferrous low spin systems an anomalous line shape behavior is found, caused by non-stationary or disturbed electric hyperfine interactions. This results in an inhomogeneous temperature dependence of line width broadening for the LT-Mössbauer spectrum. The interpretation possibilities for RT-measurements were already discussed.

To find an adequate fit model all fitting parameters should be set free and the influence of the line width has to be considered. Indeed, the fitting of multi-component systems, as it is the case for most synthesized Fe-N-C catalysts, makes a free running fit model hard to invest, as it possibly results in a model without or wrong physical meaning. Fixing the line width seems the smallest error and is done by almost every group applying Mössbauer spectroscopy for Fe-N-C characterization. Nevertheless, it should be clear that fixing the line width can result in a misleading assumption of component area, isomer shift and quadrupole splitting. Comparing the RT-Mössbauer spectrum with the LT-SMS spectrum, almost half of

the D1 site contributes to the found sextets, whereas the other two doublet species are almost not affected. Again, this underlines the findings of the previous analysis and show the need of LT-Mössbauer investigation to distinguish between the organic and inorganic contributions to the D1 site.

Table 15: Mössbauer parameters of the investigated catalyst at RT.

	$\delta_{\text{iso}} / \text{mm s}^{-1}$	$\Delta E_{\text{Q}} / \text{mm s}^{-1}$	B_{hf} / T	$\Gamma / \text{mm s}^{-1}$	Area / %
RT					
D1	0.338 (0.002)	1.015 (0.005)	–	0.641 (0.008)	44.8
D2	0.303 (0.004)	3.017 (0.013)	–	0.858 (0.018)	29.6
D3	0.421 (0.004)	1.955 (0.012)	–	0.855 (0.053)	25.6
SMS-LT					
D1	0.524 (0.01)	0.777 (0.02)	–	0.68 ^{*1}	20.8
D2	0.459 (0.008)	3.291 (0.02)	–	0.79 [*]	29.4
D3	0.559 (0.008)	1.941 (0.023)	–	0.71 [*]	24.9
Sext1	0 [*]	–	33 ^{*1}	1 [*]	7.7
Sext2	0.225 (0.085)	–	47.2 (0.1)	1 [*]	7.0
Sext3	0.456 (0.035)	–	22.3 [*]	0.7 [*]	10.2

¹Parameters with * were set constant.

Beside the SMS measurements of the fresh prepared MEA, SMS was used to characterize the MEAs after fuel cell tests under high and low operation temperature. The experimental details are given in 4.3. In addition, each MEA were measured under applying an external magnetic field from 0.5 T to 5 T and position C was studied in detail to compare the different degradation characteristics of each MEA.

For the fresh prepared MEA (Figure 43, left) three different positions on the MEA were investigated by SMS to confirm the homogeneity of fabrication. As the measuring time and the cross section of the sample were similar for all positions, a spectra transmission of more than 50% is observed and a homogenous spraying of the catalyst layer being verified. The line shape model with site contribution of the fresh prepared MEA is given in Figure 42 and was already discussed. In Figure 43 (left, inset) the flow field position of each investigated piece of the untreated MEA is given.

By applying an external magnetic field perpendicular to the beam, the line shape of components changes (Figure 43 right) similar as for the discussed LT-MS investigation described in chapter 5.1., Figure 30. The straight lines in Figure 43 giving the position of the D3 site splitting. Indeed, the features are less pronounced as found for HT600HCL (Figure 30). Further, the spectrum at 5 T is much broader. The contribution of a variety of small iron and iron oxide particles as concluded from the fit model, results

in the observed line shape characteristics. Based on the less pronounced splitting of D3, it is assumed that the appearance of inorganic sites results in an undefined contribution, and an overestimation of the heme-like site. Again, the advantage of LT-MS or LT-SMS is underlined, as only both techniques are suitable to identify the overall composition of Fe-N-C catalysts.

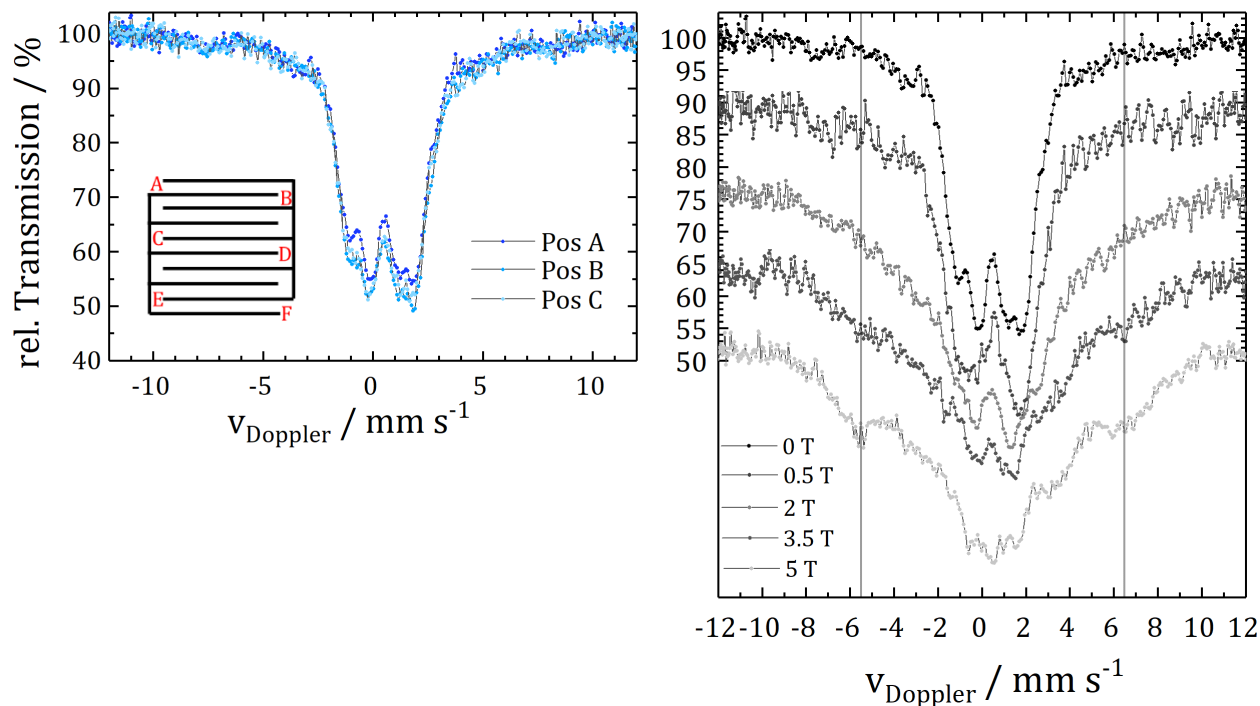


Figure 43: LT-SMS spectra obtained at 4 K of the fresh prepared MEA at three different positions. The insert gives schematically the flow field with the investigated positions. (left) Magnetic field dependent LT-SMS spectra at position C. (right)

After running the MEA for 24 hours at 0.6 V with a fuel cell operation temperature of 80 °C, a drop of the current density of 25% is observed (S 6). The inlet of Figure 44 (left) shows the four positions of LT-SMS investigations with the resulting spectra. Even though, the spectrum of position B seems different, the spectra line shapes are identical for all positions, whereas the total transmission varies. The difference results from the absolute cross section of each sample during the measurement and the leaching out of iron. Indeed, the total absorption decreases to an average of 35%. Especially α -iron seem to be removed, as it is washed out and oxidized, during the operation of the fuel cell. The inorganic site of Sext3 seems not to change but becomes more pronounced, due to the missing of Sext1. In Kramm et al.²²⁶, post mortem analyses of complete MEAs were investigated and the loss of iron sites due to leaching and carbon degradation processes were described. It was further shown that all organic iron sites are affected by demetallation. Indeed, in the here described case an increase of iron oxide site is explained mainly due to the conversion of α -iron to iron oxide or iron hydroxide, as well as demetallation of organic sites and agglomeration during operation. In Figure 44 (right) the magnetic field dependent measurements are given and underline the formation of iron hydroxide during fuel cell operation. At 5 T

an overlay of different sextets is found. As one site is assigned to iron oxide the second site, with a magnetic field of 52 T and $\delta_{\text{iso}} = 0.57 \text{ mm s}^{-1}$ has parameters typical for ferric iron in octahedral coordination of oxygen ($\delta - \text{FeOOH}$) as shown by Dézsi et al.²⁶³. From the magnetic field dependent measurements, it becomes apparent that applying a magnetic field of $\sim 3.5 \text{ T}$ or larger, will result in better resolved sextet lines. They split-up into a high field sextets with smaller linewidths and a more broaden sextet with lower magnetic field, indicates a variety of particle sizes²⁶⁴.

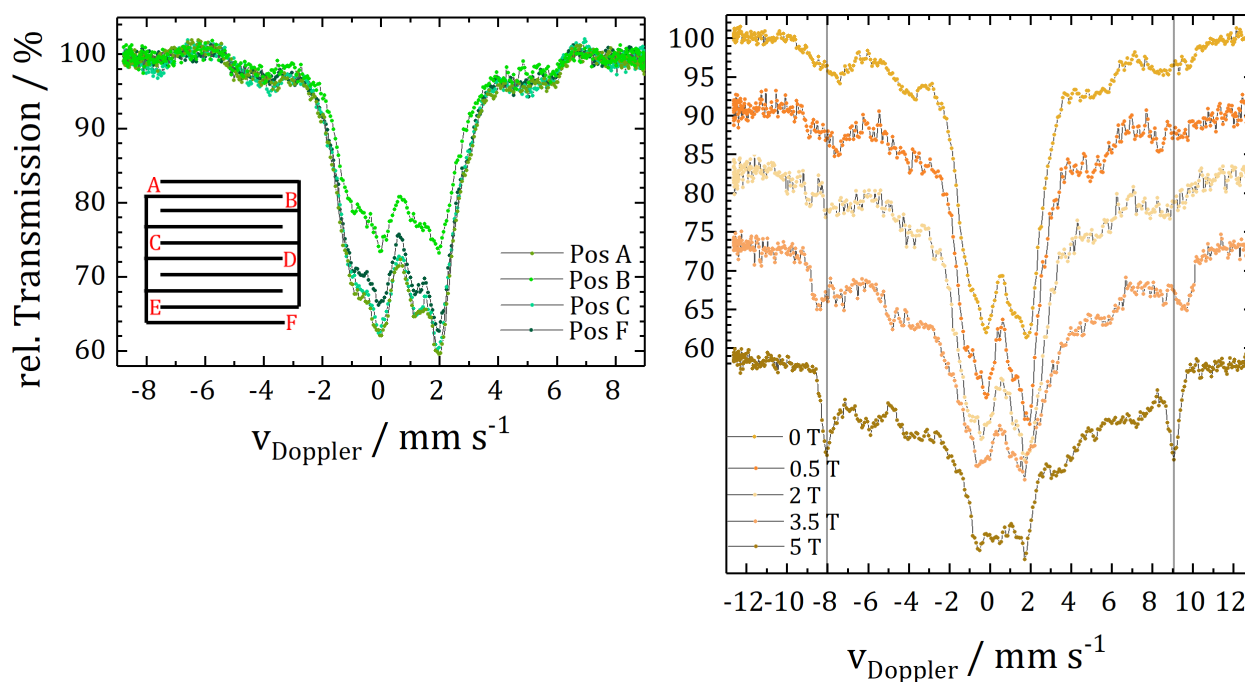


Figure 44: LT-SMS spectra obtained at 4 K of the low temperature treated MEA at four different positions. The insert gives schematically the flow field with the investigated positions. (left) Magnetic field dependent LT-SMS spectra at position C. (right)

The LT-SMS spectra of the high temperature operated MEA (Figure 45, left) show a completely different line shape characteristic as seen before. The operation temperature of $165 \text{ }^\circ\text{C}$ for 12 hours of operation at a constant potential of 0.6 V is far behind useful conditions for metal organic active sites as the high temperature result in a very fast degradation and a dramatic drop of performance during the fuel cell test (Appendix S 7). The position dependent measurements show a clear trend. The spectrum obtained at position A, has the lowest absorption (Figure 45, bottom) of all investigated positions. Further, the line shape of each position varies. Different sextet species are fitted into the spectra, containing iron oxide or hydroxide species. Whereas the doublet sites decrease to less than 10% of the previous area of each doublet. This dramatic decrease results in an almost deactivated MEA under operation with a net current close to zero. The remaining doublet sites have no or little direct access to the ORR as they are part of the bulk material and therefore, not able to participate during operation. Beside the change in line shape and the loss of active sites, the transmission of the single spectra is strongly affected by the

measurement position. Due to the harsh operation conditions, the catalyst shows a strong position dependency of demetallation. It becomes apparent that the degradation of the catalyst layer at the gas inlet is higher compare to positions closer to the gas outlet (Figure 45, left, bottom). As the higher concentration of oxygen results in a faster oxidation (burn) of carbon, the degradation and washing out of metal containing sites depends strongly on the oxygen supply. It is not clear, if most of the leached iron ions have left the fuel cell or stay inside the membrane or GDL even though the relative transmission strongly decreases for the HT-MEA which can only be explained by the loss of iron out of the matrix. The different line shape characteristics observed at each position is explained by further ion or particle migration. The iron ions seem to move, agglomerate and react during the way through the flow field until they leave the fuel cell system. Due to the higher operation temperature the catalyst becomes faster degraded compared to the lower temperature operated MEA. The resulting degradation products are the same but the amount changes over time. As seen in the Pourbaix diagram^{265, 266}, Fe(II) ions have a significant solubility at a potential of 0.6 V and acidic pH-value. As the soluble iron Fe(II) ions are not bounded in a lattice, Mössbauer spectroscopy cannot be used for detection of free ions as the recoil free absorption and emission will not be possible. Whereas, iron oxide/hydroxide particles are detected and found after fuel cell operation. The formation of hydroxide species seems only stable in a very narrow window in the alkaline regime. Nevertheless, the Mössbauer parameters found by LT-SMS make the existence of those species likely. It is possible that iron ions got trapped in the pores during operation and reacted to hydroxide species after the fuel cell was shot down. As discussed in chapter 3.2, Figure 5 hydroxy species are part of the ORR reaction, even though they do not exist as Fe(OH₂) or FeOH⁺ in the catalyst layer but bond to FeN₄ centers.

By the direct comparison of the different treated MEAs (Figure 46) the influence of operation time and temperature become obvious. Under high operation temperatures the degradation of the catalyst layer is much faster compared to the low operation conditions of 80 °C. As expected, the loss in peak power density was higher for HT-operation conditions (−40%) compared to LT-operation condition (−25%) although the time of operation was only half.

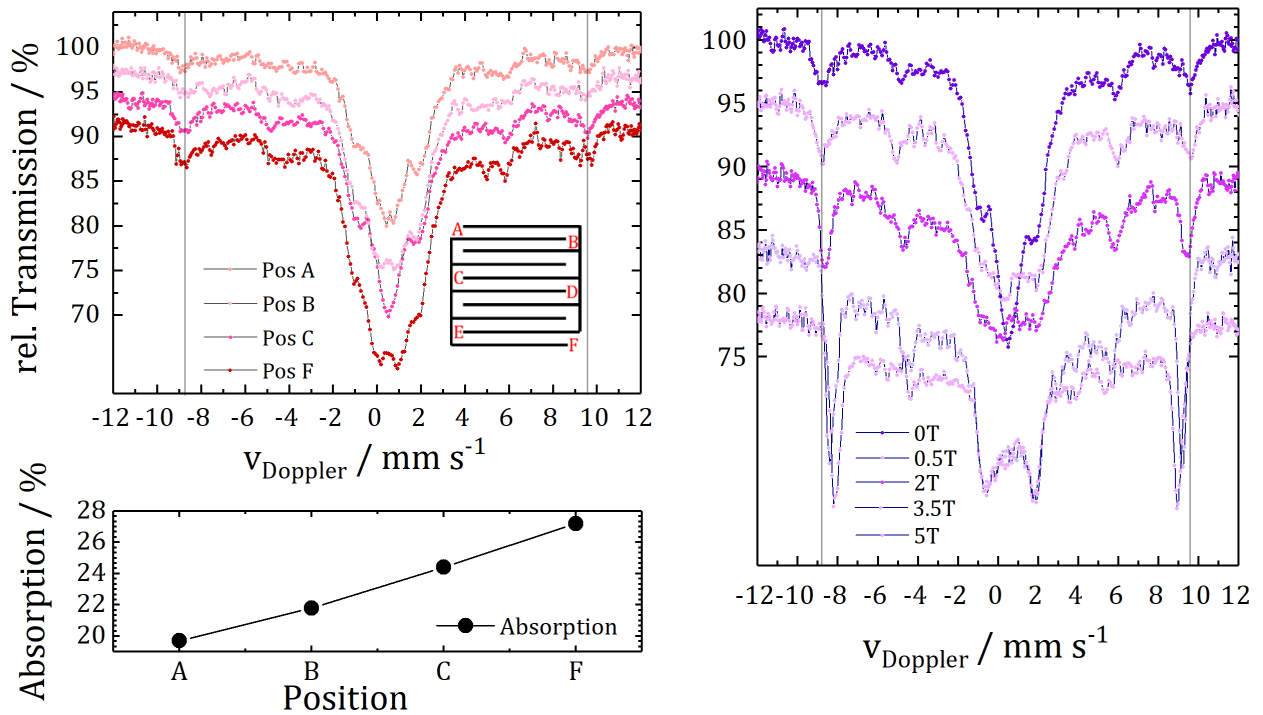


Figure 45: (left) LT-SMS spectra obtained at 4 K of the HT-PEM MEA at four different positions. The insert gives schematically the flow field with the investigated positions. (bottom) the resulting loss of absorption for each position. (right) Magnetic field dependent SMS LT-Mössbauer spectra at position C.

From the line shape characteristics of the LT-SMS measurements it is assumed that the resulting degradation products are similar while the dynamics are different. The appearance of a superparamagnetic phase (singlet in the LT-SMS measurement without external magnetic field) is a result of particle migration of iron particles through the MEA during operation. This assumption is plausible as it is very likely that agglomerates of iron are formed during the demetallation process and further react under operation and become additional oxidized after the fuel cell is shutdown.

In summary, the post mortem analysis of MEA operated at different fuel cell temperatures indicate that the relative absorption area (related to iron content) and – more important – the shape of the spectra (related to changes of iron species) varies for high- and low-temperature treated MEAs. It is confirmed that the degradation of the catalyst layer depends on the related position. Catalyst layers which are closer to the gas inlet show a stronger degradation as at positions closer to the gas outlet. This is explained by a faster oxidation of the carbon and a faster demetallation due to the operation temperature and the applied potential as well as the higher concentration of reactive species. The formation of oxides and hydroxides is verified caused by the demetallation and oxidation of iron sites.

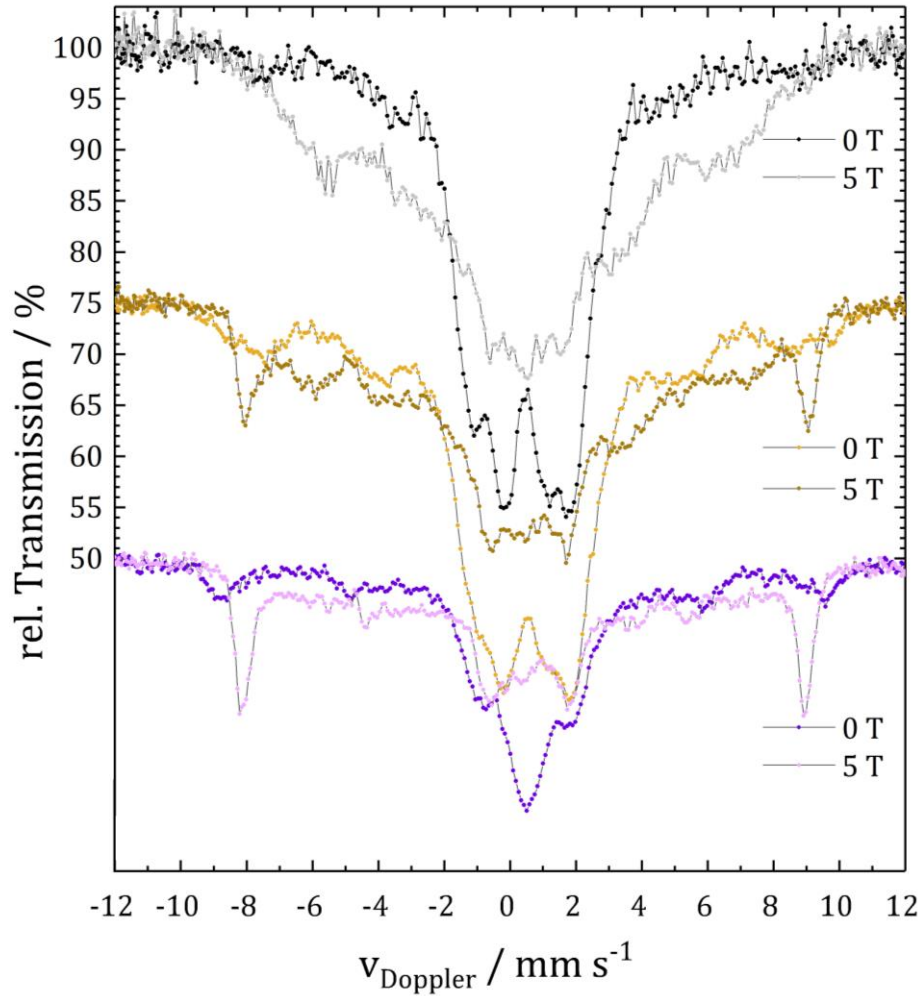


Figure 46: Direct comparison of the different MEAs measured with LT-SMS. Untreated MEA at 0 T (black), MEA with applied magnetic field of 5 T (grey). MEA after fuel cell test at low operation temperature (orange) and with applied magnetic field (dark yellow). MEA treated at high operation temperature during fuel cell operation without magnetic field (purple), whereas the field depend Mössbauer spectrum is given (rose).

Beside the post mortem analysis the low temperature treated MEA was investigated by temperature depended Mössbauer measurements similar to the work of Sougrati et al.¹⁶⁵ to gain additional information about the temperature dependency of isomer shift (δ_{iso}), quadrupole splitting (ΔE_Q) and species area change at different measuring temperatures, respectively. In Figure 47 the temperature dependent SMS spectra with related fittings are given. The measurements were prepared without applying an external magnetic field and the related Mössbauer parameters are summarized in Figure 48, whereas the changes of corresponding spectral area sites are visualized in Figure 49.

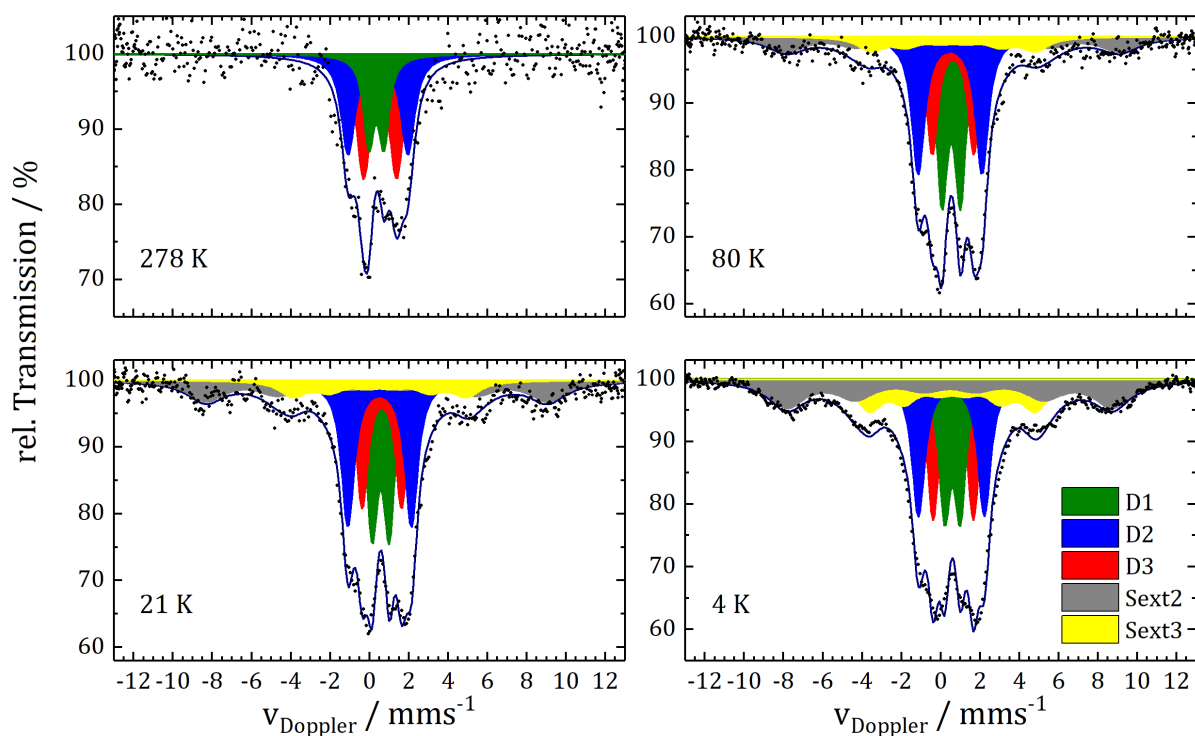


Figure 47: Temperature depend SMS measurements of the sample for four different temperatures are shown.

The temperature dependency of isomer shift and the change of corresponding spectral area sites over the temperature range is seen in Figure 47. By decreasing the temperature, from 278 K to 80 K iron oxide (Sext2, grey) and iron nitride species (Sext3, yellow) appear. These species become more pronounced by decreasing the temperature to lower values. At 4 K a relative surface area of 23.9% and 18.3% for Sext2 and Sext3 is found, respectively. The existence of iron oxide is explained by the synthesis's procedure of the catalyst powder, as well as demetallation and oxidation of iron sites during fuel cell operation, whereas the increase of iron nitride species is not clear. From the kinetic point of view iron oxide should be the preferred species after demetallation inside the fuel cell, as verified by LT-SMS measurements of the high temperature treated MEA and the discussed kinetics by Graat et al.²⁶⁷ and Nishimaki et al.²⁶⁸. It is unlikely that iron nitride is formed during operation. However, it is possible that the resulting carbon corrosion during operation explains the finding, as FeN_xC -sites are washed out and agglomerate. Further, it is possible that the iron nitride content decreases in the same way as discussed by Kramm et al.²²⁶ but overlap with other, mainly oxide containing species, due to the very broad assumed line width and result in a misleading interpretation.

It is important to mention that for all investigated fittings the line width was fixed. This was done because the multi component fit would otherwise result in an unphysical fitting model. Especially ferrous low spin sites like oxy-derivatives come up with a non-stationary or distributed electric hyperfine field which

result in an anomalies line shape behavior and in an inhomogeneous temperature dependency of the line width Γ and a distribution of quadrupole splitting¹⁷⁹. The appearance of sextet sites and the relative similar doublet sites, make reasonable fittings even more complex as the degree of freedom increases. To give reliable border conditions for the fittings the line width for D1, D2, D3 Sext2 and Sext3) were set constant to 0.68, 0.79, 0.71, 2.2 and 1.6 mm s⁻¹, respectively. Especially the line widths for the sextet sites are unusual broad due to the existence of different particle sizes and species sites distribution, formed during fuel cell operation and summed up in only two iron containing sextet species. Sougrati et al.¹⁶⁵ found for their temperature dependent ⁵⁷Fe Mössbauer investigation an increase of Γ by nearly 30%, going from room temperature down to 5 K. A similar behavior was found for the described D2-site. Even though, the given Γ for the lowest temperatures are extremely high and make the contribution of a further doublet site very likely, but were not suggested in their work. Unfortunately, the line width was not reported for all found iron sites by the group, therefore no further temperature dependencies of the line width relation are possible. In addition, one vulnerability of their work is the assumption of pure species sites. As described in the present work, even under very mild preparation condition relaxed oxide and iron clusters exist and partly contribute to the found doublet sites even after an addition acid leaching step. It is only possible to identify those sites by using LT-MS or LT-SMS with applying an external magnetic field as the fast relaxation of domain sites would otherwise result in a collapse of Zeeman-splitting and an overlap of different sites. This was not done by the authors and therefore a multi-site contribution cannot be excluded.

For ferric, Fe(III) high spin sites like the discussed heme site (D3) a temperature dependency of quadrupole splitting, due to the thermal admixture of different orbital states, caused by the crystal field is found. In general, a fivefold coordination with a substantial displacement by the iron, out of the porphyrin plane, towards the axial ligand, is observed. In case of a six-fold coordination a weak ligand field appears¹⁷⁹. Instead, ferrous low spin sites are diamagnetic and the iron is normally centered in the porphyrin plane. If a fivefold coordination appears, a displacement towards the axial ligand is observed, whereas if a six-fold coordination appears, two weak axial ligands are bonded. By decreasing the temperature of the sample, the magnitude of quadrupole splitting decreases too.

Oxy-heme proteins like the discussed D1 sites show an anomalous Mössbauer behavior compare to other ferrous low spin iron porphyrins. Beside the mentioned line shape characteristic, the magnitude of quadrupole splitting decreases by decreasing temperature¹⁷⁹. Indeed, the quadrupole splitting in a diamagnetic compound is generated by an asymmetric covalent bonding. The electronic configuration and orbital occupation are not sensitive to temperature as the first excited electronic level is not accessible by thermal activation. Therefore, the quadrupole splitting should not be affected by temperature. For paramagnetic compounds a substantial degree of thermal excitation electronic levels exists and thermal excitation by a change of $k_B T$ is possible¹⁷⁵. Even with the view data points provided

herein the published trends are confirmed for our catalyst in Figure 48. Here, the temperature dependency of the isomer shift for D1, D2 and D3 is found, whereas the quadrupole splitting is only slightly affected as found by Sougrati et al.¹⁶⁵. It is clear, that the lack of data points, the fixation of line width and the similarity of iron sites, result in observations which can only give trends but is not suitable for giving precise values.

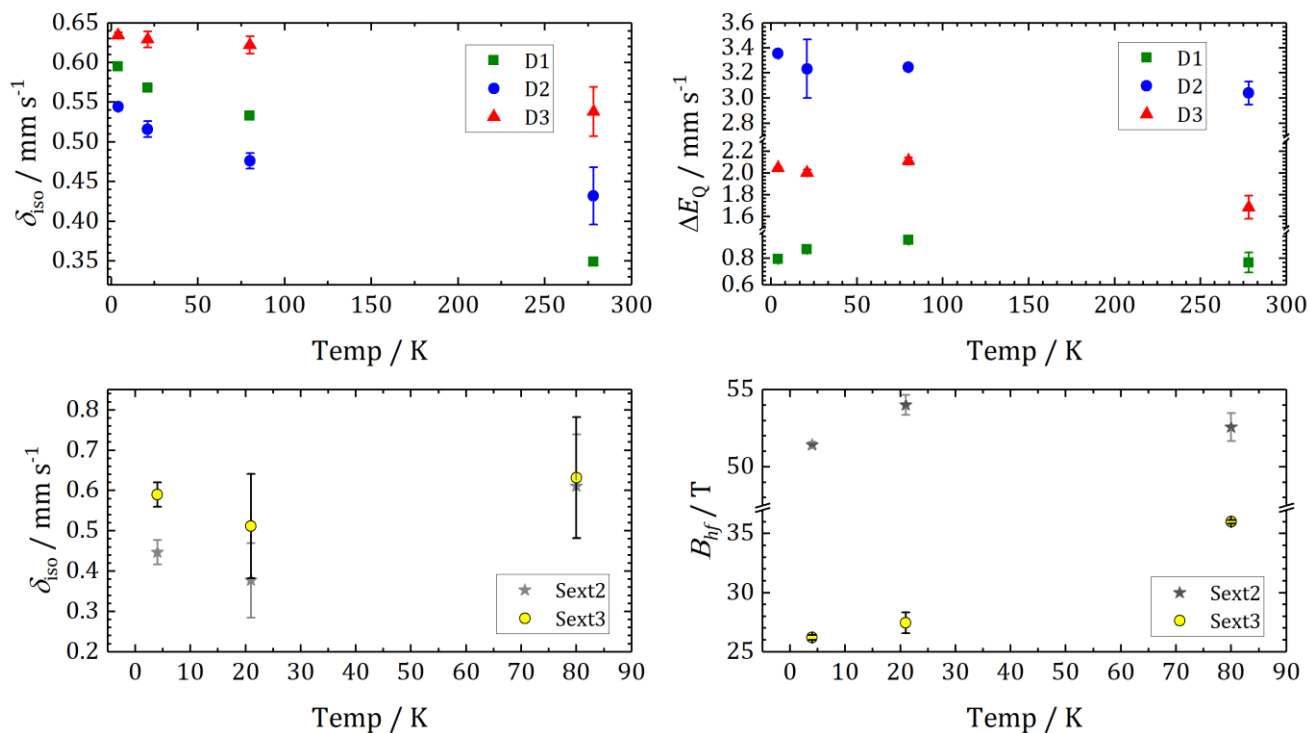


Figure 48: Temperature dependence of isomer shift (δ_{iso}) from the found doublet species (left, top), whereas the temperature dependence of the quadrupole splitting is depicted (ΔE_Q). (right, top)

Comparing the change of surface area for the different iron sites over the temperature shows a decrease of the D2 and D3 with an increase of the sextet species (Figure 49). The area contribution for the D1 site increases from room temperature till 80 K to 24% and decreases to 16% at 4 K. From this point it is not clear if this is caused by the temperature dependency of the isomer shift or the fitting model.

Herein, it is necessary to go for a very pure catalyst system, were in best case only the active iron species exist. Even though, the catalyst would be less active, the mechanism and the species site are more defined. Caused by the temperature dependence of f_{LM} reasonable values can only be determined by a high number of measurement points, as small variations of θ_M result in a significant error of f_{LM} .¹⁶⁸ (Figure 50).

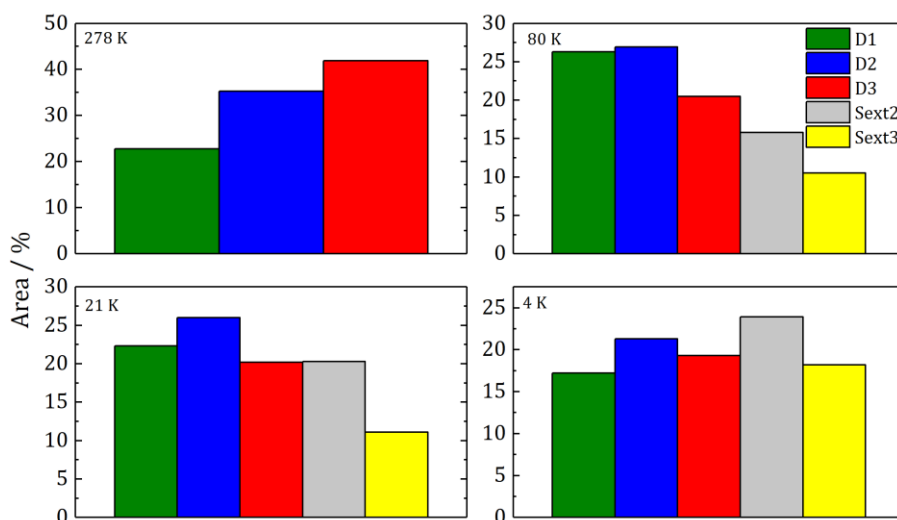


Figure 49: Temperature dependency of the relative species area. The value of the relative species area is given on the vertical-axis in percent.

Further, the contribution of the sextet species to the doublet sites is not clear. Therefore, a defined assignment of the species cannot be made. The calculation of θ_M would result in meaningless f_{LM} -values. In Figure 50 (left), f_{LM} was calculated using θ_M values for the D1 and D2 site as found by Sougrati et al.¹⁶⁵. Here, the dashed lines representing the temperatures of the related measurements. From this, two conclusions can be made. Metallic systems show a high θ_M between $300 \leq 10^3$ K, whereas for metallic-organic complexes and iron proteins θ_M is normally in the range of 100 – 200 K¹⁵¹. This finding is in good agreement with the given data. It is not appropriate to use one and the same f_{LM} for two different systems, even though they might be similar. The Lamb-Mössbauer factor is a system specific parameter of the investigate iron site and influenced by the bonding forces to nearest neighbors. Due to the inhomogeneous character of Fe-N-C catalysts and the dimensional structure with covalent bonding forces to the nearest neighbor atoms, it is not appropriate to assume similar vibration masses. Herber²⁶⁹ pointed out that those systems show an effective vibrating mass different from the mass of the iron site. For the calculation of f_{LM} an effective mass $M_{\text{eff}} = 57$ (^{57}Fe) was used. To reveal more reliable values for M_{eff} of the different iron sites (with $M_{\text{eff}} > 57$), the temperature dependent second order Doppler shift should be considered¹⁵¹.

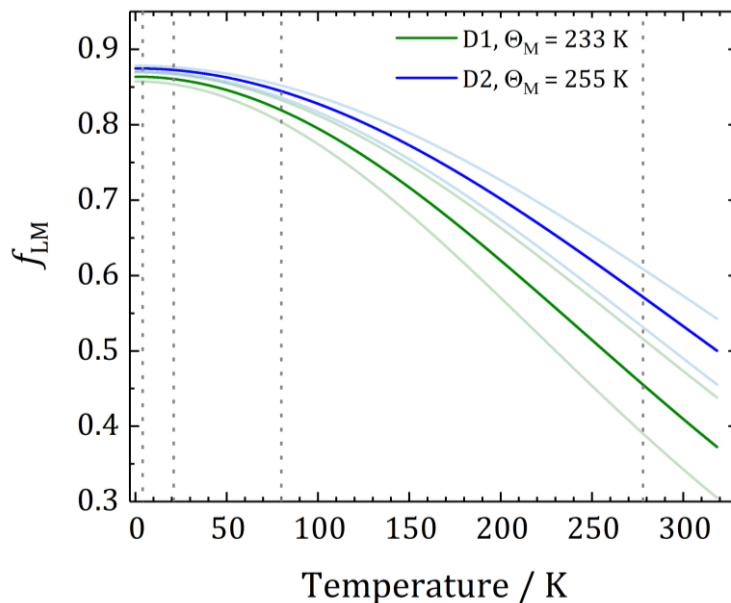


Figure 50: Temperature dependency calculated with θ_M values and related errors as published by Sougrati et al. ¹⁶⁵.

In general, it is possible to calculate the temperature dependent second-order Doppler shift (δ_{SOD}) from the values given in Figure 48 (left, top) by using equation (36). Due to the mentioned accuracy of data, reliable information will not be obtained as the signal to noise ratio result in a high error of fitting parameters and therefore, in a misleading interpretation. Nevertheless, the possibility to investigate the specific values of f_{LM} , θ_M and M_{eff} of the related iron site will push the understanding of Fe-N-C catalyst forward. Therefore, it is important to improve the catalyst purity and invest high resolution temperature dependent synchrotron based Mössbauer measurements. So, information about the vibrating mass and additional, about the ligands are able to gain.

In this section, three different MEA's were investigated at different local positions with LT-SMS. It was proven that a higher operation temperature results in a faster degradation of the catalyst, found by the formation of oxide- and hydroxide iron sites and the measured performance loss. The out washing of iron, is caused most likely by carbon corrosion and the destruction of the carbon matrix. Additionally, the magnetic field dependent measurements at low temperatures show a position dependent degradation during operation and the agglomeration of iron oxide- and hydroxide sites in the MEA's. The investigation of temperature dependent measurements to illuminate the specific values for f_{LM} , θ_M and M_{eff} was assumed but not able to implement due to the low number of data sets and quality.

5.4. Operando Fuel Cell Setup for Synchrotron based Nuclear Resonant Techniques

Electrochemical experiments like RDE are very helpful to get an impression of the catalytic activity but do not ultimately represent its properties under real fuel cell conditions. For example, it is well known that a fuel cell catalyst which performs very well in an RDE experiment can show the opposite behavior in a fuel cell⁴⁰. Catalysts that provide very good stability in RDE durability tests are poorly stable under FC operation. Due to the different operation conditions in an RDE and fuel cell setup, the impact of mass transport mechanisms, conductivity, layer properties, temperature and pressure can result in a different performance. Therefore, it is very important to use fuel cell tests for characterizing the performance of any catalyst under real operation conditions. Similarly, the degradation of active site or the mechanism of ORR could possibly be affected by the change in condition. To get a first impression of the porphyrin-based reference system, Mössbauer spectroscopy was performed for the origin catalyst powder, the sprayed GDL and after the fuel cell test (Figure 51).

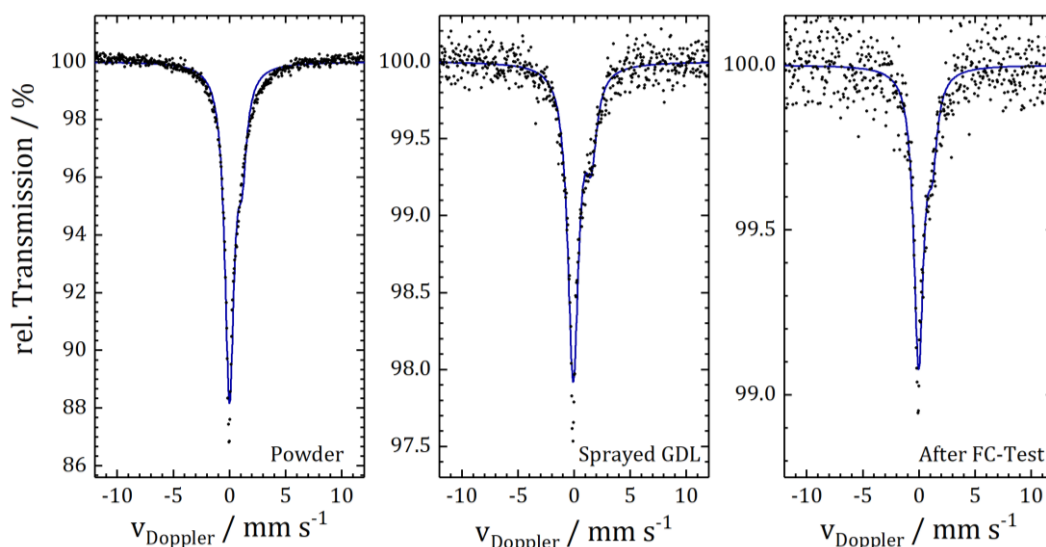


Figure 51: RT Mössbauer spectra of the porphyrin (FeTMPPCl/CB) based reference system (left), the freshly sprayed GDL with FeTMPPCl/CB (middle), and Mössbauer spectrum after the fuel cell operation in the standard fuel cell test station ($t = 2 \text{ h } 20 \text{ min}$) (right), are given.

An asymmetric doublet, well known for porphyrin systems^{212, 230, 270} is seen in the Mössbauer spectra. The asymmetric line characteristic of the high-spin Fe(III) porphyrin is caused by spin-spin relaxation effects as a consequence of the large zero field splitting for such ferric porphyrins^{186, 271}. At room temperature the relaxation times of the two excited states are different, while the population remain the same. Based on this, an asymmetric doublet is found. Here, the amplitude of the first line was set to 1 and of the second line was set to 0.2. As described by Hambright et al.²⁷² a symmetric quadrupole doublet is only observed at temperatures below about 10 K. Whereas, above this temperature, the lines show

equal absorption areas, and widths approach the ratio 3 : 1 as seen in Figure 51. The resulting Mössbauer parameters are given in the following table.

Table 16: RT Mössbauer parameters of the porphyrin (FeTMPPCl/CB) based reference system and at different preparation steps.

	$\delta_{\text{iso}} / \text{mm s}^{-1}$	$\Delta E_Q / \text{mm s}^{-1}$	$\Gamma / \text{mm s}^{-1*}$	Area / %
Powder	0.351 (0.007)	0.807 (0.006)	0.365 (0.003)	100
GDL	0.364 (0.043)	0.981 (0.043)	0.378 (0.013)	100
AF FC	0.404 (0.026)	0.973 (0.024)	0.425 (0.033)	100

*Values are given for the dominant line

The strong decrease in absorption seen from the powder (12%) to the MEA after the fuel cell test (1%) is obvious. Here, the different sample thicknesses have to be considered as the overall change is not directly related to the loss of iron sites during operation. Indeed, in Kramm et al. ²²⁶, it was shown that induced by the preparation steps with NafionTM for GDL and MEA fabrication, the absorption was tremendously lowered. The thickness of the powder sample is 3 mm with an overall of 158.1 mg sample mass, whereas for the GDL measurement, three prepared GLDs were laid above each other to increase the total iron amount during the measurement ($3.5 \text{ mg cm}^{-2} \times 3$ of catalyst loading) as well as the signal to noise ratio and foreshorten the measuring time. In case of the measurement after the fuel cell test, the whole MEA was used (3.5 mg cm^{-2} catalyst loading + anode and membrane) which causes an additional absorption. The related fuel cell polarization curve was recorded in H_2/O_2 and is given in Figure 52 (left). More interesting are the changes in Mössbauer parameters (Table 16). For the GDL, an increase in quadrupole splitting from 0.807 mm s^{-1} (powder) to 0.981 mm s^{-1} is found. For the MEA after fuel cell (AF FC) operation, almost identical parameters are found compared to the GDL, which is caused by the interaction of NafionTM and the catalyst.

It is well known that carbon supported porphyrins reveal some ORR activity but are not very well suited as fuel cell catalysts because of their low stability. Nevertheless, their well-defined characteristics are assumed to enable a good starting point and thus an easier interpretation of NFS results. The direct comparison between the porphyrin model catalyst in the standard and operando fuel cell setup is given in Figure 52. The catalyst loadings for both fuel cell tests, were 3.5 mg cm^{-2} for the cathode, whereas for the anode $0.14 \text{ mg}_{\text{Pt}} \text{ cm}^{-2}$ were used. In the standard setup (Figure 52, left), an OCP of 0.72 V and a power density at 0.6 V of 4.07 mW cm^{-2} is found. Using the porphyrin-based reference in the operando fuel cell (Figure 52, right) the curve behavior looks similar. The OCP reaches 0.74 V, but the power density at 0.6 V is with 3.90 mW cm^{-2} slightly lower. The discrepancy in performance is far smaller for this worse performing reference material in comparison to the Pt-Pt MEA. This could indicate, that the

negative effect of hindered mass transport does not apply as much, as in any way the current densities are only low in this potential regime. The drop in performance becomes then specifically visible in the higher current density regime. As discussed in chapter 3.3.2, Figure 9, deviations of the OCP from the standard potential of the ORR are mainly caused by parasitic loss reactions. It seems, due to the lower OCP for the porphyrin system, that these losses are not as pronounced compare to the Pt-system in the cell. Indeed, the cathodic losses and the ohmic resistance losses are the dominant losses in the region of ohmic polarization but not in the region of activation. Whereas in the ohmic polarization region, the setup parameters have a big impact on the cell performance and result in a reduced maximum power point for both catalysts investigated in the operando setup. As activation losses are dominated by reaction rate losses the setup itself has only a minor portion on these losses. Further, the OCP is affected by the wetting behavior of the MEA and the accessibility of reactants. Both parameters can differ as the flow field design is not comparable, as discussed before. In both setups the region of concentration polarization is not reached as the cell was automatically shut down before by the setup, due to possible cell damages by reaching low cell voltages. Herein, it is concluded that gas transport losses are not crucial for this model catalyst measured in the standard and operando fuel cell setup. The comparison of the standard fuel cell and the custom-made operando setup shows that the operando fuel cell provides similar functionalities in the investigated potential range and is therefore well suited for operando fuel cell investigations.

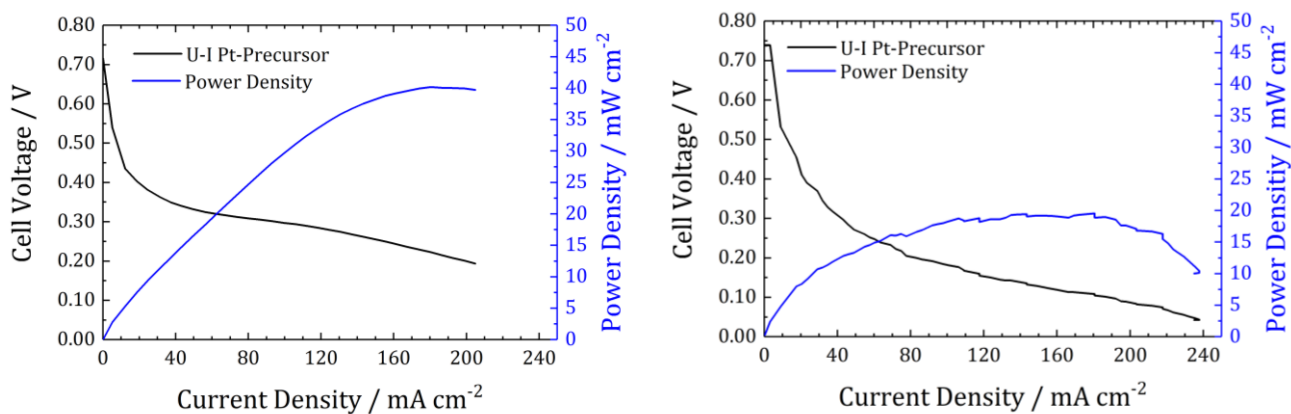


Figure 52: Standard fuel cell measurement of the porphyrin-model system as obtained in the SCRIBNER Associates Inc. setup (left). Operando fuel cell measurement recorded during the beamtime (right). Experimental conditions for the standard setup: H₂/O₂, cathode loading 3.2 – 3.5 mg cm⁻², N212 membrane, 1 bar gauge back pressure, 0.2 L min⁻¹ oxidant and fuel flow, cell temperature 80 °C, 100% relative humidity, whereas for the operando cell, the temperature of the pipes were set to 75 °C to avoid condensation inside the cell. All other conditions were kept the same.

The normalized NFS spectra of the porphyrin-based model catalyst powder, GDL and after the fuel cell test measured at the P01 beamline at DESY are given in Figure 53 (top), whereas the related NFS spectra recorded under operation conditions in the operando fuel cell setup, are given in Figure 53 (bottom).

Nuclear forward scattering (NFS) is a time domain sensitive technique with a spectral line shape not comparable with an energy recorded spectrum like obtained by Mössbauer spectroscopy. Based on this, the obtained data of e.g., two Mössbauer sites are not simply their sum curve as discussed in 3.4.4. Thus, the detailed knowledge of the number of contributing iron environments and their related Mössbauer parameters are required to fit a reliable model. At the current stage, this information is only limited available for the reference system and Fe-N-C catalyst. Therefore, the data interpretation of the NFS spectra will mainly be made qualitatively, to see if distinct changes appear by a variation of the conditions, or not.

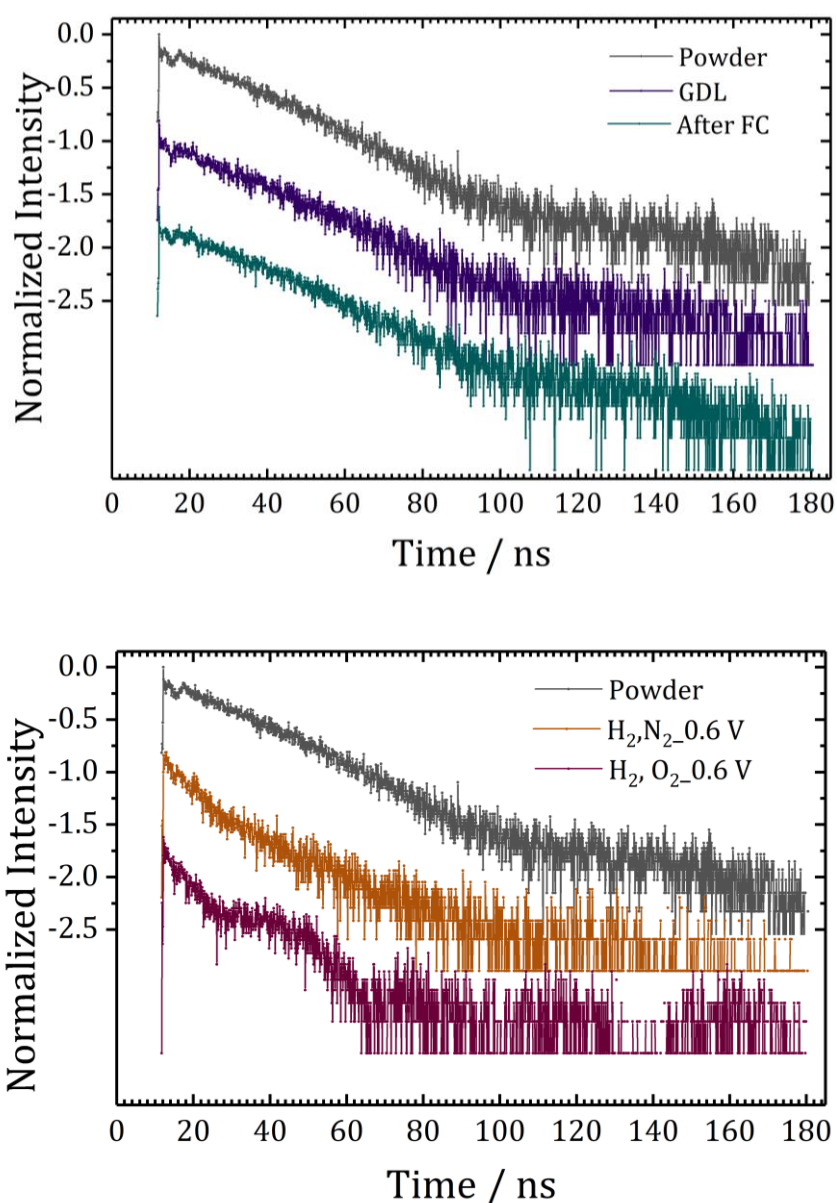


Figure 53: NFS spectra of the porphyrin-based model catalyst powder, GDL and after the fuel cell test (top), and recorded under operation conditions in the operando fuel cell setup at the P01 beamline at DESY (bottom). Given intensity values reflect logarithmic plots of normalized data.

As for the powder sample, the GDL and the sample after fuel cell test, the Mössbauer spectra are available. In the NFS spectra a fast decrease in intensity is found for all three conditions, without a significant contribution of resolved quantum beats. Only the slope of the NFS spectrum changes due to the hyperfine splitting of the nuclear levels which result in a quantum beat modulation of the spatially coherent decay rate. The porphyrin model catalyst shows a high asymmetry in the line shape which looks more like a broad singlet in the Mössbauer spectrum. The similar Mössbauer characteristic results in almost identical NFS features for the three samples.

Going to reaction conditions (~ 0.6 V) the NFS spectra obtained in H_2/N_2 and H_2/O_2 are compared in Figure 53 (bottom). Whereas, the averaged potential and current density that were applied for the two conditions are given in Figure 54. Under H_2/N_2 condition (Figure 54, left) the current density was 0.20 ± 0.12 mA cm⁻² with $U = 0.553 \pm 0.01$ V, while during H_2/O_2 condition (Figure 54, right) the current density was 13.05 ± 1.3 mA cm⁻², at the same potential. For the investigated catalyst system all preparation steps are analyzed by both, Mössbauer spectroscopy and NFS as it will be discussed later. As expected, under wet conditions in the operando setup, the slope of the NFS spectra is different from the powder or GDL system, where a linear slope is seen, the slope of the wetted cell at ~ 0.6 V under H_2/N_2 looks more like the exponential slope of the fresh prepared MEA with a less strong gradient. The investigated conditions under H_2/N_2 show, only little impact on the porphyrin model catalyst in the fuel cell. The small variations in both potential values under H_2/N_2 vs. H_2/O_2 condition could indicate that still to some extent, gas residuals of either O_2 (in case of H_2/N_2) or N_2 (in case of H_2/O_2) remained in the system. Most likely, trapped and stepwise released from the humidifiers. Due to the very limited time at the beamline, long purging times during the gas changes were not possible to be realized, but should be considered for future beamtimes.

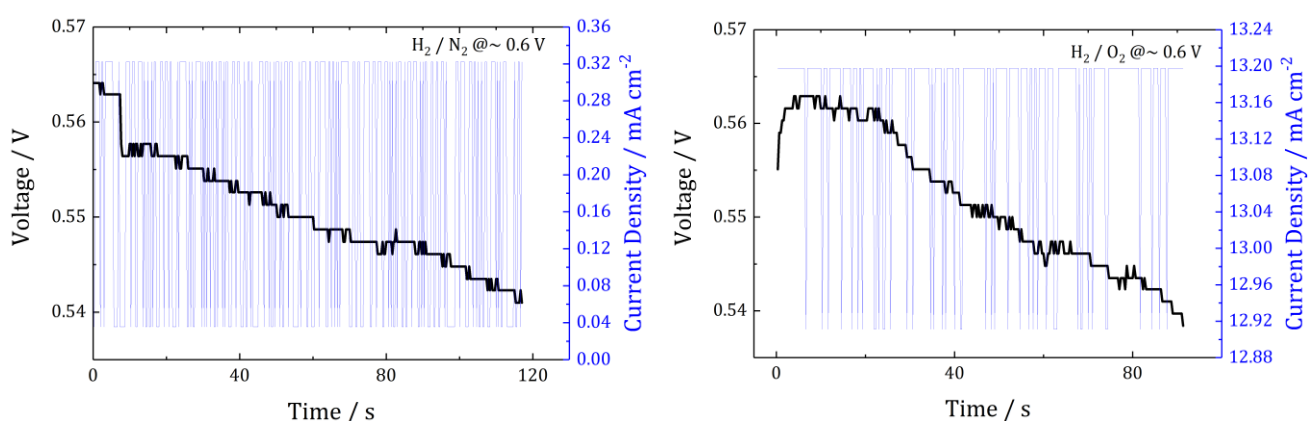


Figure 54: Averaged potential and current density that were applied during the recording of the NFS spectra. Under H_2/N_2 (left) and H_2/O_2 conditions (right).

By changing the gas supply from nitrogen to oxygen and applying a potential of 0.6 V, the oxygen reduction reaction changes the NFS spectrum and a defined quantum beat signature becomes visible. This is the direct proof of the ORR using a porphyrin model catalyst in an operando fuel cell setup, investigated by NFS. The successful experiment underlines the power and possibilities given by synchrotron based resonant techniques in combination with real performing setups. So far, it was not possible to see the ORR under real operation conditions in a fuel cell system.

Another big advantage is the high-count rate and the short measuring time in comparison to Mössbauer spectroscopy. Based on this, a fast measurement of the catalytic reaction without the impact of degradation processes - as it is the case for a long-term measurement over several hours - is possible. The found quantum beat has a periodicity of ~ 40 ns and assigned to quadrupole species. Here, the lack of Mössbauer reference data for similar conditions, hinder a further analysis, as at this stage it is not clear if only one or two doublet species arise. Nevertheless, it is proven that the local environment of the model catalyst changes during fuel cell operation and underlines the participation of the iron center during ORR. Thanks to the first NFS simulations calculated by V. Potapkin a fit with two new possible sites with isomer shifts of $\delta_{\text{iso}} = 0.46 \text{ mm s}^{-1}$ and $\delta_{\text{iso}} = 0.35 \text{ mm s}^{-1}$ and quadrupole splitting's of $\Delta E_{\text{Q}} = 2.60 \text{ mm s}^{-1}$ and $\Delta E_{\text{Q}} = 3.64 \text{ mm s}^{-1}$, respectively, were indicated under ORR conditions. and make the appearance of a Fe(II) in the intermediate spin state and a Fe(III), low spin species likely. The resulting fittings of the NFS are given in the supplementing Figure S 8, whereas the simulated Mössbauer fits and parameters are given in Figure S 9 and Table S 3 but need to be used with caution due to low statistics of the measurement. As the NFS fitting approach under H_2/O_2 condition shows a discrepancy from the middle-time range onwards due to low statistics, it is necessary to increase the measuring time. Further, the adjusted time window of 180 ns needs to be extended to record later appearing relaxations rates.

When the system is then switched back to the initial state (MEA after fuel cell operation), both Mössbauer (Figure 51) and NFS (Figure 53, top) show similar spectra as compared to the GDL state. This indicates that the changes observed during the reaction conditions were reversible and not related to an irreversible degradation.

For the first time it is possible to examine a porphyrin-based model catalyst under real fuel cell conditions by NFS and demonstrate the power of synchrotron-based methods for operando setups. But it needs to be taken into account that further knowledge is required to get familiar with the complex data analysis of NFS spectra for such multicomponent systems.

Beside the posed problems with the data analysis, the investigation of a real Fe-N-C catalyst is the next step to validate the operando fuel cell setup for a real performing catalyst and gain further insides in the sluggish ORR. Therefore, a polypyrrole nanotube-based Fe-N-C catalyst was prepared following a

preparation route developed by Markus Kübler and described in Ni et al.⁴². The single membrane preparation steps, from the powder to the sprayed GDL, the fresh prepared MEA and after the fuel cell test were characterized by Mössbauer spectroscopy and NFS, each. The preparation of inks and MEAs were identical to the procedure described before. A Fe-N-C catalyst loading of 4.17 mg cm^{-2} and $0.16 \text{ mg}_{\text{Pt}} \text{ cm}^{-2}$ for the cathode and anode were calculated, respectively. In Figure 55 the Mössbauer spectra of the catalyst powder, the sprayed GDL, the freshly prepared MEA and the MEA after the fuel cell test are given whereas the Mössbauer parameters are summarized in Table 17.

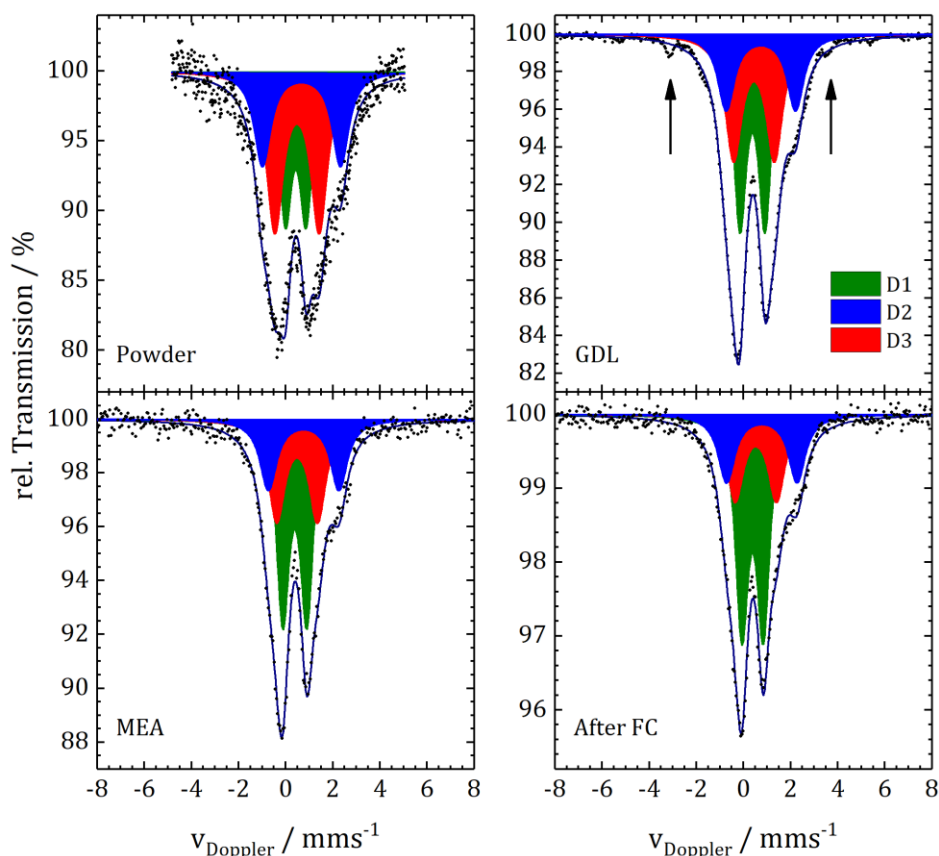


Figure 55: RT Mössbauer spectra of the investigated Fe-N-C catalyst at different stages of MEA preparation and after operation. Mössbauer spectrum of the fresh prepared catalyst powder (left, top), sprayed GDL without considering the sextet species (right top), hot pressed MEA (left bottom) and MEA after the fuel cell operation in the standard fuel cell test station are given (right, bottom).

The different iron sites are labeled as mentioned before. Three doublet sites were identified to fit each spectrum. All line widths were fixed to values obtained from previous fitting models beside the sextet species, which appeared only for the GDL sample but cannot be completely excluded for the other spectra due to spectra resolution. The found sextet species (Sext4) is assigned to iron carbide^{35, 273, 274}, formed as a byproduct of the oven process and remains in the catalyst due to an insufficient acid leaching. As seen in Figure S 8 and Table S 3 the consideration of the sextet species results in a shift of δ_{iso} of the

doublet site D2 and is not considered for the fitting in Figure 55 due to the total amount of the iron carbide species (< 2%), and is further not considered in the discussion.

The most pronounced changes of the Mössbauer parameters are observed going from the powder sample to the prepared electrode. It is related to an increase in absorption area of the D1 doublet from 30% in the powder to 40 – 50%. (GDL, MEA). In a previous work a similar change was found for a differently prepared catalyst. Based on reference samples it was shown that this change is due to the mixing with Nafion™ rather than an effect of alcohol ²²⁶. As described earlier, at RT Mössbauer spectroscopy the D1 doublet is an overlay of different oxygenated FeN₄ environments and small iron oxide particles/clusters ^{42, 247}. Thus, identifying the exact origin of the increase in D1 is difficult on the basis of the given data, but low temperature Mössbauer spectroscopy would be required to identify those sites.

Table 17: Mössbauer parameters of the catalyst investigated in the operando fuel cell at the different preparation steps.

Site	$\delta_{\text{iso}} / \text{mm s}^{-1}$	$\Delta E_{\text{Q}} / \text{mm s}^{-1}$	B_{hf} / T	$\Gamma / \text{mm s}^{-1}$	Area / %
Powder					
D1	0.434 (0.007)	0.873 (0.015)	–	0.641*	29.7
D2	0.678 (0.010)	3.312 (0.026)	–	0.859*	26.6
D3	0.488 (0.006)	1.884 (0.024)	–	0.857*	25.6
GDL					
D1	0.381 (0.001)	1.057 (0.003)	–	0.641*	41.1
D2	0.735 (0.003)	2.942 (0.007)	–	0.859*	22.6
D3	0.447 (0.002)	1.733 (0.010)	–	0.857*	36.3
MEA					
D1	0.385 (0.004)	1.013 (0.01)	–	0.641*	46.0
D2	0.760 (0.028)	2.995 (0.028)	–	0.859*	22.5
D3	0.484 (0.009)	1.733 (0.039)	–	0.857*	31.5
After FC					
D1	0.384 (0.002)	0.908 (0.007)	–	0.641*	50.6
D2	0.775 (0.011)	2.989 (0.026)	–	0.859*	22.1
D3	0.525 (0.009)	1.755 (0.033)	–	0.857*	27.3

*Fixed value

The electrochemical characterization of the Fe-N-C catalyst was done by fuel cell tests and enables the comparison of the standard fuel cell setup with the custom-made setup in combination with NFS spectra under operation. The fuel cell curves of both setups and related power densities are given in Figure 56.

On the left-hand side of Figure 56, the fuel cell curve of the prepared Fe-N-C catalyst measured in the standard setup is seen. The OCP is 0.97 V close to the value obtained for the reference Pt-Pt system. A maximum current density of 807.74 mA cm⁻² was reached. A power density at 0.6 V of 134.46 mW cm⁻² is found with a maximum power density of 205.19 mW cm⁻². This is almost one third of the performance obtained by the Pt-Pt reference but a dramatic increase compared to the porphyrin model system. The catalyst performance in the operando setup (Figure 56, right) follows a similar curve characteristic. An OCP of 0.98 V and a maximum current density of 503.95 mA cm⁻² are measured. Here, the discrepancy between the operando measurement and the standard setup is higher. Reasons for the deviation between standard and operando setup were discussed before. As already indicated, they specifically apply for more active catalysts at higher current densities. Based on this, the MEA with the Fe-N-C catalysts only reach a power density of 80 mW cm⁻² at 0.6 V (-65% compare to the standard setup).

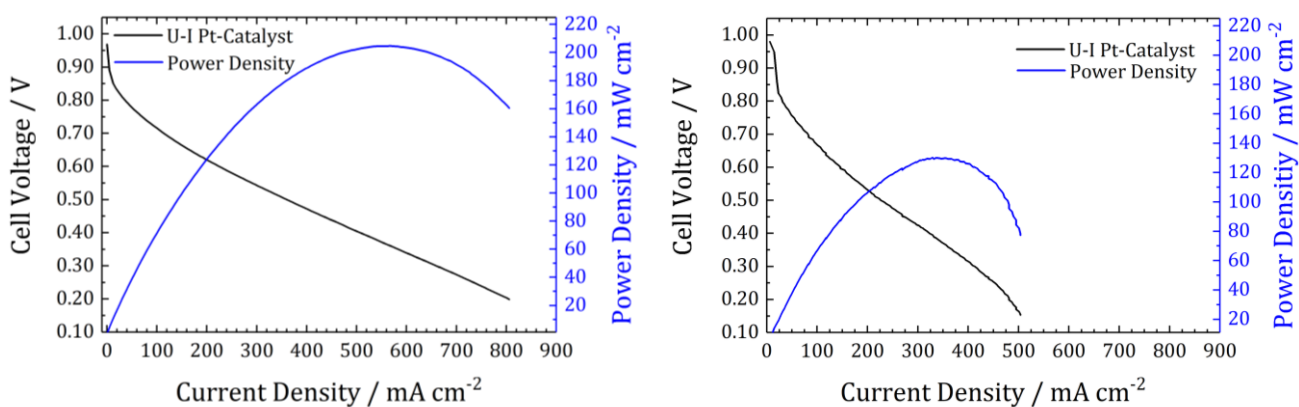


Figure 56: Pt-Fe-N-C catalyst reference measurement in the standard fuel cell setup (left). Operando fuel cell measurement with Pt-catalyst on the anode, MEA measured during the beamtime (right). Experimental conditions for the standard setup: H₂/O₂, cathode loading 3.2 – 3.5 mg_{Pt} cm⁻², N212 membrane, 1 bar gauge back pressure, 0.2 L min⁻¹ oxidant and fuel flow, cell temperature 80 °C, 100% relative humidity, whereas for the operando cell, the temperature of the pipes were set to 75 °C to avoid condensation inside the cell.

In Figure 57 the comparison of the catalyst powder, sprayed GDL, fresh prepared MEA and the MEA after the fuel cell test are shown. While in Mössbauer as main change the increase in absorption area of D1 was found, during NFS a more complex spectra interaction between the different preparation steps appear. As for the porphyrin a fast decrease in intensity was seen for all related measurements, without a significant contribution of resolved quantum beats, the real catalyst shows for the different preparation steps a complex spectrum.

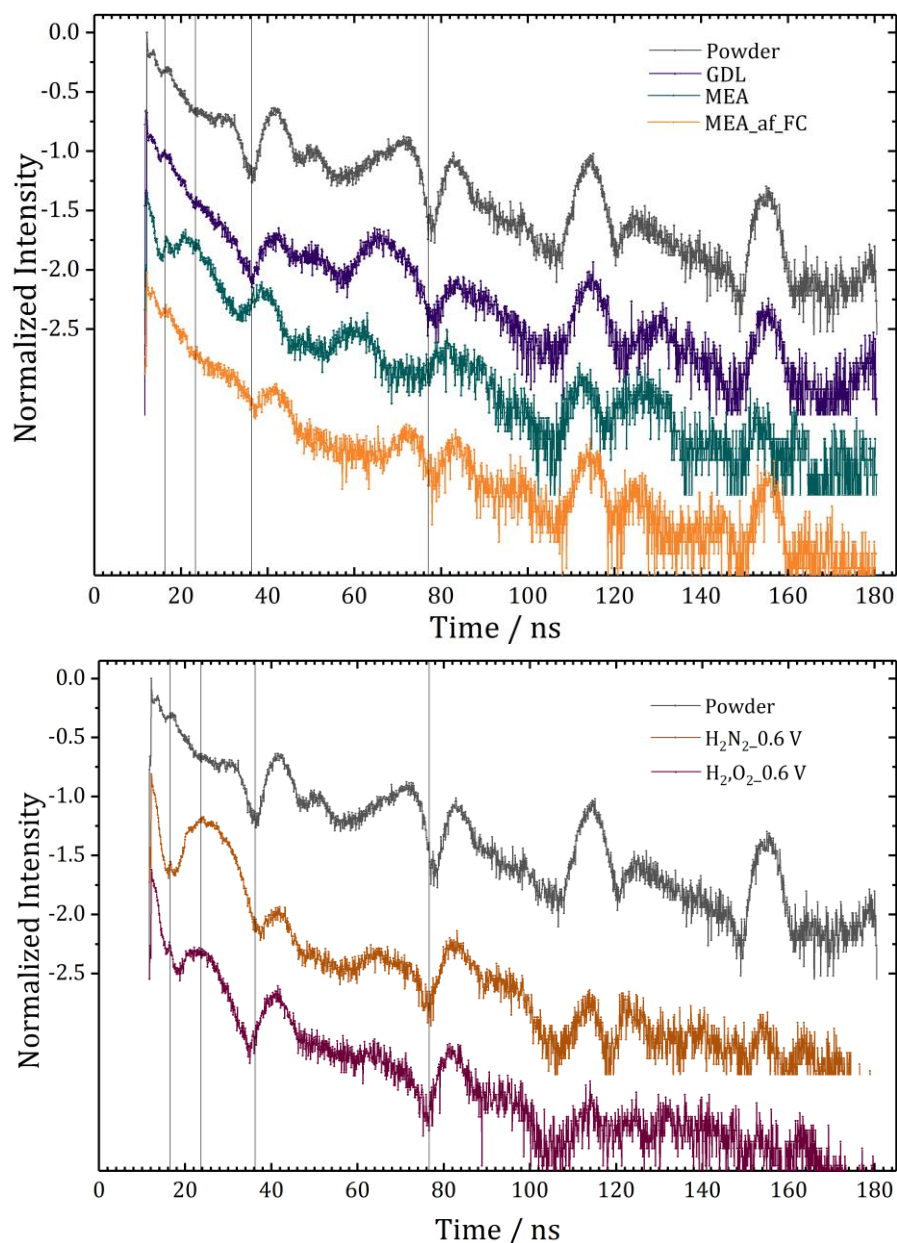


Figure 57: NFS spectra at three different states in the operando fuel cell. (dark green) Reduced catalyst state under nitrogen (cathode) and hydrogen (anode) at 0.6 V. (blue). The catalyst during oxygen reduction reaction with oxygen at the cathode and hydrogen on the anode, measured at a potential of 0.6 V. (light green) Same condition as for the dark green spectrum but after the degradation test and the measurement of a second polarization curve.

The influence of different sites results in a speed up of quantum beats and make a qualitative interpretation of the spectra hard to place. Nevertheless, the NFS spectra of the powder, GDL and MEA after the fuel cell test show a similar quantum beat characteristics, even though the intensity after the fuel cell test is reduced. This means, that the preparation steps, GDL spraying and MEA fabrication, do not result in a permanent change of the catalyst nature, similar result has been found for the iron-porphyrin model catalyst system. The obvious differences in the beat characteristics are found for the powder and the fresh prepared MEA which indicates the interaction of atmospheric water/oxygen with

the catalyst powder and the release of at least water after hot pressing of the MEA. By comparing the fresh prepared MEA a likewise beat structure as seen at H_2/N_2 condition ($H_2, N_2_{-0.6 V}$), but missing the dominant beat around 150 and 160 ns, is found. In general, it is interesting to see, that beat structure above 100 ns are suppressed or vanish during fuel cell operation but found again after the fuel cell test. It is assumed that the contribution of water inside the fuel cell is one possible reason. In Figure 57 (bottom) the NFS spectra mapped the catalyst powder, at reduced operation condition ($N_2, H_2_{-0.6 V}$) and during ORR ($O_2, H_2_{-0.6 V}$). The dominant beats around 115 ns and 150 ns are missing under operation conditions, compared to the powder. Whereas under operation conditions the beat characteristic between 15 ns and 20 ns is more dominant due to the increased interaction of the catalyst with water and oxygen.

In a previous study, the LT Mössbauer spectrum of the same catalyst found a proportion of 55 % assigned to inorganic side phases⁴². Based on this, only limited changes are expected. From this observation it is clear, that changes in the NFS spectra cannot be such dramatic as found for the reference porphyrin system, where only the pure porphyrin contribute to the carbon site and accelerate the ORR. The three NFS spectra are normalized and logarithmized in the same way as discussed for Figure 53 and plotted with the same shift to each other. Nevertheless, changes of the NFS spectra are identified for the catalyst system for the compared conditions. To quantify the changes, the spectra are separate in five regions to make the discussion easier. The first region is set from 0 to 16 ns, the second region from 16 to 24 ns the third region from 24 to 36 ns, the fourth from 36 to 76 ns and the fifth region from 76 to 180 ns. In the first region a fast linear decay of the signal under operation condition is found, whereas the powder shows already a beating characteristic with a less strong decay. A minimum is found (first gray line) with a small gap at 16.8 ns. Under ORR conditions ($H_2/O_2_{-0.6 V}$) this gap is shifted to 18.5 ns. The following beat with a maximum at 23.7 ns has almost a double intensity under H_2/N_2 condition compare to the ORR condition. Further, the beat is flatter under $H_2/O_2_{-0.6 V}$. In the third regime a minimum at 37 ns is found for the reduced systems, whereas under ORR condition this minimum is shifted to 34.7 ns. In the fourth region the slope characteristic of the catalyst under ORR conditions is flatter and the quantum beat with a maximum at 66.48 ns is less pronounced as under H_2/N_2 condition and for the catalyst powder. The beat characteristic in the fifth region looks similar for both operation conditions, with a stronger pronounced quantum beat behavior under $H_2/O_2_{-0.6 V}$. Here, the powder shows dominant beats around 83 ns, 114 ns and 154 ns, whereas under operation condition only the beat around 83 ns is dominant.

In Figure 58 the current-led potential adjustment during operation condition at $\sim 0.6 V$ is given. Under nitrogen flow, a constant increase of the potential over the measuring time is seen, whereas under oxygen flow a leap is seen. As described before those effects are caused by the insufficient gas separation during operation. Indeed, the absolute impact is very little as the average discrepancy is small compare

to the value. Therefore, those parasitic reaction have no significant impact to the observation made, but should be avoid for a future measuring time.

Thus, to conclude, while NFS provides a good way to proof changes in the local environment of Fe-N-C catalysts induced by fuel cell operation, the complexity in data analysis makes a full and also quantitative analysis quite challenging. Consequently, the technique might be useful for catalysts with higher purification but synchrotron based Mössbauer spectroscopy will be important in the near future for catalysts of similar degree of purity.

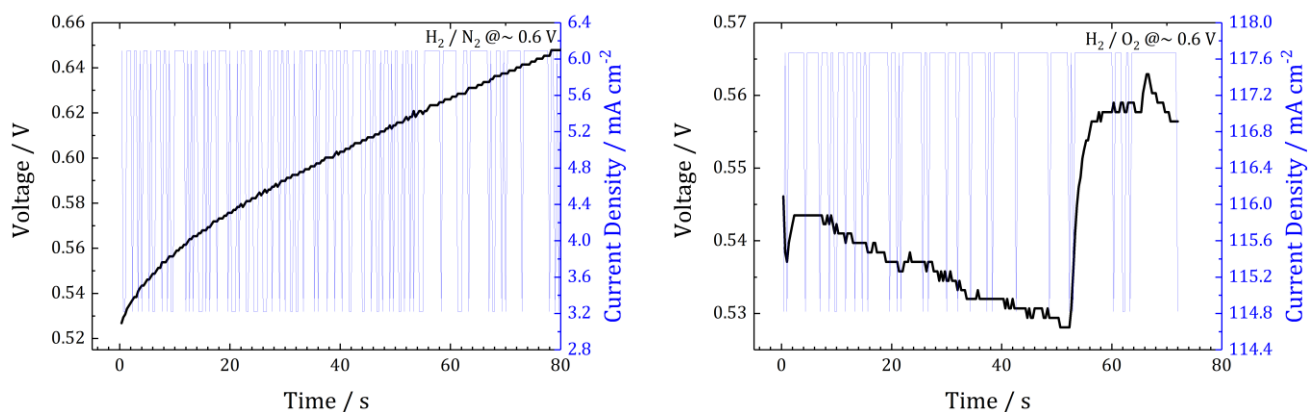


Figure 58: Averaged potential and current density that were applied during the recording of the Fe-N-C NFS spectra. Under H₂/N₂ (left) and H₂/O₂ (right) conditions.

For future work the following aspects should be considered: - the current flow field design enables a comparison of the catalyst close to the gas inlet, the center of the MEA and close to the gas outlet. However, for first operando studies, possibly a simpler flow field design that enables a performance closer to the standard setup is more desirable. The very high aspect ratio found for the operando flow field results in a strong turbulent gas stream inside the channels which influences the working properties. Therefore, a wave-like flow field would smoothen the gas flow, which would result in a smoother potential curve. For degradation investigations a linear flow field would be of interest, as parallel alignment of channels will increase the cross section during nuclear resonant measurements and enhance the spectrum quality by reducing the measuring time due to the penetration of several channels under the same conditions. But therefore, it must be clarified that for a multi-channel flow field the gas amount and pressure in each channel are identical. To avoid this, a single-line flow field could be an alternative.

Another issue might be the existence of temperature gradients within the cell. As the cell is only heated from the middle, a homogenous temperature gradient over the whole cell, caused by the geometry and the relative thin cell itself, is rather unlikely. This can result in cold spots, condensation of vapor and a floating of channels and should be avoided. Here, the temperature gradient could be visualized and

optimized by using an infrared camera and wire-heating systems on the back instead of a single-spot heater.

In addition, it remains unclear to what extent reaction kinetics and humidity are constant over the flow field. Based on this, conclusions on mechanism or degradation should basically focus on a similar spot to enable comparable conditions. The last big issue, which need to be improved are the sealings of the cell. The sealings make the handling of the cell rather challenging, as it is difficult to seal the cell without impairing the membrane. This is an important part of optimization as a small displacement of the sealing can result in a leakage or short cut of the cell. In the described experiment, custom made silicon sealings were used, placed like seen on the cross section in the supplemented Figure S 12. The new mentioned design would close the cell, fix the membrane and should have a higher beam transmission as carbon based sealings would be used instead of silicon-based ones, which absorb less radiation.

In a long-term perspective, it would be necessary to overcome the problems with the standard setup and implement the operando single cell to the standard fuel cell test station, to measure impedance curves and determine the specific ohmic resistance, as mentioned before. This is not possible with the electric load build for the custom-made setup but would be of big interest for easier comparison of measurements and further information of catalyst performance.

In general, it is useful to investigate Fe-N-C catalyst by synchrotron based Mössbauer spectroscopy (SMS) instead of nuclear forward scattering (NFS) to overcome the difficulties of data fitting. SMS is more suitable as the fitting procedure is identical to laboratory based Mössbauer spectroscopy. Unfortunately, Europe hosts only one SMS source at the ESRF so far, which was not accessible due to the maintenance shutdown of the synchrotron. The installation of a new SMS source at the PETRA III accelerator and the reopening for users of the ESRF, will push the scientific opportunities for the demonstrated operando setup dramatically. By taking the above-mentioned upgrades into account, the use of operando investigations by synchrotron techniques will help to identify the catalyst nature and intermediate states during operation or visualize degradation processes and help to improve the development of new Fe-N-C catalysts for fuel cell applications.

6. Summary and Outlook

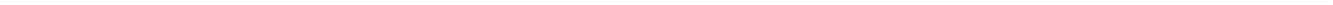
In the present work, nuclear resonant techniques were used to investigate Fe-N-C catalysts in the initial, deactivated or post mortem state as well as under operando conditions. For realization, new measuring setups were developed, successfully constructed and fully implemented, to illuminate the nature of the ORR participating active site. Thanks to the combination of nuclear resonant techniques with DFT calculations, it was proven that even under very mild preparation conditions and subsequent acid leaching, the Fe-N-C catalyst contains a considerable fraction of inorganic clusters (iron and iron oxides). Those contribute to the D1 site at RT and are not distinguishable without using low temperature Mössbauer spectroscopy (LT MS). Comparison of the partial Fe pDOS and DFT calculations, strongly indicate the presence of an oxy-heme-type site (sixfold coordinated ferrous low spin state), that might be at the origin of the ORR activity in Fe-N-C catalysts. It was demonstrated that pDOS and DFT calculations are very powerful tools to investigate the chemical composition of Fe-N-C catalyst, even though, the heterogeneous composition of Fe-N-C systems result in a broadened vibration mode characteristic. Ideally, in future experiments, a Fe-N-C catalyst that is pure in composition would be the ideal starting point for further investigation of the active site. The purification of the catalyst and the characterization with NIS will help to understand the ORR accelerated by Fe-N-C catalysts, as the vibration mode characteristics are used to clarify the chemical composition and ligand motion.

By introducing a SO_3^{-2} anion the successful deactivation of different Fe-N-C catalysts were proven by RDE experiments and confirmed by RT- and LT-Mössbauer spectroscopy as well as NIS and NFS measurements. After treating the catalysts with the anion, a new doublet that seems to be assigned to an axial ligation of sulfite to the FeN_4 -site was revealed. Based on DFT calculations it became likely that the attachment of the anion takes place by the interaction through the oxygen site of the sulfite ion. But DFT calculation cannot clarify the origin of the sixth ligand. Nevertheless, either parts of the active sites do not get deactivated or the active sites assigned to D1 still perform the ORR but with lower turn-over frequency. Here, the question of the sixth ligand becomes crucial but need to be further investigated. By in-situ and operando electrochemical experiments with a systematic variation of the anion concentration further insights are possible to obtain.

Post mortem analysis of low and high temperature treated MEAs gave insides to degradation products which appear after or during, fuel cell operation. An increase of oxidic iron and an overall loss of iron were found to go hand in hand with performance losses. Synchrotron based Mössbauer spectroscopy was figured out as best suited method, as the composition characterization has a position resolution to spot a degradation gradient for different positions within the MEA. Nonetheless, post mortem characterizations have the disadvantage that they cannot distinguished whether the observed changes appeared already during operation or after. Due to the change of the electrochemical environment,

additional side reactions are possible and able to change the chemical character of the sample after operation. The advantage of operando methods is already a part of this work and demonstrate the big advantage over post mortem characterizations. However, the use of post mortem characterization as an additional tool, helps to understand processes which take place after operation and are easier to implement. Again, the purification of the catalyst, in case of contributed iron sites and chemical structure, is important to obtain reliable data, further to determine specific values for f_{LM} , θ_M and M_{eff} . The successful observation of the catalyst with an operando fuel cell setup has the hugest potential to access the sluggish ORR and will help to understand reaction paths and participating chemical sites, in future. As synchrotron based Mössbauer spectroscopy was not available, the proof-of-concept experiment was successfully performed by NFS. Electronical and chemical changes induced by the operation conditions were clearly indicated, but the complexity of the reaction and overlaying contribution of different iron sites hinder a full quantitative analysis. Nevertheless, a change in the local environment of iron was proven, indicating the participation of iron in the ORR. These findings underline the enormous possibilities of synchrotron-based techniques in combination with operando fuel cell tests. Nonetheless, for future experiments, the setup should be further optimized to enable conditions as close as possible to a standard fuel cell setup. Beside the power of the shown methods to analyze and characterize Fe-N-C catalysts at different states and environments it is only possible to access information directly related and interacting with the iron site. A possible participation of non-iron sites to the ORR are not accessible. Here, neutron-based experiments are necessary to investigate e.g., possible contribution of nitrogen sites in the catalyst system to the ORR.

The discussed methods in combination with their further developments will help to enhance the knowledge of the participating active sites, degradation mechanisms and reaction pathways. Thus, new Fe-N-C catalyst will be developed which are more stable and better performing to reach the benchmarks for future applications.



7. Bibliography

1. Quéré, C. L.; Andrew, R. M.; Friedlingstein, P.; Sitch, S.; Hauck, J.; Pongratz, J.; Pickers, P. A.; Korsbakken, J. I.; Peters, G. P.; Canadell, J. G.; Arneeth, A.; Arora, V. K.; Barbero, L.; Bastos, A.; Bopp, L.; Chevallier, F.; Chini, L. P.; Ciais, P.; Doney, S. C.; Gkritzalis, T.; Goll, D. S.; Harris, I.; Haverd, V.; Hoffman, F. M.; Hoppema, M.; Houghton, R. A.; Hurtt, G.; Ilyina, T.; Jain, A. K.; Johannessen, T.; Jones, C. D.; Kato, E.; Keeling, R. F.; Goldewijk, K. K.; Landschützer, P.; Lefèvre, N.; Lienert, e.; Liu, Z.; Lombardozzi, D.; Metzl, N.; Munro, D. R.; Nabel, J. E. M. S.; Nakaoka, S.-i.; Neill, C.; Olsen, A.; Ono, T.; Patra, P.; Peregón, A.; Peters, W.; Peylin, P.; Pfeil, B.; Pierrot, D.; Poulter, B.; Rehder, G.; Resplandy, L.; Robertson, E.; Rocher, M.; Rödenbeck, C.; Schuster, U.; Schwinger, J.; Séférian, R.; Skjelvan, I.; Steinhoff, T.; Sutton, A.; Tans, P. P.; Tian, H.; Tilbrook, B.; Tubiello, F. N.; Laan-Luijckx, I. T. v. d.; Werf, G. R. v. d.; Viovy, N.; Walker, A. P.; Wiltshire, A. J.; Wright, R.; Zaehle, S.; Zheng, B., Global Carbon Budget 2018. *Earth Syst. Sci. Data* 2018, 10, 2141–2194.
2. Jackson, R. B.; Quéré, C. L.; Andrew, R. M.; Canadell, J. G.; Korsbakken, J. I.; Liu, Z.; Peters, G. P.; Zheng, B., Global energy growth is outpacing decarbonization. *Environ. Res. Lett.* 2018, 13.
3. Figueres, C., Emissions are still rising: ramp up the cuts. *Nature* 2018, 564.
4. Nations, U., Paris Agreement Nations, U., Ed. 2015.
5. Ausfelder, F., Von Kohlehalden und Wasserstoff
Energiespeicher-zentrale Elemente der Energieversorgung. In *Imprint*, Chemie, D. B.-G. f. p.; DECHEMA; Materialkunde, D. G. f.; DGNK; Gesellschaft, D. p.; Chemiker, G. D.; Industrie, V. d. C., Eds. Deutsche Bunsen-Gesellschaft: Selters, 2013.
6. Zellner, R., Zu viel CO₂ aus dem Verkehr: Ist Elektromobilität die Lösung? *GDCh* 2019.
7. Umweltbundesamt, Szenario zur Entwicklung des Strommixes in Deutschland im Jahr 2050 (in Gigawatt). . Statista: <https://de.statista.com/statistik/daten/studie/162540/umfrage/prognose-zum-stromix-in-deutschland-im-jahr-2050/>, 2010.
8. Chenitz, R.; Kramm, U. I.; Lefèvre, M.; Glibin, V.; Zhang, G.; Sun, S.; Dodelet, J.-P., A specific demetalation of Fe–N₄ catalytic sites in the micropores of NC_Ar + NH₃ is at the origin of the initial activity loss of the highly active Fe/N/C catalyst used for the reduction of oxygen in PEM fuel cells. *Energy & Environmental Science* 2018, 11 (2), 365-382.
9. Proietti, E.; Jaouen, F.; Lefevre, M.; Larouche, N.; Tian, J.; Herranz, J.; Dodelet, J. P., Iron-based cathode catalyst with enhanced power density in polymer electrolyte membrane fuel cells. *Nature Communications* 2011, 2:416.
10. Ardo, S.; Fernandez Rivas, D.; Modestino, M. A.; Schulze Greiving, V.; Abdi, F. F.; Alarcon Llado, E.; Artero, V.; Ayers, K.; Battaglia, C.; Becker, J.-P.; Bederak, D.; Berger, A.; Buda, F.; Chinello, E.; Dam, B.; Di Palma, V.; Edvinsson, T.; Fujii, K.; Gardeniers, H.; Geerlings, H.; H. Hashemi, S. M.; Haussener, S.; Houle, F.; Huskens, J.; James, B. D.; Konrad, K.; Kudo, A.; Kunturu, P. P.; Lohse, D.; Mei, B.; Miller, E. L.; Moore, G. F.; Muller, J.; Orchard, K. L.; Rosser, T. E.; Saadi, F. H.; Schüttauf, J.-W.; Seger, B.; Sheehan, S. W.; Smith, W. A.; Spurgeon, J.; Tang, M. H.; van de Krol, R.; Vesborg, P. C. K.; Westerik, P., Pathways to electrochemical solar-hydrogen technologies. *Energy & Environmental Science* 2018, 11 (10), 2768-2783.
11. Sims, R.; Schaeffer, R.; Creutzig, F.; Cruz-Núñez, X.; D’Agosto, M.; Dimitriu, D.; Meza, M. J. F.; Fulton, L.; Kobayashi, S.; Lah, O.; McKinnon, A.; Newman, P.; Ouyang, M.; Schauer, J. J.; Sperling, D.; G. Tiwari, Transport. In *Climate Change 2014: Mitigation of Climate Change. Contribution of Working Group III to the Fifth Assessment Report of the Intergovernmental Panel on Climate Change*, Edenhofer, O.; Pichs-Madruga, R.; Sokona, Y.; Farahani, E.; Kadner, S.; Seyboth, K.; A. Adler; Baum, I.; Brunner, S.; Eickemeier, P.; Kriemann, B.; Savolainen, J.; Schlömer, S.; Stechow, C. v.; Zwickel, T.; Minx, J. C., Eds. Cambridge University Press: Cambridge, United Kingdom and New York, NY, USA., 2014.
12. Commission, E., A European Strategy for Low-Emission Mobility
COMMISSION STAFF WORKING DOCUMENT

Accompanying the document

COMMUNICATION FROM THE COMMISSION TO THE EUROPEAN PARLIAMENT, THE COUNCIL, THE EUROPEAN ECONOMIC AND SOCIAL COMMITTEE AND THE COMMITTEE OF THE REGIONS. Commission, E., Ed. European Commission: Brussels, Belgium, 2016.

13. Leonard, N.; Ju, W.; Sinev, I.; Steinberg, J.; Luo, F.; Varela, A.; Roldan, B.; Strasser, P., The chemical identity, state and structure of catalytically active centers during the electrochemical CO₂ reduction on porous Fe-nitrogen-carbon (Fe-N-C) materials. *Chemical Science* 2018.

14. Ziegahn, K.-F., Energiespeicherung als Schlüssel zur Energiewende. In *Von Kohlehalden und Wasserstoff*

Energiespeicher-zentrale Elemente der Energieversorgung, Chemie, D.-B.-G. f. p., Ed. Seltersdruck GmbH: Selters, 2013.

15. Ausfelder, F.; Dura, H. E., 1. Roadmap des Kopernikus-Projektes "Power-to-X" Flexible Nutzung erneuerbarer Resource (P2X)

Optionen für ein nachhaltiges Energiesystem mit Power-to-X Technologien

Herausforderungen-Potenziale-Methoden-Auswirkungen. Kopernikus Projekt, P. J., Ed. 2018.

16. Audi h-tron. Audi: 2018.

17. Miotti, M.; Hofer, J.; Bauer, C., Integrated environmental and economic assessment of current and future fuel cell vehicles. *Int J Life Cycle Assess* 2015.

18. Bundesministerium für Umwelt, N. u. n. S. B., Wie umweltfreundlich sind Elektroautos?

Eine ganzheitliche Bilanz. BMU, R. I. I.-U. u. V., Elektromobilität, Ed. BMU: 2018.

19. Jülich, F. *Vergleichende Infrastrukturanalyse*

für das Betanken von Wasserstoff-Brennstoffzellen-Fahrer; Jülich Forschungszentrum: Jülich, 2017.

20. Sternberg, A.; Hank, C.; Hebling, C., Treibhausgas-Emissionen für Batterie- und Brennstoffzellenfahrzeuge mit Reichweiten über 300 km Fraunhofer-Institut für Solare Energiesysteme ISE: 2019.

21. Mobility, N. I.-H., Comparative-Analysis-of-Infrastructures

Hydrogen Fuelling and Electric Charging of Vehicles. In *H2 Mobility*, 2017.

22. Hessisches Ministerium für Umwelt, E., Landwirtschaft und Verbraucherschutz, Wasserstoff-Tankstellen

Ein Leitfadens für Anwender und Entscheider. Hessisches Ministerium für Umwelt, E., Landwirtschaft und Verbraucherschutz, Ed. Hessisches Ministerium für Umwelt, Energie, Landwirtschaft und Verbraucherschutz: Wiesbaden.

23. Mobility, H., H2M_IAC-AnnualReport2018. 2018.

24. Wilson, A.; Marcinkoski, J.; Papageorgopoulos, D., Fuel Cell System Cost - 2016. *DOE Hydrogen and Fuel Cells Program Record* 2016.

25. DOE DOE EERE Program Record; DOE: 2016.

26. Cowley, A. *Pgm Market Report*

February 2019; Johnson Matthey's: 2019.

27. Jaouen, F.; Jones, D.; Coutard, N.; Artero, V.; Strasser, P.; Kucernak, A., Toward Platinum Group Metal-Free Catalysts for Hydrogen/Air Proton-Exchange Membrane Fuel Cells. *Johnson Matthey Technology Review* 2018, 62 (2), 231-255.

28. Ott, S.; Orfanidi, A.; Schmies, H.; Anke, B.; Nong, H. N.; Hübner, J.; Gernert, U.; Glich, M.; Lerch, M.; Strasser, P., Ionomer distribution control in porous carbon supported catalyst layers for high-power and low Pt-loaded proton exchange membrane fuel cells. *Nature Materials* 2019.

29. Undertaking, F. C. a. H. J. *Hydrogen Roadmap Europe*; 2019.

30. Council, H. *Path to hydrogen competitiveness*

A cost perspective; 2020.

31. Deloitte; Ballard *Fueling the Future of Mobility Hydrogen and fuel cell solutions for transportation*; 2020.

32. Liquide, A.; American Honda Motor Co., I.; Audi; Chevron; Inc., C.; Engie, D. A. M.-B. F. C. G. M.-B. R. D. N. A.; Corporation, E.; Company, H. M.; Microsoft; Motors, N.; Hydrogen, N.; Power,

Executive Summary

Reducing emissions and driving growth across the nation; 2019.

33. Systems, B. P. Ballard Receives Follow-On Order For Next Stage in Development of Non Precious Metal Catalyst-Based Fuel Cells for Material Handling (accessed 2019-10-10).
34. Koslowski, U. I.; Abs-Wurmbach, I.; Fiechter, S.; Bogdanoff, P., Nature of the Catalytic Centers of Porphyrin-Based Electrocatalysts for the ORR: A Correlation of Kinetic Current Density with the Site Density of Fe-N₄ Centers. *J. Phys. Chem. C* 2008, 112 (39), 15356–15366.
35. Kramm, U. I.; Lefèvre, M.; Larouche, N.; Schmeisser, D.; Dodelet, J.-P., Correlations between Mass Activity and Physicochemical Properties of Fe/N/C Catalysts for the ORR in PEM Fuel Cell via 57Fe Mössbauer Spectroscopy and Other Techniques. *J. Am. Chem. Soc.* 2014, 136, 978–985.
36. Kramm, U. I.; Herrmann-Geppert, I.; Behrends, J.; Lips, K.; Fiechter, S.; Bogdanoff, P., On an Easy Way To Prepare Metal–Nitrogen Doped Carbon with Exclusive Presence of MeN₄-type Sites Active for the ORR. *J. Am. Chem. Soc.* 2016, 138, 635–640.
37. Zitolo, A.; Goellner, V.; Armel, V.; Sougrati, M. T.; Mineva, T.; Stievano, L.; Fonda, E.; Jaouen, F., Identification of catalytic sites for oxygen reduction in iron- and nitrogen-doped graphene materials. *Nature Materials* 2015, 14 (9), 937-942.
38. Li, J.; Ghoshal, S.; Liang, W.; Sougrati, M.-T.; Jaouen, F.; Halevi, B.; McKinney, S.; McCool, G.; Ma, C.; Yuan, X.; Ma, Z.-F.; Mukerjee, S.; Jia, Q., Structural and mechanistic basis for the high activity of Fe–N–C catalysts toward oxygen reduction. *Energy Environ. Sci.* 2016, 9 (2418).
39. Kramm, U. I.; Abs-Wurmbach, I.; Herrmann-Geppert, I.; Radnik, J.; Fiechter, S.; Bogdanoff, P., Influence of the Electron-Density of FeN₄-Centers Towards the Catalytic Activity of Pyrolyzed FeTMPPCl-Based ORR-Electrocatalysts. *Journal of The Electrochemical Society* 2011, 158 (1), B69-B78.
40. Sahraie, N. R.; Kramm, U. I.; Steinberg, J.; Zhang, Y.; Thomas, A.; Reier, T.; Paraknowitsch, J.-P.; Strasser, P., Quantifying the density and utilization of active sites in non-precious metal oxygen electroreduction catalysts. *Nature Communications* 2015, 6:8618.
41. Kramm, U. I., Non Precious Catalysts for Fuel Cells - A short review on Mössbauer spectroscopy of Fe-N-C catalysts for ORR. *ECS Transactions* 2013, 58 (1), 119-127.
42. Ni, L.; Gallenkamp, C.; Paul, S.; Kübler, M.; Theis, P.; Chhabra, S.; Hofmann, K.; Bill, E.; Schnegg, A.; Albert, B.; Krewald, V.; Kramm, U. I., Active Site Identification in FeNC Catalysts and Their Assignment to the Oxygen Reduction Reaction Pathway by In Situ 57Fe Mössbauer Spectroscopy. *Advanced Energy and Sustainability Research* 2021, 2 (2), 2000064.
43. Scherson, D. A.; Fierro, C. A.; Tryk, D.; Gupta, S. L.; Yeager, E. B.; Eldrige, J.; Hoffman, R. W., In-situ Mössbauer Spectroscopy and Electrochemical Studies of the Thermal Stability of Iron Phthalocyanine Dispersed in High Surface Area Carbon. *J. Electroanal. Chem.* 1985, 184 419-426.
44. Fierro, C. A.; Mohan, M.; Scherson, D. A., In Situ Mossbauer Spectroscopy of a Species Irreversibly Adsorbed on an Electrode Surface. *Langmuir* 1990, 6, 1338-1342.
45. Bouwkamp-Wijnoltz, A. L.; Visscher, W.; Veen, J. A. R. v.; Boellaard, E.; Kraan, A. M. v. d.; Tang, S. C., On Active-Site Heterogeneity in Pyrolyzed Carbon-Supported Iron Porphyrin Catalysts for the Electrochemical Reduction of Oxygen: An In Situ Mössbauer Study. *J. Phys. Chem. B* 2002, 106, 12993-13001.
46. Niemantsverdriet, J. W.; Delgass, W. N., In situ Mössbauer spectroscopy in catalysis. *Topics in Catalysis* 1999, 8, 133–140.
47. Li, J.; Sougrati, M. T.; Zitolo, A.; Ablett, J. M.; Oğuz, I. C.; Mineva, T.; Matanovic, I.; Atanassov, P.; Huang, Y.; Zenyuk, I.; Di Cicco, A.; Kumar, K.; Dubau, L.; Maillard, F.; Dražić, G.; Jaouen, F., Identification of durable and non-durable FeN_x sites in Fe–N–C materials for proton exchange membrane fuel cells. *Nature Catalysis* 2021, 4 (1), 10-19.
48. Li, X.; Cao, C.-S.; Hung, S.-F.; Lu, Y.-R.; Cai, W.; Rykov, A. I.; Miao, S.; Xi, S.; Yang, H.; Hu, Z.; Wang, J.; Zhao, J.; Alp, E. E.; Xu, W.; Chan, T.-S.; Chen, H.; Xiong, Q.; Xiao, H.; Huang, Y.; Li, J.; Zhang, T.; Liu, B., Identification of the Electronic and Structural Dynamics of Catalytic Centers in Single-Fe-Atom Material. *Chem* 2020, 6 (12), 3440-3454.

49. Meyer, Q.; Zeng, Y.; Zhao, C., In Situ and Operando Characterization of Proton Exchange Membrane Fuel Cells. *Adv Mater* 2019, 31 (40), e1901900.
50. Kneebone, J. L.; Daifuku, S. L.; Kehl, J. A.; Wu, G.; Chung, H. T.; Hu, M. Y.; Alp, E. E.; More, K. L.; Zelenay, P.; Holby, E. F.; Neidig, M. L., A Combined Probe-Molecule, Mössbauer, Nuclear Resonance Vibrational Spectroscopy, and Density Functional Theory Approach for Evaluation of Potential Iron Active Sites in an Oxygen Reduction Reaction Catalyst. *The Journal of Physical Chemistry C* 2017, 121 (30), 16283-16290.
51. Wagner, S.; Auerbach, H.; Tait, C. E.; Martinaiou, I.; Kumar, S. C. N.; Kübel, C.; Sergeev, I.; Wille, H.-C.; Behrends, J.; Wolny, J. A.; Schünemann, V.; Kramm, U. I., Elucidating the Structural Composition of an Fe–N–C Catalyst by Nuclear- and Electron-Resonance Techniques. *Angewandte Chemie* 2019, 131 (31), 10596-10602.
52. Wagner, S.; Martinaiou, I.; Shahraei, A.; Weidler, N.; Kramm, U. I., On the effect of sulfite ions on the structural composition and ORR activity of Fe-N-C catalysts. *Hyperfine Interact* 2018, 239:10.
53. Kramm, U. I.; Lefèvre, M.; Larouche, N.; Schmeisser, D.; Dodelet, J.-P., Correlations between Mass Activity and Physicochemical Properties of Fe/N/C Catalysts for the ORR in PEM Fuel Cell via 57Fe Mössbauer Spectroscopy and Other Techniques. *Journal of the American Chemical Society* 2014, 136, 978–985.
54. Paquot, C., The catalytic oxidizing properties of the phthalocyanines. *C.R. Acad. Sci.* 1939, 209, 171-173.
55. Jasinski, R., A New Fuel Cell Cathode Catalyst. *Nature* 1964, 201, 1212-1213.
56. Jasinski, R., Cobalt Phthalocyanine as a Fuel Cell Cathode. *Journal of the electrochemical Society* 1965, 112 (5), 526-528.
57. Zagal, J. H.; Bedioui, F.; Dodelet, J. P., *N4-Macrocyclic Metal Complexes*. Springer: United States of America, 2006.
58. Ali, M. E.; Sanyal, B.; Oppeneer, P. M., Electronic Structure, Spin-States, and Spin-Crossover Reaction of Heme-Related Fe-Porphyrins: A Theoretical Perspective. *The Journal of Physical Chemistry B* 2012, 116 (20), 5849-5859.
59. Jahnke, D. H.; Schönborn, D. M.; Zimmermann, D. G., Organic Dyestuffs as Catalysts for Fuel Cells. *Physical and Chemical Applications of Dyestuffs. Topics in Current Chemistry* 1976, 61.
60. Bagotzky, V. S.; Tarasevich, M. R.; Radyushkina, K. A.; Levina, O. A.; Andrusyova, S. I., Electrocatalysis of the Oxygen Reduction Process on Metal Chelates in Acidic Electrolyte *Journal of Power Sources* 1977/78, 2 233 - 240.
61. Gupta, S.; Tryk, D.; Bae, I.; Aldred, W.; Yeager, E., Heat-treated polyacrylonitrile-based catalysts for oxygen electroreduction. *Journal of Applied Electrochemistry* 1989, 19, 19-27.
62. Putten, A. v. d.; Elzing, A.; Visscher, W.; Barendrecht, E., Oxygen reduction on pyrolysed carbon-supported transition metal chelates. *Journal of Electroanalytical Chemistry* 1986, 205, 233-244.
63. Vasudevan, P.; Santosh; Mann, N.; Tyagi, S., Transition metal complexes of porphyrins and phthalocyanines as electrocatalysts for dioxygen reduction. *Transition Met. Chem.* 1990, 15, 81-90.
64. Schulenburg, H.; Stankov, S.; Schünemann, V.; Radnik, J.; Dorbandt, I.; Fiechter, S.; Bogdanoff, P.; Tributsch, H., Catalysts for the Oxygen Reduction from Heat-Treated Iron(III) Tetramethoxyphenylporphyrin Chloride: Structure and Stability of Active Sites. *J. Phys. Chem. B* 2003, 107, 9034-9041.
65. Yuan, X.; Li, L.; Ma, Z.; Yu, X.; Wen, X.; Ma, Z. F.; Zhang, L.; Wilkinson, D. P.; Zhang, J., Novel nanowire-structured polypyrrole-cobalt composite as efficient catalyst for oxygen reduction reaction. *Sci Rep* 2016, 6, 20005.
66. Toh, R. J.; Sofer, Z.; Pumera, M., Transition Metal Oxides for the Oxygen Reduction Reaction: Influence of the Oxidation States of the Metal and its Position on the Periodic Table. *Chemphyschem* 2015, 16 (16), 3527-31.
67. Chen, M.; Liu, J.; Zhou, W.; Lin, J.; Shen, Z., Nitrogen-doped Graphene-Supported Transition-metals Carbide Electrocatalysts for Oxygen Reduction Reaction. *Sci Rep* 2015, 5, 10389.

68. Yin, H.; Zhang, C.; Liu, F.; Hou, Y., Hybrid of Iron Nitride and Nitrogen-Doped Graphene Aerogel as Synergistic Catalyst for Oxygen Reduction Reaction. *Advanced Functional Materials* 2014, 24 (20), 2930-2937.
69. Brüller, S.; Liang, H.-W.; Kramm, U. I.; Krumpfer, J. W.; Feng, X.; Müllen, K., Bimetallic Porous Porphyrin Polymer-Derived Nonprecious Metal Electrocatalysts for Oxygen Reduction Reactions. *J. Mater. Chem. A* 2015, 3 (23799), 23799–23808
70. Lefèvre, M.; Proietti, E.; Jaouen, F.; Dodelet, J. P., Iron-based catalysts with improved oxygen reduction activity in polymer electrolyte fuel cells. *Science* 2009, 324 (5923), 71-74.
71. Wu, G.; More, K. L.; Johnston, C. M.; Zelenay, P., High-Performance Electrocatalysts for Oxygen Reduction Derived from Polyaniline, Iron, and Cobalt. *Science* 2011, 332 (6028), 443-447.
72. Meng, H.; Larouche, N.; Lefèvre, M.; Jaouen, F.; Stansfield, B.; Dodelet, J.-P., Iron porphyrin-based cathode catalysts for polymer electrolyte membrane fuel cells: Effect of NH₃ and Ar mixtures as pyrolysis gases on catalytic activity and stability. *Electrochimica Acta* 2010, 55 (22), 6450-6461.
73. Park, M.; Lee, J.; Hembram, K.; Lee, K.-R.; Han, S.; Yoon, C.; Nam, S.-W.; Kim, J., Oxygen Reduction Electrocatalysts Based on Coupled Iron Nitride Nanoparticles with Nitrogen-Doped Carbon. *Catalysts* 2016, 6 (6).
74. Shui, J. L.; Karan, N. K.; Balasubramanian, M.; Li, S. Y.; Liu, D. J., Fe/N/C composite in Li-O₂ battery: studies of catalytic structure and activity toward oxygen evolution reaction. *J Am Chem Soc* 2012, 134 (40), 16654-61.
75. Jaouen, F.; Goellner, V.; Lefèvre, M.; Herranz, J.; Proietti, E.; Dodelet, J. P., Oxygen reduction activities compared in rotating-disk electrode and proton exchange membrane fuel cells for highly active FeNC catalysts. *Electrochimica Acta* 2013, 87, 619-628.
76. Deng, Y.; Chi, B.; Tian, X.; Cui, Z.; Liu, E.; Jia, Q.; Fan, W.; Wang, G.; Dang, D.; Li, M.; Zang, K.; Luo, J.; Hu, Y.; Liao, S.; Sun, X.; Mukerjee, S., g-C₃N₄ promoted MOF derived hollow carbon nanopolyhedra doped with high density/fraction of single Fe atoms as an ultra-high performance non-precious catalyst towards acidic ORR and PEM fuel cells. *Journal of Materials Chemistry A* 2019, 7 (9), 5020-5030.
77. Uddin, A.; Langhorst, L.; Zhang, H.; Hu, L.; Wu, G.; Litster, S., High Power Density PGM-Free Cathodes for Polymer Electrolyte Fuel Cells. *ACS Appl Mater Interfaces* 2019.
78. Yao, Y.; Xiao, H.; Wang, P.; Su, P.; Shao, Z.; Yang, Q., CNTs@Fe-N-C core-shell nanostructures as active electrocatalyst for oxygen reduction. *Journal of Materials Chemistry A* 2014, 2 (30), 11768.
79. Sa, Y. J.; Seo, D. J.; Woo, J.; Lim, J. T.; Cheon, J. Y.; Yang, S. Y.; Lee, J. M.; Kang, D.; Shin, T. J.; Shin, H. S.; Jeong, H. Y.; Kim, C. S.; Kim, M. G.; Kim, T. Y.; Joo, S. H., A General Approach to Preferential Formation of Active Fe-N_x Sites in Fe-N/C Electrocatalysts for Efficient Oxygen Reduction Reaction. *J Am Chem Soc* 2016, 138 (45), 15046-15056.
80. Sarapuu, A.; Samolberg, L.; Kreek, K.; Koel, M.; Matisen, L.; Tammeveski, K., Cobalt- and iron-containing nitrogen-doped carbon aerogels as non-precious metal catalysts for electrochemical reduction of oxygen. *Journal of Electroanalytical Chemistry* 2015, 746, 9-17.
81. Zion, N.; Cullen, D. A.; Zelenay, P.; Elbaz, L., Heat-Treated Aerogel as a Catalyst for the Oxygen Reduction Reaction. *Angew Chem Int Ed Engl* 2019.
82. Jaouen, F.; Proietti, E.; Lefèvre, M.; Chenitz, R.; Dodelet, J.-P.; Wu, G.; Chung, H. T.; Johnston, C. M.; Zelenay, P., Recent advances in non-precious metal catalysis for oxygen-reduction reaction in polymer electrolyte fuelcells. *Energy Environ. Sci.* 2011, 4 (1), 114-130.
83. Leonard, N. D.; Wagner, S.; Luo, F.; Steinberg, J.; Ju, W.; Weidler, N.; Wang, H.; Kramm, U. I.; Strasser, P., Deconvolution of Utilization, Site Density, and Turnover Frequency of Fe-Nitrogen-Carbon Oxygen Reduction Reaction Catalysts Prepared with Secondary N-Precursors. *ACS Catalysis* 2018, 1640-1647.
84. Liu, Z.; Sun, F.; Gu, L.; Chen, G.; Shang, T.; Liu, J.; Le, Z.; Li, X.; Wu, H. B.; Lu, Y., Post Iron Decoration of Mesoporous Nitrogen-Doped Carbon Spheres for Efficient Electrochemical Oxygen Reduction. *Advanced Energy Materials* 2017, 7 (22), 1701154.

85. Wu, R.; Wang, J.; Chen, K.; Chen, S.; Li, J.; Wang, Q.; Nie, Y.; Song, Y.; Chen, H.; Wei, Z., Space-Confined Pyrolysis for the Fabrication of Fe/N/C Nanoparticles as a High Performance Oxygen Reduction Reaction Electrocatalyst. *Electrochimica Acta* 2017, 244, 47-53.
86. Ferrandon, M.; Kropf, A. J.; Myers, D. J.; Artyushkova, K.; Kramm, U.; Bogdanoff, P.; Wu, G.; Johnston, C. M.; Zelenay, P., Multitechnique Characterization of a Polyaniline–Iron–Carbon Oxygen Reduction Catalyst. *The Journal of Physical Chemistry C* 2012, 116 (30), 16001-16013.
87. Jiao, L.; Li, J.; Richard, L. L.; Sun, Q.; Stracensky, T.; Liu, E.; Sougrati, M. T.; Zhao, Z.; Yang, F.; Zhong, S.; Xu, H.; Mukerjee, S.; Huang, Y.; Cullen, D. A.; Myers, D. J.; Jaouen, F.; Jia, Q., Chemical vapor deposition of Fe-N-C oxygen reduction catalysts with full utilization of dense Fe-N₄ sites. *ChemRxiv* 2020.
88. Veen, J. A. R. v.; Visser, C., Oxygen Reduction on Monomeric Transition Metal Phtalocyanines in Acidic Electrolyte *Electrochimica Acta* 1979, 24, 921-928.
89. Veen, J. A. R. v.; Baar, J. F. v.; Kroes, K. J., Effect of Heat Treatment on the Performance of Carbon-supported Transition-metal Chelates in the Electrochemical Reduction of Oxygen. *J. Chem. Soc., Faraday Trans. I* 1981, 77, 2827-2843.
90. Veen, J. A. R. v.; Colijn, H. A.; Baar, J. F. v., On the Effect of a Heat Treatment on the Structure of Carbon-Supported Metalloporphyrins and Phtalocyanines. *Electrochimica Acta* 1988, 33 (6), 801-804.
91. Yeager, E., Electrocatalyst for O₂ Reduction *Electrochimica Acta* 1984, 29 (11), 1527-1537.
92. Wiesener, K., N₄-Chelates as Electrocatalyst for Cathodic Oxygen Reduction. *Electrochimica Acta* 1986, 31 (8), 1073-1078.
93. Wiesener, K.; Ohms, D.; Neumann, V.; Franke, R., N₄ Macrocycles as Electrocatalysts for the Cathodic Reduction of Oxygen. *Materials Chernistry and Physics* 1989, 22, 457-415.
94. Franke, R.; Ohms, D.; Wiesener, K., Investigation of the influence of thermal treatment on the properties of carbon materials modified by N₄-chelates for the reduction of oxygen in acidic media. *J. Electrtoanal. Chem.* 1989, 260 63-73.
95. Dodelet, J.-P., The Controversial Role of the Metal in Fe- or Co-Based Electrocatalysts for the Oxygen Reduction Reaction in Acid Medium. In *Electrocatalysis in Fuel Cells*, 2013; pp 271-338.
96. Singh, K.; Razmjooei, F.; Yu, J.-S., Active sites and factors influencing them for efficient oxygen reduction reaction in metal-N coordinated pyrolyzed and non-pyrolyzed catalysts: a review. *Journal of Materials Chemistry A* 2017, 5 (38), 20095-20119.
97. Herranz, J.; Lefèvre, M.; Larouche, N.; Stansfield, B.; Dodelet, J.-P., Step-by-Step Synthesis of Non-Noble Metal Electrocatalysts for O₂ Reduction under Proton Exchange Membrane Fuel Cell Conditions. *J. Phys. Chem. C* 2007, 111, 19033-19042.
98. Chung, H. T.; Cullen, D. A.; Higgins, D.; Sneed, B. T.; Holby, E. F.; More, K. L.; Zelenay, P., Direct atomic-level insight into the active sites of a high-performance PGM-free ORR catalyst. *Science* 2017, 357, 479–484.
99. Martinez, U.; Holby, E. F.; Babu, S. K.; Artyushkova, K.; Lin, L.; Choudhury, S.; Purdy, G. M.; Zelenay, P., Experimental and Theoretical Trends of PGM-Free Electrocatalysts for the Oxygen Reduction Reaction with Different Transition Metals. *Journal of The Electrochemical Society* 2019, 166 (7), F3136-F3142.
100. Kramm, U. I.; Herranz, J.; Larouche, N.; Arruda, T. M.; Lefevre, M.; Jaouen, F.; Bogdanoff, P.; Fiechter, S.; Abs-Wurmbach, I.; Mukerjee, S.; Dodelet, J. P., Structure of the catalytic sites in Fe/N/C-catalysts for O₂-reduction in PEM fuel cells. *Phys Chem Chem Phys* 2012, 14 (33), 11673-88.
101. Shao, Y.; Dodelet, J.-P.; Wu, G.; Zelenay, P., PGM-Free Cathode Catalysts for PEM Fuel Cells: A Mini-Review on Stability Challenges. *Advanced Materials* 2019, 1807615.
102. Kramm, U. I., Non Precious Catalysts for Fuel Cells - A short review on Mößbauer spectroscopy of Fe-N-C catalysts for ORR. *ECS Transactions* 2013, 58 (1), 119-127
103. Banham, D.; Ye, S.; Pei, K.; Ozaki, J.-i.; Kishimoto, T.; Imashiro, Y., A review of the stability and durability of non-precious metal catalysts for the oxygen reduction reaction in proton exchange membrane fuel cells. *Journal of Power Sources* 2015, 285, 334-348.

104. Weng, L. T.; Bertrand, P.; Lalande, G.; Guay, D.; Dodelet, J. P., Surface characterization by time-of-flight SIMS of a catalyst for oxygen electroreduction: pyrolyzed cobalt phthalocyanine-on-carbon black. *Applied Surface Science* 1995, *84*, 9-21.
105. Faubert, G.; Côté, R.; Dodelet, J. P.; Lefèvre, M.; Bertrand, P., Oxygen reduction catalysts for polymer electrolyte cells from the pyrolysis of Fe(II) acetate adsorbed 3,4,9,10-perylenetetracarboxylic dianhydride. *Electrochimica Acta* 1999, *44*, 2589-2603.
106. Lefèvre, M.; Dodelet, J. P., Molecular Oxygen Reduction in PEM Fuel Cells: Evidence for the Simultaneous Presence of Two Active Sites in Fe-Based Catalysts. *J. Phys. Chem. B* 2002, *106*, 8705-8713.
107. Kramm, U. I.; Ni, L.; Wagner, S., ⁵⁷Fe Mössbauer Spectroscopy Characterization of Electrocatalysts. In *Research News Advanced Materials*, 1805623, Ed. WILEY-VCH, 2019.
108. Walker, F. A.; Simonis, U., *Iron Porphyrin Chemistry*. John Wiley & Sons, Ltd.: 2006.
109. Zagal, J. H.; Paez, M. A.; Silva, J. F., Fundamental aspects on the catalytic activity of metallomacrocyclics for the electrochemical reduction of O₂. In *N4-macrocyclic metal complexes*, Zagal, J. H.; Bedioui, F.; Dodelet, J. P., Eds. Springer: New York, 2006; pp 41–82.
110. Kramm, U. I.; Herrmann-Geppert, I.; Bogdanoff, P.; Fiechter, S., Effect of an Ammonia Treatment on Structure, Composition, and Oxygen Reduction Reaction Activity of Fe–N–C Catalysts. *The Journal of Physical Chemistry C* 2011, *115* (47), 23417-23427.
111. Jaouen, F.; Marcotte, S.; Dodelet, J.-P.; Lindbergh, G., Oxygen Reduction Catalysts for Polymer Electrolyte Fuel Cells from the Pyrolysis of Iron Acetate Adsorbed on Various Carbon Supports. *J. Phys. Chem. B* 2003, *107*, 1376-1386.
112. Charretre, F.; Ruggeri, S.; Jaouen, F.; Dodelet, J. P., Increasing the activity of Fe/N/C catalysts in PEM fuel cell cathodes using carbon blacks with a high-disordered carbon content. *Electrochimica Acta* 2008, *53*, 6881–6889.
113. Mineva, T.; Matanovic, I.; Atanassov, P.; Sougrati, M. T.; Stievano, L.; Clémancey, M.; Kochem, A.; Latour, J.-M.; Jaouen, F., Understanding active sites in pyrolyzed Fe-N-C catalysts for fuel cell cathodes by bridging density functional theory calculations and ⁵⁷Fe Mössbauer Spectroscopy. *ACS Catalysis* 2019.
114. Martinaiou, I.; Videla, A. H. A. M.; Weidler, N.; Kübler, M.; Wallace, W. D. Z.; Paul, S.; Wagner, S.; Shahraei, A.; Stark, R. W.; Specchia, S.; Kramm, U. I., Activity and degradation study of an Fe-N-C catalyst for ORR in Direct Methanol Fuel Cell (DMFC). *Applied Catalysis B: Environmental* 2020, *262* (118217).
115. Santori, P. G.; Speck, F. D.; Li, J.; Zitolo, A.; Jia, Q.; Mukerjee, S.; Cherevko, S.; Jaouen, F., Effect of Pyrolysis Atmosphere and Electrolyte pH on the Oxygen Reduction Activity, Stability and Spectroscopic Signature of FeN_x Moieties in Fe-N-C Catalysts. *Journal of The Electrochemical Society* 2019, *166* (7), F3311-F3320.
116. Kumar, K.; Dubau, L.; Mermoux, M.; Li, J.; Zitolo, A.; Nelayah, J.; Jaouen, F.; Maillard, F., On the Influence of Oxygen On the Degradation of Fe-N-C Catalysts. *Angew Chem Int Ed Engl* 2019.
117. Goellner, V.; Baldizzone, C.; Schuppert, A.; Sougrati, M. T.; Mayrhofer, K.; Jaouen, F., Degradation of Fe/N/C catalysts upon high polarization in acid medium. *Phys Chem Chem Phys* 2014, *16* (34), 18454-62.
118. Yan, X.; Jia, Y.; Yao, X., Defects on carbons for electrocatalytic oxygen reduction. *Chem Soc Rev* 2018, *47* (20), 7628-7658.
119. Nørskov, J. K.; Rossmeisl, J.; Logadottir, A.; Lindqvist, L.; Kitchin, J. R.; Bligaard, T., Origin of the Overpotential for Oxygen Reduction at a Fuel-Cell Cathode. *J. Phys. Chem. B* 2004, *108*, 17886-17892.
120. Wroblowa, H. S.; Xyen-Chi-Pan; Razumney, G., Electroreduction of Oxygen a new Mechanistic Criterion. *J. Electroanal. Chem.* 1976, *69*, 195-201
121. Choi, C. H.; Lim, H.-K.; Chon, G.; Chung, M. W.; Altin, A.; Sahraie, N. R.; Sougrati, M.-T.; Stievano, L.; Oh, H. S.; Park, E. S.; Luo, F.; Strasser, P.; Dražić, G.; Mayrhofer, K. J. J.; Kim, H.; Jaouen, F., Achilles' heel of iron-based catalysts during oxygen reduction in acidic medium. *Energy & Environmental Science* 2018, *11*, 3176-3182.

122. Robson, M. H.; Serov, A.; Artyushkova, K.; Atanassov, P., A mechanistic study of 4-aminoantipyrine and iron derived non-platinum group metal catalyst on the oxygen reduction reaction. *Electrochimica Acta* 2013, 90, 656-665.
123. Casalongue, H. S.; Kaya, S.; Viswanathan, V.; Miller, D. J.; Friebel, D.; Hansen, H. A.; Nørskov, J. K.; Nilsson, A.; Ogasawara, H., Direct Observation of the Oxygenated Species during Oxygen Reduction on a Platinum Fuel Cell Cathode. *Nature Communications* 2013, 4 (2817).
124. Busch, M.; Halck, N. B.; Kramm, U. I.; Siahrostami, S.; Krttil, P.; Rossmeisl, J., Beyond the top of the volcano? – A unified approach to electrocatalytic oxygen reduction and oxygen evolution. *Nano Energy* 2016, 29, 126-135.
125. Szakacs, C. E.; Lefevre, M.; Kramm, U. I.; Dodelet, J. P.; Vidal, F., A density functional theory study of catalytic sites for oxygen reduction in Fe/N/C catalysts used in H(2)/O(2) fuel cells. *Phys. Chem. Chem. Phys.* 2014, 16 (27), 13654-61.
126. Boulatov, R., Billion-Year-Old Oxygen Cathode that Actually Works: Respiratory Oxygen Reduction and Its Biomimetic Analogs. In *N4-Macrocyclic Metal Complexes*, Zagal, J. H.; Bedioui, F.; Dodelet, J.-P., Eds. Springer New York: New York, NY, 2006; pp 1-40.
127. Glibin, V. P.; Dodelet, J.-P., Thermodynamic Stability in Acid Media of FeN4-Based Catalytic Sites Used for the Reaction of Oxygen Reduction in PEM Fuel Cells. *Journal of The Electrochemical Society* 2017, 164 (9), F948-F957.
128. Xuan, Y.; Xie, L.; Huang, X.; Su, B., Molecular electrocatalysis of oxygen reduction by iron(II) phthalocyanine at the liquid/liquid interface. *Journal of Electroanalytical Chemistry* 2016, 766, 37-43.
129. Malko, D.; Kucernak, A.; Lopes, T., In situ electrochemical quantification of active sites in Fe–N/C non-precious metal catalysts. *Nature Communications* 2016, 7 (13285).
130. Jia, Q.; Ramaswamy, N.; Tylus, U.; Strickland, K.; Li, J.; Serov, A.; Artyushkova, K.; Atanassov, P.; Anibal, J.; Gumeci, C.; Barton, S. C.; Sougrati, M.-T.; Jaouen, F.; Halevi, B.; Mukerjee, S., Spectroscopic insights into the nature of active sites in iron–nitrogen–carbon electrocatalysts for oxygen reduction in acid. *Nano Energy* 2016.
131. Artyushkova, K.; Workman, M. J.; Matanovic, I.; Dzara, M. J.; Ngo, C.; Pylypenko, S.; Serov, A.; Atanassov, P., Role of Surface Chemistry on Catalyst/Ionomer Interactions for Transition Metal–Nitrogen–Carbon Electrocatalysts. *ACS Applied Energy Materials* 2017, 1 (1), 68-77.
132. Martinaiou, I.; Wolker, T.; Shahraei, A.; Zhang, G.-R.; Janßen, A.; Wagner, S.; Weidler, N.; Stark, R. W.; Etzold, B. J. M.; Kramm, U. I., Improved electrochemical performance of Fe-N-C catalysts through ionic liquid modification in alkaline media. *Journal of Power Sources* 2018, 375, 222-232.
133. Zhang, J., *PEM Fuel Cell Electrocatalysts and Catalyst Layers Fundamentals and Applications*. Springer: 2008.
134. Herranz, J.; Jaouen, F.; Lefevre, M.; Kramm, U. I.; Proietti, E.; Dodelet, J.-P.; Bogdanoff, P.; Fiechter, S.; Abs-Wurbach, I.; Bertrand, P.; Arruda, T.; Mukerjee, S., Unveiling N-Protonation and Anion-Binding Effects on Fe/N/C-Catalysts for O₂ Reduction in PEM Fuel Cells. *J. Phys. Chem. C* 2011, 115, 16087–16097.
135. Lalande, G.; Côté, R.; Tamizhmani, G.; Guay, D.; Dodelet, J. P.; Dignard-Bailey, L.; Weng, L. T.; Bertrand, P., Physical, Chemical and Electrochemical Characterization of Heat-Treated Tetracarboxylic Cobalt Phthalocyanine Absorbed on Carbon Black as Electrocatalyst for Oxygen Reduction on Polymer Electrolyte Fuel Cells. *Electrochimica Acta* 1995, 40 (16), 2635-2646.
136. Wu, G.; Chen, Z.; Artyushkova, K.; Garzon, F. H.; Zelenay, P., Polyaniline-derived Non-Precious Catalyst for the Polymer Electrolyte Fuel Cell Cathode. *ECS Transactions* 2008, 16 (2), 159-170.
137. Hamann, C. H.; Vielstich, W., *Elektrochemie*. Wiley-VCH: Weinheim, 2005; Vol. 4.
138. Grove, W. R., XXIV. On voltaic series and the combination of gases by platinum. *The London, Edinburgh, and Dublin Philosophical Magazine and Journal of Science* 1839, 14 (86-87), 127-130.
139. Thomas, J. M., W.R. Grove and the fuel cell. *Philosophical Magazine* 2012, 92 (31), 3757-3765.
140. Bossel, U., *The birth of the fuel cell : 1835-1845. Including the first publication of the complete correspondence from 1839 to 1868 between Christian Friedrich Schoenbein (discoverer of the fuel cell effect) and William Robert Grove (inventor of the fuel cell)*. European Fuel Cell Forum: Oberrohrdorf/Switzerland, 2000.

141. Burke, K. A. Fuel Cells for Space Science Applications *NASA/TM—2003-212730* [Online], 2003. (accessed 2019-09-30T07:53:28+00:00Z).
142. Kordesch, K.; Hacker, V.; Reichmann, K.; Cifrain, M.; Hejze, T., The Safe and Economic Revival of Alkaline Hydrogen/Air Fuel Cells with Circulating Electrolytes, Recommended for Vehicles Using Battery Hybrid Systems and H₂ from Ammonia Crackers. *ECS Transactions* 2008, 11.
143. EG&G Technical Services, I., *Fuel Cell Handbook*. U.S. Department of Energy Office of Fossil Energy National Energy Technology Laboratory P.O. Box 880 Morgantown, West Virginia 26507-0880: 2004.
144. Basu, S., *Recent Trends in Fuel Cell Science and Technology*. Springer: 2007.
145. Yumiya, H.; Kizaki, M.; Asai, H., Toyota Fuel Cell System (TFCS). *World Electric Vehicle Journal* 2015, 7, 85-92.
146. Banham, D.; Ye, S., Current Status and Future Development of Catalyst Materials and Catalyst Layers for Proton Exchange Membrane Fuel Cells: An Industrial Perspective. *ACS Energy Letters* 2017, 2 (3), 629-638.
147. Cooper, K. R., *Experimental Methods and Data Analyses for Polymer Electrolyte Fuel Cells*. Scribner: 2016.
148. de Frank Bruijn, A.; Janssen, G. J. M., PEM Fuel Cell Materials: Costs, Performance and Durability. In *Fuel Cells*, 2013; pp 249-303.
149. Milliken, J. *Hydrogen, Fuel Cells and Infrastructure Technologies Program: Multiyear Research, Development and Demonstration Plan*; DOE/GO-102007-2430; TRN: US200803%%133 United States 10.2172/920934 TRN: US200803%%133 NREL English; ; National Renewable Energy Lab. (NREL), Golden, CO (United States): 2007; p Medium: ED; Size: 332 pp.
150. Greenwood, N. N.; Gibb, T. C., *Mössbauer Spectroscopy*. Chapman and Hall Ltd.: London, 1971.
151. Gütlich, P.; Bill, E.; Trautwein, A. X., *Mössbauer Spectroscopy and Transition Metal Chemistry Fundamentals and Applications*. Springer: Heidelberg, 2011.
152. Röhlsberger, R., *Nuclear Condensed Matter Physics with Synchrotron Radiation Basic Principles, Methodology and Applications*. Springer Berlin Heidelberg New York, 2004.
153. Ruffer, R., Nuclear resonance scattering. *Comptes Rendus Physique* 2008, 9 (5-6), 595-607.
154. Huenges, A.; Achterhold, K.; Parak, F. G., Mössbauer Spectroscopy in the Energy and in the Time Domain, a Crucial Tool for the Investigation of Protein Dynamics. *Hyperfine Interactions* 2002, 144/145, 209-222.
155. Yoshida, Y.; Langouche, G., *Mössbauer Spectroscopy*. Springer Heidelberg New York Dordrecht London, 2013.
156. van Bürck, U.; Siddons, D. P.; Hastings, J. B.; Bergmann, U.; Hollatz, R., Nuclear forward scattering of synchrotron radiation. *Physical Review B* 1992, 46 (10), 6207-6211.
157. Kuhn, W., LXVIII. Scattering of thorium C'' γ -radiation by radium G and ordinary lead. *The London, Edinburgh, and Dublin Philosophical Magazine and Journal of Science* 1929, 8 (52), 625-636.
158. Mössbauer, R. L., Kernresonanzabsorption von γ -Strahlung in Ir191. *The Science of Nature* 1958 45 (22), 538-539.
159. Kalvius, M.; Kienle, P., *The Rudolf Mössbauer Story His Scientific Work and Its Impact on Science and History*. Springer Heidelberg Dordrecht London New York, 2012.
160. Mössbauer, R. L., Recoilless Nuclear Resonance Absorption of Gamma Radiation. In *Noble Prize Organisation, Nobel Lecture*: 1961.
161. Frauenfelder, H., *The Mössbauer Effect*. 1962.
162. DeBenedetti, S.; Lang, G.; Ingalls, R., Electric Quadrupole Splitting and the Nuclear Volume Effect in the Ions of Fe⁵⁷. *Physical Review Letters* 1961, 6 (2), 60-62.
163. Cerantola, V.; Bykova, E.; Kuppenko, I.; Merlini, M.; Ismailova, L.; McCammon, C.; Bykov, M.; Chumakov, A. I.; Petitgirard, S.; Kantor, I.; Svitlyk, V.; Jacobs, J.; Hanfland, M.; Mezouar, M.;

- Prescher, C.; Ruffer, R.; Prakapenka, V. B.; Dubrovinsky, L., Stability of iron-bearing carbonates in the deep Earth's interior. *Nature Communications* 2017, 8, 15960.
164. Herranz, J.; Jaouen, F.; Lefevre, M.; Kramm, U. I.; Proietti, E.; Dodelet, J. P.; Bogdanoff, P.; Fiechter, S.; Abs-Wurmbach, I.; Bertrand, P.; Arruda, T. M.; Mukerjee, S., Unveiling N-protonation and anion-binding effects on Fe/N/C-catalysts for O₂ reduction in PEM fuel cells. *J Phys Chem C Nanomater Interfaces* 2011, 115 (32).
165. Sougrati, M. T.; Goellner, V.; Schuppert, A. K.; Stievano, L.; Jaouen, F., Probing active sites in iron-based catalysts for oxygen electro-reduction: A temperature-dependent ⁵⁷Fe Mössbauer spectroscopy study. *Catalysis Today* 2016, 262, 110-120.
166. Schünemann, V., Grundlagen der Mößbauer Spektroskopie. Kaiserslautern, 2017.
167. Schünemann, V.; Winkler, H., Structure and Dynamics of Biomolecules studied by Mössbauer Spectroscopy. *Reports on Progress in Physics* 2000, 63, 263-353.
168. Grave, E. D.; Alboom, A. V., Evaluation of Ferrous and Ferric Mössbauer Fractions. *Phys. Chem. Minerals* 1991, 18, 337-342.
169. Nussbaum, R. H.; Housley, R. M., Internal Conversion in Fe⁵⁷ from the Mössbauer Effect in Iron *Nuclear Physics* 1965, 68, 145-152.
170. Grave, E. D.; Vochten, R., An ⁵⁷Fe Mössbauer Effect Study of Ankerite. *Phys. Chem. Minerals* 1985, 12, 108-113.
171. Sturhahn, W.; Chumakov, A., Lamb-Mössbauer factor and second-order Doppler shift from inelastic nuclear resonant absorption. *Hyperfine Interactions* 1999, 123/124, 809-824.
172. Chumakov, A. I.; Sturhahn, W., Experimental aspects of inelastic nuclear resonance scattering. *Hyperfine Interactions* 1999, 123/124, 781-808.
173. Sturhahn, W., CONUSS and PHOENIX: Evaluation of nuclear resonant scattering data. *Hyperfine Interactions* 2000, 125 149-172.
174. Gütlich, P.; Garcia, Y., Chemical Applications of Mössbauer Spectroscopy. 2013, 23-89.
175. Gibb, T. C., *Principles of Mössbauer Spectroscopy* Springer U.S.: 1976.
176. Fluck, E.; Kerler, W.; Neuwirth, W., The Mössbauer Effect and its Significance in Chemistry. *Angewandte Chemie International Edition* 1963, 2 (6), 211-332.
177. Gütlich, P., Mössbauer Spectroscopy-Principles and Applications. Grunert, M.; Ksenofontov, V.; Seredyuk, M.; Stumm, U., Eds. Universität Mainz: https://www.blogs.uni-mainz.de/fb09akguetlich/files/2017/11/Moessbauer_Lectures.pdf, 2017.
178. Pound, R. V.; G. A. Rebka, J., Variation with Temperature of the Energy of Recoil-free Gamma Rays from Solids. *Physical Review Letters* 1960, 4 (6).
179. Debrunner, P. G., 2 Mößbauer Spectroscopy of Iron Porphyrins. In *Iron Porphyrins Part 3*, Lever, A. B. P.; Gray, H. B., Eds. Wiley-VCH: 1989; pp 139-234.
180. Debrunner, P. G., *Mössbauer Spectroscopy of Iron Porphyrins*. 1989.
181. Münck, E.; Groves, J. L.; Toumolillo, T. A.; Debrunner, P. G., Computer Simulations of Mössbauer Spectra for an effective Spin $S = 1/2$ Hamiltonian. *Computer Physics Communications* 1973, 5, 225-238.
182. Huynh, B. H.; Kent, T. A., Advances in inorganic Biochemistry. In *Advances in Inorganic Biochemistry*, Eichhorn, G. L.; Marzilli, L. G., Eds. Elsevier: NewYork, Amsterdam, Oxford, 1984.
183. Trautwein, A. X.; Bill, E.; Bominaar, E. L.; Winkler, H., Iron-containing proteins and related analogs — complementary Mössbauer, EPR and magnetic susceptibility studies. *Struct. Bonding* 1991, 78 (1), 1.
184. Jung, C. W.; Jacobs, P., Physical and chemical properties of superparamagnetic iron oxide MR contrast agents: Ferumoxides, ferumoxtran, ferumoxsil. *Magnetic Resonance Imaging* 1995, 13 (5), 661-674.
185. Knyazev, Y. V.; Balaev, D. A.; Kirillov, V. L.; Bayukov, O. A.; Mart'yanov, O. N., Mössbauer Spectroscopy Study of the Superparamagnetism of Ultrasmall ϵ -Fe₂O₃ Nanoparticles. *JETP Letters* 2018, 108 (8), 527-531.
186. Blume, M., Temperature-Dependent Spin-Spin Relaxation Times: Application to the Mössbauer Spectra of Ferric Hemin. *Physical Review Letters* 1967, 18 (9), 305-308.

187. Janoschka, A.; Svenconis, G.; Schünemann, V., A closed cycle-cryostat for high-field Mössbauer spectroscopy. *Journal of Physics: Conference Series International Conference on the Applications of the Mössbauer Effect (ICAME 2009)* 2010, 217.
188. Trautwein, A. X.; Bill, E.; Bominaar, E. L.; Winkler, H., Iron-Containing Proteins and Related Analogs-Complementary Mössbauer, EPR and Magnetic Susceptibility Studies. In *Bioinorganic Chemistry. Structure and Bonding*, Springer: Berlin, Heidelberg, 1991; Vol. 78.
189. Morozan, A.; Sougrati, M. T.; Goellner, V.; Jones, D.; Stievano, L.; Jaouen, F., Effect of Furfuryl Alcohol on Metal Organic Framework-based Fe/N/C Electrocatalysts for Polymer Electrolyte Membrane Fuel Cells. *Electrochimica Acta* 2014, 119, 192-205.
190. Wickman, H. H.; Klein, M. P.; Shirley, D. A., Paramagnetic Hyperfine Structure and Relaxation Effects in Mössbauer Spectra: Fe⁵⁷ in Ferrichrome. *Physical Review* 1966, 152 (1).
191. Bill, E.; Schünemann, V.; Trautwein, A. X.; Weiss, R.; Fischer, J.; Tabard, A.; Guillard, R., Mössbauer investigations of the hexachlorantimonate salt of the phenyliron 2,3,7,8,12,13,17,18-octaethyl-5,10,15,20-tetraphenylporphyrinate, [Fe(oetpp)Ph]SbCl₆ and X-ray structure of the phenyliron(III) precursor Fe(III)(oetpp)Ph. *Inorganica Chimica Acta* 2002, 420, 420-426.
192. Kohn, V. G.; Smirnov, G. V., Synchrotron radiation time spectra affected by diffusion: theory. *Hyperfine Interactions* 1999, 123/124 327-345.
193. Sturhahn, W.; Alp, E. E.; Toellner, T. S.; Hession, P.; Hu, M.; Sutter, J., Introduction to nuclear resonant scattering with synchrotron radiation. *Hyperfine Interactions* 1998, 113, 47-58.
194. Scheidt, W. R.; Li, J.; Sage, J. T., What Can Be Learned from Nuclear Resonance Vibrational Spectroscopy: Vibrational Dynamics and Hemes. *Chem Rev* 2017, 117 (19), 12532-12563.
195. Visscher, W. M., Study of lattice vibrations by resonance absorption of nuclear gamma rays. *Annals of Physics* 1960, 9 (2), 194-210.
196. Seto, M.; Yoda, Y.; Kikuta, S.; Zhang, X. W.; Ando, M., Observation of Nuclear Resonant Scattering Accompanied by Phonon Excitation Using Synchrotron Radiation. *Physical Review B* 1995, 74 (19).
197. Vankó, G.; Bottyán, L.; Nagy, D. L.; Szilágyi, E.; Vértes, A., Nuclear Inelastic Scattering of Synchrotron Radiation on Solutions of ⁵⁷Fe Complexes. *Journal of Radioanalytical and Nuclear Chemistry* 2000, 246 (1), 97-100.
198. Chumakov, A. I.; Niesen, L.; Nagy, D. L.; Alp, E. E., Nuclear resonant scattering of synchrotron radiation by multilayer structures. *Hyperfine Interactions* 1999, 123/124, 427-454.
199. Chumakov, A. I.; Ruffer, R.; Baron, A. Q. R.; Grünsteudel, H.; Grünsteudel, H. F., Temperature dependence of nuclear inelastic absorption of synchrotron radiation in alpha-Fe 57. *PHYSICAL REVIEW B* 1996, 54 (14).
200. Ruffer, R.; Chumakov, A. I., Nuclear Resonance Beamline at ESRF. *Hyperfine Interactions* 1996, 97/98, 589-604.
201. Scheidt, W. R.; Durbin, S. M.; Sage, J. T., Nuclear resonance vibrational spectroscopy--NRVS. *J Inorg Biochem* 2005, 99 (1), 60-71.
202. Zeng, W.; Silvernail, N. J.; Scheidt, W. R.; Sage, J. T., Nuclear Resonance Vibrational Spectroscopy (NRVS). In *Encyclopedia of Inorganic Chemistry*, 2008.
203. Lipkin, H. J., Mössbauer sum rules for use with synchrotron sources. *Hyperfine Interactions* 1999, 123/124, 349-366.
204. Sage, J. T.; Paxson, C.; Wyllie, G. R. A.; Sturhahn, W.; Durbin, S. M.; Champion, P. M.; Alp, E. E.; Scheidt, W. R., Nuclear Resonance Vibrational Spectroscopy of a Protein Active-Site Mimic. *J. Phys.: Condens. Matter* 2001, 13.
205. Trammell, G. T.; Hannon, J. P., Quantum beats from nuclei excited by synchrotron pulses. *Physical Review B* 1978, 18 (1), 165-172.
206. Hannon, J. P.; Trammell, G. T., Coherent Excitation of Nuclei in Crystals by Synchrotron Radiation Pulses *Physica B* 1989, 159, 161-167.
207. Winkler, H., Myoglobin and Related Biomolecular Systems Studied with Mössbauer Spectroscopy and Nuclear Forward Scattering. *Hyperfine Interactions* 2002, 144/145, 199-207.

208. Haas, M.; Realo, E.; Winkler, H.; Meyer-Klaucke, W.; Trautwein, A. X.; Leupold, O.; Rüter, H. D., Nuclear resonant forward scattering of synchrotron radiation by randomly oriented iron complexes which exhibit nuclear Zeeman interaction. *Physical Review B* 1997, 56 (21).
209. Paulsen, H.; Schünemann, V.; Trautwein, A. X.; Winkler, H., Mössbauer studies of coordination compounds using synchrotron radiation. *Coordination Chemistry Reviews* 2005, 249 (1-2), 255-272.
210. Potapkin, V.; Chumakov, A. I.; Smirnov, G. V.; Celse, J.-P.; Rüffer, R.; McCammon, C.; Dubrovinsky, L., The ^{57}Fe Synchrotron Mössbauer Source at the ESRF. *Journal of Synchrotron Radiation* 2012, 19, 559–569.
211. Drescher, M., Elektronenspinresonanz-Spektroskopie. *Chem. Unserer Zeit* 2012, 46 (3), 150 – 157.
212. Kramm, U. I.; Fiechter, S.; Abs-Wurmbach, I.; Herrmann-Geppert, I.; Radnik, J.; Bogdanoff, P., Influence of the Electron-Density of FeN₄-Centers Towards the Catalytic Activity of Pyrolyzed FeTMPPCl-Based ORR-Electrocatalysts. *J. Electrochem. Soc.* 2011, 158 (1), B69-B78.
213. Klencsár, D. Z., Mosswin Manual.
214. Gunnlaugsson, H. P., Spreadsheet based analysis of Mössbauer spectra. *Hyperfine Interact* 2016, 237:79.
215. 09, G.; D.01, R.; Frisch, M. J., *Gaussian Inc. Wallingford CT* 2009.
216. Stoll, S.; Schweiger, A., EasySpin, a comprehensive software package for spectral simulation and analysis in EPR. *Journal of Magnetic Resonance* 2006, 178 (1), 42-55.
217. Birry, L.; Zagal, J. H.; Dodelet, J.-P., Does CO poison Fe-based catalysts for ORR? *Electrochemistry Communications* 2010, 12, 628–631.
218. Thorum, M. S.; Hankett, J. M.; Gewirth, A. A., Poisoning the Oxygen Reduction Reaction on Carbon-Supported Fe and Cu Electrocatalysts: Evidence for Metal-Centered Activity. *J. Phys. Chem. Lett.* 2011, 2, 295–298.
219. Gupta, S.; Fierro, C.; Yeager, E., The effects of cyanide on the electrochemical properties of transition metal macrocycles for oxygen reduction in alkaline solutions. *J. Electroanal. Chem.* 1991, 306, 239-250.
220. Burgess, J.; Twigg, M. V., Iron: Inorganic & Coordination Chemistry. In *Encyclopedia of Inorganic Chemistry*, John Wiley & Sons, Ltd.: 2006.
221. Li, W.; Yu, A.; Higgins, D. C.; Llanos, B. G.; Chen, Z., Biologically Inspired Highly Durable Iron Phthalocyanine Catalysts for Oxygen Reduction Reaction in Polymer Electrolyte Membrane Fuel Cells. *J. AM. CHEM. SOC.* 2010, 132, 17056–17058.
222. Malko, D.; Kucernak, A.; Lopes, T., In-situ Electrochemical Quantification of Active Sites in Fe-N/C Non-Precious Metal Catalysts. 2016.
223. Boldrin, P.; Malko, D.; Mehmood, A.; Kramm, U. I.; Wagner, S.; Paul, S.; Weidler, N.; Kucernak, A., Deactivation, reactivation and super-activation of Fe-N/C oxygen reduction electrocatalysts: Gas sorption, physical and electrochemical investigation using NO and O₂. *Applied Catalysis B: Environmental* 2021, 292, 120169.
224. Knauer, M. Elektrochemische Untersuchung zur Inhibitierung von Cobalt- und Eisenhaltigen Katalysatoren für die Sauerstoffreduktion. Freie Universität Berlin, Berlin, 2006.
225. Janßen, A.; Martinaiou, I.; Wagner, S.; Weidler, N.; Shahraei, A.; Kramm, U. I., Influence of Sulfur in the Precursor Mixture on the Structural Composition of Fe-N-C Catalysts. *Hyperfine Interaction submitted* 2017.
226. Kramm, U. I.; Lefèvre, M.; Bogdanoff, P.; Schmeißer, D.; Dodelet, J.-P., Analyzing Structural Changes of Fe–N–C Cathode Catalysts in PEM Fuel Cell by Mössbauer Spectroscopy of Complete Membrane Electrode Assemblies. *J. Phys. Chem. Lett.* 2014, 5, 3750–3756.
227. Schröder, A.; Wippermann, K.; Arlt, T.; Sanders, T.; Baumhöfer, T.; Kardjilov, N.; Hilger, A.; Mergel, J.; Lehnert, W.; Stolten, D.; Banhart, J.; Manke, I., Neutron radiography and current distribution measurements for studying cathode flow field properties of direct methanol fuel cells. *International Journal of Energy Research* 2014, 38 (7), 926-943.
228. Yang, L.; Larouche, N.; Chenitz, R.; Zhang, G.; Lefèvre, M.; Dodelet, J.-P., Activity, Performance, and Durability for the Reduction of Oxygen in PEM Fuel Cells, of Fe/N/C Electrocatalysts

Obtained from the Pyrolysis of Metal-Organic-Framework and Iron Porphyrin Precursors. *Electrochimica Acta* 2015, 159, 184-197.

229. Yin, X.; Lin, L.; Chung, H.-T.; Babu, S. K.; Martinez, U.; Purdy, G. M.; Zelenay, P., Effects of MEA Fabrication and Ionomer Composition on Fuel Cell Performance of PGM-free ORR Catalyst. *ECS Transactions* 2017, 77 (11), 1273-1281.

230. Blomquist, J.; Lång, H.; Larsson, R.; Widelöv, A., Pyrolysis Behaviour of Metalloporphyrins Part 2.-A Mossbauer Study of Pyrolysed Fe(III) Tetraphenylporphyrin Chloride. *J. Chem. Soc. Faraday Trans.* 1992, 88 (14), 2007-2011.

231. Kramm, U. I.; Zana, A.; Vosch, T.; Fiechter, S.; Arenz, M.; Schmeißer, D., On the Structural Composition and Stability of Fe-N-C Catalysts Prepared by an Intermediate Acid Leaching. *J. Solid State Electrochem.* 2016, 20, 969-981.

232. Bominaar, E. L.; Ding, X. Q.; Gismelseed, A.; Bill, E.; Winkler, H.; Trautwein, A. X.; Nasri, H.; Fischer, J.; Weiss, R., Structural, Mössbauer, and EPR investigations on two oxidation states of a five-coordinate, high-spin synthetic heme. Quantitative interpretation of zero-field parameters and large quadrupole splitting. *Inorganic Chemistry* 1992, 31 (10), 1845-1854.

233. Subramanian, J., *Electron Paramagnetic Resonance Spectroscopy of Porphyrins and Metalloporphyrins*. Elsevier Sci Publishing, Amsterdam: 1975; Vol. 1.

234. Schünemann, V.; Trautwein, A. X.; Rietjens, I. M. C. M.; Boersma, M. G.; Veeger, C.; Mandon, D.; Weiss, R.; Bahl, K.; Colapietro, C.; Piech, M.; Austin, R. N., Characterization of Iron(III) Tetramesitylporphyrin and Microperoxidase-8 Incorporated into the Molecular Sieve MCM-41. *Inorganic Chemistry* 1999, 38 (21), 4901-4905.

235. Ohgo, Y.; Chiba, Y.; Hashizume, D.; Uekusa, H.; Ozeki, T.; Nakamura, M., Novel spin transition between $S = 5/2$ and $S = 3/2$ in highly saddled iron(III) porphyrin complexes at extremely low temperatures. *Chemical Communications* 2006, (18), 1935-1937.

236. Petasis, D. T.; Hendrich, M. P., Quantitative Interpretation of Multifrequency Multimode EPR Spectra of Metal Containing Proteins, Enzymes, and Biomimetic Complexes. *Methods in enzymology* 2015, 563, 171-208.

237. Kozłowski, P. M.; Spiro, T. G.; Bérces, A.; Zgierski, M. Z., Low-Lying Spin States of Iron(II) Porphine. *The Journal of Physical Chemistry B* 1998, 102 (14), 2603-2608.

238. Barabanschikov, A.; Demidov, A.; Kubo, M.; Champion, P. M.; Sage, J. T.; Zhao, J.; Sturhahn, W.; Alp, E. E., Spectroscopic identification of reactive porphyrin motions. *The Journal of Chemical Physics* 2011, 135 (1), 015101.

239. Zeng, W.; Barabanschikov, A.; Wang, N.; Lu, Y.; Zhao, J.; Sturhahn, W.; Alp, E. E.; Sage, J. T., Vibrational dynamics of oxygenated heme proteins. *Chem. Commun.* 2012, 48, 6340-6342.

240. Sutherland, K. D.; Liu, L. V.; Lee, Y. M.; Kwak, Y.; Yoda, Y.; Saito, M.; Kurokuzu, M.; Kobayashi, Y.; Seto, M.; Que, L., Jr.; Nam, W.; Solomon, E. I., Nuclear Resonance Vibrational Spectroscopic Definition of Peroxy Intermediates in Nonheme Iron Sites. *J. Am. Chem. Soc.* 2016, 138 (43), 14294-14302.

241. Li, J.; Penp, Q.; Barabanschikov, A.; Pavlik, J. W.; Alp, E. E.; Sturhahn, W.; Zhao, J.; Schulz, C. E.; Sage, J. T.; Scheidt, W. R., New Perspectives on Iron-Ligand Vibrations of Oxyheme Complexes. *Chem. Eur. J.* 2011, 17, 11178 - 11185.

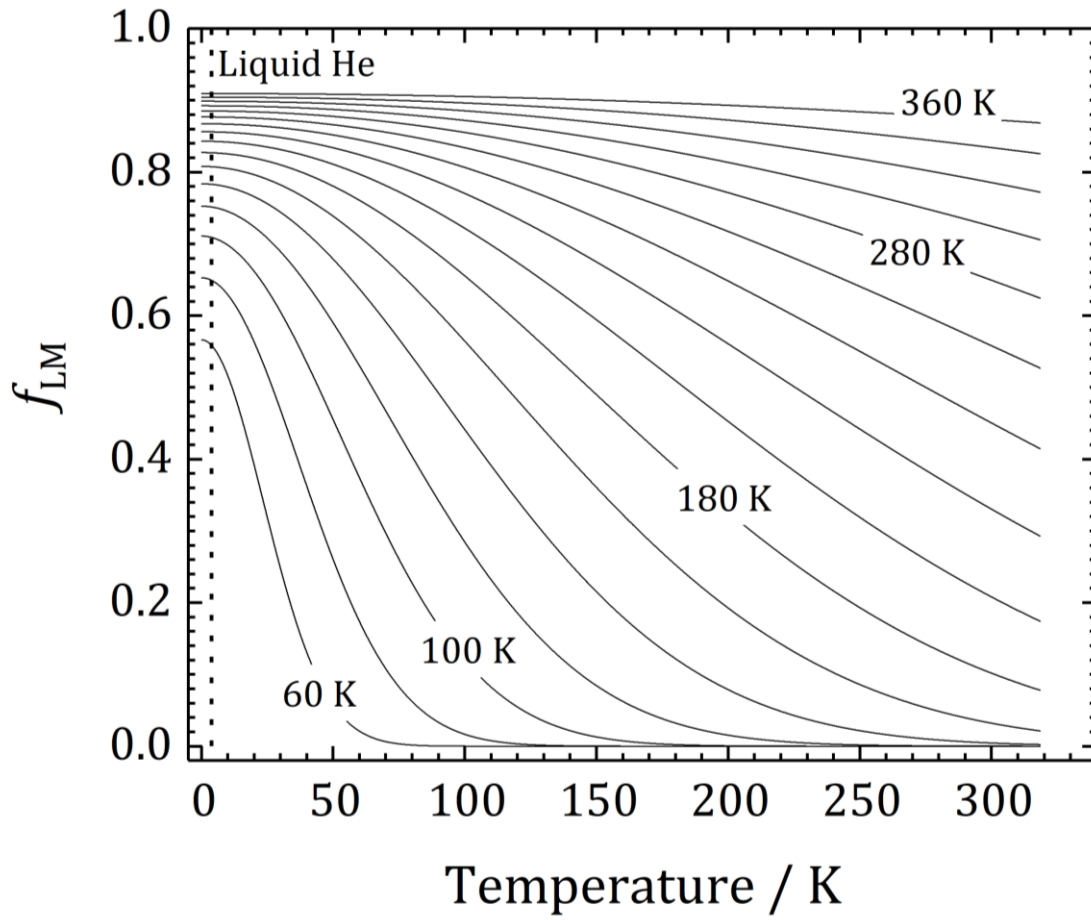
242. Rai, B. K.; Durbin, S. M.; Prohofskey, E. W.; Sage, J. T.; Wyllie, G. R. A.; Scheidt, W. R.; Sturhahn, W.; Alp, E. E., Iron Normal Mode Dynamics in (Nitrosyl)iron(II)tetraphenylporphyrin from X-ray Nuclear Resonance Data. *Biophysical Journal* 2002, 82, 2951-2963.

243. Roldan Cuenya, B.; Ono, L. K.; Croy, J. R.; Paredis, K.; Kara, A.; Heinrich, H.; Zhao, J.; Alp, E. E.; DelaRiva, A. T.; Datye, A.; Stach, E. A.; Keune, W., Size-dependent evolution of the atomic vibrational density of states and thermodynamic properties of isolated Fe nanoparticles. *Physical Review B* 2012, 86 (16).

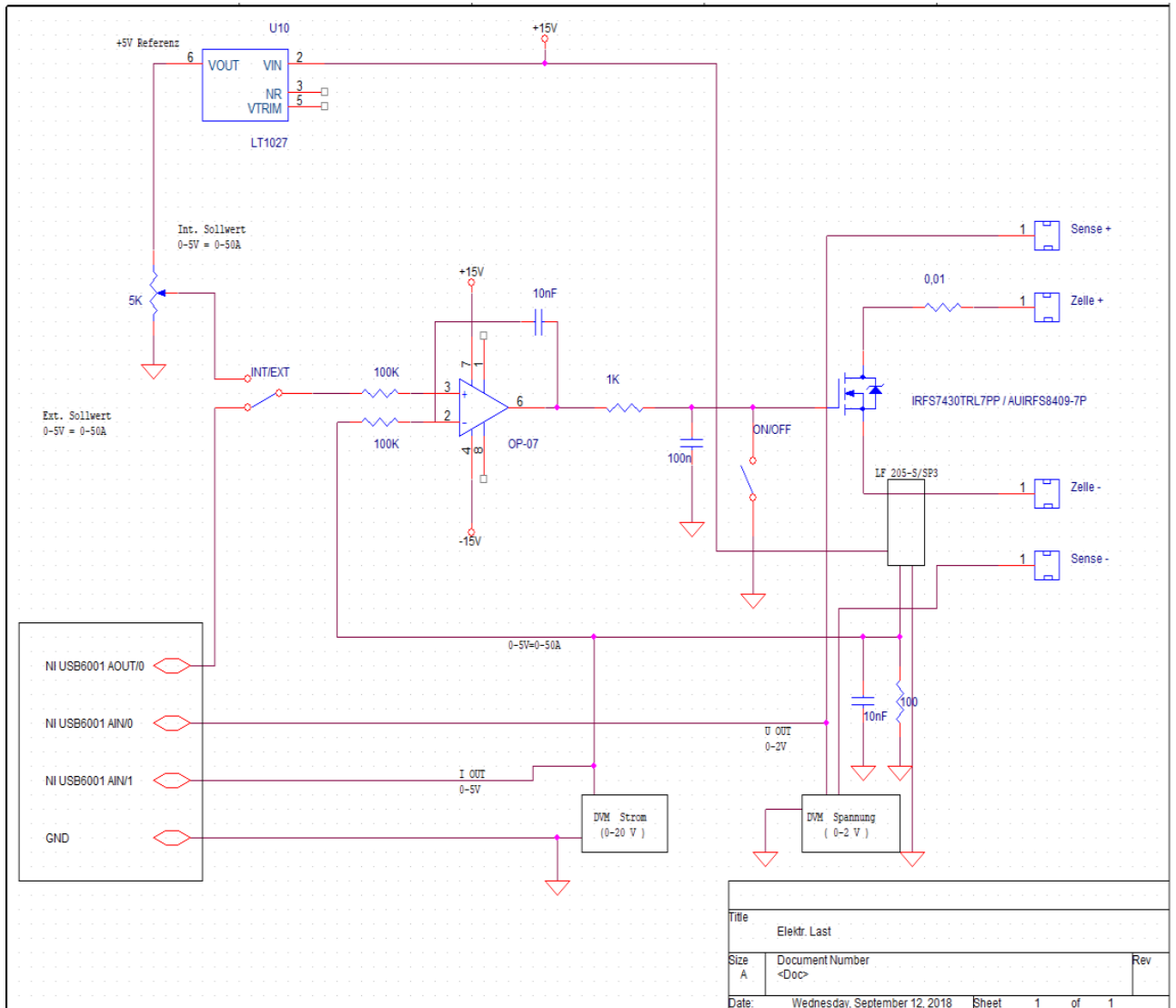
244. Marx, J.; Huang, H.; Faus, I.; Rackwitz, S.; Wolny, J. A.; Schlage, K.; Ulber, R.; Wille, H. C.; Schünemann, V., Simultaneous characterization of protein coated iron oxide nanoparticles with nuclear inelastic scattering and atomic force microscopy. *Hyperfine Interactions* 2013, 226 (1-3), 661-665.

245. Kramm, D. I. P. T. F. U. I. Die strukturelle Einbindung des Eisens in pyrolysierten Eisenporphyrin-Elektrokatalysatoren - eine ^{57}Fe Mößbauerspektroskopische Studie. Technischen Universität Berlin, Berlin, 2009.
246. Shylesh, S.; Schunemann, V.; Thiel, W. R., Magnetically separable nanocatalysts: bridges between homogeneous and heterogeneous catalysis. *Angew Chem Int Ed Engl* 2010, 49 (20), 3428-59.
247. Wagner, S.; Auerbach, H.; Tait, C. E.; Martinaiou, I.; Kumar, S. C. N.; Kubel, C.; Sergeev, I.; Wille, H. C.; Behrends, J.; Wolny, J. A.; Schunemann, V.; Kramm, U. I., Elucidating the Structural Composition of an Fe-N-C Catalyst by Nuclear- and Electron-Resonance Techniques. *Angew Chem Int Ed Engl* 2019, 58 (31), 10486-10492.
248. Li, H.; Tsay, K.; Wang, H.; Shen, J.; Wu, S.; Zhang, J.; Jiab, N.; Wessel, S.; Abouatallah, R.; Joos, N.; Schrooten, J., Durability of PEM fuel cell cathode in the presence of Fe^{3+} and Al^{3+} . *Journal of Power Sources* 2010, 195, 8089–8093.
249. Sulek, M.; Adams, J.; Kaberline, S.; Mark Ricketts; Waldecker, J. R., In situ metal ion contamination and the effects on proton exchange membrane fuel cell performance. *Journal of Power Sources* 2011, 196, 8967– 8972.
250. Roldan Cuenya, B.; Naitabdi, A.; Croy, J.; Sturhahn, W.; Zhao, J. Y.; Alp, E. E.; Meyer, R.; Sudfeld, D.; Schuster, E.; Keune, W., Atomic vibrations in iron nanoclusters: Nuclear resonant inelastic x-ray scattering and molecular dynamics simulations. *Physical Review B* 2007, 76 (19).
251. Li, J.; Noll, B. C.; Oliver, A. G.; Schulz, C. E.; Scheidt, W. R., Correlated ligand dynamics in oxyiron picket fence porphyrins: structural and Mossbauer investigations. *J. Am. Chem. Soc.* 2013, 135 (41), 15627-41.
252. Dale, B. W.; Williams, R. J. P.; Edwards, P. R.; Johnson, C. E., S=1 Spin State of Divalent Iron. II. A Mössbauer Effect Study of PhthalocyanineIron (II). *The Journal of Chemical Physics* 1968, 49 (3445).
253. Andres, H.; Bominaar, E. L.; Smith, J. M.; Eckert, N. A.; Holland, P. L.; Münck, E., Planar Three-Coordinate High-Spin FeII Complexes with Large Orbital Angular Momentum: Mössbauer, Electron Paramagnetic Resonance, and Electronic Structure Studies. *Journal of the American Chemical Society* 2002, 124 (12), 3012-3025.
254. Taube, R., New Aspects of the Chemistry of Transition Metal Phthalcyanines *Pure & Applied Chemistry* 1974, 38, 427.
255. Sahraie, N. R.; Kramm, U. I.; Steinberg, J.; Zhang, Y.; Thomas, A.; Reier, T.; Paraknowitsch, J.-P.; Strasser, P., Quantifying the Density and Utilization of Active Sites in Non-Precious Metal Oxygen Electroreduction Catalysts. *Nature Communications* 2015, 6, 8618.
256. Zitolo, A.; Goellner, V.; Armel, V.; Sougrati, M. T.; Mineva, T.; Stievano, L.; Fonda, E.; Jaouen, F., Identification of catalytic sites for oxygen reduction in iron- and nitrogen-doped graphene materials. *Nat Mater* 2015, 14 (9), 937-942.
257. Klug, D. D.; Zgierski, M. Z.; Tse, J. S.; Liu, Z.; Kincaid, J. R.; Czarnecki, K.; Hemley, R. J., Doming modes and dynamics of model heme compounds. *Proc Natl Acad Sci U S A* 2002, 99 (20), 12526-12530.
258. Ohta, T.; Shibata, T.; Kobayashi, Y.; Yoda, Y.; Ogura, T.; Neya, S.; Suzuki, A.; Seto, M.; Yamamoto, Y., A Nuclear Resonance Vibrational Spectroscopic Study of Oxy Myoglobins Reconstituted with Chemically Modified Heme Cofactors: Insights into the Fe-O₂ Bonding and Internal Dynamics of the Protein. *Biochemistry* 2018, 57 (48), 6649-6652.
259. Borsa, D. M.; Boerma, D. O., Phase Identification of Iron Nitrides and Iron Oxy-Nitrides with Mössbauer Spectroscopy. *Hypertfine Interactions* 2003, 151/152, 31-48.
260. Kurian, S.; Gajbhiye, N. S., Non-collinear spin structure of $\epsilon\text{-Fe}_x\text{N}$ ($2 < x < 3$) observed by Mössbauer spectroscopy. *Chemical Physics Letters* 2010, 489 (4-6), 195-197.
261. Borsa, D. M.; Boerma, D. O., Phase Identification of Iron Nitrides and Iron Oxy-Nitrides with Mössbauer Spectroscopy. *Hypertfine Interactions* 2003, 151/152 31-48.
262. Frątczak, E.; Gonzalez-Arrabal, R.; Borsa, D.; Boerma, D., Study of the phases of iron–nitride with a stoichiometry near to FeN. *Nuclear Instruments & Methods in Physics Research Section B-beam Interactions With Materials and Atoms - NUCL INSTRUM METH PHYS RES B* 2006, 249, 838-842.

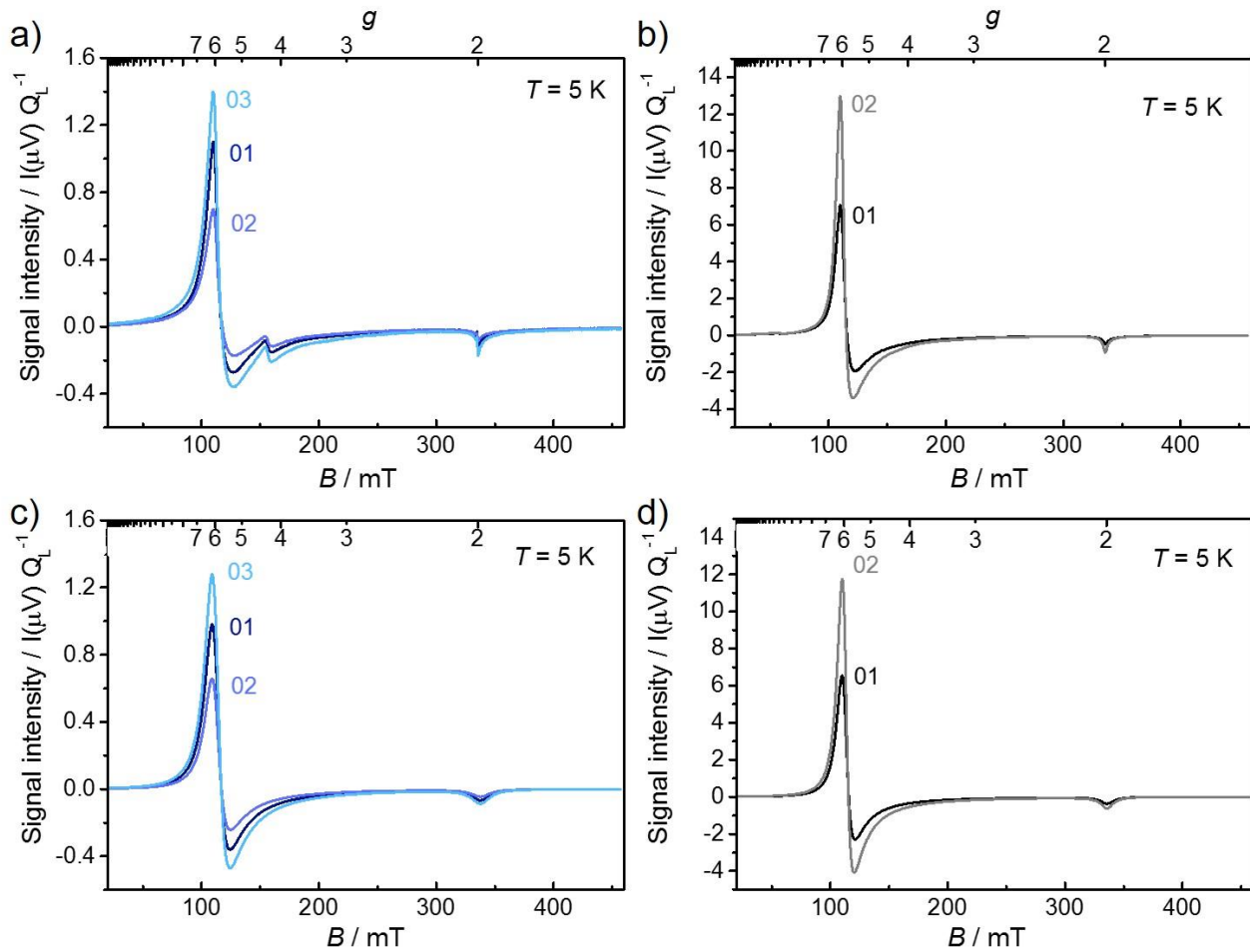
263. Dézsi, I.; Keszthelyi, L.; Kulgawczuk, D.; Molnár, B.; Eissa, N. A., Mossbauer Study of β - and δ -FeOOH and their Disintegration Products *phys. stat. sol.* 1967, 22, 617-629.
264. Kündig, W.; Bömmel, H.; Constabaris, G.; Lindquist, R. H., Some Properties of Supported Small α -Fe₂O₃ Particles Determined with the Mössbauer Effect. *Physical Review* 1966, 142 (2), 327-333.
265. Eisele, T. C.; Gabby, K. L., Review of Reductive Leaching of Iron by Anaerobic Bacteria. *Mineral Processing and Extractive Metallurgy Review: An International Journal* 2013, 35:2, 75-105.
266. Holby, E. F.; Wang, G.; Zelenay, P., Acid Stability and Demetalation of PGM-Free ORR Electrocatalyst Structures from Density Functional Theory: A Model for "Single-Atom Catalyst" Dissolution. *ACS Catalysis* 2020, 10 (24), 14527-14539.
267. Graat, P.; Somers, M.; Mittemeijer, E., On the kinetics of the initial oxidation of iron and iron nitride. *Zeitschrift für Metallkunde*, v.93, 532-539 (2002) 2002, 93.
268. Nishimaki, K.; Ohmae, S.; Yamamoto, T. A.; Katsura, M., Formation of Iron -Nitrides by the Reaction of Iron Nanoparticles with Stream of Ammonia. *Nano Structured Materials* 1999, 12, 527-530,.
269. Herber, R. H., Structure, Bonding, and the Mössbauer Lattice Temperature. In *Chemical Mössbauer Spectroscopy* Herber, R. H., Ed. Plenum Press: New York 1984.
270. Kaczmarzyk, T.; Jackowski, T.; Dziliński, K.; Sinyakov, G. N., Asymmetry in Mössbauer spectra of FeIII-azaporphyrin complexes. *NUKLEONIKA* 2007, 52, 93–98.
271. Blume, M., Magnetic Relaxation and Asymmetric Quadrupole Doublets in the Mössbauer Effect. *Physical Review Letters* 1965, 14 (4), 96-98.
272. Hambright, P.; Bearden, A. J., Mössbauer Spectroscopy and Magnetochemistry of Metalloporphyrins In *Porphyrins and Metalloporphyrins*, Smith, K. M., Ed. Elsevier Scientific Publishing Company: Netherlands, 1975.
273. Ruskov, T.; Asenov, S.; Spirov, I.; Garcia, C.; Mönch, I.; Graff, A.; Kozhuharova, R.; Leonhardt, A.; Mühl, T.; Ritschel, M.; Schneider, C. M.; Groudeva-Zotova, S., Mössbauer transmission and back scattered conversion electron study of Fe nanowires encapsulated in multiwalled carbon nanotubes. *Journal of Applied Physics* 2004, 96 (12), 7514-7518.
274. Kramm, U. I.; Herrmann-Geppert, I.; Fiechter, S.; Zehl, G.; Zizak, I.; Dorbandt, I.; Schmeißer, D.; Bogdanoff, P., Effect of Iron-Carbide Formation on the Number of Active Sites in Fe–N–C Catalysts for the Oxygen Reduction Reaction in Acidic Media. *J. Mater. Chem. A* 2014, 2, 2663–2670
275. Chen, Y.-L.; Yang, D.-P., *Mössbauer Effect in Lattice Dynamics: Experimental Techniques and Applications*. Wiley-VCH Verlag GmbH & Co. KGaA: 2007.



S 1: Calculated Lamb-Mössbauer factor based on equation (29) for ^{57}Fe . Different values for θ_M (from $\theta_M = 60$ K to $\theta_M = 360$ K) are given ²⁷⁵.



S 2: Circuit diagram of the electronic load to measure and manipulate the potential and current of the fuel cell during operation. The IFRS7430TRL7PP is the electric consumer made of a MOSFET.



S 3: Experimental X-band EPR spectra of the catalyst powder (a) and the precursor (b) ($\nu_{\text{mw}} = 9.39$ GHz and EPR spectral simulations for (c) the catalyst powder (Simulation parameters: $g_{\text{eff}} = [5.983 \ 5.983 \ 1.985]$ and Lorentzian line broadening of 10.6 – 10.9 mT) and (d) the precursor (Simulation parameters: $g_{\text{eff}} = [5.982 \ 5.983 \ 1.9956]$ and Lorentzian line broadening of 7 – 7.7 mT for the precursor.). See also SI of Wagner et al.⁵¹

Table S 1: Spectral areas and spin counts determined from X-band EPR ($\nu_{\text{mw}} = 9.39$ GHz) on two precursor samples (FeTMPPCl/CB) with known Fe(III) content⁵¹.

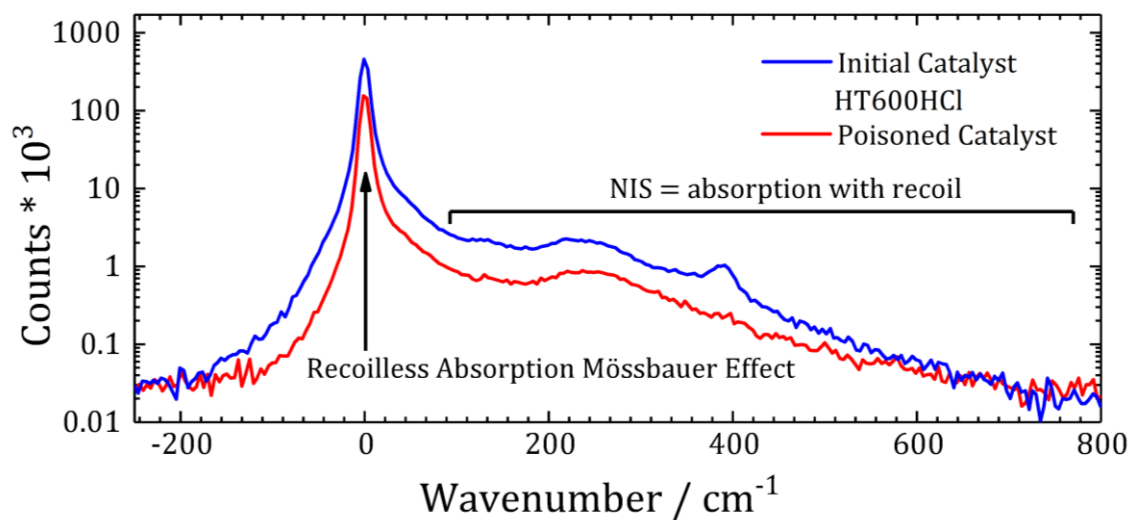
	Weight / mg	wt % Fe(III)	N_{spins}	Area (exp.*)	Area (simul.*)
FeTMPPCl/CB 01	2.08	1.62	$3.63 \cdot 10^{17}$	$4.83 \cdot 10^{-3}$	$4.84 \cdot 10^{-3}$
FeTMPPCl/CB 02	2.69	1.62	$4.69 \cdot 10^{17}$	$7.06 \cdot 10^{-3}$	$7.61 \cdot 10^{-3}$

Table S 2: Spectral areas, spin count and Fe(III) content determined from X-band EPR measurements on three samples of the catalyst by comparison with the precursor sample. Spin quantitation was performed based on a simulation of the high-spin Fe(III) EPR signal (values in parentheses are determined from the experimental data directly) ⁵¹.

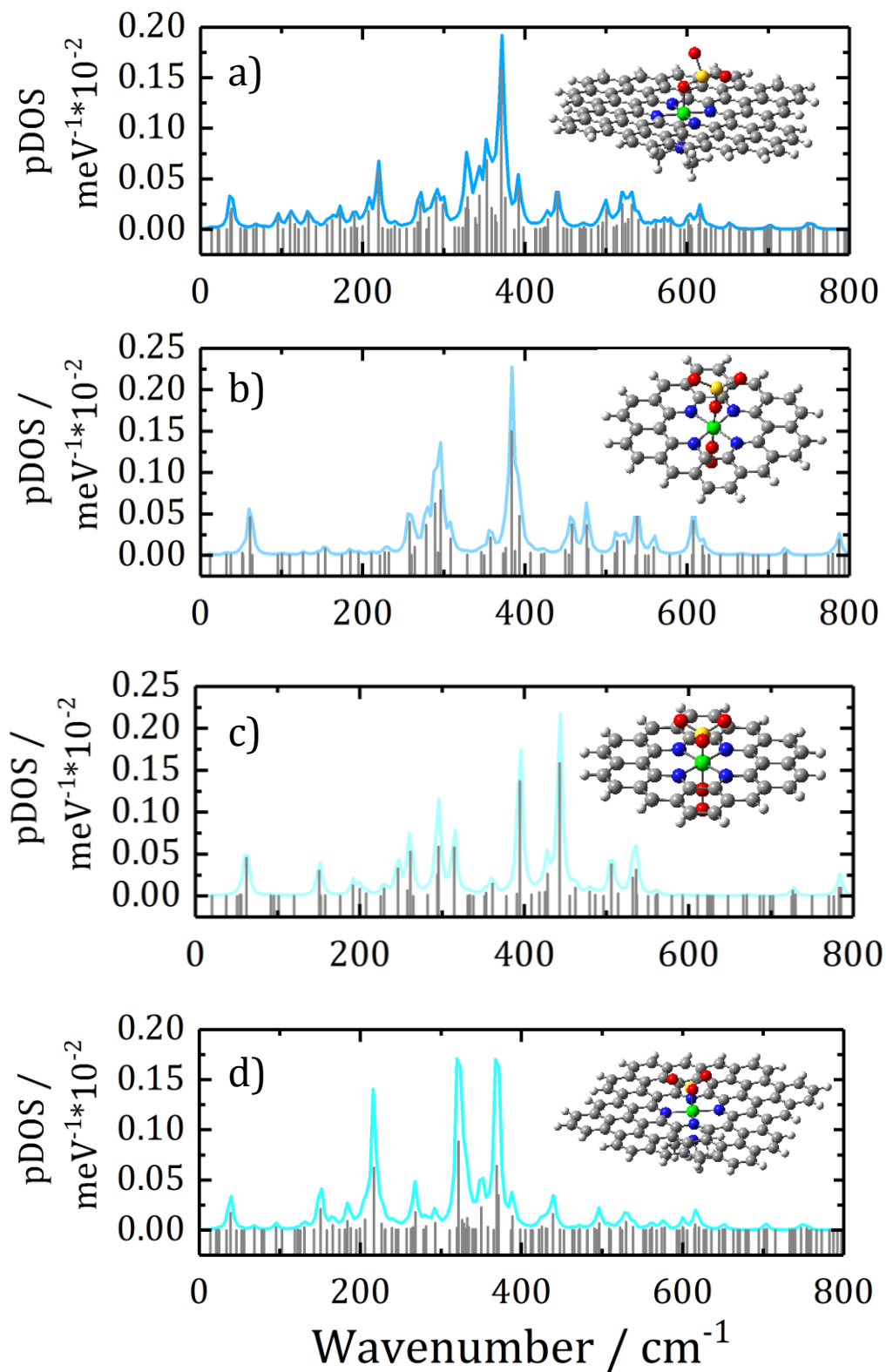
	weight / mg	Area* simul. (exp.)	N_{spins}		wt% Fe(III)		wt % Fe(III)	St. Dev.
			Ref 01	Ref 02	Ref 01	Ref 02		
Cat 01	2.38	$1.12 \cdot 10^{-3}$ ($1.42 \cdot 10^{-3}$)	$8.42 \cdot 10^{16}$ ($1.07 \cdot 10^{17}$)	$6.94 \cdot 10^{16}$ ($9.47 \cdot 10^{16}$)	0.33 (0.42)	0.27 (0.37)		
Cat 02	2.42	$7.84 \cdot 10^{-4}$ ($1.14 \cdot 10^{-3}$)	$5.87 \cdot 10^{16}$ ($8.57 \cdot 10^{16}$)	$4.83 \cdot 10^{16}$ ($7.59 \cdot 10^{16}$)	0.23 (0.33)	0.19 (0.29)		
Cat 03	2.46	$1.47 \cdot 10^{-3}$ ($1.82 \cdot 10^{-3}$)	$1.10 \cdot 10^{17}$ ($1.37 \cdot 10^{17}$)	$9.05 \cdot 10^{16}$ ($1.21 \cdot 10^{17}$)	0.41 (0.52)	0.34 (0.46)	0.29 (0.40)	0.08 (0.08)

corresponding measurement. All other measurement parameters were the same.

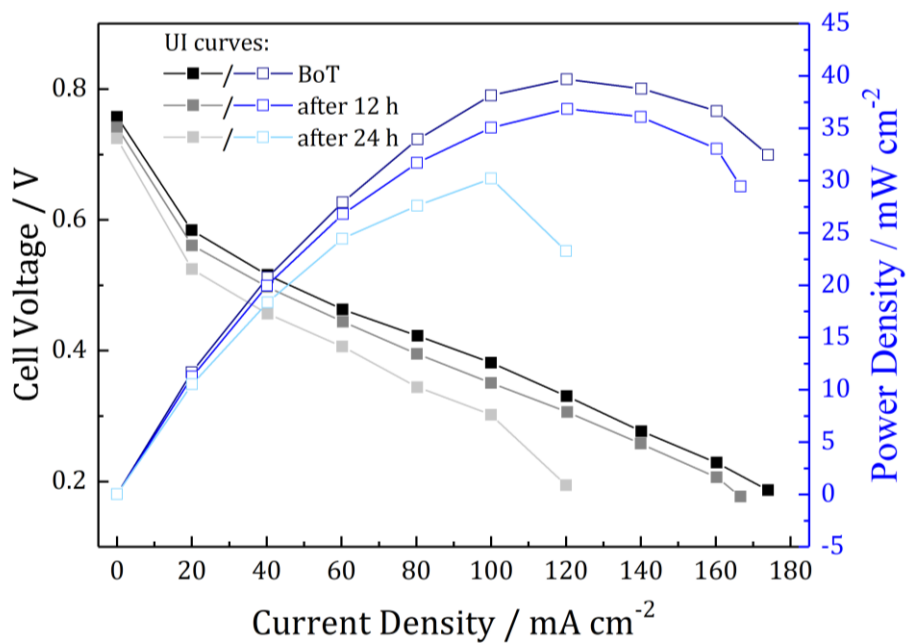
*The area corresponds to the double integral of the EPR spectrum divided by the Q-value determined for the



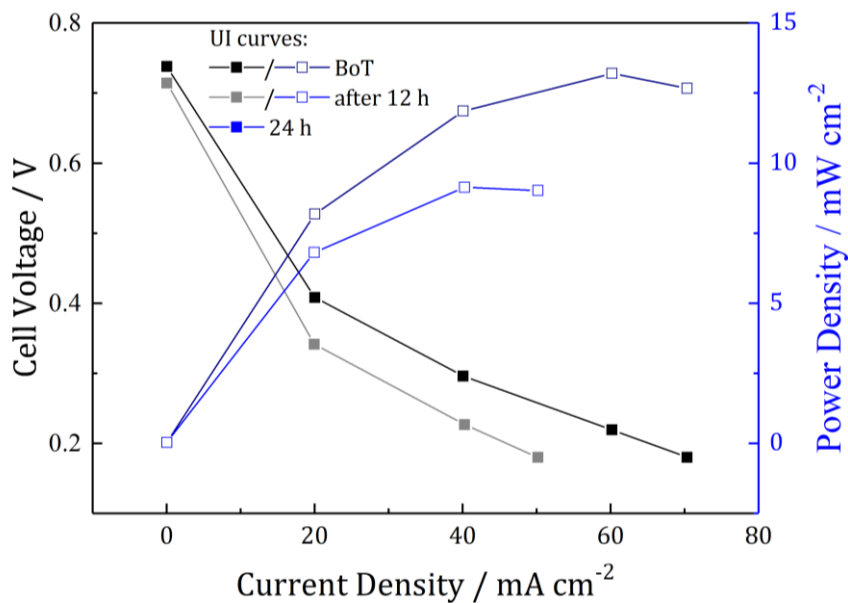
S 4: NIS spectrum of HT600HCl in the pristine and deactivated state.



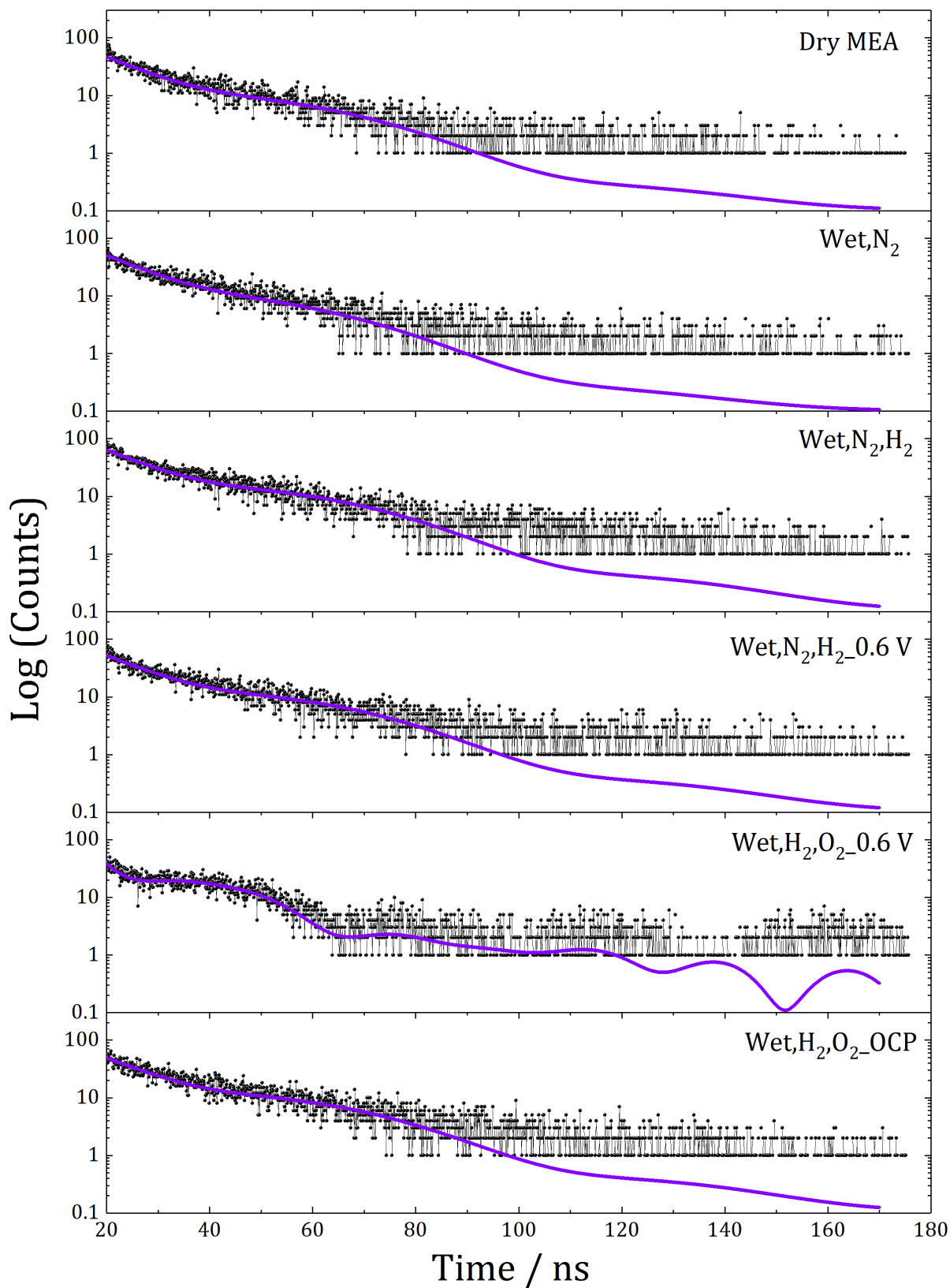
S 5: DFT calculations of four possible ways of sulfite ion attachment on FeN₄-site, a) Trimethylamin + SO₃²⁻ over O, b) O₂ + SO₃²⁻ over O, c) O₂ + SO₃²⁻ over S and d) Trimethylamin + SO₃²⁻ over S.



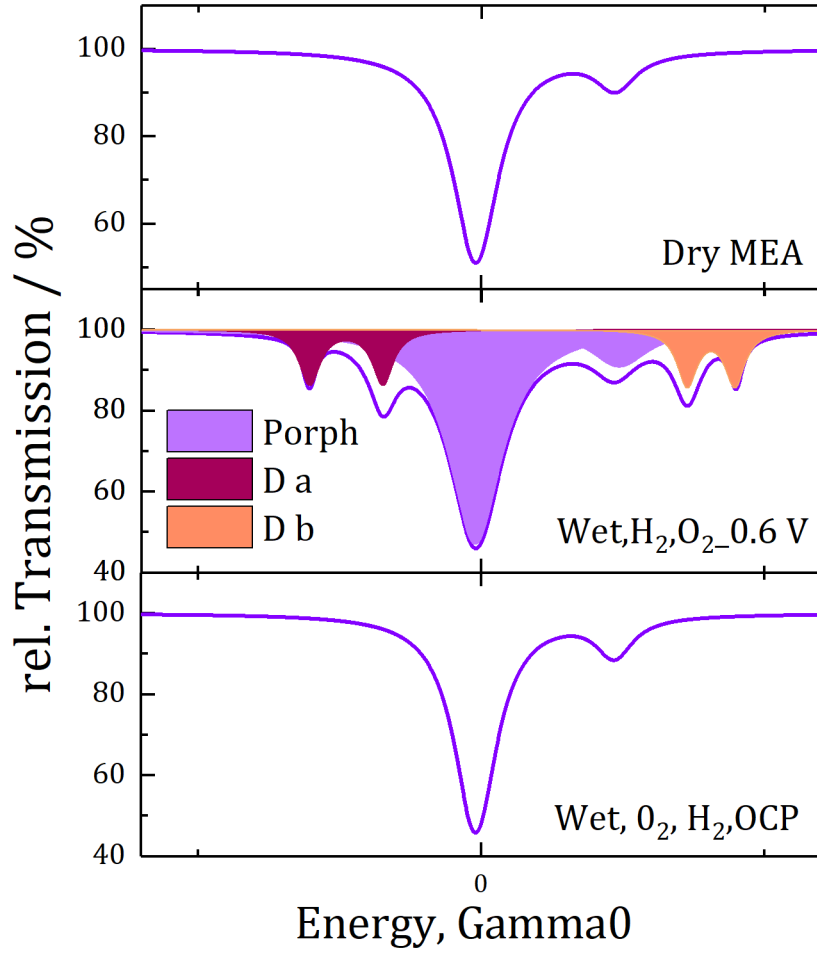
S 6: Low temperature (80 °C) fuel cell polarization curves of the Fe-N-C catalyst used for the post mortem Mössbauer study (5.3) at beginning of test, after 12h and 24 h. MEA 6 PEMFC was used for in total 24 hours.



S 7: High temperature (165 °C) fuel cell polarization curves of the Fe-N-C catalyst used for the post mortem Mössbauer study (5.3) at beginning of test and after 12h



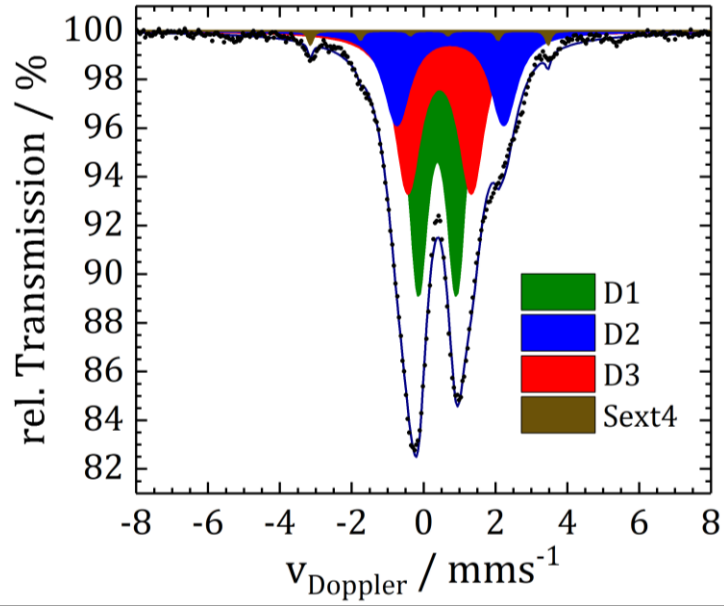
S 8: Fitting approach of the resulting operando NFS data of the model catalyst under different operation conditions.



S 9: Simulated Mössbauer spectra considering the iron species that were used for the fit of the NFS data. Data are provided in Table S 3.

Table S 3: Calculated Mössbauer parameters based on the model approach of S 9 and S 10.

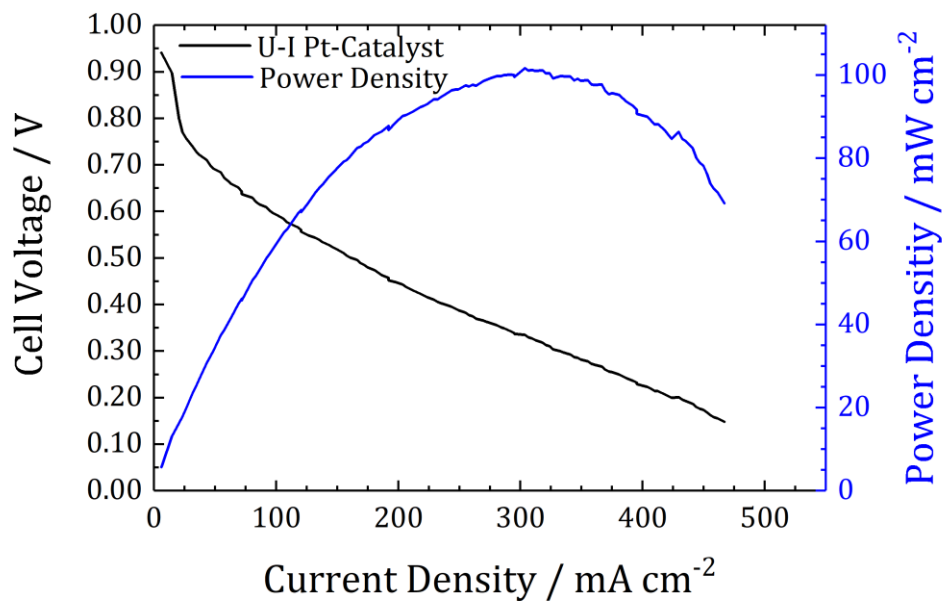
GDL	$\delta_{\text{iso}} / \text{mm s}^{-1}$	$\Delta E_{\text{Q}} / \text{mm s}^{-1}$	$\Gamma / \text{mm s}^{-1*}$	Area / %
Porph	0.48		1.58	75.6
D a	0.35	2.60	0.63	12.4
D b	0.46	3.64	0.60	12.0



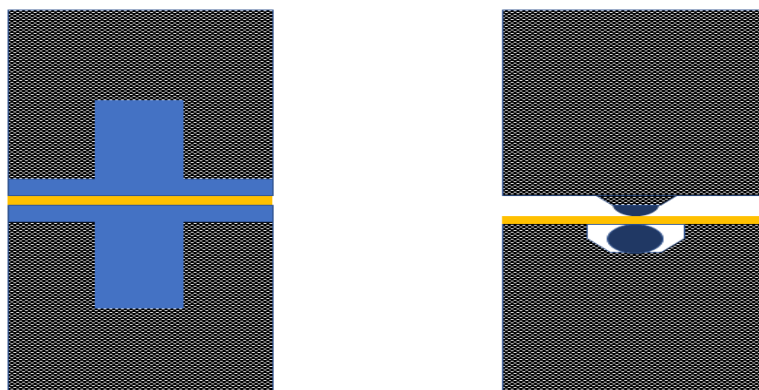
S 10: Mössbauer fitting with the Sext4 species.

Table S 4: Mössbauer parameters for the fitting approach including the sextet species.

GDL	$\delta_{\text{iso}} / \text{mm s}^{-1}$	$\Delta E_Q / \text{mm s}^{-1}$	B_{hf} / T	$\Gamma / \text{mm s}^{-1*}$	Area / %
D1	0.384 (0.002)	1.062 (0.003)	—	0.641*	42.0
D2	0.303 (0.004)	3.017 (0.013)	—	0.859*	21.3
D3	0.421 (0.004)	1.955 (0.012)	—	0.857*	35.4
Sext4	0.159 (0.007)		20.572 (0.048)	0.166	1.3



S 11: fuel cell polarization curve measured at the synchrotron after 1 h of operation with the operando FC setup. The test was performed for the Fe-N-C catalyst, catalyst loading and further conditions can be found in chapter 5.4.



S 12: (left) The sealing like it was used for the operando cell. The custom-made silicon sealing (blue) fix the membrane (orange) and tied the cell. (right) An advanced sealing design is shown. Here, two O-rings are used to close the cell. The lower O-ring (dark blue) is placed in a hollow, whereas the upper O-ring is fixed on a stamp. By bringing both flow field (black) together the membrane is fixed in between the O-rings and the cell is closed tightly without cutting through the membrane.

1. Conferences / Meetings

Energy Science and Engineering PhD Platform Conference 2019

September 27, 2019, Darmstadt

Oral presentation “In Situ Fuel Cell Tests of Fe-N-C Catalyst with Nuclear Forward Scattering”

7. PhD Candidate Conference “Darmstadt Graduate School of Excellence Energy Science and Engineering”

24.09. – 26.09.2019, Bad Buchenau

Bunsentagung 2019, 118th General Assembly of the German Bunsen Society for Physical Chemistry

30.05.-01.06.2019, Jena

Oral Presentation “Analysis of the structural composition of the Fe-N-C catalyst by nuclear resonance techniques“

28. Frankfurter Sonderkolloquium "Batterien und Brennstoffzellen - Elektrochemie für die Energiewende" DECHEMA Sonderkolloquium

07.02.2019, Frankfurt

DESY UsersMeeting

23.01. - 25.01.2019, Hamburg

Poster:

Analysis of the structural composition of the Fe-N-C catalyst by nuclear and electron resonance techniques

6. PhD Candidate Conference “Darmstadt Graduate School of Excellence Energy Science and Engineering”

26.09. – 28.09.2018, Friedrichsdorf

Main Organizer

Konferenz zur Forschung mit Synchrotronstrahlung (SNI)

16.09. – 19.09.2018, Garching

Poster: New insights on the identification of iron structures in Fe-N-C catalysts by Mössbauer spectroscopy and related techniques

International Society of Electrochemistry (ISE)

02.09.2019 – 07.09.2018, Bologna

Poster: New insights on the identification of iron structures in Fe-N-C catalysts by Mössbauer spectroscopy and related techniques

User Meeting ESRF 2018,

05.02.-07.02.2018, Grenoble

GeCat Infoday

23.10.2017, Frankfurt

Poster: "On the Application of Nuclear Forward Scattering for the Characterization of Fe-N-C Catalysts in PEM-Fuel Cells"

5. PhD Candidate Conference "Darmstadt Graduate School of Excellence Energy Science and Engineering"

27.09. – 29.09.2017, Trieste

ICAME 2017 (Mössbauer Conference), (St. Petersburg, Russia)

02.09.-08.09.2017

Oral presentation "On the effect of sulfate ions on the structural composition and ORR activity of Fe-N-C catalysts for PEM-fuel cells"

DGM Symposium "The Great Transition"

13.07.2017, Darmstadt

9. Darmstädter ENERGIEKONFERENZ Multidisziplinäre und digitale Perspektiven der Energiewende

02.03.2017, Darmstadt

KickOff Meeting NUKFER, BMBF-Project

23.01.2017, Kaiserlautern

4. PhD Candidate Conference "Darmstadt Graduate School of Excellence Energy Science and Engineering"

12.10. – 14.10.2016, Wald-Michelbach

2. List of Publications

Wagner, Stephan; Auerbach, Hendrik; Tait, Claudia E; Martinaiou, Ioanna; Kumar, Shyam CN; Kübel, Christian; Sergeev, Ilya; Wille, Hans-Christian; Behrends, Jan; Wolny, Juliusz A.; Elucidating the structural composition of a Fe-N-C catalyst by nuclear and electron resonance techniques, *Angewandte Chemie International Edition*, 2019, Wiley Online Library

Wagner, Stephan; Martinaiou, Ioanna; Shahraei, Ali; Weidler, Natascha; Kramm, Ulrike Ingrid.; On the effect of sulfite ions on the structural composition and ORR activity of Fe-NC catalysts, *Hyperfine Interactions*, 239, 1, 10, 2018, Springer

Boldrin, Paul; Malko, Daniel; Mehmood, Asad; Kramm, Ulrike I; Wagner, Stephan; Paul, Stephen; Weidler, Natascha; Kucernak, Anthony.; Deactivation, reactivation and super-activation of Fe-N/C oxygen reduction electrocatalysts: Gas sorption, physical and electrochemical investigation using NO and O₂, *Applied Catalysis B: Environmental*, 292, 120169, 2021, Elsevier

Luo, Fang; Wagner, Stephan; Onishi, Ichiro; Selve, Sören; Li, Shuang; Ju, Wen; Wang, Huan; Steinberg, Julian; Thomas, Arne; Kramm, Ulrike I.; Surface site density and utilization of platinum group metal (PGM)-free Fe-NC and FeNi-NC electrocatalysts for the oxygen reduction reaction, *Chemical Science*, 12, 1, 384-396, 2021, Royal Society of Chemistry

Fang Luo, Aaron Roy, Luca Silvioli, David A Cullen, Andrea Zitolo, Moulay Tahar Sougrati, Ismail Can Oguz, Tzonka Mineva, Detre Teschner, Stephan Wagner, Ju Wen, Fabio Dionigi, Ulrike Ingrid Kramm, Jan Rossmeisl, Frédéric Jaouen, Peter Strasser.; P-block single-metal-site tin/nitrogen-doped carbon fuel cell cathode catalyst for oxygen reduction reaction, *Nature Materials*, 19, 11, 1215-1223, 2020, Nature Publishing Group

Kübler, Markus; Wagner, Stephan; Jurzinsky, Tilman; Paul, Stephen; Weidler, Natascha; Gomez Villa, Eduardo D; Cremers, Carsten; Kramm, Ulrike I.; Impact of Surface Functionalization on the Intrinsic Properties of the Resulting Fe-N-C Catalysts for Fuel Cell Applications, *Energy Technology*, 8, 9, 2000433, 2020,

Martinaiou, Ioanna; Videla, Alessandro HA Monteverde; Weidler, Natascha; Kübler, Markus; Wallace, W David Z; Paul, Stephen; Wagner, Stephan; Shahraei, Ali; Stark, Robert W; Specchia, Stefania.; Activity and Degradation Study of an Fe-NC catalyst for ORR in Direct Methanol Fuel Cell (DMFC), *Applied Catalysis B: Environmental*, 118217, 2020, Elsevier

Zhang, Hanguang; Chung, Hoon Taek; Cullen, David A; Wagner, Stephan; Kramm, Ulrike Ingrid; More, Karren L; Zelenay, Piotr; Wu, Gang.; High-performance Fuel Cell Cathodes Exclusively Containing Atomically Dispersed Iron Active Sites, *Energy & Environmental Science*, 2019, Royal Society of Chemistry

Kramm, Ulrike I; Ni, Lingmei; Wagner, Stephan.; 57Fe Mössbauer Spectroscopy Characterization of Electrocatalysts, *Advanced Materials*, 1805623, 2019, Wiley Online Library

Leonard, Nathaniel D; Wagner, Stephan; Luo, Fang; Steinberg, Julian; Ju, Wen; Weidler, Natascha; Wang, Huan; Kramm, Ulrike I; Strasser, Peter.; Deconvolution of Utilization, Site Density, and Turnover Frequency of Fe-Nitrogen-Carbon Oxygen Reduction Reaction Catalysts Prepared with Secondary N-Precursors, *ACS Catalysis*, 8, 3, 1640-1647, 2018, ACS Publications

Martinaiou, Ioanna; Wolker, Thomas; Shahraei, Ali; Zhang, Gui-Rong; Janßen, Arne; Wagner, Stephan; Weidler, Natascha; Stark, Robert W; Etzold, Bastian JM; Kramm, Ulrike I; Improved electrochemical performance of Fe-NC catalysts through ionic liquid modification in alkaline media, *Journal of Power Sources*, 375, 222-232, 2018, Elsevier

Janßen, A; Martinaiou, I; Wagner, S; Weidler, N; Shahraei, A; Kramm, UI; Influence of sulfur in the precursor mixture on the structural composition of Fe-NC catalysts, *Hyperfine Interactions*, 239, 1, 7, 2018, Springer

Ziegler, Jürgen; Yang, Florent; Wagner, Stephan; Kaiser, Bernhard; Jaegermann, Wolfram; Urbain, Félix; Becker, Jan-Philipp; Smirnov, Vladimir; Finger, Friedhelm; Interface engineering of titanium oxide protected a-Si: H/a-Si: H photoelectrodes for light induced water splitting, *Applied Surface Science*, 389, 73-79, 2016, Elsevier

AJ Westphal, C Allen, S Bajt, R Bastien, H Bechtel, P Bleuet, J Borg, F Brenker, J Bridges, DE Brownlee, M Burchell, M Burghammer, AL Butterworth, P Cloetens, G Cody, T Ferroir, C Floss, GJ Flynn, D Frank, Z Gainsforth, E Grün, P Hoppe, B Hudson, A Kearsley, B Lai, L Lemelle, H Leroux, R Lettieri, W Marchant, A Nanz, LR Nittler, R Oglione, F Postberg, SA Sandford, S Schmitz, G Silversmit, A Simionovici, R Srama, F Stadermann, T Stephan, RM Stroud, J Susini, S Sutton, R Toucoulou, M Trieloff, P Tsou, A Tsuchiyama, T Tyliczszak, B Vekemans, L Vincze, J Warren, S Wagner, D Zevin, ME Zolensky; Analysis of "Midnight" Tracks in the Stardust Interstellar Dust Collector: Possible Discovery of a Contemporary Interstellar Dust Grain, *Lunar and Planetary Science Conference*, 41, 2050, 2010

Ni, Lingmei; Gallenkamp, Charlotte; Wagner, Stephan; Wallace, David; Paul, Stephen; Kübler, Markus; Krewald, Vera; Kramm, Ulrike Ingrid; Comparison of in-Situ 57 Fe Mössbauer Spectroscopic Data for Differently Prepared Fe-NC Catalysts, *ECS Meeting Abstracts*, 35, 1612, 2019, IOP Publishing

Kübler, Markus; Theis, Pascal; Ni, Lingmei; Wagner, Stephan; Jurzinsky, Tilman; Kramm, Ulrike Ingrid; Multiwalled Carbon Nanotubes As Non-Precious Metal Catalyst for the Oxygen Reduction Reaction, *ECS Meeting Abstracts*, 35, 1603, 2019, IOP Publishing

Chumakov, Aleksandr; Wagner, Stephan; Kübler, Markus; Kramm, Ulrike; Experiment title: Post mortem analysis of Fe-N-C catalysts for the oxygen reduction reaction (ORR) in proton exchange fuel cells-a synchrotron-based Mößbauer spectroscopic study, 2018,

Weidler, Natascha; Babu, Deepu J; Martinaiou, Ioanna; Paul, Stephen; Wagner, Stephan; Shahraei, Ali; Janßen, Arne; Stark, Robert W; Schneider, Jörg J; Kramm, Ulrike Ingrid; Effect of rf-Plasma Treatment on the Activity and Selectivity of Me-NC Electrocatalysts for the Oxygen Reduction Reaction, *ECS Transactions*, 80, 8, 691-700, 2017, The Electrochemical Society

